Fermions and bosons : excitons in strongly correlated materials
Rademaker, L.

Citation
Rademaker, L. (2013, December 11). *Fermions and bosons : excitons in strongly correlated materials*. *Casimir PhD Series*. Retrieved from https://hdl.handle.net/1887/22839

Version: Not Applicable (or Unknown)
License: Leiden University Non-exclusive license
Downloaded from: https://hdl.handle.net/1887/22839

Note: To cite this publication please use the final published version (if applicable).

Cover Page

Universiteit Leiden

Leiden University
Repository

The handle http://hdl.handle.net/1887/22839 holds various files of this Leiden University dissertation.

Author: Rademaker, Louk
Title: Fermions and bosons : excitons in strongly correlated materials
Issue Date: 2013-12-11

Fermions and Bosons
Excitons in strongly correlated materials

Proefschrift

ter verkrijging van
de graad van Doctor aan de Universiteit Leiden,
op gezag van Rector Magnificus prof. mr. C. J. J. M. Stolker,
volgens besluit van het College voor Promoties
te verdedigen op 11 december 2013
te klokke 15:00 uur

door

Louk Rademaker
geboren te Vleuten-De Meern (Utrecht), Nederland in 1986

Promotiecommissie

Promotoren:	prof. dr. J. Zaanen (Universiteit Leiden)
	prof. dr. ir. H. Hilgenkamp (Universiteit Twente and Universiteit Leiden)
Overige leden:	prof. dr. J. van den Brink (IFW Dresden)
	prof. dr. A. J. Millis (Columbia University)
	prof. dr. H. T. C. Stoof (Universiteit Utrecht)
	prof. dr. E. R. Eliel (Universiteit Leiden)
	prof. dr. C. W. J. Beenakker (Universiteit Leiden)

The cover shows the painting *Contra-compositie van dissonanten XVI* by Theo van Doesburg, Collectie Gemeentemuseum Den Haag. Reprinted with permission. Van Doesburg founded the famous 'De Stijl' art movement in Leiden. This painting is created in 1925, the year of birth for fermions: Pauli presented his exclusion principle and Uhlenbeck and Goudsmit discovered the electron spin.

The research presented in this thesis was supported by the Netherlands Organization for Scientific Research (NWO) through a Vici grant.

Casimir PhD Series, Delft-Leiden, 2013-25
ISBN 978-90-8593-166-9

Contents

1 *Introduction: Quantum Matters* 7

2 *Phenomenology of exciton bilayers* 13

2.1 *Bilayer excitons and condensation* 13

2.2 *Ginzburg-Landau theory and flux quantisation* 16

3 *Fermionic models of correlated bilayers* 23

3.1 *The Hubbard model and its problems* 23

3.2 *The BCS theory of electron-hole pairing* 26

3.3 *Numerical approach: Determinant Quantum Monte Carlo* 29

4 *Exciton-spin dynamics in the Mott insulating state* 47

4.1 *Strong coupling limit and the $t - J$ model* 47

4.2 *Frustration of a single exciton in an antiferromagnet* 57

5 *Exciton condensation in the $t - J$ model* 75

5.1 *Enhanced spin itineracy in the exciton condensate* 76

5.2 *Finite exciton densities: the full phase diagram* 82

6 *Influence of long-range interactions* 117

6.1 *Complex ordering phenomena* 117

6.2 *Generalized Wigner crystals, domain walls and stripes* 121

7 *Conclusions and outlook* 135

7.1 *Propositions on quantum matter* 138

Bibliography 145

Samenvatting 163

Curriculum Vitae 171

Publications 173

Acknowledgements 175

1

Introduction: Quantum Matters

EINSTEIN'S EXPLANATION of the photoelectric effect is often quoted as the birthplace of quantum mechanics, the theory used in this thesis. I think it is misleading to take the thus-proposed quantization, which was already apparent in experiments, as the starting point of the quantum. Instead, in my opinion, we should start with Planck's theory of blackbody radiation. On 14 December 1900 Max Planck presented his idea that electromagnetic radiation can only be emitted in quantized form in order to explain the relation between temperature, frequency and intensity. Without the ability to detect the postulated quantum directly, the idea of quantization is truly revolutionary.

Similarly, the Einstein and Debye theories of the low temperature anomalies in the specific heat of crystalline solids proposed the quantization of vibrational energy. What these theories have in common is that they combine both quantization of energy levels with a large number of degrees of freedom. The in popular culture so frequently mentioned 'uncertainty' associated with quantum mechanics is completely irrelevant for these quantum statistical systems,[1] such as the complex materials studied in this thesis.

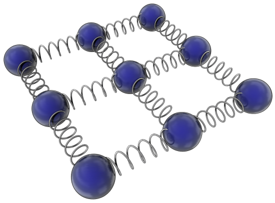

Figure 1.1: A crystal solid can be viewed as atoms connected by springs. In the quantum theory of a solid, the springs can only vibrate at fixed frequencies. This quantization of vibrational modes explains the low-temperature behavior of solids.

When it comes to statistics it is relevant, however, that energy quanta are indistinguishable. Indistinguishable can be best explained by the following coin-flipping example. If I flip two coins elementary probability theory will tell you that the chance of two heads is 25%. However, as Bose famously discovered while making an error during a lecture, if the two coins are fundamentally indistinguishable the probability is 33%. This is the case for **bosons** and from there the Bose-Einstein distribution function

$$n_{BE}(E) = \frac{1}{e^{E/kT} - 1} \tag{1.1}$$

directly follows. Bosons have the unique property that they want

[1] More on quantum statistics can be found in Lifshitz and Pitaevskii, 1980, Abrikosov et al., 1965, Mahan, 2000, Wen, 2007 and Coleman, 2013.

to do the same thing as other bosons around them, which can already be inferred from the coin-flipping thought-experiment where the probability of finding the same sides is greatly increased.[2]

This is in stark contrast to electrons in atomic orbitals. There the Pauli exclusion principle dictates that no more than two electrons can be in one orbital. Hence a second species of particles must exist that go by the name of **fermions**, described by the Fermi-Dirac distribution

$$n_{FD}(E) = \frac{1}{e^{E/kT} + 1}. \tag{1.2}$$

The Pauli exclusion principle applied to electrons in a crystal immediately suggests that electrons have a very high energy. The lowest energy state of a collection of electrons amounts to filling up energy levels up to the Fermi level E_F, which is typically several electronvolts. Therefore, even at low temperatures the average kinetic energy per electron is huge. In fact, it equals $\frac{3}{5}E_F$ whereas such a kinetic energy per particle in a classical gas is only obtained at a temperature of thousands of Kelvins. Indeed, the Pauli exclusion principle implies that the seemingly boring Fermi sea is in fact a hot boiling active soup of electrons.

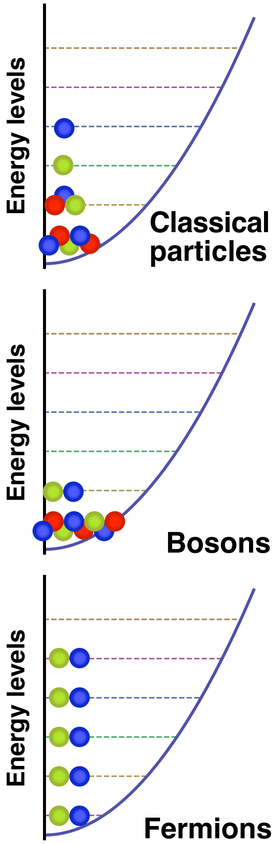

Figure 1.2: An ensemble of particles is distributed among a set of energy levels. Classical particles obey the Maxwell-Boltzmann distribution. Relative to that the conformist bosons tend to cluster together in the lowest energy state. Fermions, on the other hand, have an exclusion principle that limits the number of particles per state.

The electron band theory that thus originated laid the foundations for our understanding of electrons in metals, insulators and last-but-not-least semiconductors. The latter class of materials have revolutionized our modern world: basically everybody on every corner of the world carries semiconductor technology in her or his pockets. To me this shows that investing in fundamental physics (in this case quantum statistics) leads to practical applications, albeit in a completely different form than Pauli and colleagues would have imagined.

We just saw that there are two quantum species: the bosonic conformist particle and the fermionic individualistic particle, see figure 1.2. However, this is not the whole story: additionally the fermions have a weird property called '**anticommutativity**', which means that creating first particle A and then particle B is equal to 'minus' creating them in the opposite order. In the language of second quantization[3] one explicitly sees the appearance of a minus sign,

$$c_A^\dagger c_B^\dagger = -c_B^\dagger c_A^\dagger, \tag{1.3}$$

[2] Dirac, 1958

[3] 'Second' quantization means that all quantum operators are expressed in terms of creation and annihilation operators of (fermionic or bosonic) particles.

Figure 1.3: The high temperature superconductors are ill understood strongly correlated materials, and they are a prime example of quantum matter. Here the author is shown levitating a piece of superconducting YBCO at the Twente University.

which causes mathematical problems when describing a large set of fermions. Often this anticommutativity, or **fermion sign problem** as it is sometimes called, does not pose a problem, when the quantum mechanical wavefunction of a system can be written as a **product state** of simpler constituents.

The first example of a product state is the non-interacting Fermi gas,

$$|\Phi\rangle_{\mathrm{FG}} = \prod_{\mathbf{k}\sigma}^{\mathbf{k}_F} c^{\dagger}_{\mathbf{k}\sigma} |\mathrm{vac}\rangle \tag{1.4}$$

where $c^{\dagger}_{\mathbf{k}\sigma}$ is the creation operator of an electron with momentum $\mathbf{k}$ and spin σ. The product now runs over all momentum states up to the Fermi momentum. Product states also arise in the case of the formation of some kind of long-range order via spontaneous symmetry breaking. Examples are (anti)ferromagnets, crystalline solids, Bose condensates and superconductors; the latter is described by the BCS wavefunction[4]

$$|\Phi\rangle_{\mathrm{BCS}} = \prod_{\mathbf{k}\sigma} \left(u_{\mathbf{k}} + v_{\mathbf{k}} c^{\dagger}_{\mathbf{k}\uparrow} c^{\dagger}_{-\mathbf{k}\downarrow} \right) |\mathrm{vac}\rangle \tag{1.5}$$

with $u_{\mathbf{k}}, v_{\mathbf{k}}$ some momentum dependent parameters. Any quantum system that can be written as a product state can be effectively described as a classical system, corrected with the proper Fermi-Dirac or Bose-Einstein statistics. The ordered product states are called **classical condensates**.[5]

There is, however, a class of materials that cannot be simply written as a product state, usually due to strong electron-electron interactions[6] and the resulting macroscopic entanglement. For these materials the quantum fermion signs do matter and the

[4] Bardeen et al., 1957; and De Gennes, 1999

[5] See Anderson, 1984 and Zaanen, 1996.

[6] Imada et al., 1998; and Lee et al., 2006

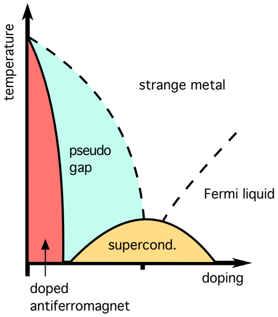

Figure 1.4: Generic phase diagram of a cuprate material such as $La_{2-x}Sr_xCuO_4$. Upon doping away from half-filling the antiferromagnetic order is reduced, and the poorly understood pseudogap and strange metal appear.

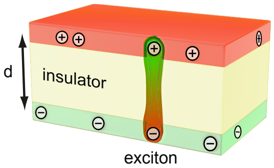

Figure 1.5: A heterostructure consisting of a hole layer and an electron layer separated by an insulator. Interlayer excitons can form as the bound state of an electron and a hole.

weird non-locality (as Wen, 2007 calls it) of fermions plays an important role. It has become customary to denote all these highly entangled materials '**quantum matter**', since no classical analogue or theory exists.

Strongly correlated electron systems are an example of quantum matter. While the observation that there exist materials that do not obey band theory was already made in the 50s by Van Vleck, Mott and others, a revived interest in **Mott insulators** sparked after the discovery of high-temperature superconductivity in cuprates (figure 1.3). Embarrassingly enough, there are still no theories that provide a satisfactory explanation of the many phenomena observed in the cuprates, from the fate of the Mott insulating state upon doping, to the pseudogap, the strange metal, the proposed electronic nematicity, etcetera, see figure 1.4. The main reason for this lack of understanding lies in the aforementioned 'weirdness' of fermionic excitations in cuprates.

Whilst doped Mott insulators are little understood, rapid progress is made in materials where the dominant excitations are bosons. The simplest way to make a bosonic system is to couple two electrons together, as is done in the BCS theory of superconductivity. Similarly, one can couple electrons and holes together into **excitons**. While the binding of an electron and a hole into an exciton has the advantage of the much stronger Coulomb attraction, the possible recombination and annihilation of an exciton prevents the practical realization of a so-called exciton condensate. However, if one is able to spatially separate the electrons and holes into separate layers, as shown in figure 1.5, annihilation can be suppressed[7] and an equilibrium density of excitons can be created. Over the last decade such bilayer systems came experimentally within reach, first in quantum Hall bilayers[8] and more recently in systems without magnetic field.[9]

In this thesis I combine the field of strongly correlated materials with the bilayer exciton community. No-one in their right mind would mix those two fields, unless driven by experiments. My theoretical pursuits are therefore rooted in the rapid technological revolution that has occurred in the fabrication of nanomaterials. Using for example pulsed laser deposition (PLD) one can make material 'sandwiches' where the chemical composition of each separate atomic layer is controlled independently. My theoretical research is in close collaboration with the experimental Interfaces

[7] Shevchenko, 1976; and Lozovik and Yudson, 1976

[8] Eisenstein and MacDonald, 2004; and Huang et al., 2012

[9] High et al., 2012

in Correlated Electron systems group of Hans Hilgenkamp at the University of Twente, where they possess such technologies.

The ill-understood Mott materials, together with bilayer exciton ideas and the technological nanorevolution form the basis for this research. My main research questions are thus: *Can we make an exciton condensate in a strongly correlated bilayer? And what are the observable properties of such a condensate?* Given these concrete research questions, we hope to understand more about the complex interplay between fermions and bosons in quantum matter.

Outline

The research on excitons in strongly correlated materials addresses the interplay between fermionic and bosonic excitations. Many properties of a system, however, do not depend on the microscopic mechanisms involved, therefore we start with a **phenomenological description** of exciton condensates in chapter 2. Using a Ginzburg-Landau theory we show that an exciton condensate exhibits a flux quantization property.

After that we dive into the microscopic degrees of freedom. The starting point is the **fermionic Hubbard model**, introduced in chapter 3. Weak coupling mean field theory and numerical analysis of the Hubbard model do give us some answers, however, the fermion sign problem plagues the theory.

On the other hand, in the strong coupling limit one can rewrite the fermionic Hubbard model into a purely **bosonic exciton** $t-J$ **model**. In chapter 4 we introduce this new model and discuss its properties. There we find the dynamical frustration of a single exciton in a Mott insulating antiferromagnet. Chapter 5 discusses the properties of the strongly correlated exciton condensate, where we find spin-exciton cooperation. Indeed, the exciton condensate can exist, but only if the kinetic energy of the excitons exceeds their dipole-dipole repulsion. The influence of this dipole-dipole repulsion on possible ordering phenomena is discussed in chapter 6.

Core concepts, like the Hubbard model or strong coupling perturbation theory, are best introduced in the context of the research findings instead of in a separate introductory chapter. Hence, whenever necessary background information will be included in the text or in references in the remaining chapters.

Finally, theoretical research should always be addressing 'actually existing materials'. The main challenge in this regard is to couple down-to-earth computations with insights in general physical concepts. In the **concluding chapter** 7 we put our findings on strongly correlated bilayers into a broader context and relate it to experimental progress, thereby addressing future directions in the theory of quantum matter.

2

Phenomenology of exciton bilayers

Without specific knowledge of microscopic details one can still describe to an amazing accuracy a large set of physical properties of any system. This is rooted in the vastness of degrees of freedom, so that statistical effects dominate the physics. An effective free energy based on symmetry principles can then be constructed, explaining macroscopic phenomena.

This was initially done by Ginzburg and Landau to describe superconductivity in the early 40s, based on the realisation that the order parameter relevant to superconductivity is a (charged) complex field. In this chapter we will introduce the field of bilayer exciton condensates in section 2.1, and use symmetry arguments to write down a phenomenological theory of these systems. In section 2.2 we deduce its magnetic response and the prediction of flux quantisation.

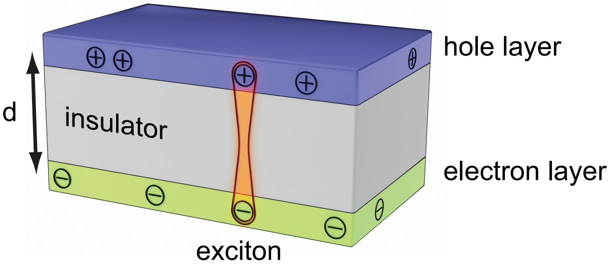

Figure 2.1: Excitons in double layer devices. Double layer devices consist of an electron layer (in green) parallel to a hole layer (blue), separated by an insulating barrier (grey). Electron-hole attraction leads to the formation of excitons. At sufficiently low temperatures the excitons can form a Bose-Einstein condensate.

2.1 *Bilayer excitons and condensation*

In a semiconductor the elementary charged excitations are particles and holes, and naturally these two excitations attract each other via the Coulomb force. A trivial non-charged excitation is therefore composed of both an electron and a hole: the **exciton**.

Directly after the BCS theory of superconductivity it was suggested that excitons, as they are in many regards comparable to Cooper pairs, can also Bose condense and exhibit superfluidity.[1] Whilst the Coulomb force that binds the exciton is indeed orders of magnitude stronger than the phonon glue in Cooper pairs, the major difficulty for exciton condensation lies in their finite lifetime. That is, excitons annihilate when the electron and hole recombine.

Nonetheless, exciton annihilation can be suppressed by spatially separating the electrons and holes. This is achieved by constructing a heterostructure where one sandwiches an insulating layer in between a two-dimensional electron gas and a two-dimensional hole gas, see figure 2.1. The Coulomb attraction is, due to its long-range nature, not substantially reduced and therefore electrons and holes can still form bound states. This is called a bilayer exciton, double layer exciton or **interlayer exciton**.

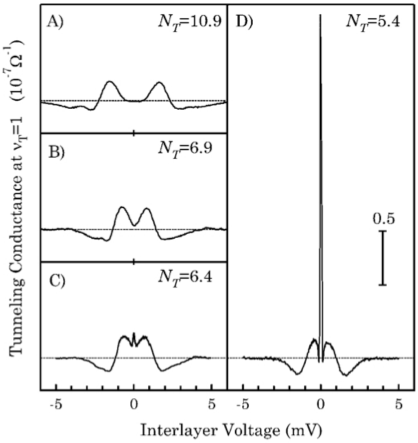

Figure 2.2: Interlayer tunneling in a quantum Hall bilayer as a function of bias voltage, for different magnetic fields. The enhancement of the interlayer tunneling at zero bias is the result of the exciton condensation and is a direct measurement of the order parameter. From Spielman et al., 2000.

At low enough temperatures these interlayer excitons form a superfluid.[2] Unlike many other superfluids, the bilayer nature allows one to directly probe the **superfluid order parameter**. The exciton condensate order parameter reads

$$\Delta_{\mathbf{k}} = \langle c^{\dagger}_{\mathbf{k}1\sigma} c_{\mathbf{k}2\sigma} \rangle . \tag{2.1}$$

where $c^{\dagger}_{\mathbf{k}1\sigma}$ creates an electron in the first layer and $c_{\mathbf{k}2\sigma}$ creates a hole in the second layer. One directly observes that this order parameter amounts to anomalous interlayer tunneling.[3] The onset of condensation is therefore sparked by a dramatic increase of the

[1] Blatt et al., 1962; Keldysh and Kopaev, 1965; and Moskalenko and Snoke, 2000

[2] Shevchenko, 1976; and Lozovik and Yudson, 1976

[3] Moon et al., 1995; Spielman et al., 2000; and Eisenstein and MacDonald, 2004

interlayer tunneling, as is shown by the experimental results in figure 2.2.

One can question, however, to what extent the system created in this way is really a superfluid. Obviously, since excitons are neutral, there cannot be an electric supercurrent in these systems. However, since the electrons and holes are spatially separated an interlayer exciton current amounts to two opposite but equal countercurrents. By connecting the two layers in series one can measure the resulting **counterflow superfluidity**[4] as is shown in figure 2.3.

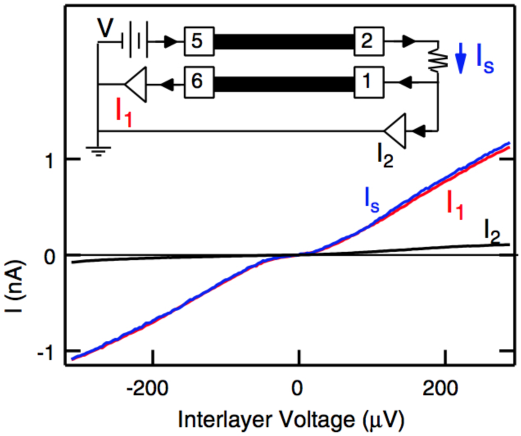

Figure 2.3: Near-perfect counterflow is observed in quantum Hall bilayers in a corbino geometry. A current is induced in the top layer (from 5 to 2) and measured in the bottom layer (from 1 to 6). The result $I_s \approx I_1$ suggests that in the bilayer the electric current is carried by superfluid excitons. From Finck et al., 2011.

As of 2013, the field of interlayer excitons is still restricted to a small class of material systems: the quantum Hall bilayers of figures 2.2, 2.3 and Huang et al., 2012; and laser-pumped quantum wells.[5] There are many other possible candidate materials to realise interlayer condensation, such as graphene sheets[6] or topological insulators[7]. In this thesis we consider strongly correlated electron bilayers as candidate materials,[8] the microscopic properties of which will be discussed in the next two chapters.

Besides different materials there are also different experimental probes possible. The current experiments focus mainly on transport properties. One can argue that these do not necessarily prove the existence of an interlayer exciton condensate. To directly probe the coherence associated with the superfluid, we propose a flux quantisation effect.

[4] Su and MacDonald, 2008; and Finck et al., 2011

[5] High et al., 2012

[6] Lozovik and Sokolik, 2008; Zhang and Joglekar, 2008; Dillenschneider and Han, 2008; Kharitonov and Efetov, 2008; and Min et al., 2008

[7] Seradjeh et al., 2009

[8] Pentcheva et al., 2010; and Millis and Schlom, 2010

2.2 *Ginzburg-Landau theory and flux quantisation*

This section is based on Rademaker et al., 2011.

We can find the flux quantisation and related magnetic properties of an exciton bilayer condensate using **Ginzburg-Landau theory**. This amounts to constructing a free energy functional $\mathcal{F}[\Psi]$ for the order parameter field. In the case of interlayer excitons, the order parameter must describe the bound state of an electron in one layer and a hole in the other layer, as in equation (2.1). The exciton is therefore charge neutral, but it does possess an electric dipole moment. This dipole moment is the starting point for the derivation of magnetic properties.

As the direction of this electric dipole is fixed, the exciton superfluid is characterized by just a complex scalar order parameter field $\Psi(\vec{x}) \equiv |\Psi(\vec{x})| e^{i\phi(\vec{x})}$ along a 2D surface, the square of which gives the superfluid density $\rho(\vec{x}) = |\Psi(\vec{x})|^2$. For a charged superfluid/superconductor with boson charge q electromagnetism is incorporated by replacing ordinary derivatives with **covariant derivatives** $\vec{D}$,

$$\hbar\vec{D} = \hbar\vec{\nabla} + iq\vec{A}(\vec{x}) \tag{2.2}$$

where $\vec{A}(\vec{x})$ is the vector potential. In the charge-neutral exciton superfluid the electron and hole constituents of an exciton form an electric dipole $e\vec{d}$ and consequently the covariant derivative associated with exciton matter must equal[9]

$$\hbar\vec{D} = \hbar\vec{\nabla} + ie\left[\vec{A}(\vec{x}+\vec{d}/2) - \vec{A}(\vec{x}-\vec{d}/2)\right] \tag{2.3}$$

where the electron is positioned at $\vec{x}-\vec{d}/2$ and the hole at $\vec{x}+\vec{d}/2$. For small interlayer distance $\vec{d}$ the vector potential can be expanded in a Taylor series. In addition, since the vector potential $\vec{A}$ along the 2D superfluid surface is only sourced by in-plane currents, we can impose that the gradient of the vector potential component perpendicular to the surface is zero,

$$\vec{\nabla}'\left(\vec{d}\cdot\vec{A}(\vec{x}')\right)\Big|_{\vec{x}'=\vec{x}} = 0. \tag{2.4}$$

This implies that the above vector potential difference can be written completely in terms of the 'real' magnetic field

$$\vec{A}(\vec{x}+\vec{d}/2) - \vec{A}(\vec{x}-\vec{d}/2) = \\ -\vec{d}\times\sum_{k=0}^{\infty}\frac{1}{(2k+1)!}\left(\frac{\vec{d}}{2}\cdot\vec{\nabla}'\right)^{2k}\vec{B}(\vec{x}')\Bigg|_{\vec{x}'=\vec{x}}. \tag{2.5}$$

---

[9] Balatsky et al., 2004

Up to first order the exciton covariant derivative turns into

$$\hbar\vec{D} = \hbar\vec{\nabla} - ie\vec{d} \times \vec{B}. \tag{2.6}$$

This is an interesting structure viewed from a theoretical perspective. Equation (2.6) corresponds to the covariant derivatives of a $SU(2)$ gauge theory with gauge fields $A_i^a = \epsilon^{iak} B_k$. Here the $SU(2)$ gauge fields are actually physical fields fixed by Maxwell's equations. Using the above considerations we can write down a general **Ginzburg-Landau free energy**

$$\begin{aligned} \mathcal{F}[\Psi] &= \int d^2x \left[\alpha|\Psi|^2 + \frac{1}{2}\beta|\Psi|^4 + \frac{\hbar^2}{2m^*}(\nabla|\Psi|)^2 \right. \\ &\left. + \frac{1}{2m^*}\left[\hbar\vec{\nabla}\phi - e\vec{d} \times \vec{B}\right]^2 |\Psi|^2 + d\frac{B^2}{2\mu_0}\right]. \end{aligned} \tag{2.7}$$

The parameters α and β can be written formally as a function of the superfluid density and the critical magnetic field B_c. Minimization of the free energy assuming a constant order parameter yields

$$\alpha = -d\frac{B_c^2}{\mu\rho}, \tag{2.8}$$

$$\beta = -\frac{\alpha}{\rho}. \tag{2.9}$$

2.2.1 *Electromagnetic response*

The direct coupling to physical fields changes the rules drastically as compared to normal superconductors. We define the exciton supercurrent as the standard Noether current[10] $\vec{j} \equiv \frac{\hbar\rho}{m^*}\vec{\nabla}\phi$. Consequently, minimizing the free energy for a fixed applied magnetic field $\vec{B}$ perpendicular to the dipole moment yields the **exciton supercurrent response**

$$\vec{j} \equiv \frac{\hbar\rho}{m^*}\vec{\nabla}\phi = \frac{\rho e}{m^*}\vec{d} \times \vec{B}. \tag{2.10}$$

This result is closely related to spin superfluids[11] where a 'physical field' $SU(2)$ structure arises through spin-orbit coupling.[12] The analogue of Eq. (2.10) is the spin Hall equation[13] $j_j^i = \sigma_s \varepsilon^{ijk} E_k \rightarrow \vec{j} = -\sigma\vec{d}_m \times \vec{E}$. We conclude that the spin-superfluid formed from magnetic dipoles is the electromagnetic dual of the exciton (electric dipole) superfluid.

[10] Leggett, 2006

[11] Leurs et al., 2008

[12] Goldhaber, 1989

[13] Murakami et al., 2003

In the double layer system the electric charges forming the exciton dipoles are confined in the separate layers. Hence the exciton supercurrent can be decomposed into the separated electron and hole surface currents. According to Ampère's law, a surface current induces a discontinuity in the magnetic field components parallel to the surface,

$$\Delta\vec{B}(\vec{x}) = \mu_0 \vec{K}(\vec{x}) \times \hat{n}, \tag{2.11}$$

where $\hat{n}$ is the normal vector to the surface and $\vec{K}(\vec{x})$ is an electric surface current density. Consequently, an exciton supercurrent reduces the magnetic field in between the electron and hole layer. The double layer therefore acts as a (non-perfect) **diamagnet** with magnetic susceptibility

$$\chi_m = -\frac{e^2 \rho d \mu_0}{m^*}. \tag{2.12}$$

For typical parameters $\rho = 0.4 \text{ nm}^{-2}$, $d = 20$ nm and $m^* = 2m_e$, the magnetic susceptibility equals $\chi_m = -10^{-4}$, comparable to what is found in good diamagnets like gold or diamond. In semiconductor quantum wells, the exciton mass is smaller than the free electron mass m_e which enhances the diamagnetic susceptibility even further.[14]

2.2.2 *Flux quantization*

Imposing single-valuedness on the order parameter implies that for any given contour C inside a superfluid $\oint_C \vec{\nabla}\phi \cdot \vec{dl} = \oint_C \vec{j} \cdot \vec{dl} = 2\pi n$ where n is an integer. Therefore, **circular supercurrents must be quantised**, which can be seen by topological defects in the dipolar superfluid.[15] In general, metastability of superflows requires a nontrivial topology of the superfluid.[16] Unlike in other superfluids, the $SU(2)$ structure of dipolar superfluids implies the possibility of more complicated topologies which cannot be obtained by creating defects in the superfluid.

Consider a cylindrical device of radius r consisting of two concentric layers as shown in figure 2.4 with the electric dipole moment $\vec{d}$ of the excitons pointing in the radial direction. For this geometry the current-dependent term in the free energy can be written as

$$\mathcal{F}[\Psi] \sim \oint d\theta \left[\frac{h}{e} \partial_\theta \phi - B_z 2\pi r d \right]^2 \tag{2.13}$$

[14] Butov, 2003

[15] Babaev, 2008; Seradjeh et al., 2008; and Leurs et al., 2008

[16] Leggett, 2006

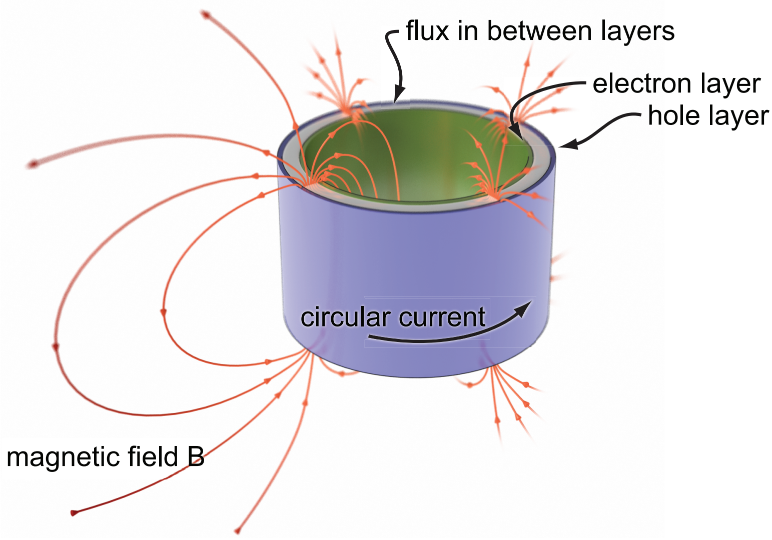

Figure 2.4: Flux trapping in a cylindrical exciton superfluid. The proposed device consists of a concentric ring structure of radius r, composed of an electron layer (green) and hole layer (blue). Due to the macroscopic coherence of the exciton superfluid the angular current must be quantised. By application of an external axial magnetic field one can induce some number of current quanta. In absence of the external field, the current quanta remain which induces a magnetic field as shown (red lines). The trapped magnetic flux in between the layers must be quantised according to $\Phi = \frac{h}{e}\chi_m\, n$ where χ_m is defined in equation (2.12).

where $\oint_C d\theta \partial_\theta \phi = 2\pi n$ with n integer valued and B_z is the external magnetic field. Note that the flux going in between the two layers equals up to first order $\Phi = B_z 2\pi r d$. Minimisation of equation (2.13) shows that current quanta can be induced by an axial magnetic field. In the absence of the external field, the current $\vec{j} \sim n$ induces a **magnetic flux** in between the layers, according to Ampère's law (2.11), with a magnitude

$$\Phi = \frac{h}{e}\chi_m\, n \equiv \Phi_0\, \chi_m\, n. \qquad (2.14)$$

This is our central result: in the cylindrical double layer geometry, the magnetic flux going in between the sample layers must be **quantised** in units of χ_m times the fundamental flux quantum $\Phi_0 = \frac{h}{e}$. Notice that this flux quantisation effect is quite different from the one realised in superconductors. In the double layer exciton condensate the supercurrent is induced by the magnetic field $\vec{B}$ rather than the gauge field $\vec{A}$ as in the London equation, while the quantised amount of flux equals $d \oint \vec{B} \cdot d\vec{l}$ instead of $\oint \vec{A} \cdot d\vec{l} = \int \int_\Sigma \vec{B} \cdot d\vec{\Sigma}$ for superconductors. In combination these two basic differences add up to an universal expression for the flux quantisation $\Phi = \frac{h}{e^*}\chi_m\, n$ that applies to both superconductors and exciton condensates, where $e^* = -2e$ and $\chi_m = -1$ for superconductors.

Is the strength of the condensate actually sufficient to trap the flux? When the external field is switched off the flux carrying state is metastable and the system can return to the ground state by locally destroying the condensate: the **phase slip**. The condensate can only be destroyed over lengths greater than the Ginzburg-Landau coherence length

$$\xi = \frac{\hbar}{\sqrt{|2m^*\alpha|}} \tag{2.15}$$

and consequently the energy required to break the condensate over a region ξ wide along a cylinder of length z is

$$\delta F_b = \frac{1}{2}\hbar z \left(\frac{d\,\rho}{2m^*\mu}\right)^{1/2} B_c. \tag{2.16}$$

Locally destroying the condensate is only favourable if this energy is lower than the energy stored in the magnetic field, which is $\delta F_m = \frac{B^2}{2\mu} 2\pi r d$. We conclude that a **phase slip** will not occur as long as the trapped magnetic flux $\Phi = \Phi_0 \chi_m n$ stays below a threshold value,

$$\Phi^2 < \left(\frac{|\chi_m|}{2}\right)^{1/2} \Phi_0 B_c\, rd. \tag{2.17}$$

where B_c is the critical magnetic field. With the typical parameters stated above and $r = 100\ \mu$m, the critical field must exceed 5 nT to trap one flux quantum. Since the critical magnetic field of bilayer superfluids is proposed to lie in the orders of tens of Teslas[17], a phase slip is improbable.

Another possible complication is that annihilation of excitons by tunneling causes the phase to be pinned which introduces a threshold for the formation of stable currents. Microscopic tunneling can be incorporated via an extra term in the Ginzburg-Landau free energy

$$\mathcal{F}_t = -2t \int d^2x \frac{|\Psi|}{L} \cos\phi, \tag{2.18}$$

where L is the in-plane lattice constant and t is a microscopic tunneling energy. This **phase pinning** lowers the energy of the state where no flux is trapped, which introduces a threshold for the trapping of magnetic flux quanta. It is only possible to trap n

[17] Balatsky et al., 2004

magnetic flux quanta if the microscopic tunneling energy t satisfies

$$2t < n^2 \frac{\hbar^2}{2m^* r^2} \sqrt{\rho} L. \tag{2.19}$$

This corresponds, given the typical parameters mentioned above, to $t < 0.3$ peV (pico-electronvolt) for the first flux quantum.

In order to estimate a value for t, let us imagine that the device is fabricated from copper-oxide layers. The hopping energy in cuprates between two adjacent CuO_2 layers ranges from approximately 10^{-1} eV for LSCO compounds to 10^{-3} eV for Bi-based compounds[18]. Let us now assume that the hopping energy between more distant CuO_2 layers falls off exponentially. A distance $d = 20$ nm between the hole and electron layer corresponds roughly to 30 CuO_2 layers, so that the tunneling energy equals $t \approx e^{-30} 10^{-3} = 10^{-16}$ eV.[19] This estimate lies well below the maximum value of t obtained in equation (2.19). However, the precise value of t is highly sample specific and needs to be checked for each separate sample.

The **experimental protocol** to test the flux quantization is as follows: apply an axial magnetic field of magnitude B_{ext} above the critical temperature T_c, and cool the device below T_c such that a circular current quantum is frozen in. The magnitude of the current is determined by the strength of the applied flux: if $\Phi_{\text{ext}} < \frac{1}{2}\Phi_0$ no current is induced, for $\frac{1}{2}\Phi_0 < \Phi_{\text{ext}} < \frac{3}{2}\Phi_0$ one current quantum is induced, etc. The magnetic field corresponding to $\frac{1}{2}\Phi_0$ is typically $B_{\text{ext}} = 0.2$ mT. Upon removing the external magnetic field, a trapped flux equal to $\Phi_0 \chi_m n$ remains, corresponding to a field strength of 50 nT. These numbers do not pose a problem of principle for the experimental realisation of such a flux trapping device.

Based on existing technology, one can envision various **practical realisations** of the concentric p-n doped ring geometry, while it is anticipated that further technology developments will create additional opportunities. Using p- and n-doped complex oxide compounds, such as cuprate perovskites, multilayer thin film structures can be fabricated in the desired ring geometry. Using the proven edge-junction technology[20] the structure sketched in figure 2.5 can readily be fabricated, by e.g., pulsed laser deposition and Ar-ion beam etching. As a barrier layer $SrTiO_3$ can be used, with a typical thickness of 10-100 nm, or another insulating oxide

---

[18] Cooper and Gray, 1994; and Clarke and Strong, 1997

[19] The tunneling energy might be viewed as a transition rate: the lower this energy the less electrons will hop in a given time period.

[20] Gao et al., 1990; and Hilgenkamp et al., 2003

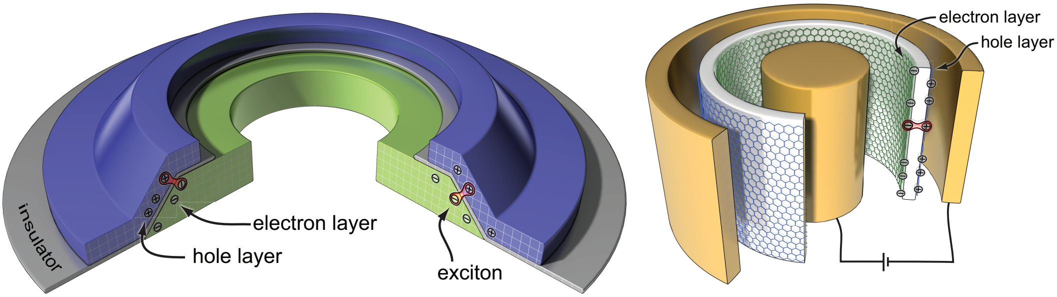

Figure 2.5: Schematic representations of possible practical realisations of the concentric ring geometry comprised of p- and n-doped layers. Left: Using epitaxially grown complex oxide thin films. Right: Using doubly-gated graphene double layers.

that grows epitaxially on top of the etched base electrode. To guarantee an epitaxial growth of all the layers, the angle α is best kept below about 25°, but this does not fundamentally alter the physics of the flux quantisation as presented in this chapter.

A second possible practical realisation is based on double-side gated, double layer graphene. Recently, the growth of large area graphene films has been demonstrated on Cu foils, using a high temperature chemical vapor deposition process.[21] Interestingly, a continuous growth was achieved over grain boundaries and surface steps. From this it is feasible to expect that one can also grow a closed graphene tube around a copper cylinder, which would basically be a carbon nanotube with predetermined radius. Covering this with an appropriate epitaxial barrier layer, e.g. 10 nm of Al_2O_3 and a second graphene sheet, which may also be grown by physical or chemical vapor deposition-techniques, would then result in the desired concentric cylinder configuration. Subsequently, the copper can be etched away and the concentric cylinder can be transferred to an appropriate carrier, which can even be made out of plastic.[22] This would straightforwardly allow realizing a doubly gated configuration as depicted in figure 2.5.

[21] Li et al., 2009

[22] Bae et al., 2010

3

Fermionic models of correlated bilayers

MANY PROPERTIES of an exciton condensate can be deduced by considering the phenomenological Ginzburg-Landau free energy. However, to find specific susceptibilities that match experiments we need a microscopic model, starting with the basic constituents of a correlated bilayer: electrons, holes, and their interactions.

We introduce the fermionic Hubbard model, a remarkably elegant model that still torments many theoretical physicists. Within the mean field theory picture it is easy to discover exciton condensation, as demonstrated in section 3.2. However, the cuprate family that we study has strong interactions and mean-field theory is at best uncontrolled, and at worst completely wrong. We therefore perform a numerical study using the Determinant Quantum Monte Carlo approach, with limitations rooted in the fermion sign problem.

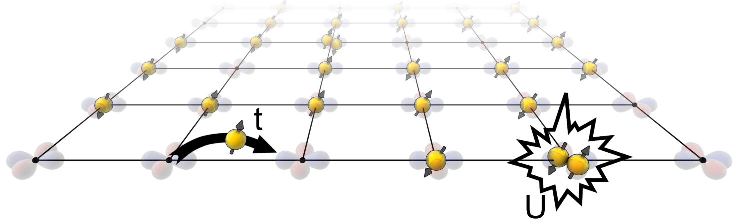

Figure 3.1: In the tight binding approximation the electron states are given by orbitals on an ionic lattice. The dynamics of the electrons is described by the Hubbard model, with hopping t and an onsite repulsion U.

3.1 The Hubbard model and its problems

Many metals and alloys such as the cuprates are crystalline solids, for which most electronic properties can be derived using the tight-binding approximation. There one assumes that the electron wavefunctions are still atomic orbitals and electrons can 'hop' from

A good introduction into the Hubbard model can be found in Zaanen, 1996 and Imada et al., 1998.

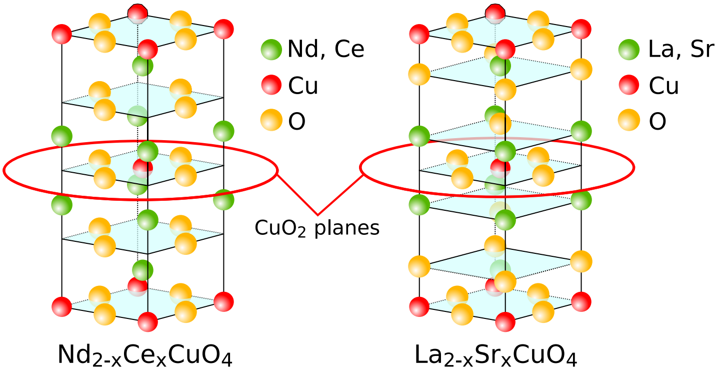

Figure 3.2: Lattice structure of electron and hole-doped cuprates. The interesting physics happens in copper oxide planes, with rare earth ions in between the layers. Doping is obtained by chemical changes in the rare earth layers.

one orbital to the other. This process is described by a **hopping Hamiltonian**

$$H_K = -\sum_{ij\sigma} t_{ij} c^\dagger_{i\sigma} c_{j\sigma} \tag{3.1}$$

where $c^\dagger_{i\sigma}$ creates an electron at site i with spin σ and t_{ij} is the overlap between two atomic orbitals. With the addition of a chemical potential μ, which tunes the electron density, this model represents the simple **Fermi gas**. A Fourier transformation turns the Hamiltonian into a diagonal form in momentum space,

$$H_{\mathrm{FG}} = \sum_{\mathbf{k}\sigma} (\varepsilon_{\mathbf{k}} - \mu)\, c^\dagger_{\mathbf{k}\sigma} c_{\mathbf{k}\sigma} \tag{3.2}$$

where $\varepsilon_{\mathbf{k}}$ is the Fourier transform of t_{ij} and is called the dispersion. We find that the ground state is an **antisymmetrized product state**, which can be viewed as a marginal extension of the classical condensates mentioned in the introduction.

Next to the hopping, which is associated with kinetic energy, there exist interactions between the electrons.[1] This is typically a density-density interaction of the form $V(r-r')n(r)n(r')$, where $V(r)$ is the (screened) Coulomb potential and $n(r) = c^\dagger(r)c(r)$ is the electron density. Landau[2] famously showed that when one slowly turns on these interactions, there remains a one-to-one correspondence between the ground state and excitations of the Fermi gas and the **Fermi liquid**. This principle of adiabatic continuation allows us to neglect electron-electron interactions (or at most treat them perturbatively) in most metals and semiconductors.

[1] There also exist ion-ion interactions and electron-ion interactions, which are commonly referred to as electron-phonon coupling. We neglect those in this thesis.

[2] Nozieres and Pines, 1999

However, there is a class of materials for which the interactions are so strong that the picture of adiabaticity breaks down. This is often the case when d- or f-orbitals are involved. Then the simplest approach is to include the **onsite Coulomb interaction**

$$H_U = U \sum_i n_{i\uparrow} n_{i\downarrow}, \tag{3.3}$$

which leads to the famous **Hubbard model**[3]

$$H_H = -t \sum_{\langle ij \rangle \sigma} c^\dagger_{i\sigma} c_{j\sigma} - \mu \sum_{i\sigma} c^\dagger_{i\sigma} c_{j\sigma} + U \sum_i n_{i\uparrow} n_{i\downarrow}, \tag{3.4}$$

where we restricted the hopping to be nearest neighbor only. Figure 3.1 illustrates the elementary physics described by such a Hubbard model on a square lattice.

It is quite embarrassing that even today the physics of the Hubbard model is not fully understood. The first reason lies in the inherent competition between kinetic and potential energy. The kinetic energy is diagonal in momentum space, which suggests we should treat the electrons as waves. The potential energy, however, is diagonal in real space, hence we should consider the electrons as particles. The quantum mechanical **particle-wave duality** reaches its apex of complexity when $zt \approx U$.[4]

Another reason that the Hubbard model is so poorly understood is the **fermion sign problem**. In numerical analysis this means that one cannot map the model onto a classical probabilistic theory. Analytical progress is difficult since the sign problem implies that wavefunctions are no longer simple product states but rather complicated long-range entangled states.[5]

Despite these issues, we can construct a microscopic model of a strongly correlated bilayer based on the Hubbard model. The **extended bilayer Hubbard model** contains a kinetic part

$$H_K = -t \sum_{\langle ij \rangle \ell\sigma} c^\dagger_{i\ell\sigma} c_{j\ell\sigma} - \sum_{i\ell} \mu_\ell n_{i\ell} - t_\perp \sum_{i\sigma} (c^\dagger_{i1\sigma} c_{i2\sigma} + h.c.) \tag{3.5}$$

where t is the intralayer hopping, $t_\perp$ is the interlayer hopping and μ_ℓ is the chemical potential per layer. We denote lattice sites by their in-plane index i and their layer number $\ell = 1, 2$. Next to the kinetic part the model contains the onsite interaction

$$H_U = U \sum_{i\ell} n_{i\ell\uparrow} n_{i\ell\downarrow} \tag{3.6}$$

[3] Anderson, 1959; and Hubbard, 1963

[4] The factor z is the coordination number of the lattice, thus zt is proportional to the bandwidth or kinetic energy.

[5] Liang et al., 1988

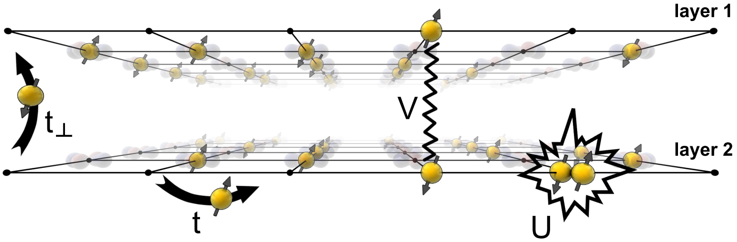

Figure 3.3: The extended bilayer Hubbard model (3.5)-(3.7) describes two layers with in-plane hopping t and interlayer $t_\perp$, onsite repulsion U and interlayer Coulomb interaction V.

and the interlayer interaction

$$H_V = \sum_{ij\sigma\sigma'} V_{ij} n_{i1\sigma} n_{j2\sigma'}. \tag{3.7}$$

A graphic representation of the extended bilayer Hubbard model is shown in figure 3.3.

The occurrence of **interlayer excitons** in this model can be investigated in various limits. Whenever the interactions U and V are relatively weak mean field theory is applicable, similar to how BCS theory describes the pairing of electrons into Cooper pairs.[6] This will be detailed in the next section.

Another limit is the Hubbard model on a bipartite and half-filled[7] lattice with strong interaction U. There the system unambiguously becomes a **Mott insulator**.[8] The electrons are localized and only their spin degree of freedom remains, which in turn order antiferromagnetically. The effective physics can then be expressed in a bosonic spin language, which will be discussed in chapter 4.

The final approach to the fermionic bilayer Hubbard model is brute force. The Determinant Quantum Monte Carlo technique allows exact computation of several interesting properties of the bilayer Hubbard model, as we will show in section 3.3.

3.2 *The BCS theory of electron-hole pairing*

This section shows an elementary computation, similar to the various **mean field computations**[9] in the literature. Mean field theory, however, grossly overestimates the tendency to form exciton condensates and it surely is not applicable to strongly correlated bilayers. Keeping this in mind, let us now derive electron-hole

[6] Bardeen et al., 1957

[7] Bipartite means I can subdivide the lattice into two sublattices, and every site is only connected to sites on the other sublattice. Half-filling means that there is on average 1 electron per lattice site.

[8] Mott, 1949; Anderson, 1952; and Marshall, 1955

[9] Amongst them most notably the prediction of room-temperature superfluidity in Min et al., 2008.

pairing in the bilayer Hubbard model.

The idea of **BCS theory** is to single out the interactions being responsible for the expected order, which is in our case the interlayer exciton condensate with order parameter (3.58). In momentum space, the **order parameter** reads

$$\Delta_{\mathbf{k}} = \frac{1}{2}\sum_{\sigma}\langle c^{\dagger}_{\mathbf{k}1\sigma}c_{\mathbf{k}2\sigma}\rangle \tag{3.8}$$

which is a spin singlet. The interaction that induces exciton condensation scatters excitons from momentum $\mathbf{k}$ to momentum $\mathbf{k}'$. Thus we need to focus on the interlayer interactions

$$H_{V,\mathrm{BCS}} = \sum_{\mathbf{k}\mathbf{k}'\sigma} V_{\mathbf{k}-\mathbf{k}'}c^{\dagger}_{\mathbf{k}1\sigma}c_{\mathbf{k}'1\sigma}c^{\dagger}_{\mathbf{k}'2\sigma}c_{\mathbf{k}2\sigma}. \tag{3.9}$$

The idea of mean field theory is to replace $c^{\dagger}_{\mathbf{k}1\sigma}c_{\mathbf{k}2\sigma}$ in the interaction terms by $\Delta_{\mathbf{k}} + \delta\left(c^{\dagger}_{\mathbf{k}1\sigma}c_{\mathbf{k}2\sigma}\right)$, and then neglect terms of order δ^2. The resulting mean field Hamiltonian is

$$\begin{aligned} H_{MF} &= \sum_{\mathbf{k}\ell\sigma}\xi_{\mathbf{k}\ell}c^{\dagger}_{\mathbf{k}\ell\sigma}c_{\mathbf{k}\ell\sigma} \\ &\quad -\sum_{\mathbf{k}\sigma}\left(t_{\perp} + \sum_{\mathbf{k}'}V_{\mathbf{k}-\mathbf{k}'}\Delta_{\mathbf{k}'}\right)\left(c^{\dagger}_{1\mathbf{k}\sigma}c_{2\mathbf{k}\sigma} + h.c.\right) \\ &\quad + \sum_{\mathbf{k}\mathbf{k}'\sigma}V_{\mathbf{k}-\mathbf{k}'}\Delta_{\mathbf{k}'}\Delta_{\mathbf{k}}. \end{aligned} \tag{3.10}$$

We have introduced $\xi_{\mathbf{k}\ell} = \varepsilon_{\mathbf{k}\ell} - \mu_{\ell}$ as the dispersion minus chemical potential for each layer. This mean field Hamiltonian is quadratic in the fermionic operators and can thus be solved exactly. The dispersion of the quasiparticles depends on the order parameter Δ

$$\begin{aligned} \omega_{\mathbf{k}\pm}(\Delta) &= \frac{1}{2}(\xi_{\mathbf{k}1} + \xi_{\mathbf{k}2}) \\ &\quad \pm\sqrt{\left(\frac{1}{2}(\xi_{\mathbf{k}1} - \xi_{\mathbf{k}2})\right)^2 + \left(t_{\perp} + \sum_{\mathbf{k}'}V_{\mathbf{k}-\mathbf{k}'}\Delta_{\mathbf{k}'}\right)^2}. \end{aligned}$$

The corresponding mean field energy

$$E(\Delta) = \sum_{\mathbf{k}\pm\sigma}\omega_{\mathbf{k}\pm}n_{\mathrm{FD}}(\omega_{\mathbf{k}\pm}) + \sum_{\mathbf{k}\mathbf{k}'\sigma}V_{\mathbf{k}-\mathbf{k}'}\Delta_{\mathbf{k}'}\Delta_{\mathbf{k}} \tag{3.11}$$

needs to be minimized to find a solution for $\Delta_{\mathbf{k}}$.

Up till here the mean field analysis is fairly general: we have not specified the shape of the dispersions $\xi_{\mathbf{k}\ell}$ or the interaction $V_{\mathbf{k}}$. A simple choice is the free electron dispersion[10]

[10] Lozovik and Yudson, 1976

$$\xi_{\mathbf{k}} = \frac{(\mathbf{k}-\mathbf{k}_0)^2}{2m} \tag{3.12}$$

which can be modified to match any lattice, such as graphene's hexagonal lattice.[11] Usually the dispersion is linearized

$$\xi_{\mathbf{k}} = v_F(\mathbf{k}-\mathbf{k}_0) \tag{3.13}$$

around the Fermi level to simplify the computations.[12] One can also introduce spin-orbit coupling which is needed for exciton condensates in topological insulator bilayers.[13] In our case of bilayer cuprates we consider the dispersion generated by nearest neighbor hopping on a square lattice,

$$\xi_{\mathbf{k}1} = -zt\frac{1}{2}(\cos k_x + \cos k_y) - \mu, \tag{3.14}$$

$$\xi_{\mathbf{k}2} = +zt\frac{1}{2}(\cos k_x + \cos k_y) + \mu, \tag{3.15}$$

see figure 3.4.

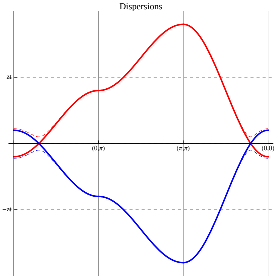

Figure 3.4: Dispersion of the electrons and holes in the absence of any interactions. The red thick line denotes the electron band, the blue thick line is the hole band. When a finite $t_\perp$ is included, a gap opens up around the Fermi surface, and the corresponding upper and lower bands are shown with dashed lines.

The type of interaction can be either nearest neighbor only, screened Coulomb or normal Coulomb. Here we choose for sake of simplicity the nearest neighbor interaction

$$V_{\mathbf{k}} = V. \tag{3.16}$$

With this choice of interaction it becomes reasonable to assume that the order parameter becomes independent of momentum $\Delta_{\mathbf{k}} = \Delta$; this amounts to only local electron-hole pairing. The mean-field energy at $T = 0$ now equals

$$E(\Delta) = 2V\Delta^2 - \frac{2}{N}\sum_{\mathbf{k}}\sqrt{\xi_{\mathbf{k}}^2 + V^2\Delta^2} \tag{3.17}$$

where $\xi_{\mathbf{k}} = \frac{1}{2}\left(\xi_{\mathbf{k}1} - \xi_{\mathbf{k}2}\right)$. The minimization condition $\partial E/\partial\Delta = 0$ yields the **gap equation**[14]

$$\frac{1}{V} = \frac{1}{2N}\sum_{\mathbf{k}}\frac{1}{\sqrt{\xi_{\mathbf{k}}^2 + V^2\Delta^2}}. \tag{3.18}$$

Let us pick some relevant parameters and solve the gap equation exactly. The typical hopping energy in cuprates is $t \approx 0.4$ eV. The interlayer hopping $t_\perp$ is set to zero because of the insulating layer that prevents exciton annihilation. A reasonable estimate for the interaction strength is to take it equal to the hopping energy:

[11] Dillenschneider and Han, 2008

[12] Shevchenko, 1976; Lozovik and Sokolik, 2008; Zhang and Joglekar, 2008; Kharitonov and Efetov, 2008; and Min et al., 2008

[13] Seradjeh et al., 2009

[14] A convenient way to express the gap equation is to replace the momentum sum by an integral over energy,

$$\frac{1}{V} = \int \frac{D(\varepsilon)d\varepsilon}{2\sqrt{\varepsilon^2 + V^2\Delta^2}},$$

where $D(\varepsilon)$ is the density of states.

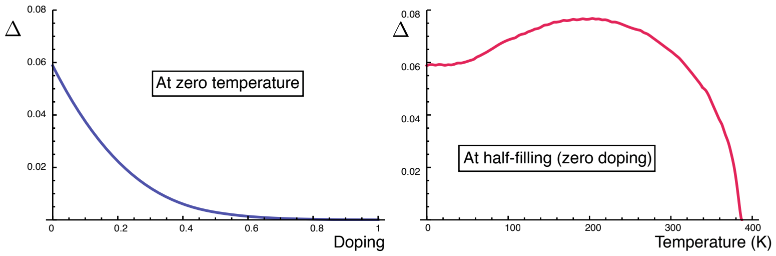

Figure 3.5: The exciton condensate order parameter Δ in mean field theory, found by the gap equation (3.18). **Left:** Δ at zero temperature as a function of doping. Note that zero doping equals half-filling. **Right:** Δ at half-filling as a function of temperature. The exciton condensate is stable up to $T_c \approx 385$ Kelvin.

$V \approx t$. Given these parameters we compute Δ as a function of particle density n at zero temperature, see figure 3.5.

The same minimization procedure can be obtained to find finite temperature behavior of the order parameter. At half-filling ($\mu = 0$) the density of states at the Fermi level is the highest, such that we find there the strongest instability towards exciton condensation. As shown in figure 3.5 the gap reduces with temperature until it vanishes at $T_c \approx 385$ K.

It is within this mean field approach quite easy to find a very large critical temperature. The predictions of room-temperature superfluidity[15] in exciton systems are obtained in this way. One must bear in mind, however, that mean field theory in general overestimates the tendency to order. On top of that, the fact that we are dealing with relatively strong Coulomb interactions makes the theory basically **unreliable**.

Besides the intrinsic problems that mean field theory has, the applicability to strongly correlated bilayers is further reduced because it does not take into account the strong onsite repulsion U. This is an example of an interaction that is not involved in the pairing mechanism, and can only be included perturbatively. Since $U > V$ a perturbative approach is unjustifiable.

We therefore need to resort to numerical approaches that treat the interactions U and V on the same footing as the kinetic energy t.

3.3 Numerical approach: Determinant Quantum Monte Carlo

This section is based on Rademaker et al., 2013c.

There are several numerical schemes available to study the Hubbard model. The straightforward manner is exact diagonaliza-

[15] Min et al., 2008

tion,[16] whereby one explicitly constructs the Hamiltonian matrix on a finite size cluster. The problem is that the Hilbert space size diverges exponentially with the system size: a simple 6×6 lattice has already a 69 billion dimensional Hilbert space. The **Determinant Quantum Monte Carlo** (DQMC)[17] technique on the other hand maps the fermionic Hubbard model onto a classical statistical problem, which can then be sampled using standard Monte Carlo methods.

Therefore we first rewrite the kinetic part of the bilayer Hubbard model in a matrix form,

$$H_K = \sum_{ij\ell\ell'\sigma} c^\dagger_{i\ell\sigma} k^\sigma_{i\ell,j\ell'} c_{j\ell'\sigma}. \tag{3.19}$$

If we have two layers of size $N \equiv N_x \times N_y$, the matrix k^σ is a $2N \times 2N$ matrix. The partition sum and the Greens function can now be exactly computed using this k-matrix,

I_{2N} is the $2N \times 2N$ identity matrix.

$$Z \equiv \mathrm{Tr}\left[e^{-\beta H_K}\right] = \det\left[I_{2N} + e^{-\beta k^\uparrow}\right] \det\left[I_{2N} + e^{-\beta k^\downarrow}\right] \tag{3.20}$$

and

$$G^\sigma_{i\ell,j\ell'} \equiv \frac{1}{Z}\mathrm{Tr}\left[c_{i\ell\sigma}c^\dagger_{j\ell'\sigma}e^{-\beta H_K}\right] = \left[I_{2N} + e^{-\beta k^\sigma}\right]^{-1}_{i\ell,j\ell'} \tag{3.21}$$

Notice that the dimension of the k-matrix grows linearly with system size, not exponentially as in the case of exact diagonalization.

To include the interaction terms we rewrite them such that half-filling is always characterized by $\mu = 0$. The onsite repulsion becomes

$$H_U = U \sum_{i\ell} \left[(n_{i\ell\uparrow} - \frac{1}{2})(n_{i\ell\downarrow} - \frac{1}{2}) - \frac{1}{4}\right] \tag{3.22}$$

while the interlayer nearest neighbor repulsion reads

$$H_V = V \sum_{i\sigma\sigma'} \left[(n_{i1\sigma} - \frac{1}{2})(n_{i2\sigma'} - \frac{1}{2}) - \frac{1}{4}\right]. \tag{3.23}$$

Obviously, for the full partition Hamiltonian $H = H_K + H_U + H_V$ we cannot use the result of (3.20). Therefore we need to perform a **Suzuki-Trotter** decomposition. The inverse temperature β is considered as a new dimension and we 'chop up' this imaginary time axis into L pieces,

$$e^{-\beta H} = \left(e^{-\Delta\tau H}\right)^L \tag{3.24}$$

[16] Kaneko et al., 2013

[17] Blankenbecler et al., 1981; White et al., 1989b; and White et al., 1989a

such that $\beta = L \times \Delta\tau$. At each imaginary time slice we split the kinetic part from the interaction parts,

$$e^{-\Delta\tau H} \approx e^{-\Delta\tau H_U} e^{-\Delta\tau H_V} e^{-\Delta\tau H_K} \tag{3.25}$$

which becomes exact in the limit $\Delta\tau \to 0$. We then introduce a discrete **Hubbard-Stratonovich transformation**. On each site and time-slice for each type of interaction we introduce a Hubbard-Stratonovich (HS) field $s(i,\tau)$ which can only take the values ± 1. As a result we decouple the onsite interactions

$$e^{-\Delta\tau U\left[(\hat{n}_\uparrow - \frac{1}{2})(\hat{n}_\downarrow - \frac{1}{2}) - \frac{1}{4}\right]} = \frac{1}{2} \sum_{s=\pm 1} e^{\lambda_U s(\hat{n}_\uparrow - \hat{n}_\downarrow)}, \tag{3.26}$$

where

$$\lambda_U = \operatorname{arccosh}\left(e^{\frac{1}{2}U\Delta\tau}\right). \tag{3.27}$$

A similar decoupling can be formulated for the interlayer interaction V. For each in-plane coordinate i we have six different HS fields $s_\alpha(i,\tau)$: in each layer one associated with the onsite repulsion U and the four possible interlayer interactions for V depending on the particle spin.

The index $\alpha = 1, \ldots, 6$ counts the specific type of HS field.

The advantage of the HS transformation is that the **interaction terms have become quadratic**. Just like we wrote the quadratic kinetic Hamiltonian in terms of a matrix k^σ, we can rewrite the transformed interaction terms using a diagonal matrix $v^\sigma(\tau)$ that depends on the HS fields $s_\alpha(i,\tau)$. Each time slice is therefore represented by the $2N \times 2N$ matrix

$$B_l^\sigma = e^{v^\sigma(l\Delta\tau)} e^{-\Delta\tau k^\sigma}, \tag{3.28}$$

the product of which represents the full evolution among the imaginary time axis

$$M^\sigma = I_{2N} + B_L^\sigma B_{L-1}^\sigma \cdots B_2^\sigma B_1^\sigma. \tag{3.29}$$

The partition sum can be computed exactly by

$$Z = \frac{1}{2^{6NL}} \sum_{s_\alpha(i,\tau)=\pm 1} \det M^\uparrow \det M^\downarrow. \tag{3.30}$$

The equal-time Greens function can be computed by

$$G^\sigma_{i\ell,j\ell'} = \frac{1}{Z}\frac{1}{2^{6NL}} \sum_{s_\alpha(i,\tau)=\pm 1} [M^\sigma]^{-1}_{i\ell,j\ell'} \det M^\uparrow \det M^\downarrow. \tag{3.31}$$

We have thus transformed the bilayer Hubbard model into a Ising-like statistical physics problem. We have $6NL$ 'sites' with ± 1 variables and each possible configuration is weighed by the determinants of the M^{σ}-matrices.

There are too many configurations to compute (3.30) and (3.31) exactly. Therefore we pick random configurations and compute Z and G and this result will become exact when the number of random configurations approaches infinity. However, one can still do better, via the procedure of **importance sampling**. Thereby we create a Markov chain of configurations, favoring configurations with a larger weight. This is done in such a way that the weight of a configuration is reflected in its occurrence in the Markov chain. In a more precise language, importance sampling requires three steps:

1. Start with a given configuration s.

2. Make a new configuration s' based on the old one, in the present case by randomly changing the six HS fields on a given site and time-slice.

3. Accept this new configuration with a transition probability $T(s \rightarrow s')$. This probability must satisfy the detailed balance condition
$$T(s \rightarrow s')P(s) = T(s' \rightarrow s)P(s') \tag{3.32}$$
where $P(s)$ is the statistical weight of configuration s. Additionally, the function $T(s \rightarrow s')$ must satisfy overall ergodicity, which means that there is always a finite chance to get from any initial configuration to any other configuration.

4. 'Measure' parameters of interest, such as the Greens function $[M^{\sigma}]^{-1}_{i\ell,j\ell'}$, given the configuration at hand. Then go back to step 1 and repeat this sequence until enough measurement points have been accumulated.

5. Do a simple average over the measurement points.

In the **Metropolis algorithm** the new configuration is accepted with probability $T_M(s \rightarrow s') = \min(1, P(s')/P(s))$. The **heat bath algorithm** has the transition probability $T_{HB}(s \rightarrow s') = P(s')/(P(s) + P(s'))$. Since the importance sampling works best when new configurations are accepted approximately 50% of the time, in our code we work with a mixture of heat bath and Metropolis prescriptions,

$$T(s \to s') = \gamma \frac{P(s')}{P(s) + P(s')} + (1-\gamma) \min\left(1, \frac{P(s')}{P(s)}\right) \tag{3.33}$$

where γ is a parameter that we can tune to get the optimal acceptance probability.

3.3.1 *DQMC and the sign problem*

So what happened to the infamous fermion sign problem? The product $\det M^{\uparrow} \det M^{\downarrow}$ can be negative, which implies that we cannot identify it as the weight of a configuration. Instead, we need to define the weight by their absolute value,

$$P(s) = \left|\det M^{\uparrow} \det M^{\downarrow}\right|. \tag{3.34}$$

We then need to measure the **average sign**

$$\text{Sign} = \text{sgn}\left(\det M^{\uparrow} \det M^{\downarrow}\right) \tag{3.35}$$

for each configuration that appears in the Markov chain. Additionally we need to multiply each measurement with the sign of the configuration. In step 5, where we do averaging, we need to divide the result by the average sign.

In the single layer Hubbard model at half-filling the particle-hole symmetry leads to sign-cancellation, such that $\det M^{\uparrow} \det M^{\downarrow}$ is always positive. However, away from half-filling at low temperatures the average sign decreases rapidly. This causes an exponential increase in the errors made since we are dividing by a number that tends to zero. For example, at 15% doping the sign problem prevents us from cooling below 1000 Kelvin: precisely the range where the interesting physics happens.

In our bilayer case it is even worse: the protection guaranteed by particle-hole symmetry is lost because of the interlayer interaction V. Even at half-filling, there will be a sign problem. Our only hope is that the interesting physics, such as exciton condensation, will show up before the average sign drops below ~ 0.2.

3.3.2 *Numerical recipes*

Before we proceed to the results of the DQMC for the bilayer Hubbard model, we need to introduce some numerical tricks that are needed to make this method work.

For some physical parameters, such as conductivity or pair-susceptibilities, one needs to compute the **unequal time Greens function**

$$G_{i\ell,j\ell'}(\tau,\tau') = \frac{1}{Z}\mathrm{Tr}\left[c_{i\ell\sigma}(\tau)c^{\dagger}_{j\ell'\sigma}(\tau')e^{-\beta H}\right] \tag{3.36}$$

for $\tau > \tau'$. Given a configuration of HS fields we define $\tau = p\Delta\tau$, $\tau' = q\Delta\tau$ and

$$\begin{aligned} A_1^{\sigma} &= B_p^{\sigma}B_{p-1}^{\sigma}\ldots B_{q+1}^{\sigma} && (3.37)\\ A_2^{\sigma} &= B_q^{\sigma}B_{q-1}^{\sigma}\ldots B_{p+1}^{\sigma}. && (3.38)\end{aligned}$$

so that the unequal time Greens function can be computed as

$$G^{\sigma}_{i\ell,j\ell'}(\tau,\tau') = \left[(A_1^{\sigma})^{-1} + A_2^{\sigma}\right]^{-1}_{i\ell,j\ell'}. \tag{3.39}$$

A major problem in computing the A, M and G matrices lies in the fact that matrix multiplication and inversion is a numerically highly unstable process. One therefore needs to use carefully developed matrix factorization algorithms. Whenever multiplications or inversions seem to become unstable, one needs to perform a **UDR decomposition**[18] of the matrix at hand: U is unitary, D is diagonal and R is an upper triangular matrix with unity pivots. The unstable part of the matrix is now cast in the diagonal part, which needs to be treated carefully.

The construction of the Greens function matrix is in general numerically costly. However, within the importance sampling algorithm one can quickly change the Greens function of the 'old' configuration into the 'new' one. Start with a known Greens Function for both spin species given the HS-fields $s_{\alpha}(i,l\Delta\tau)$ and then change all the six HS fields at site and time-slice $(i,l\Delta\tau)$ yielding a s_{new}. Define

$$\Delta s_{\alpha} = s_{\alpha,\mathrm{new}}(i,l\Delta\tau) - s_{\alpha,\mathrm{old}}(i,l\Delta\tau) = \pm 2 \text{ or } 0. \tag{3.40}$$

Under this change, we note that[19]

$$\begin{aligned} A^{\sigma} &= B_l^{\sigma}B_{l-1}^{\sigma}\cdots B_1^{\sigma}B_L^{\sigma}\cdots B_{l+1}^{\sigma} && (3.41)\\ &\longrightarrow A^{\sigma\,\prime} = \left[I+\Delta^{\sigma}\right]A^{\sigma}. && (3.42)\end{aligned}$$

---

[18] White et al., 1989b

[19] The equal-time Greens function $G(l\Delta\tau, l\Delta\tau)$ is given by $[I + A^{\sigma}]^{-1}$. The explicit l-dependence is dropped in the following derivation.

The matrix Δ^σ has only two nonzero elements, namely

$$\begin{aligned}
\Delta^{\uparrow}_{i1,i1} &= \exp\left[\lambda_U \Delta s_1 + \lambda_V(\Delta s_3 + \Delta s_4)\right] - 1 && (3.43)\\
\Delta^{\downarrow}_{i1,i1} &= \exp\left[-\lambda_U \Delta s_1 + \lambda_V(\Delta s_5 + \Delta s_6)\right] - 1 && (3.44)\\
\Delta^{\uparrow}_{i2,i2} &= \exp\left[\lambda_U \Delta s_2 - \lambda_V(\Delta s_3 + \Delta s_5)\right] - 1 && (3.45)\\
\Delta^{\downarrow}_{i2,i2} &= \exp\left[-\lambda_U \Delta s_2 - \lambda_V(\Delta s_4 + \Delta s_6)\right] - 1. && (3.46)
\end{aligned}$$

The **ratio of weights** between the new $M^{\sigma\,\prime}$ and the old M^σ equals

$$\begin{aligned}
R^\sigma &= \frac{\det[I + A^{\sigma\,\prime}]}{\det[I + A^\sigma]}\\
&= \det\left[(I + A^{\sigma\,\prime})G^\sigma\right]\\
&= \det\left[I + \Delta^\sigma A^\sigma G^\sigma\right]\\
&= \det\left[I + \Delta^\sigma (I - G^\sigma)\right]\\
&= \left[1 + (1 - G^\sigma_{i1,i1})\Delta^\sigma_{i1,i1}\right]\left[1 + (1 - G^\sigma_{i2,i2})\Delta^\sigma_{i2,i2}\right]\\
&\quad - G^\sigma_{i2,i1} G^\sigma_{i1,i2} \Delta^\sigma_{i1,i1} \Delta^\sigma_{i2,i2}. && (3.47)
\end{aligned}$$

Using this formula, we can quickly decide whether we want to accept a change or not, instead of explicitly recalculating the whole determinant. If the change is accepted, we can use a similar trick to update the Greens function. Recall that

$$G^\sigma \to G^{\sigma\,\prime} = \left[1 + A^\sigma + \Delta^\sigma A^\sigma\right]^{-1}. \qquad (3.48)$$

Because the matrix Δ is sparse (it has only two nonzero elements, at i and $i + N$), we can use the **Woodbury matrix identity** to do a fast update of the Greens function. In single layer DQMC one uses the Sherman-Morrison matrix identity, but the interlayer correlations force us to use a generalization. The Woodbury identity amounts to

$$G^\sigma_{ab} \to G^\sigma_{ab} - \sum_{\ell,\ell'} G^\sigma_{a,i\ell} \Delta^\sigma_{i\ell,i\ell} (R^{-1})_{\ell\ell'} (1 - G^\sigma)_{i\ell',b} \qquad (3.49)$$

where the spin-dependent R-matrix is given by

$$R_{\ell\ell'} = \begin{pmatrix} 1 + (1 - G^\sigma_{i1,i1})\Delta^\sigma_{i1,i1} & -G^\sigma_{i1,i2}\Delta^\sigma_{i2,i2} \\ -G^\sigma_{i2,i1}\Delta^\sigma_{i1,i1} & 1 + (1 - G^\sigma_{i2,i2})\Delta^\sigma_{i2,i2} \end{pmatrix}. \qquad (3.50)$$

Note that the determinant of the R-matrix equals the ratio as defined in equation (3.47). Thus the inverse is trivially given by

$$(R^{-1})_{\ell\ell'} = \frac{1}{R^\sigma} \begin{pmatrix} 1 + (1 - G^\sigma_{i2,i2})\Delta^\sigma_{i2,i2} & G^\sigma_{i1,i2}\Delta^\sigma_{i2,i2} \\ G^\sigma_{i2,i1}\Delta^\sigma_{i1,i1} & 1 + (1 - G^\sigma_{i1,i1})\Delta^\sigma_{i1,i1} \end{pmatrix}. \qquad (3.51)$$

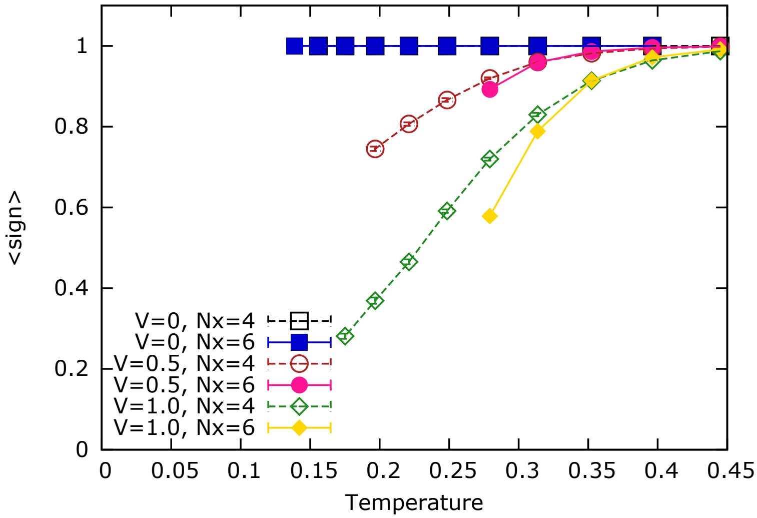

Figure 3.6: The average sign at half-filling for various interlayer interactions V. When $V \neq 0$ the average sign drops rapidly. Parameters are $U = 4t$, $t_\perp = 0.05t$ and $\mu = 0$.

These equations combined yield the full Woodbury update in the case of a bilayer system with interlayer interactions.

The Woodbury identity requires that we consider the equal-time Greens functions $G(\tau, \tau)$ at different imaginary times. A simple trick to get from one time-slice to the next is called **wrapping**,

$$\begin{aligned} G^\sigma(l+1) &= \left[I + B^\sigma_{l+1} B^\sigma_l \cdots B^\sigma_{l+2}\right]^{-1} && (3.52) \\ &= B^\sigma_{l+1} G^\sigma(l) [B^\sigma_{l+1}]^{-1}. && (3.53) \end{aligned}$$

So for a full update of the Greens function we start at the first time slice. Then we update the HS fields at each site using the importance sampling and the Woodbury identity. Once all sites at a given time-slice are done, we use wrapping to get to the next time-slice. This procedure is repeated until all time-slices are updated. In the mean-time we perform various physically relevant measurements, such as density, spin correlations, etcetera.

Finally we require a numerical recipe for the **error analysis** of the results. A simple root mean-squared error of all configurations is not a good measure.[20] Additionally, the measurements should be independent which is clearly not the case for a Markov chain of configurations. We therefore compute 8 independent Markov chains in parallel, and the error bars are obtained as root mean-squared errors over the averages of each Markov chain. This

[20] For example: if we measure the energy, then the root mean-squared of all independent measurements gives you the specific heat, not the uncertainty in the average energy.

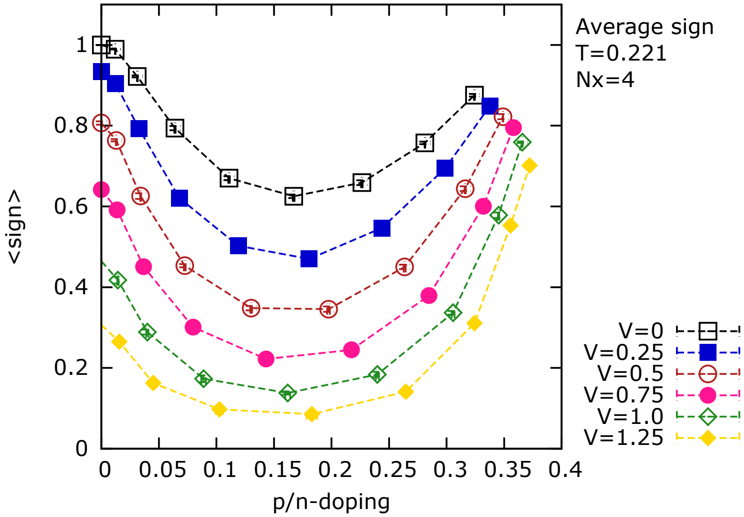

Figure 3.7: The average sign versus density for increasing interlayer interaction V. The temperature is fixed at $T = 0.221$, other parameters are $U = 4t$ and $t_\perp = 0.05t$.

measures the degree to which two independent sampling chains lead to the same average.

3.3.3 *Results on the fermion sign problem*

The applicability of the DQMC method just described is limited by the **measured average sign**, which depends on the specific model parameters such as temperature and interaction strength. We therefore present first our results regarding the average sign, both its value and the impact on the statistical errors on other measurements.

As we briefly mentioned in section 3.3.1, in the absence of the interlayer interaction V at **half-filling** the average sign is always 1 due to particle-hole symmetry. This can be understood by considering the determinants of M^σ for both spin species. Since the Hubbard-Stratonovich fields couple to both the up and down spins, a change of sign in $\det M^\uparrow$ is accompanied by the same sign change in $\det M^\downarrow$. Consequently, at half-filling for $V = 0$ all weights $\det M^\uparrow \det M^\downarrow$ are positive. One can directly infer that this sign cancellation fails when $V \neq 0$, since there are now HS fields that couple to only one type of spin. Indeed, as can be seen in figure 3.6, inclusion of a nonzero interlayer interaction V drastically reduces the sign.

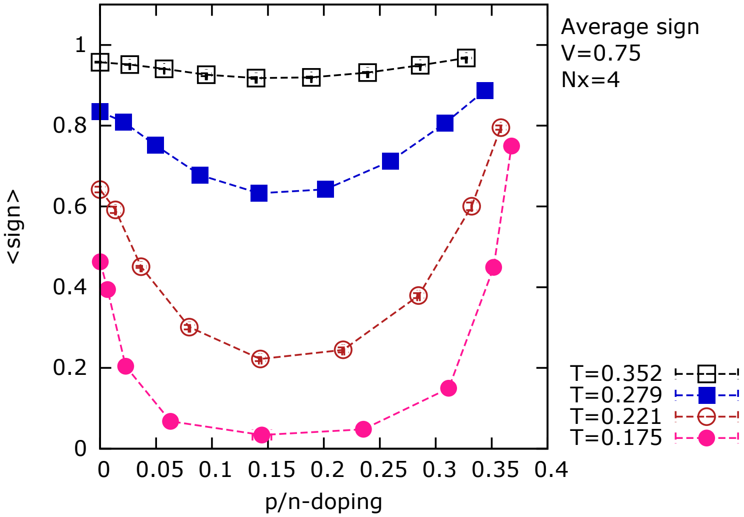

Figure 3.8: The average sign versus density at various temperatures. The interlayer interaction is fixed at $V = 0.75$, other parameters are $U = 4t$ and $t_{\perp} = 0.05t$. The sign is lowest around $15 - 20\%$ doping.

At **finite densities**, in the case of equal p-type and n-type doping of the two different layers, the average sign is further reduced. Even in the absence of interlayer V, the sign drops so rapidly that the physically interesting regime (with the pseudogap, d-wave superconductivity, etc.) is inaccessible. Figure 3.7 displays how the average sign depends on both doping and interlayer V for a fixed temperature. It is worthwhile to note that the physical temperature corresponding to these parameters is about 900 Kelvins, still an order of magnitude higher than for example the onset of superconductivity in the cuprates. In figure 3.8 we show the average sign as a function of doping for a fixed interlayer coupling $V = 0.75$.

In all cases the sign problem is the **worst around** $15 - 20\%$ **p/n-doping**. Remember that we have one layer doped with holes and another layer doped with the same number of electrons, relative to half-filling. Inclusion of V does not change the qualitative doping dependence of the average sign, it does reduce it significantly.

This is in stark contrast to the suggestion, made in the context of the exciton $t - J$ model of the next chapters,[21] where we consider the limit $V \gg t$, that the sign problem could be reduced upon increasing V. That is based on the idea that the increased interlayer interaction makes it more likely that electrons and holes in the

[21] See Sheng et al., 1996; Wu et al., 2008 and section 4.1.4.

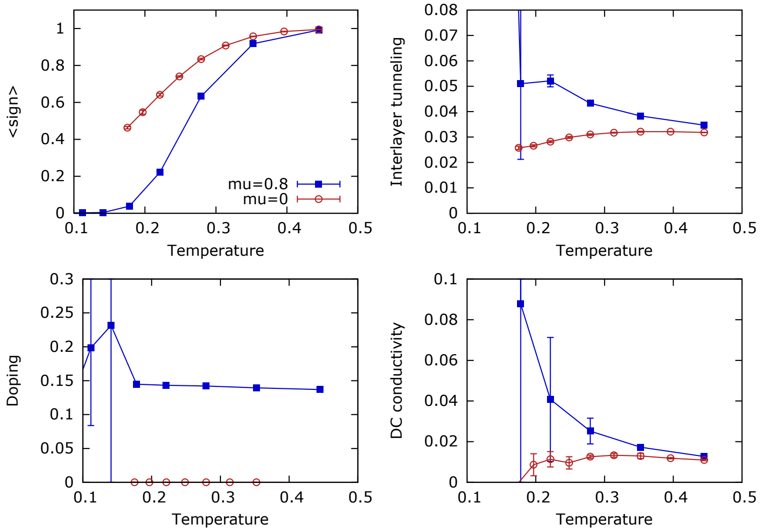

Figure 3.9: Average sign, doping, interlayer tunneling and dc conductivity for $V = 0.75$ and $N_x = 4$ as a function of temperature. Static measurements, such as density and interlayer tunneling, are still reliable as long as the sign > 0.1. The dynamic measurements such as dc conductivity become unstable when the sign < 0.5. For comparison, both $\mu = 0$ and $\mu = 0.8t$ is shown.

two layers move simultaneously, so that the signs of the electrons could be cancelled by the signs of the hole. Based on our DQMC results, this is obviously not the case when the interlayer coupling V is of the same order as t.

Whenever the average sign becomes low, the **uncertainty of measurements increases**. Let us give a rough quantitative estimate of what average sign is still acceptable. Therefore we need to distinguish between two kinds of measurements. **'Static' measurements**, such as the doping and interlayer tunneling, involve only the equal-time Greens function

$$G^{\sigma}_{i\ell,j\ell'} = \langle c_{i\ell\sigma} c^{\dagger}_{j\ell'\sigma} \rangle \tag{3.54}$$

and are more stable than **'dynamic' measurements** involving the unequal-time Greens function

$$G^{\sigma}_{i\ell,j\ell'}(\tau) = \langle T_{\tau} c_{i\ell\sigma}(\tau) c^{\dagger}_{j\ell'\sigma} \rangle. \tag{3.55}$$

In the latter category, we computed the **dc conductivity** based on the current-current correlation function for each layer,

$$\Lambda^{\ell}_{xx}(\mathbf{q},\tau) = \sum_i \langle j_x(\mathbf{r}_{i\ell},\tau) j_x(0,0) \rangle e^{i\mathbf{q}\cdot\mathbf{r}_{i\ell}} \tag{3.56}$$

Instead of performing the analytic continuation, we approximate the dc conductivity by[22]

[22] Trivedi et al., 1996

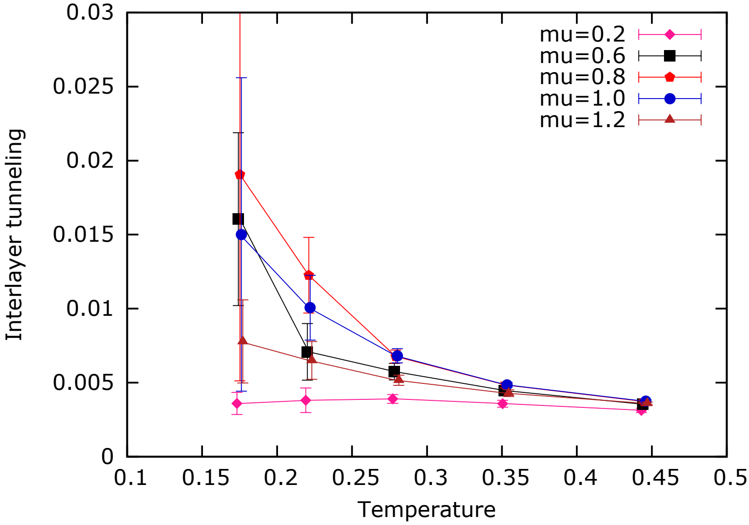

Figure 3.10: Interlayer tunneling at $V = 0.75t$ for $N_x = 4$, relative to the $V = 0$ case. A clear enhancement of the tunneling, which is equal to the exciton condensate order parameter, can be seen around $\mu = 0.8$, where the doping level is approximately 15%.

$$\frac{\pi\sigma_{dc}}{\beta^2} = \Lambda^{\ell}_{xx}(\mathbf{q} = 0, \tau = \beta/2) \tag{3.57}$$

which is valid as long as the density of states is not rapidly varying around the Fermi surface.

In figure 3.9 we show the average sign dependence as a function of temperature for $V = 0.75$, for $\mu = 0$ and $\mu = 0.8$, and relate it to interlayer tunneling, doping and dc conductivity measurements. As long as the average sign is above 0.5, all measurements are statistically trustworthy. Below 0.5, the dc conductivity results have statistical error bars more than half of σ_{dc} itself. Therefore we limit our **dynamical** measurements to regions where the **sign is** < 0.5. Similarly, the error bars on the **static** measurements suggest that we cannot use static data when the average **sign is** < 0.1. This implies that the window for which DQMC is applicable for all doping levels is **limited to about** $\beta < 5$ **and** $V < 1$.

3.3.4 *Exciton condensation*

Our main goal is to investigate whether exciton condensation might occur in the bilayer Hubbard model. Recall that the **order parameter of an interlayer exciton condensate** is[23]

$$\Delta_{\mathbf{k}} = \langle c^{\dagger}_{\mathbf{k}1\sigma} c_{\mathbf{k}2\sigma} \rangle. \tag{3.58}$$

[23] See chapter 2, specifically equation (2.1).

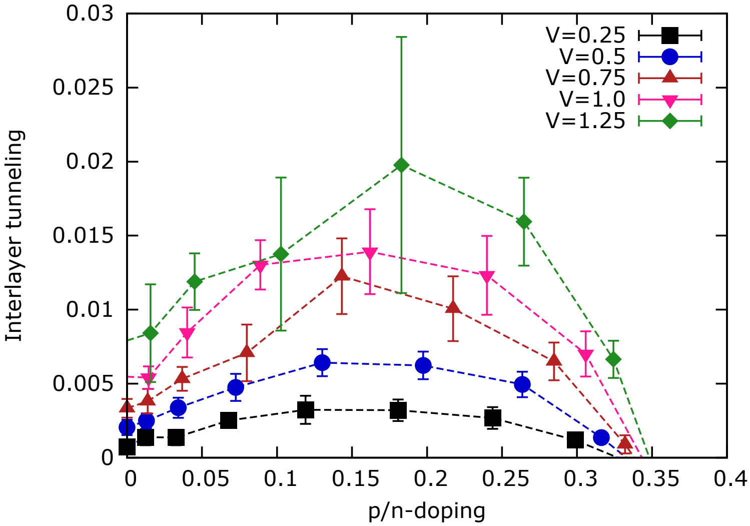

Figure 3.11: Interlayer tunneling for $N_x = 4$, relative to the $V = 0$ case, for all densities and interaction V. A clear enhancement of the tunneling, which is equal to the exciton condensate order parameter, can be seen around the doping level of $15 - 20\%$.

In the presence of strong local interactions **excitons will be formed locally** as well, which means that the electron and hole are above each other. The order parameter becomes independent of momentum and equals

$$\Delta = \frac{1}{N} \sum_i \langle c^\dagger_{i1\sigma} c_{i2\sigma} \rangle. \tag{3.59}$$

The condensate order parameter equals interlayer tunneling,[24] which is directly measurable in experimental set-ups.

Within the DQMC method, the interlayer tunneling can be directly read off from the Greens function constructed during the algorithm. The ideal exciton condensate occurs when the interlayer hopping is completely suppressed, $t_\perp = 0$. However, in that case the order parameter calculated in DQMC is identically zero. We **need to include a finite** $t_\perp$, which acts as a symmetry breaking field just like a magnetic field would induce magnetization. The inclusion of a nonzero $t_\perp$ requires us, however, to extrapolate to the perfect $t_\perp \to 0$ case. For this we propose two different schemes.

First, we note that in the absence of an exciton pairing interaction V the interlayer hopping $t_\perp$ will automatically create a doping dependence of the interlayer tunneling. Therefore we separate the contribution to interlayer tunneling that arises due to exciton

[24] Spielman et al., 2000; and Eisenstein and MacDonald, 2004

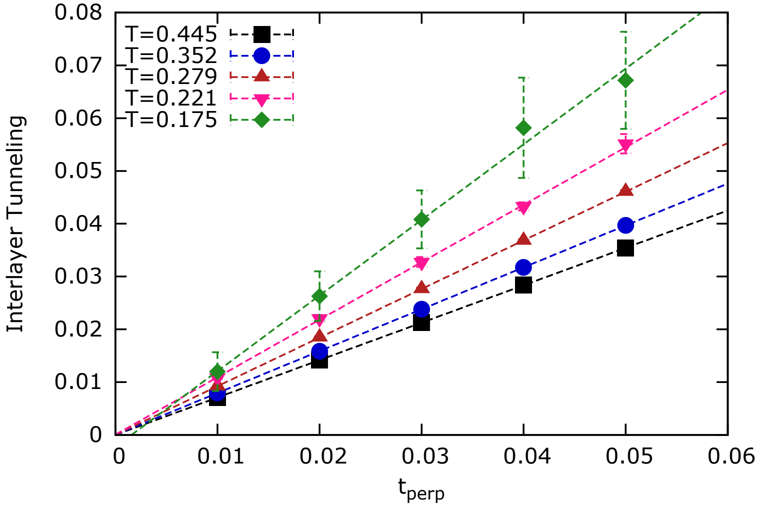

Figure 3.12: Interlayer tunneling at $V = 0.75t$ as a function of $t_\perp$ for $\mu = 1$ and $N_x = 4$. The scaling for $t_\perp$ suggests that there is no exciton condensation.

formation from the part that is already present at $V = 0$. In figure 3.10 we show how this **relative interlayer tunneling** depends on temperature and chemical potential for fixed $V = 0.75$. There is a clear enhancement of the interlayer tunneling around $\mu = 0.8$, which amounts to 15% doping.

At a given temperature of $T = 0.221$ we present the interlayer tunneling as a function of p/n-doping and interlayer interaction V in figure 3.11. The **strongest tendency towards interlayer tunneling is at** $15 - 20\%$ **doping**, for the largest values of interaction V.

Our second strategy to determine the possibility of exciton condensation is to **look at the** $t_\perp$**-dependence of the interlayer tunneling**. Following the standard BEC/BCS condensation theories,[25] the exciton condensate is represented in the Hamiltonian by the symmetry breaking term

$$-V\Delta \sum_{i\sigma} \left(c^\dagger_{i1\sigma} c_{i2\sigma} + h.c. \right) \tag{3.60}$$

which just adds to the interlayer hopping term $t_\perp$. When $U = V = 0$ we can compute the interlayer tunneling analytically which yields

$$\langle c^\dagger_{i1\sigma} c_{i2\sigma} \rangle \sim \frac{t_\perp + V\Delta}{t}. \tag{3.61}$$

[25] See section 3.2.

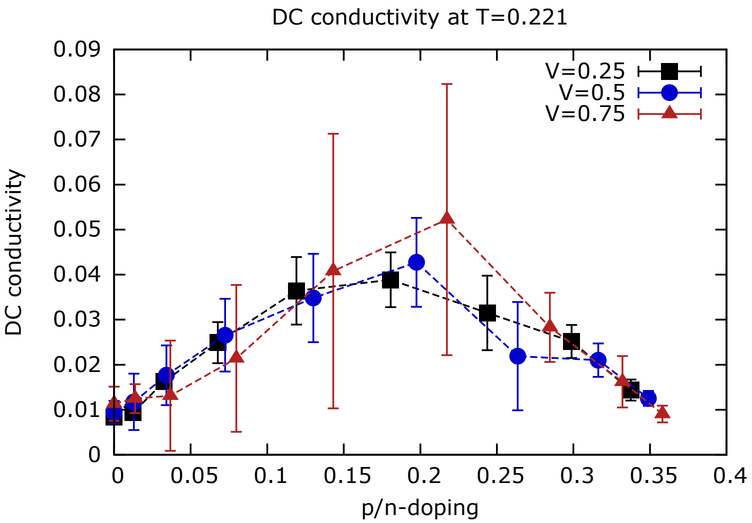

Figure 3.13: The dc conductivity σ_{dc} following equations (3.56)-(3.57) at $T = 0.221$ as a function of doping and V for $N_x = 4$. We only included data points where the error bar on the measurements is less than 50% of σ_{dc} itself. The dc conductivity is the largest at a doping around 20%,

For finite U and V we therefore assume that the interlayer tunneling is a linear function of $t_\perp$, and the order parameter can be found by taking the limit $t_\perp \to 0$. This is done for $V = 0.75$ and $\mu = 1$, parameters for which the interlayer tunneling is the largest, in figure 3.12. As the temperature is lowered the interlayer tunneling increases. However, the scaling behavior as a function of $t_\perp$ suggests that there is **no exciton condensation present**. Unfortunately, due to the sign problem, we cannot go lower in temperatures.

Next to direct measurements of the order parameter, one can **probe related properties of the exciton condensate**. Since in an exciton condensate the charge carriers are bound into charge neutral excitons, it is expected that exciton condensates are **insulating**. Let us therefore look at the conductivity measurements, which are severely limited by the sign problem as pointed out in the previous section. In figure 3.13 we display measurements on the dc conductivity following equations (3.56)-(3.57). The conductivity is largest at a p/n-doping of 15-20%, and fairly independent of the interlayer coupling V.

Instead of the conductivity one can look at the **density of states at the Fermi level**, which is approximated by $G(\mathbf{r} = 0, \tau = \beta/2)$.[26] The density of states at the Fermi level indeed closely follows the

[26] Trivedi and Randeria, 1995; and Nowadnick et al., 2012

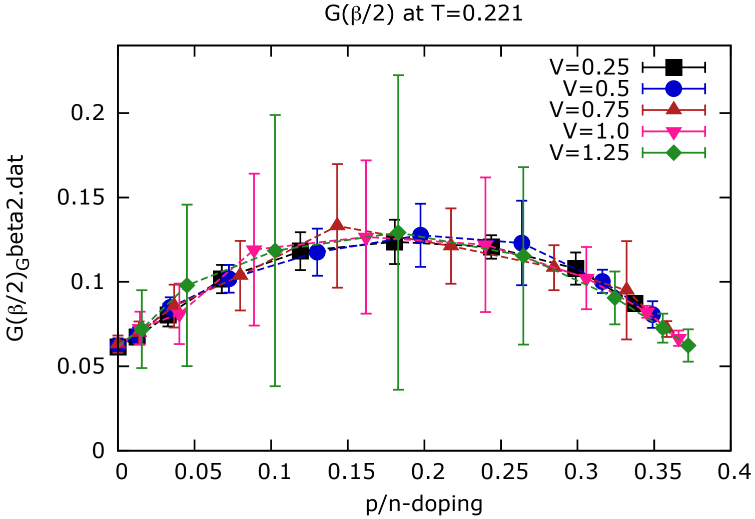

Figure 3.14: The density of states at the Fermi level, approximated by $G(\beta/2)$, at $T = 0.221$ for $N_x = 4$. The density of states is highest around 20% doping, independent of the interlayer interaction V.

p/n-doping dependence of the dc conductivity. Counterintuitively, the increase of conductivity occurs in the region where there is also an increase in the interlayer tunneling. This, together with the $t_\perp$-scaling performed in figure 3.12, rules out exciton condensation at the temperature that are attainable within the DQMC set-up.

In conclusion, we have found no evidence of exciton condensation in the bilayer Hubbard model in the parameter regime accessible by DQMC. However, the increased interlayer tunneling suggests that exciton physics might be relevant for large V, around 15-20% p/n-doping and at temperatures lower than $\beta = 5$.

3.3.5 *Magnetic measurements*

Strong correlations can lead to the localization of electron degrees of freedom, resulting in magnetic correlations. For the Hubbard model on a square lattice this results in **antiferromagnetic order** at half-filling.[27] Experiments on the cuprates show that this antiferromagnetism quickly disappears upon doping.[28] Next to the excitonic physics, we will therefore study the magnetic correlations of the Hubbard bilayer.

[27] See chapter 4.

[28] Imada et al., 1998

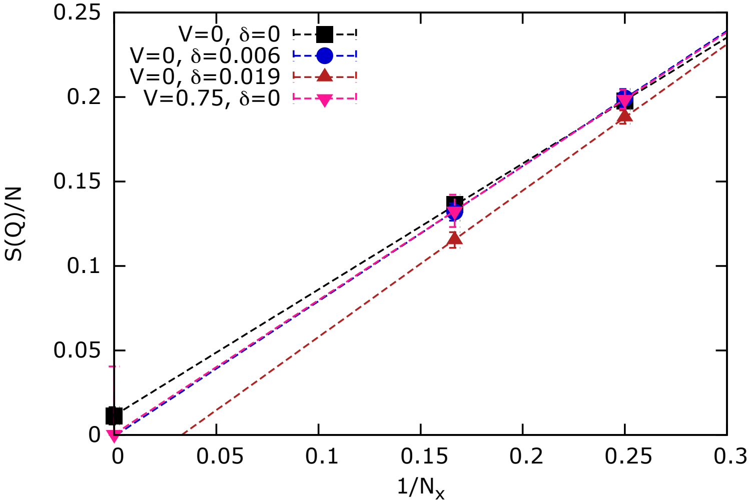

Figure 3.15: Antiferromagnetic correlations at $T = 0.175$ for various V and doping. Only at half-filling ($\delta = 0$) we find antiferromagnetism in the thermodynamic limit.

The antiferromagnetic structure factor in each layer is given by

$$S_\ell(\mathbf{Q}) = \frac{1}{N}\sum_{ij} e^{i\mathbf{Q}\cdot(\mathbf{r}_i-\mathbf{r}_j)}\langle\left(n_{i\ell\uparrow}-n_{i\ell\downarrow}\right)\left(n_{j\ell\uparrow}-n_{j\ell\downarrow}\right)\rangle \tag{3.62}$$

where $\mathbf{Q} = (\pi, \pi)$ is the antiferromagnetic wave vector. Spin wave theory[29] suggests that $S(\mathbf{Q})$ scales with $1/N_x$ on a finite cluster. The thermodynamic limit $N_x \rightarrow$ of $S(\mathbf{Q})$ can be found from a linear extrapolation of the $N_x = 4$ and $N_x = 6$ data, as is done in figure 3.15. Indeed, the antiferromagnetic order is rapidly destroyed as one dopes the layers. However, under the inclusion of V the antiferromagnetic order remains up to $V = 0.75$.

Even though the antiferromagnetic order is rapidly destroyed, the **localization of electrons** associated with the strong onsite repulsion U is reduced less drastically by p/n-doping. The local moment, which measures the degree of localization, is defined as

$$m_{i\ell} = \langle\left(n_{i\ell\uparrow}-n_{i\ell\downarrow}\right)\rangle. \tag{3.63}$$

The site-averaged local moments are shown in figure 3.16. The localization of electrons is for all intents and purposes independent of the interlayer interaction strength V.

[29] Huse, 1988

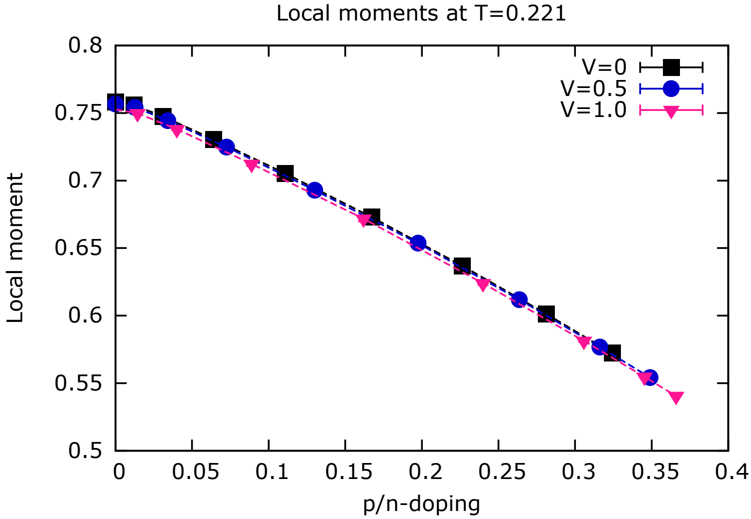

Figure 3.16: The local moments as a function of V and doping at $T = 0.221$ for $N_x = 4$. The localization of electrons is the strongest at half-filling, and almost independent of the interlayer interaction V.

3.3.6 *Conclusion*

The Determinant Quantum Monte Carlo is a brute-force technique that is in principle able to exactly compute physical quantities associated with the Hubbard model. However, the bilayer Hubbard model seems remarkablyunfi unfit for the DQMC approach. Whereas several physical properties such as the conductivity and the magnetic properties are almost independent of interlayer interaction V, the average sign rapidly reduces with increasing V. The desired exciton condensation, measured by interlayer tunneling, is therefore out of reach. Given our data for $\beta < 5$ and $V < 1.25$ we find the **strongest tendency towards exciton condensation around 15-20% doping and at large interaction strength** V. In the next chapter, therefore, we will approach the problem of condensation from the strong coupling limit.

4
Exciton-spin dynamics in the Mott insulating state

Two fermions form a boson, which is precisely what happens when an electron and a hole bind together into an exciton. A completely different way to find emergent bosonic physics is to have strong electron-electron interactions near half-filling. In the Mott insulating state, the effective degrees of freedom are bosonic spin waves.

Whenever the electron-electron and electron-hole interactions are strong, which we expect in the case of cuprates, we can model the system in terms of bosons only: spins and excitons. In this chapter we derive the corresponding **exciton $t-J$ model**. Close to the Mott insulating state the insertion of excitons leads to frustration, as is described in section 4.2. The full phase diagram of the exciton $t-J$ model is discussed in the next chapter.

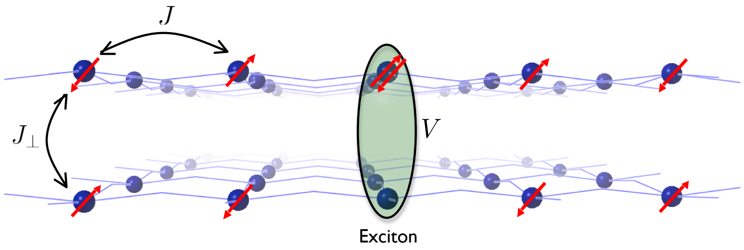

Figure 4.1: Naive real space picture of an exciton in a strongly correlated bilayer, as viewed from the side. Two square lattices (blue balls) are placed on top of each other. The red arrows denote the spin ordering, which forms a perfect Néel state. The exciton consists of a bound pair of a double occupied and a vacant site on an interlayer rung. The energy required to break this doublon-holon pair is V. The magnetic ordering is governed by the in-plane Heisenberg J and the interlayer $J_\perp$, as described by the Hamiltonian (4.12).

4.1 *Strong coupling limit and the $t-J$ model*

When the onsite Coulomb repulsion in the Hubbard model (3.4) is much larger than the kinetic energy, $U \gg t$, it becomes impossible for two electrons to occupy the same orbital. At half-filling this results in a traffic jam of electrons: on each lattice site there is one electron, unable to move due to the restraint on double occupancy. This is the **Mott insulator**.[1]

4.1.1 *The Mott insulating state and the $t - J$ model*

The Mott insulating phase is thus characterized by a large interaction U and the corresponding localization of electrons at half-filling.[2] Due to this localization only the spin degree of freedom remains. A perturbation method by Kato, 1949 has been applied to the Hubbard model[3] to obtain an effective low energy model for the spins: the $t - J$ model.

The key to this **strong coupling perturbation theory** is that we project out the states that contain double occupied sites.[4] The hopping terms H_t are treated as a perturbation on the exactly solvable interaction term H_U,

$$H_\lambda = H_U + \lambda H_t. \tag{4.1}$$

We introduce a projection operator $\mathbf{P}_0$ that projects onto the eigenspace U_0 of H_U with eigenvalue E_0 associated with a fixed number of double occupied sites. The hopping term is then adiabatically turned on, that is $\lambda \to 1$. Introduce an operator $\mathbf{P}_\lambda$ that projects onto the eigenspace U that is adiabatically connected to the eigenspace U_0. This operator is expressed in terms a contour integral over the resolvent operator,

$$\mathbf{P}_\lambda = \frac{1}{2\pi i} \oint_C \frac{dz}{z - H_\lambda} \tag{4.2}$$

where the contour C goes around the eigenvalue E_0 but not around any other eigenvalues of H_U. A series expansion of the resolvent operator yields

$$\mathbf{P}_\lambda = \mathbf{P}_0 + \lambda \left[\mathbf{P}_0 H_t \left(\frac{1 - \mathbf{P}_0}{E_0 - H_U} \right) + \left(\frac{1 - \mathbf{P}_0}{E_0 - H_U} \right) H_t \mathbf{P}_0 \right] + \mathcal{O}(\lambda^2). \tag{4.3}$$

Now an effective Hamiltonian on the eigenspace U exists, with exactly the same spectrum as the full H_λ, given by

$$H_{\text{eff}} = \mathbf{P}_0 (H_\lambda - E_0) \mathbf{P}_\lambda \mathbf{P}_0, \tag{4.4}$$

which can be constructed using the expansion of $\mathbf{P}_\lambda$. At zeroth order in λ the effective Hamiltonian consists of the electron hopping

[1] Mott, 1949; Anderson, 1952; and Marshall, 1955

[2] This is in stark contrast with the band theory picture, where electrons are completely delocalized.

[3] Klein and Seitz, 1973; Takahashi, 1977; and Chao et al., 1977

[4] On the electron doped side of half-filling we project out states with more double occupied sites than necessary, which is equivalent to projecting out the empty sites.

term with the no double occupancy constraint,

$$H_{\text{eff}}^{(0)} = \mathbf{P}_0 H_t \mathbf{P}_0. \tag{4.5}$$

From now on the projection $\mathbf{P}_0$ is included as implicit constraint on the double occupancy.

The first order correction in λ is given by

$$H_{\text{eff}}^{(1)} = -\frac{1}{U}\mathbf{P}_0 H_t (1 - \mathbf{P}_0) H_t \mathbf{P}_0. \tag{4.6}$$

It contains two-hopping processes, where the intermediate state contains an additional double occupied state as shown in table 4.1. The remaining Hamiltonian can be expressed in **spin operators** only, which are

$$\begin{aligned} s_i^z &= \frac{1}{2}\left(c_{i\uparrow}^\dagger c_{i\uparrow} - c_{i\downarrow}^\dagger c_{i\downarrow}\right), && (4.7) \\ s_i^+ &= c_{i\uparrow}^\dagger c_{i\downarrow}, && (4.8) \\ s_i^- &= c_{i\downarrow}^\dagger c_{i\uparrow}. && (4.9) \end{aligned}$$

Since the virtual exchange processes can only occur when neighboring spins are opposite, the Hamiltonian now equals the **antiferromagnetic Heisenberg model** with $J = \frac{t^2}{4U}$,

$$H_{\text{eff}}^{(1)} = J \sum_{\langle ij \rangle} \mathbf{s}_i \cdot \mathbf{s}_j. \tag{4.10}$$

The hopping term (4.5) together with the superexchange term (4.10) form the famous $t - J$ **model**.[5] It is a low-energy description of the Hubbard model close to half-filling and in the limit of large U. Note that now the concept of doping near this Mott insulating state has a different meaning than in standard semiconductors. The addition of electrons, known as electron-doping or n-doping, leads to extra double occupied sites which are called **doublons**. Similarly the removal of an electron (hole-doping or p-doping) introduces vacant sites which are called **holons**.

Table 4.1: The first order in λ processes in the strong coupling perturbation series for the Mott insulating state, given by $\mathbf{P}_0 H_t (1 - \mathbf{P}_0) H_t \mathbf{P}_0$. The initial and final states cannot have double occupied sites.

Initial state	Intermediate states (with double occupied site)	Final states	Process (in units of t^2)	
$\cdots \uparrow_i \downarrow_j \cdots$	$\cdots \uparrow\downarrow_i \, o_j \cdots$	$\cdots \uparrow_i \downarrow_j \cdots$	$2\hat{n}_{i\sigma}\hat{n}_{j\bar{\sigma}}$	$= -4 s_i^z s_j^z + 1$
	$\cdots o_i \, \uparrow\downarrow_j \cdots$	$\cdots \downarrow_i \uparrow_j \cdots$	$2\hat{c}_{j\bar{\sigma}}^\dagger \hat{c}_{i\bar{\sigma}} \hat{c}_{i\sigma}^\dagger \hat{c}_{j\sigma}$	$= -2 s_i^\pm s_j^\mp$

---

[5] Strictly speaking, the perturbation series at first order in λ also contains a density-density interaction and a three-site hopping process. Those are usually neglected (Imada et al., 1998).

4.1.2 The p- and n-doped bilayer

Heterostructures of p- and n-doped cuprates can be typically described by a **bilayer $t-J$ model**: two single-layer $t-J$ models together with interlayer interactions. The hopping of electrons in each layer is given by

$$H_t = -t_e \sum_{\langle ij\rangle\sigma\ell} c^\dagger_{i\ell\sigma} c_{j\ell\sigma} + h.c. \tag{4.11}$$

with the double occupancy constraint left implicit. The undoped Mott insulating state is described by the bilayer Heisenberg model

$$H_J = J \sum_{\langle ij\rangle\ell} \mathbf{s}_{i\ell} \cdot \mathbf{s}_{j\ell} + J_\perp \sum_i \mathbf{s}_{i1} \cdot \mathbf{s}_{i2}. \tag{4.12}$$

Here $c^\dagger_{il\sigma}$ and $\mathbf{s}_{il}$ denote the electron and spin operators respectively on site i in layer $l = 1, 2$. The Heisenberg H_J is antiferromagnetic with $J > 0$ and $0 < J_\perp < J$.

Additionally we need to include the interlayer Coulomb attraction between a vacant site (holon) and double-occupied site (doublon) on the same rung, described by

$$H_V = V \sum_i n_{i1} n_{i2}. \tag{4.13}$$

This is the force that binds interlayer excitons. Without loss of generality, we assume that layer '1' contains the excess electrons with the constraint $\sum_\sigma c^\dagger_{i1\sigma} c_{i1\sigma} \geq 1$ and layer '2' has the constraint $\sum_\sigma c^\dagger_{i2\sigma} c_{i2\sigma} \leq 1$. In other words: we have n- and p-type doping in layer '1' and '2', respectively.

The full **bilayer $t-J$ model**

$$H_{bt-J} = H_t + H_J + H_V \tag{4.14}$$

is the large U limit of the extended bilayer Hubbard model (3.7). Understanding the **bilayer Heisenberg model** (4.12) will be an important step towards analyzing physics of a p/n-doped bilayer.

The bilayer Heisenberg Hamiltonian has been studied quite extensively using Quantum Monte Carlo (QMC) methods,[6] dimer expansions[7] and the closely related bond operator theory,[8] the nonlinear sigma model[9] and spin wave theory.[10] All results indicate a O(3) quantum nonlinear sigma model universality class quantum phase transition at a critical value of $J_\perp/J$ from an antiferromagnetically ordered to a disordered state, see figure 4.2. A

[6] Sandvik et al., 1995; and Sandvik and Scalapino, 1994

[7] Weihong, 1997; Gelfand, 1996; and Hida, 1992

[8] Matsushita et al., 1999; and Yu et al., 1999

[9] van Duin and Zaanen, 1997; and Chakravarty et al., 1989

[10] Miyazaki et al., 1996; Millis and Monien, 1993; Matsuda and Hida, 1990; and Hida, 1990

naive mean field picture of the antiferromagnetic ground state is provided by the Néel state, in which each of the sublattices are occupied by either spin up or spin down electrons as shown in figure 4.1. However, the exact ground state is scrambled by spin flip interactions reducing the Néel order parameter to about 60% of its mean field value.[11] A finite interlayer coupling $J_\perp$ generically reduces the antiferromagnetic order further. In the limit of infinite $J_\perp$, the electrons will form a valence bond solid of pair-singlets living on the interlayer rungs, destroying the antiferromagnetic order.

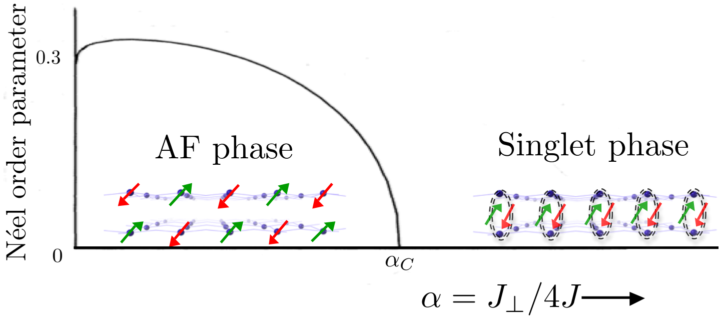

Figure 4.2: Zero temperature phase diagram of the bilayer Heisenberg model as a function of interlayer coupling strength $\alpha = \frac{J_\perp}{4J}$ on the horizontal axis. At a critical value α_c a quantum phase transition exists from the antiferromagnetic to the singlet phase. The vertical axis shows the Néel order parameter signaling antiferromagnetism. Note that even at $\alpha = 0$ the Néel order parameter is reduced from the mean field value $\frac{1}{2}$ to approximately 0.3 due to spin flip interactions. (Adapted from Chubukov and Morr, 1995.)

Standard linear spin wave theories cannot quite account for the critical value of $J_\perp/J \sim 2.5$ found in QMC and series expansion studies. This discrepancy between numerical results and the spin wave theory has a physical origin. Chubukov and Morr, 1995 pointed out that standard spin wave theories do not take into account the longitudinal (that is, the interlayer) spin modes. By incorporating such longitudinal spin waves one can derive analytically the right phase diagram.[12]Another correct method is to introduce an auxiliary interaction which takes care of the hard-core constraint on the spin modes.[13]

If one wants to study the doped bilayer antiferromagnet however, one needs explicit expressions of how a moving **dopant** (be it a hole, electron or exciton) **interacts with the spin excitations**. Even though the Néel state is just an approximation to the antiferromagnetic ground state, it provides an intuitive explanation for the major role spins play in the dynamics of any dopant. As can be seen in figure 4.3, a moving exciton causes a mismatch in the previously perfect Néel state. Consequently, the motion of an

[11] Manousakis, 1991

[12] Sommer et al., 2001

[13] Kotov et al., 1998

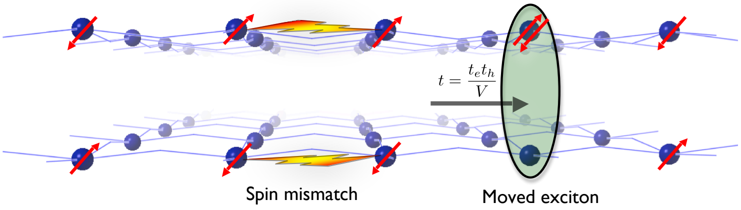

Figure 4.3: Exciton motion in a naive real space picture. In a perfect Néel state, the motion of an exciton (with respect to the situation in figure 4.1) causes a mismatch in the spin ordering. The kinetic energy gained by moving the exciton is proportional to the energies of the doublon t_e and holon t_h divided by the exciton binding energy V.

exciton is greatly hindered and a full understanding of possible spin wave interactions is needed to describe the exciton dynamics. This is of course similar to the motion of a single hole in a single Mott insulator layer.[14] It is also similar to the works of Vojta and Becker, 1999, who have computed the spectral function of a single hole in the Heisenberg bilayer. Therefore a rung linear spin wave approximation[15] is needed to obtain the expressions for the spin waves in terms of single site spin operators. Let us, however, first focus on the exciton properties of the p/n-doped bilayer.

4.1.3 The exciton $t - J$ model

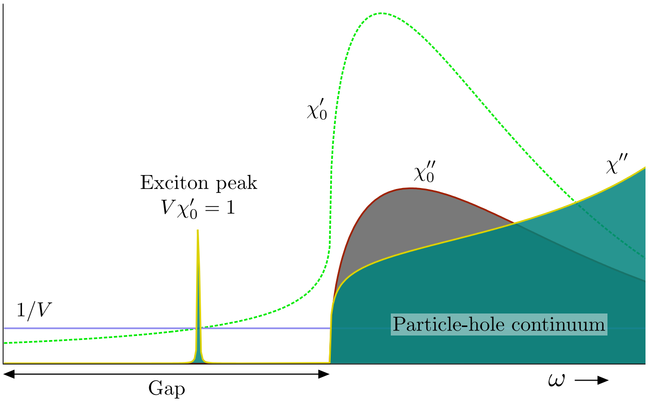

Figure 4.4: For small exciton coupling the spectrum of an exciton is obtained by the ladder diagram approximation from the spectrum of the single doped hole. The χ_0'' and χ_0' are respectively the imaginary and real part of the bare exciton susceptibility. The χ'' is the imaginary part of the full exciton susceptibility obtained in the ladder diagram approximation (4.15). Besides the continuous particle-hole spectrum above the gap, there can only be a single exciton peak determined by $V\chi_0' = 1$ in the weak coupling limit.

The bilayer $t - J$ model (4.14) describes generally the p/n-doped bilayer antiferromagnet. The behavior of a bound exciton, however, depends on the magnitude of the Coulomb force V in H_V, equation (4.13). If this Coulomb repulsion is relatively weak, the motion of holons and doublons will be rather independent of each other and the H_V can be treated as a perturbation on

[14] Schmitt-Rink et al., 1988; and Kane et al., 1989

[15] Sommer et al., 2001

$H_t + H_J$. The full **exciton-susceptibility** $\chi(\omega)$ can be obtained from the bare susceptibility $\chi_0(\omega)$ in the absence of the Coulomb force using the ladder diagram approximation,

$$\chi(\omega) = \frac{\chi_0(\omega)}{1 - V\chi_0(\omega)}. \tag{4.15}$$

Since the undoped state is a Mott insulator, there is a gap in the imaginary part of the bare susceptibility χ_0''. Above this gap there is an onset of the particle-hole continuum. In the ladder diagram approximation, there can only be a single delta function peak in the full susceptibility at $V\chi_0' = 1$ signaling the formation of an exciton. We conclude that in the weak coupling limit no special exciton features other than a single delta function peak can appear in the gap. Following our expectation that realistic materials are in fact in the strong coupling limit we will henceforth focus our attention to the strong coupling limit.

In the **strong coupling limit** $(V \gg t)$, the hopping term H_t can be treated as a perturbation on the unperturbed H_V using the perturbation method developed by Kato,[16] in a manner similar to the derivation of the $t - J$ model from the Hubbard model in the previous section 4.1.1.[17] In the limit of strong V we consider the interlayer Coulomb interaction H_V, which has eigenvalues

$$E_{\widetilde{N}} = V(N - N_0 + \widetilde{N}) = E_0 + V\widetilde{N} \tag{4.16}$$

where N is the total number of sites, N_0 is the number of dopants per layer and $\widetilde{N}$ is the number of double occupied sites that do not lie above a vacant site. It is clear that the ground state of H_V is given by the state where all double occupied and vacant sites lie above each other, as depicted in figure 4.1. As mentioned before an **exciton** consists of a double occupied and a vacant site bound on top of each other. Consequently, the ground state of H_V is the state where all dopants are bound into excitons.

The essence of Kato's perturbation method is that we now forbid all states with higher H_V eigenvalues. This implies that we forbid states such as the one depicted in figure 4.5 where the double occupied site is not on top of the vacant site. In zeroth order, hopping of electrons is forbidden since that would break up an exciton state. Therefore the zeroth order Hamiltonian only contains Heisenberg terms $H^{(0)}_{\text{eft}} = H_J$.

[16] Kato, 1949

[17] Klein and Seitz, 1973; Takahashi, 1977; and Chao et al., 1977

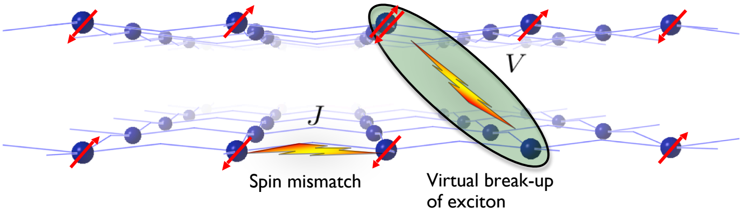

Figure 4.5: The motion of the composite exciton can be related to the motion of its constituents via Kato's perturbation method. In this method a virtual intermediate breakup of the exciton is in between the initial state (figure 4.1) and the final state (figure 4.3). The kinetic energy of the exciton is therefore the product of the kinetic energies of the holon and doublon divided by the energy of this virtual state, $t_{ex} = t_e t_h / V$.

In second order we consider intermediate processes that virtually break up excitons, as shown in figure 4.5. The corresponding effective Hamiltonian is given by

$$-\frac{1}{2V}\mathbf{P}_e H_t (1-\mathbf{P}_e) H_t \mathbf{P}_e \tag{4.17}$$

where $\mathbf{P}_e$ is the operator that projects out states with unbound dopants. Let us define the exciton operator in terms of electron creation operators

$$E_i^\dagger = c^\dagger_{i1\uparrow} c^\dagger_{i1\downarrow} (1-\rho_{i2}), \tag{4.18}$$

where $\rho_{i2} = \sum_\sigma c^\dagger_{i2\sigma} c_{i2\sigma}$ is the density operator in the p-type layer. The perturbation theory now yields an exciton hopping term, which can be formulated as

$$H_{t,ex} = -\frac{t_e t_h}{V} \sum_{<ij>\sigma\sigma'} E_j^\dagger \left[c^\dagger_{i1\sigma'} c^\dagger_{i2\sigma} c_{j2\sigma} c_{j1\sigma'} \right] E_i \tag{4.19}$$

Note that in this Hamiltonian, no break-up of the exciton is required. The virtual process as described before enables us to relate the single layer kinetic energies to the bilayer exciton kinetic energy,

$$t = \frac{t_e t_h}{V}. \tag{4.20}$$

Here t_e is the hopping energy for a single electron, t_h the hopping energy for a single hole and t is the hopping energy for a bound exciton. In addition to this hopping process there are also second order processes that equal a shift in chemical potential of the excitons.

Hence the strong coupling limit of H_V describes the motion of bound excitons in a Mott insulator double layer. The corresponding Hamiltonian is

$$H = H_{t,ex} + H_J \tag{4.21}$$

We will refer to this model as the **exciton $t-J$ model**.

The hopping term (4.19) represents an exciton E_i on site i swapping places with the spin background $c_{jp\sigma}c_{jn\sigma'}$ on site j. This Hamiltonian is in the electron Fock state representation with the background determined by the bilayer Heisenberg model (4.12). Unlike the fermionic holes in the single layer case, the exciton is composed of a fermionic doublon and holon in the same rung, and hence is a bosonic particle. We can therefore rewrite the Hamiltonian in terms of **bosonic operators**. The local Hilbert space on each interlayer rung is five dimensional with a basis in terms of five hard-core bosons: one interlayer exciton state $|E\rangle_i$ and four different spin states. In the **singlet-triplet basis**, which is valid for both the doped and undoped case, we cast the exciton $t-J$ model explicitly in a purely bosonic language. The four hard core spin bosons are one singlet state and three triplet states,

$$|0\ 0\rangle_i = \frac{1}{\sqrt{2}}(c^\dagger_{i1\uparrow}c^\dagger_{i2\downarrow} - c^\dagger_{i1\downarrow}c^\dagger_{i2\uparrow})|0\rangle \tag{4.22}$$

$$|1\ 0\rangle_i = \frac{1}{\sqrt{2}}(c^\dagger_{i1\uparrow}c^\dagger_{i2\downarrow} + c^\dagger_{i1\downarrow}c^\dagger_{i2\uparrow})|0\rangle \tag{4.23}$$

$$|1\ 1\rangle_i = c^\dagger_{i1\uparrow}c^\dagger_{i2\uparrow}|0\rangle \tag{4.24}$$

$$|1\ -1\rangle_i = c^\dagger_{i1\uparrow}c^\dagger_{i2\uparrow}|0\rangle. \tag{4.25}$$

The hopping term (4.19) can be re-expressed as:

$$H_{t,ex} = -t\sum_{<ij>}|E_j\rangle\left(|0\ 0\rangle_i\langle 0\ 0|_j + \sum_m |1\ m\rangle_i\langle 1\ m|_j\right)\langle E_i|. \tag{4.26}$$

We can introduce the total spin operator

$$\mathbf{S}_i = \mathbf{s}_{i1} + \mathbf{s}_{i2} \tag{4.27}$$

and the spin difference operator

$$\widetilde{\mathbf{S}} = \mathbf{s}_{i1} - \mathbf{s}_{i2}. \tag{4.28}$$

Explicitly in terms of singlet and triplet rung states for $S=\frac{1}{2}$, this reads[18]

$$S^z_i = |1\ 1\rangle\langle 1\ 1| - |1\ -1\rangle\langle 1\ -1| \tag{4.29}$$

$$S^+_i = \sqrt{2}\left(|1\ 1\rangle\langle 1\ 0| + |1\ 0\rangle\langle 1\ -1|\right) \tag{4.30}$$

$$\widetilde{S}^z_i = -|0\ 0\rangle\langle 1\ 0| - |1\ 0\rangle\langle 0\ 0| \tag{4.31}$$

$$\widetilde{S}^+_i = \sqrt{2}\left(|1\ 1\rangle\langle 0\ 0| - |0\ 0\rangle\langle 1\ -1|\right). \tag{4.32}$$

[18] van Duin and Zaanen, 1997

In general, we see that the operator $\mathbf{S}_i$ conserves the total onsite spin, while $\widetilde{\mathbf{S}}$ always changes the total spin number s by a unit. The z-components of the spin operators do not change the magnetic number m, while the $\pm$-components of the spin operators change the magnetic number by a unit. The bilayer Heisenberg model is now written as

$$H_J = \frac{J}{2}\sum_{\langle ij\rangle}\left(\mathbf{S}_i\cdot\mathbf{S}_j + \widetilde{\mathbf{S}}_i\cdot\widetilde{\mathbf{S}}_j\right) + \frac{J_\perp}{4}\sum_i\left(\mathbf{S}_i^2 - \widetilde{\mathbf{S}}_i^2\right). \tag{4.33}$$

From now on we will study the **exciton t-J model in the singlet-triplet basis**, which is given by the hopping term (4.26) and the Heisenberg terms (4.33).

4.1.4 Sign problem

Notice that the Hilbert space no longer contains fermionic degrees of freedom. The question is whether the disappearance of the fermionic structure also leads to the disappearance of the fermionic **sign structure**, which causes so much difficulties in the single layer $t-J$ model.[19]

The sign structure can be investigated by considering the off-diagonal matrix elements of the Hamiltonian. At half-filling the fermionic signs in the standard $t-J$ model on a bipartite lattice can be removed by a Marshall sign transformation.[20] Upon doping, signs reappear whenever a hole is exchanged with (for example) a down spin. Which matrix elements of the Hamiltonian become positive (and thus create a minus sign in the path integral loop expansion) depends on the specific basis and on the specific Marshall sign transformation.

For the double layer exciton model, define a spin basis state with a built-in Marshall sign transformation of the form[21]

$$|\phi\rangle = (-1)^{N^{\downarrow}_{An}+N^{\downarrow}_{Bp}}\left|\begin{matrix}\cdots & \downarrow & \uparrow\downarrow & \uparrow & \cdots\\ & \downarrow & 0 & \downarrow & \end{matrix}\right\rangle \tag{4.34}$$

where $N^{\downarrow}_{An}$ is the number of down spins on the A sublattice in the n-layer and similarly we define $N^{\downarrow}_{Bp}$. With these basis states the Heisenberg terms are sign-free and the only positive matrix elements come from the exchange of an exciton with a $m=\pm 1$ triplet.

[19] Wu et al., 2008

[20] Marshall, 1955

[21] Compare to Weng, 2007.

We conclude that, even though the model is purely bosonic, the exciton $t - J$ model is not sign-free and it is not possible to remove this sign structure using a Marshall or similar transformation.[22] However, as will be further elaborated upon in section 4.2.2, for both the antiferromagnetic and singlet ground states these signs do cancel out. Therefore for such ordered bilayers the problem of exciton motion turns out to be effectively bosonic.

4.2 *Frustration of a single exciton in an antiferromagnet*

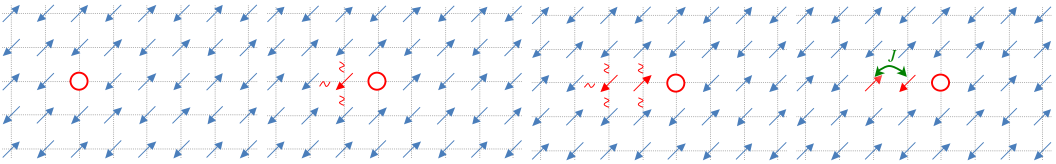

Figure 4.6: A moving hole in an antiferromagnet creates a string of upturned spins. With increasing distance the energy associated with the frustrated bonds increases, which leads to confinement of the hole to its initial position. Upon inclusion of quantum JS^+S^- corrections, the hole can still move, albeit with renormalized bandwidth.

The discovery of high T_c superconductivity triggered a concerted theoretical effort aimed at understanding the physics of doped Mott insulators.[23] Although much is still in the dark, the problem of **an isolated carrier in the insulator** is regarded as well understood.[24] It turned out to be a remarkable affair, rooted in the quantum-physical conflict between the antiferromagnetism of the spin system and the delocalizing carrier. This conflict is at its extreme dealing with a classical Ising spin system, where a famous cartoon arises for the idea of confinement (see figure 4.6): the hopping causes a ‘magnetic string’ of overturned spins between the delocalizing charge and the spin left at the origin with an exchange energy increasing linearly in their separation. It was realized that the quantummechanical nature of the $S = 1/2$ Heisenberg spin system changes this picture drastically. The quantum spin-corrections repair efficiently this ‘confinement damage’ in the spin background and one finds a ‘spin-liquid polaron’ as quasiparticle that propagates coherently through the lattice on a scale set by the exchange constant. This physics can be reliably addressed by parametrizing the spin system in terms of its linear spin waves (LSW), while the strong coupling between the spin waves and the propagating hole is well described in terms of the self consistent Born approximation (SCBA). This turned out to be accurate to a degree that the photoemission results in insulating

This section is based on Rademaker et al., 2012a and Rademaker et al., 2012b.

[22] We are not claiming that the sign structure cannot be removed. Of course, if we would know the exact eigenstates of the Hamiltonian there would be no sign problem. However, finding a basis where the sign structure vanishes is in general a NP-hard problem (Troyer and Wiese, 2005).

[23] Imada et al., 1998; and Lee et al., 2006

[24] Bulaevskii et al., 1968; Brinkman and Rice, 1970; Schmitt-Rink et al., 1988; Kane et al., 1989; Martinez and Horsch, 1991; and Dagotto, 1994

cuprates were quantitatively explained in this framework.[25]

A related problem is the delocalization of an exciton (bound electron-hole pair, or more exactly the bound state of a double occupied and vacant site) through the antiferromagnetic background. It is easy to see that the propagation of an **exciton in a single layer** is barely affected by the antiferromagnetism since the combined motion of the electron and the hole neutralize the 'damage' in the spin system.[26] A problem of interest for this thesis is the exciton formed in a bilayer, where the electron and the hole reside in the different layers. Here we report the discovery that such **bilayer excitons** couple extremely strongly through their quantum motion to the spin system.

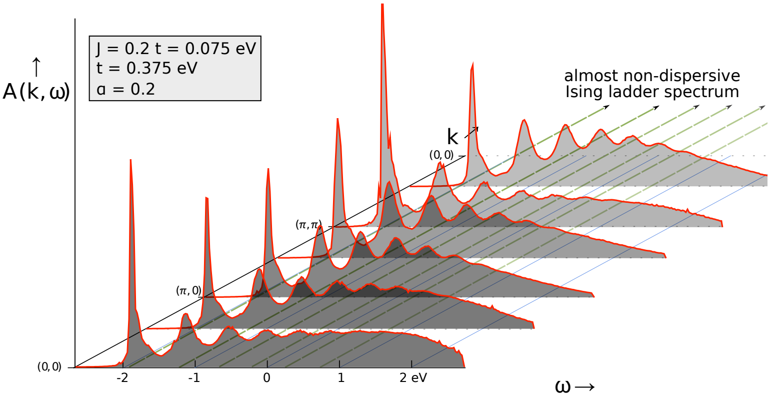

Figure 4.7: Exciton spectral function for $J = 0.2t$ and $\alpha = 0.2$. On top of the incoherent bump a strong ladder spectrum has developed, signaling Ising confinement. The exact Ising ladder spectrum is shown in green dotted lines. The Ising peaks are very weakly dispersive, with bandwidth of order J.

In fact, when the interlayer exchange coupling is small and the exciton hopping rate is large, one enters a regime that is similar to the **confinement** associated with the Ising spins, although the spin system is in the quantized Heisenberg regime. This is illustrated by the exciton spectral function shown in figure 4.7 as computed with the LSW-SCBA method, showing the non-dispersive 'ladder spectrum' which is a fingerprint of confinement. Figure 4.3 depicts a cartoon of the confinement mechanism: every time the exciton hops it creates two spin flips in the different layers that can only be repaired by quantum spin superexchange driven by the interlayer exchange coupling. The rapid intralayer quantum spin flips are now ineffective, because the restoration of the antiferromagnetism requires quantum spin flips that occur simultaneously in the two layers with a probability that is strongly suppressed.

[25] Damascelli et al., 2003

[26] Zhang and Ng, 1998

This confinement effect can be studied directly in experiment by measuring the exciton spectrum in **c-axis optical absorption of the $\mathbf{YBa_2Cu_3O_6}$ (YBCO)** insulating bilayer system. Using realistic parameters we anticipate that this will look like figure 4.8: the main difference with figure 4.7 is that the exciton hopping rate is now of order of the exchange energy and in this adiabatic regime the spectral weight in the ladder spectrum states is reduced.

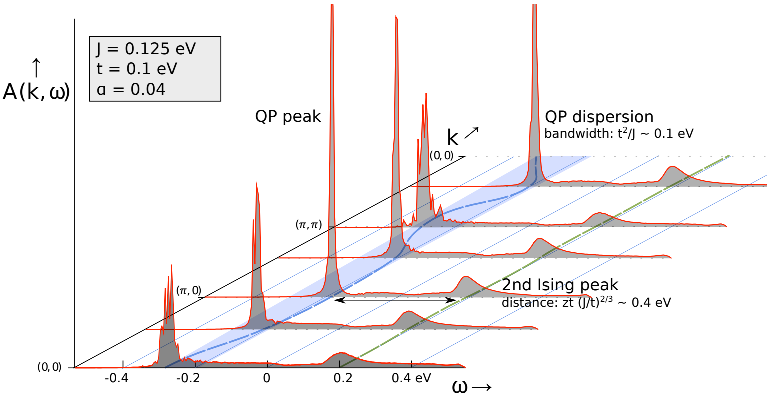

Figure 4.8: Expected exciton spectral function for the *c*-axis charge-transfer exciton in YBCO bilayers. We used model parameters $J = 0.125$ eV, $t = 0.1$ eV and $\alpha = 0.04$. The exciton quasi-particle peak has a dispersion with bandwidth t^2/J, and the quasiparticle peak is the most pronounced at the line between $(\pi, 0)$ and $(0, \pi)$. Following at a distance of $zt(J/t)^{2/3}$, a secondary peak develops as a sign of Ising confinement.

4.2.1 *Undoped case: the bilayer Heisenberg model*

As described in section 4.1, we need to derive a spin wave theory for the bilayer Heisenberg model before considering the dynamics of the exciton. Similar to the traditional Holstein-Primakoff spin-wave theory, we need a classical reference state, i.e. the mean field ground state of the bilayer Heisenberg model, and subsequently develop the linear corrections of the spin wave theory from the mean field ground state. The method we present here is similar to the one presented in Sommer et al., 2001.

The singlet-triplet basis (4.33) of the bilayer Heisenberg model is convenient for **mean field theory**. Mean field theory tells us that for large ratio $J_\perp/J$ the ground state is the singlet configuration $|0\ 0\rangle$. For small $J_\perp/J$, we expect antiferromagnetic ordering, which amounts to a staggered condensation of $\widetilde{S}^z$. By setting $\langle \widetilde{S}^z \rangle = (-1)^i \widetilde{m}$ we obtain a mean field Hamiltonian

$$H_J^{MF} = \sum_i \left[\frac{1}{4} J z \widetilde{m}^2 + \frac{J_\perp}{4} \left(S_i^2 - \widetilde{S}_i^2 \right) - \frac{1}{2} J z \widetilde{m} (-1)^i \widetilde{S}_i^z \right] \qquad (4.35)$$

which has a order-disorder transition point at

$$\alpha_c \equiv \left(\frac{J_\perp}{Jz}\right)_c = \frac{4}{3}S(S+1) \tag{4.36}$$

where S is the magnitude of spin of the spin operator on each site.[27]

The basic idea of a **spin wave theory**[28] is to start from this semiclassical (mean field) ground state and describe the local excitations with respect to this ground state. One can immediately infer why the Holstein-Primakoff or Schwinger approach to spin wave theories fails for the bilayer Heisenberg model. First, the mean field ground state is no longer a Néel state for finite α. Secondly, while Holstein-Primakoff describes one, and Schwinger describes two onsite spin excitations, the bilayer Heisenberg has in fact three types of excitations. This has been pointed out by Chubukov and Morr, 1995, who called the 'third' excitation the longitudinal mode.

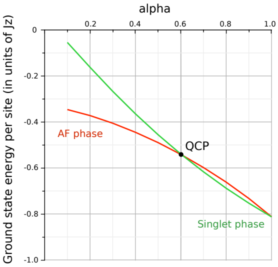

Figure 4.9: Ground state energies of the bilayer Heisenberg model, with the spin wave corrections included. At $\alpha \approx 0.605$ there is a phase transition from the antiferromagnetic phase (in red) to the singlet phase (in green).

With the mean field ground state as described by (4.35) we can 'reach' all states in the local Hilbert space with three types of excitations: a longitudinal $e^\dagger$ which keeps the magnetic quantum number m constant, and two transversal $b^\dagger_\pm$ who change m by ± 1. In the limit of large S these excitations tend to become purely bosonic. We will take the mean field ground state of (4.35) and these three excitations as the starting point for the linear spin wave theory.

We must mention the obvious flaw in the above reasoning. Where we criticized earlier spin wave theories because they predicted the wrong critical value of $J_\perp / Jz$, we now apparently adopt such a 'wrong' theory since (4.36) predicts $\alpha_c = 1$ for $S = \frac{1}{2}$! Nevertheless, the presence of spin waves changes the ground state energy which makes the disordered state more favorable even below the mean field critical $\left(\frac{J_\perp}{Jz}\right)_c$ calculated in the above, see figure 4.9. Hence, when the ground state energy shifts are taken into account in linear order, one finds an accurate critical value for α consistent with numerical calculations.

Let us now construct explicitly the spin wave theory described in the above for $S = \frac{1}{2}$. First, one needs to find the ground state according to equation (4.35). In the $S = \frac{1}{2}$ case, this amounts to a competition between the singlet state $|s = 0, m = 0\rangle$ and the triplet $|s = 1, m = 0\rangle$. The **mean field ground state on each rung**

[27] A proof of this result can be found in Rademaker et al., 2012b.

[28] Anderson, 1952; Kubo, 1952; and Dyson, 1956

is given by a linear superposition of those two,

$$|G\rangle_i = \eta_i \cos\chi |0\ 0\rangle_i - \sin\chi |1\ 0\rangle_i, \tag{4.37}$$

which interpolates between the Néel state ($\chi = \pi/4$) and the singlet state ($\chi = 0$). The onset of antiferromagnetic order can thus be viewed as the condensation of the triplet state in a singlet background.[29] With $\eta_i = (-1)^i$ alternating we have introduced a sign change between the two sublattices A and B. The angle χ will be determined later by self-consistency conditions.

The three operators that describe excitations with respect to the ground state are

$$\begin{aligned} e_i^\dagger &= (\eta_i \sin\chi |0\ 0\rangle_i + \cos\chi |1\ 0\rangle_i)\, \langle G|_i, & (4.38)\\ b_{i+}^\dagger &= |1\ 1\rangle_i \langle G|_i, & (4.39)\\ b_{i-}^\dagger &= |1\ -1\rangle_i \langle G|_i. & (4.40) \end{aligned}$$

The e-operators will later turn out to represent the longitudinal spin waves, whereas the b-operators represent the two possible transversal spin waves.

The bilayer Heisenberg model can be rewritten in terms of these operators. For completeness we include the parameter λ that enables a comparison with the Ising limit ($\lambda = 0$) with the Heisenberg limit ($\lambda = 1$),

$$\mathbf{S}_1 \cdot \mathbf{S}_2 = S_1^z S_2^z + \frac{1}{2}\lambda (S_1^+ S_2^- + S_1^- S_2^+). \tag{4.41}$$

Given this, we can explicitly write down the spin operators in terms of the new e and b operators,

$$\begin{aligned} S_{i\sigma}^z &= b_{+i\sigma}^\dagger b_{+i\sigma} - b_{-i\sigma}^\dagger b_{-i\sigma} & (4.42)\\ S_{i\sigma}^+ &= \sqrt{2}\left(-\sin\chi (b_{+i\sigma}^\dagger + b_{-i\sigma}) + \cos\chi (b_{+i\sigma}^\dagger e_{i\sigma} + e_{i\sigma}^\dagger b_{-i\sigma})\right) & (4.43)\\ \widetilde{S}_{i\sigma}^z &= (-1)^{\sigma_i} \left(\sin 2\chi (1 - \sum_{\pm} b_{\pm i\sigma}^\dagger b_{\pm i\sigma} - 2 e_{i\sigma}^\dagger e_{i\sigma}) - \cos 2\chi (e_{i\sigma}^\dagger + e_{i\sigma})\right) & (4.44)\\ \widetilde{S}_{i\sigma}^+ &= \sqrt{2}(-1)^{\sigma_i} \left(\cos\chi (b_{+i\sigma}^\dagger - b_{-i\sigma}) + \sin\chi (b_{+i\sigma}^\dagger e_{i\sigma} - e_{i\sigma}^\dagger b_{-i\sigma})\right). & (4.45) \end{aligned}$$

From the requirement that the Hamiltonian does not contain terms linear in spin wave operators we obtain the self-consistent mean field condition for the ground state angle χ,

$$(\cos 2\chi - \alpha\lambda) \sin 2\chi = 0 \tag{4.46}$$

[29] van Duin and Zaanen, 1997; and Sommer et al., 2001

which has two possible solutions: either $\chi = 0$, which corresponds to a singlet ground state configuration (the **disordered phase**), or $\cos 2\chi = \alpha\lambda$ corresponding with an **antiferromagnetic ordered phase**. These are indeed the two phases represented in figure 4.2. Which of the two solutions ought to be chosen, depends on the ground state energy competition. In figure 4.9 we compare the ground state energy of both phases, from which we can deduce that the critical point lies at $\alpha_c \approx 0.6$, consistent with the numerical literature.[30]

The dispersion of the spin wave excitations can be found when we consider only the quadratic terms in the Hamiltonian. This is called the **'linear' spin wave approximation**, and it amounts to neglecting the cubic and quartic interaction terms. First take a Fourier transform of the spin wave operators

$$e^\dagger_{i\sigma} = \sqrt{\frac{2}{N}} \sum_k e^\dagger_{k\sigma} e^{ik\cdot r_i} \tag{4.47}$$

where the sum over k runs over the $2/N$ momentum points in the domain $[-\pi, \pi] \times [-\pi, \pi]$ and $\sigma = A, B$ represents the sublattice index. A similar definition is used for the b-operators.

Upon Fourier transformation, we can decouple the spin waves from the two sublattices A and B by introducing

$$e^\dagger_{k,p} = \frac{1}{\sqrt{2}}(e^\dagger_{kA} + p e^\dagger_{kB}) \tag{4.48}$$

where $p = \pm$ stand for the phase of the spin mode. Modes with $p = -1$ are out-of-phase and have the same dispersion as the in-phase $p = 1$ modes but shifted over the antiferromagnetic wavevector $Q = (\pi, \pi)$. Similar considerations apply to the b operators.

Next we perform the **Bogolyubov transformation** on the magnetic excitations,

$$\begin{aligned} e^\dagger_{k,p} &= \cosh\varphi_{k,p}\zeta^\dagger_{k,p} + \sinh\varphi_{k,p}\zeta_{-k,p} && (4.49)\\ b^\dagger_{k,p,+} &= \cosh\theta_{k,p}\alpha^\dagger_{k,p} + \sinh\theta_{k,p}\beta_{-k,p} && (4.50)\\ b^\dagger_{k,p,-} &= \cosh\theta_{k,p}\beta^\dagger_{k,p} + \sinh\theta_{k,p}\alpha_{-k,p} && (4.51) \end{aligned}$$

The corresponding transformation angles are set by the requirement that the Hamiltonian becomes diagonal in the new operators ζ (the longitudinal spin wave) and α, β (the transversal spin waves).

[30] Sandvik et al., 1995; and Sandvik and Scalapino, 1994

In doing so, we introduced the **'ideal' spin wave approximation** in which we assume that the spin wave operators obey bosonic commutation relations.[31] This assumption is exact in the large S limit. For $S = \frac{1}{2}$ this approximation turns out to work extremely well,[32] since the corrections to the bosonic commutation relations are expressed as higher order spin-wave interactions. The Bogolyubov angles are given by

$$\begin{aligned}
\tanh 2\varphi_{k,p} &= \frac{-p\frac{1}{2}\cos^2 2\chi\gamma_k}{\sin^2 2\chi + \lambda\alpha\cos 2\chi - p\frac{1}{2}\cos^2 2\chi\gamma_k}, && (4.52)\\
\tanh 2\theta_{k,p} &= \frac{p\lambda\gamma_k}{\sin^2 2\chi + (1+\lambda)\alpha\cos^2\chi - p\lambda\cos 2\chi\gamma_k} && (4.53)
\end{aligned}$$

The factor γ_k encodes for the lattice structure, and it equals for a square lattice

$$\gamma_k = \frac{1}{z}\sum_{\delta} e^{ik\cdot\delta} = \frac{1}{2}\left(\cos k_x + \cos k_y\right) \qquad (4.54)$$

where the sum runs over all nearest neighbor lattice sites δ. The Bogolyubov angles still depend on χ, which characterizes the ground state. In the antiferromagnetic phase $\cos 2\chi = \lambda\alpha$ and for the Heisenberg limit $\lambda = 1$ these angles reduce to

$$\begin{aligned}
\tanh 2\varphi_{k,p} &= \frac{-p\alpha^2\gamma_k}{2 - p\alpha^2\gamma_k}, && (4.55)\\
\tanh 2\theta_{k,p} &= \frac{p\gamma_k}{1 + \alpha - p\alpha\gamma_k}. && (4.56)
\end{aligned}$$

We can distinguish between the **longitudinal** and **transversal spin excitations**, with their dispersions given by

$$\begin{aligned}
\epsilon^L_{k,p} &= Jz\sqrt{1 - p\alpha^2\gamma_k} && (4.57)\\
\epsilon^T_{k,p} &= \frac{1}{2}Jz\sqrt{(1 + \alpha(1 - p\gamma_k))^2 - \gamma_k^2} && (4.58)
\end{aligned}$$

The longitudinal spin wave is gapped and becomes in the limit where the layers are decoupled ($\alpha = 0$) completely non-dispersive, while the transversal spin wave is always linear for small momentum k. This type of spectrum is similar to a phonon spectrum, which contains a linear k-dependent acoustic mode and a gapped flat optical mode. This correspondence between spin waves and phonons enables us to use techniques from electron-phonon interaction studies for the exciton-spin wave interactions.

[31] Dyson, 1956

[32] Manousakis, 1991

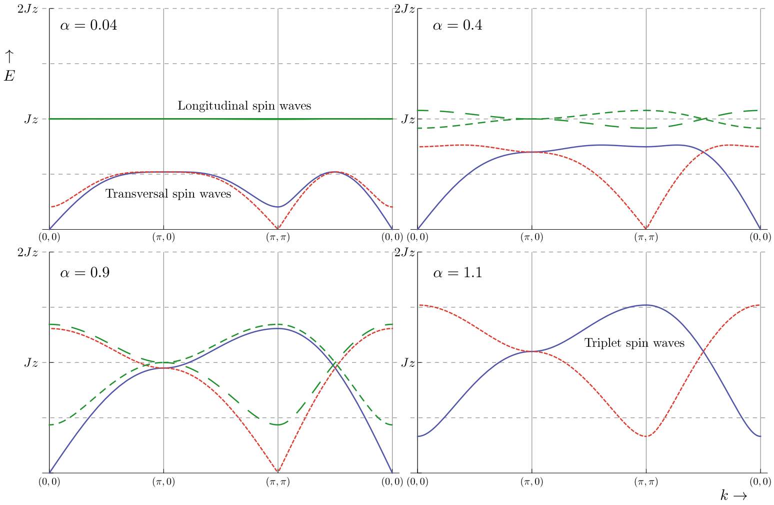

Figure 4.10: Dispersion of the bilayer Heisenberg spin waves for different values of α. The top row has $\alpha = 0.04$ and $\alpha = 0.4$, the bottom row $\alpha = 0.9$ and $\alpha = 1.1$. In the antiferromagnetic phase (first three pictures) there is a clear distinction between the longitudinal spin waves (long dashed lines in green) and the transversal spin waves (solid line in blue; and the short dashed in red). The first is gapped, whilst the latter is zero at either $k = (0,0)$ or (π, π) with a linear energy-momentum dependence. In the singlet phase, all spin waves are gapped triplet excitations (depicted as solid blue line and dashed red line).

On the other hand, in the singlet phase ($\alpha > 1$) one has trivially three identical **triplet spin excitations**. The Bogolyubov angles are given by

$$\tanh 2\varphi_{k,p} = -\tanh 2\theta_{k,p} = \frac{-p\gamma_k}{2\alpha - p\gamma_k} \tag{4.59}$$

and the dispersion of the triplet spin waves is

$$\epsilon_{k,p} = Jz\sqrt{\alpha(\alpha - p\gamma_k)}. \tag{4.60}$$

These dispersions correspond to earlier numerical and series expansions results.[33] In fact, these results are exactly equal to the dispersions obtained in the non-linear sigma model.[34]

The above derivation adds to earlier studies of the bilayer Heisenberg model in that we now found explicit expressions of how the spin waves are related to local spin flips, equations (4.49)-(4.53). This microscopic understanding of the magnetic excitations of the system enables us in the next section to derive how magnetic interactions influence the dynamics of excitons.

4.2.2 *A single exciton in a correlated bilayer*

We are now in the position to derive the **dynamics of a single exciton** in the undoped bilayer. Note that in the thermodynamic limit a single exciton will not change the ground state. Following

[33] Kotov et al., 1998; Weihong, 1997; Gelfand, 1996; and Chubukov and Morr, 1995

[34] van Duin and Zaanen, 1997

the exciton hopping Hamiltonian (4.26) we can express the dynamics of the exciton upon interaction with the spin wave modes. A single exciton can be physically realized by either exciting a interlayer charge-transfer exciton in the undoped bilayer, or by infinitesimal small chemical doping of layered structures.

Similar to the single layer case,[35] we consider the mean field state $|G\rangle$ as the vacuum state and from there we write the effective hopping Hamiltonian for a single exciton as

$$H_{t,ex} = t \sum_{\langle ij \rangle} E_j^\dagger E_i \left[\cos 2\chi (1 - e_i^\dagger e_j) + \sin 2\chi (e_i^\dagger + e_j) - \sum_\sigma b_{i\sigma}^\dagger b_{j\sigma} \right] + h.c.. \tag{4.61}$$

The dynamics of a single exciton are contained in the **dressed Greens function**, formally written as

$$G^p(k,\omega) = \langle \psi_0 | E_{k,p} \frac{1}{\omega - H + i\epsilon} E_{k,p}^\dagger | \psi_0 \rangle \tag{4.62}$$

where $E_{k,p}^\dagger$ is the Fourier transformed exciton creation operator, and p indicates the same phase index as used for the spin waves in equation (4.48). The $|\psi_0\rangle$ denotes the ground state that arises from the spin wave approximation,[36] hence $|\psi_0\rangle$ is defined by the conditions

$$\zeta_{k,p} |\psi_0\rangle = \alpha_{k,p} |\psi_0\rangle = \beta_{k,p} |\psi_0\rangle = 0 \tag{4.63}$$

for all k, p. Note that $|\psi_0\rangle$ is not equal to the mean field ground state $|G\rangle$ defined in equation (4.37).

The Greens function cannot be solved exactly and one needs to develop a diagrammatic expansion in the parameter t. For this purpose, we have derived the corresponding Feynman rules of the exciton $t - J$ model, see appendix D of Rademaker et al., 2012b.

Using **Dyson's equation** one can rephrase the diagrammatic expansion in terms of the self-energy $\Sigma^p(k,\omega)$ such that

$$G^p(k,\omega) = \frac{1}{\omega - \epsilon_0^p(k) - \Sigma^p(k,\omega) + i\epsilon} \tag{4.64}$$

where $\epsilon_0^p(k)$ is the dispersion in the absence of spin excitations for the exciton with phase p. The self-energy can be computed by summing all one-particle irreducible Feynman diagrams. The degree to which exciton motion contains a free part grows with α, and indeed the free dispersion is

$$\epsilon_0^p(k) = p\, zt \cos 2\chi\ \gamma_k \tag{4.65}$$

[35] Schmitt-Rink et al., 1988

[36] Manousakis, 1991

where $\cos 2\chi$ equals $\alpha\lambda$ in the antiferromagnetic phase and equals 1 in the singlet phase.

As we noted before, the spin wave spectrum resembles a phonon spectrum. Hence we can compute the exciton self-energy using the **Self-Consistent Born Approximation (SCBA)**,[37] an approximation scheme developed for electron-phonon interactions but subsequently successfully applied to the single layer $t - J$ model.

The SCBA is based on two assumptions: 1) that one can neglect vertex corrections and 2) one uses only the bare spin wave propagators. The first assumption is motivated by an extension of **Migdal's theorem**. For electron-phonon interaction, higher order vertex corrections are of order $\frac{m}{M}$ where m is the electron mass and M is the ion mass. This justifies that for electron-phonon interactions the SCBA is right.[38] Comparisons between the SCBA and exact diagonalization methods for the single layer $t - J$ model have shown that it is justified to neglect the vertex correction there as well.[39] The second assumption is motivated by the linear spin wave approximation. Consequently, all remaining diagrams are of the 'rainbow' type which can be summed over using a self-consistent equation. The assumption that the vertex corrections are irrelevant allows us to completely resum Feynman diagrams up to all orders in t. The SCBA is therefore not a perturbation series expansion and consequently t does not necessarily has to be a small parameter.

For the exciton $t - J$ model, the SCBA amounts to computing the self-energy for the in-phase exciton, as shown diagrammatically in figure 4.11. The usual Feynman rules dictate that we need to integrate over all intermediate frequencies of the virtual spin waves. However, under the linear spin wave approximation the spin wave propagator is $i/(\omega' - \epsilon(k) + i\epsilon)$ which amounts to a Dirac delta function in the frequency domain integration.[40] For example, the first diagram of figure 4.11 is reduced as follows,

$$\frac{1}{N}\sum_{q,p}\int_{-\infty}^{\infty}\frac{d\omega'}{\pi}M^2_{k,q}G^p(k-q,\omega-\omega')\left[\frac{i}{\omega'-\epsilon^L_{k,p}+i\epsilon}\right]$$
$$=\frac{1}{N}\sum_{q,p}M^2_{k,q}G^p(k-q,\omega-\epsilon^L_{q,p}), \quad (4.66)$$

where $M_{k,q}$ is the vertex contribution and $G^p(k,\omega)$ is the exciton

[37] Schmitt-Rink et al., 1988; and Kane et al., 1989

[38] Fetter and Walecka, 2003

[39] Martinez and Horsch, 1991

[40] Schmitt-Rink et al., 1988

propagator. Emission (or absorption) of a spin wave by an exciton can thus be incorporated by changing the momentum and energy of the exciton propagator. Analytically we write for the in-phase **exciton self-energy**,

$$
\begin{aligned}
\Sigma^{+}(k,\omega) = {} & \frac{z^2t^2}{N}\sin^2 2\chi \sum_{q,p}\Big(\gamma_{k-q}\cosh\varphi_{q,p} + p\gamma_k \sinh\varphi_{q,p}\Big)^2 G^{p}(k-q,\omega-\epsilon^{L}_{q,p}) \\
& + \frac{z^2t^2}{N^2}\cos^2 2\chi \sum_{q,q'}\sum_{\pm,p}\Big(\gamma_{k+q'}\cosh\varphi_{q,p}\sinh\varphi_{q',\pm p} \pm \gamma_{k+q}\cosh\varphi_{q',\pm p}\sinh\varphi_{q,p}\Big)^2 \\
& \qquad \times G^{\pm}\Big(k-q-q',\omega-\epsilon^{L}_{q,p}-\epsilon^{L}_{q',\pm p}\Big) \\
& + \frac{z^2t^2}{N^2}\sum_{q,q'}\sum_{\pm,p}\Big(\gamma_{k-q}\cosh\theta_{q,p}\sinh\theta_{q',\pm p} \pm \gamma_{k-q'}\cosh\theta_{q',\pm p}\sinh\theta_{q,p}\Big)^2 \\
& \qquad \times G^{\pm}\Big(k-q-q',\omega-\epsilon^{T}_{q,p}-\epsilon^{T}_{q',\pm p}\Big)
\end{aligned}
\tag{4.67}
$$

which depends on the exciton propagator and the Bogolyubov angles derived in the previous section. A similar formula to (4.67) applies to Σ^{-}. However, it is easily verified that

$$
\Sigma^{-}(k,\omega) = \Sigma^{+}(k+(\pi,\pi),\omega) \tag{4.68}
$$

since $\gamma_{k+(\pi,\pi)} = -\gamma_k$. In general the SCBA (4.67) cannot be solved analytically, and hence we have obtained the exciton spectral function

$$
A(k,\omega) = -\frac{1}{\pi}\mathrm{Im}\left[G(k,\omega)\right] \tag{4.69}
$$

using an iterative procedure with Monte Carlo integration over the spin wave momenta discretized on a 32 × 32 momentum grid. We start with $\Sigma = 0$ and after approximately 20 iterations the spectral function converged. The results for typical values of α, J and t are shown in figures 4.12 to 4.15.

We start from the situation with $\alpha > 1$ where the magnetic background is a **disordered phase** with all spin singlet configuration in

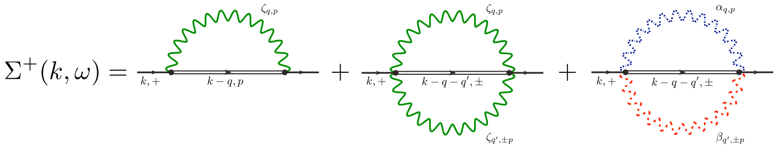

Figure 4.11: Feynman diagram representation of the Self-Consistent Born Approximation (SCBA) of equation (4.67). The self-energy of the exciton depends self-consistently on 'rainbow' diagrams where it emits and absorbs either one or two spin waves. The left two diagrams contain interaction with the longitudinal spin wave (solid green wavy propagators with ζ labels). The diagram to the right contains the interaction with the transversal spin waves; where the dotted (blue, upper, wavy) propagator denotes the α spin wave and the dashed (red, lower, wavy) propagator denotes the β spin wave. The definitions of ζ, α and β are given in equations (4.49)-(4.51). Note that vertex corrections are neglected in the SCBA.

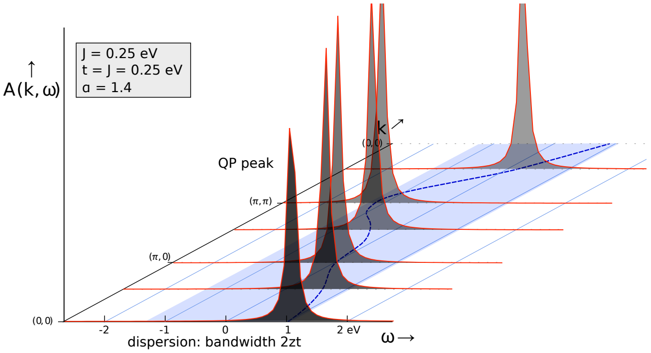

Figure 4.12: Exciton spectral function for parameters $J = t$ and $\alpha = 1.4$. The only relevant feature is the strong quasiparticle peak with dispersion equal to $8t$, where t is the hopping energy of the exciton. The horizontal axis describes energy, the vertical axis is the spectral function in arbitrary units.

the same rung. In this case, the free dispersion of the exciton with bandwidth proportional to t survives because all the magnetic triplet excitations are gapped, with a gap energy of $Jz\sqrt{\alpha(\alpha-1)}$. For $t < J$, the exciton-magnetic interactions will barely change the free dispersion while for $t > J$ such exciton-magnetic interactions can still occur, leading to a small 'spin polaron' effect where the exciton quasiparticle (QP) peak is diminished and spectral weight is transferred to a polaronic bump at a higher energy than the quasiparticle peak. For most values of t/J this effect is, however, negligible already for α just above the critical point. The exciton spectral function for $t = J$ and $\alpha = 1.4$ can be seen in figure 4.12.

As α decreases towards the **quantum critical point** at $\alpha = 1$, the gap of the triplet excitations also decreases. The effect of the exciton-magnetic interactions become more significant, which leads to an increasing transfer of spectral weight from the free coherent peak to the incoherent parts. When α hits the quantum critical point the gap to all spin excitations vanishes. There the motion of the exciton is strongly scattered by the spin excitations, completely destroying the coherent peak and leading to an incoherent critical hump in the spectrum as shown in figure 4.13. When α further decreases to values $\alpha < 1$, the magnetic background becomes antiferromagnetically ordered with two gapless transverse modes and one gapped longitudinal mode. In this case, the motion of the exciton is still strongly scattered with the spin excitations leaving a footprints in the exciton spectrum.

A most **striking phenomenon happens at** $\alpha = 0$, when the two layers are effectively decoupled and we would expect a similar behavior for an interlayer exciton as for a hole or electron in a single

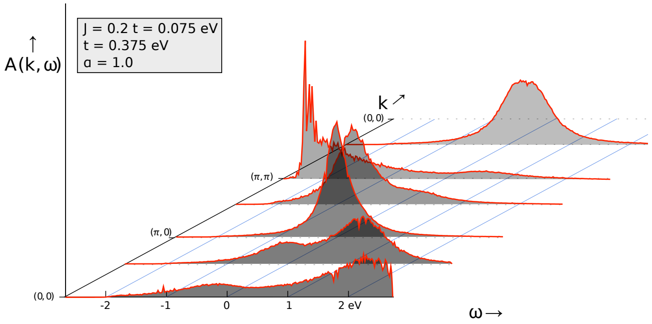

Figure 4.13: Exciton spectral function at the quantum critical point, for $J = 0.2t$ and $\alpha = 1$. No distinct quasiparticle peak is observable, and at all momenta a broad critical bump appears in the spectrum.

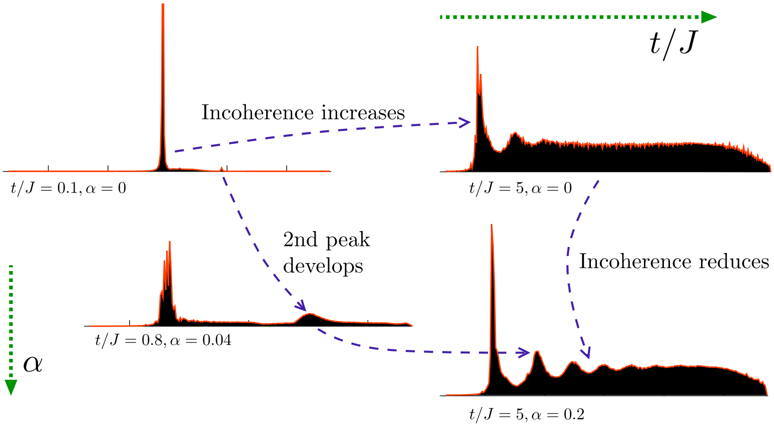

Figure 4.14: A qualitative overview of zero momentum exciton spectral functions $A(k = 0, \omega)$ for various parameters of t/J and small interlayer coupling α. For α identically zero, the ratio t/J determines the amount of excited spin waves. In the adiabatic limit $t \ll J$ no spin waves can be excited by and the exciton is localized with a clear quasiparticle peak. Upon increase of t/J more and more spectral weight is transferred to higher order spin wave peaks, which in the anti-adiabatic limit $t \gg J$ leads to the formation of a broad incoherent spectrum. The inclusion of a small nonzero interlayer coupling α reduces the incoherence of this spectrum, see equation (4.71). As a result the Ising-like ladder spectrum becomes more pronounced. Here we only show the zero momentum spectra, in figures 4.7, 4.8, 4.12, and 4.13 the momentum dependence of these spectra is shown.

layer. Indeed conform with the single hole in the $t - J$ model[41] we find that a moving exciton causes spin frustration with an energy proportional to J. In the limit where $J \gg t$ the kinetic energy of the exciton becomes too small for it to propagate coherently through the magnetic background. Therefore, we expect a localization of the exciton which is reflected in the spectral data by an almost non-dispersive quasiparticle peak. This peak has a bandwidth proportional to t^2/J and carries most of the spectral weight, $1 - \mathcal{O}(t^2/J^2)$. The remaining spectral weight is carried by a second peak, at an energy Jz above the main peak.

More complex behavior at $\alpha = 0$ arises in the **anti-adiabatic limit** $t \gg J$, where the kinetic energy of the exciton is large compared to the energy required to excite (and absorb) spin waves. Consequently, many spin waves are excited as the exciton moves and the exciton becomes 'overdressed' with multiple spin waves.

[41] Schmitt-Rink et al., 1988; and Kane et al., 1989

At nonzero J, however, a very small quasiparticle peak remains with a bandwidth of order J. Nonetheless the majority of spectral weight is carried in the incoherent many-spin wave part.

However, **realistic physical systems** are expected to have a small nonzero value of α and an intermediate value of t/J. What happens here? A simple extrapolation of the two aforementioned cases yields that the bandwidth of the quasiparticle peak will reach its maximum value at $J \approx t$. Similar extrapolations suggest that about half of the spectral weight will be carried by the QP peak. However, inclusion of a finite value of α is not so trivial on an analytical level. Numerical results are therefore needed, and an overview of spectral functions for different ratios of t/J and small values of α is given in figure 4.14.

4.2.3 *The mechanism of Ising-like confinement*

Upon the inclusion of a small nonzero interlayer coupling α a ladder spectrum seems to appear, reminiscent of the spectrum of a single hole in a Ising antiferromagnet. Physically, this can be understood as follows. In the $\alpha = 0$ limit, the magnetic interactions are dominated by the transverse excitations which are just single layer spin waves. For any finite $\alpha > 0$ the (interlayer) longitudinal spin waves become increasingly relevant. To understand their effect on the exciton spectral function, consider the SCBA equation (4.67), neglect the diagrams involving transversal spin waves and expand the self-energy up to first order in α. Only the single spin wave diagram contributes and it equals

$$\Sigma^{+}(k,\omega) = \frac{z^2 t^2}{N} \sum_{q,\pm} \gamma_{k-q}^2 G^{\pm}(k-q, \omega - Jz) \tag{4.70}$$

from which we deduce, observing that $\Sigma^{-} = \Sigma^{+}$ and shifting the momentum summation, that the self-energy must be momentum-independent and given by the **self-consistent equation**

$$\Sigma(\omega) = \frac{\frac{1}{2} z^2 t^2}{\omega - Jz - \Sigma(\omega - Jz)}. \tag{4.71}$$

This self-energy is exactly the same as the self-energy of a single dopant moving through an **Ising antiferromagnet**.[42] In fact, in any system where a moving particle automatically excites a gapped and flat mode the self-consistent equation (4.71) applies.

[42] Kane et al., 1989

As described in Kane et al., 1989, a hole in an Ising antiferromagnet is effectively confined by the surrounding magnetic texture. Each hop away from its initial point increases the energy, thus creating a linear potential well for the hole. In such a linear confinement potential a ladder spectrum appears where the energy distance between the to lowest peaks scales as $t(J/t)^{2/3}$. The spectral weight carried by higher order peaks vanishes as $t/J \to 0$.[43]

The Ising-like features in the exciton spectral function are explicitly visible in the numerically computed dispersions shown in figures 4.7 and 4.14. We indeed conclude that the visibility of the ladder spectrum is actually enhanced in the bilayer case presented here relative to the hole in the single layer due to the nondispersive interlayer spin excitations.

Of course the exciton ladder spectrum in figure 4.7 is not exactly sharp. By the above analysis, we can infer that the incoherent broadening of peaks is due to interactions with the transversal spin waves. Indeed, the transversal spin waves can be viewed as the equivalent of the single layer spin waves. Therefore for small α the effect of transversal spin waves is to mildly quantize the Ising limit, and the results become reminiscent of a single hole in the $t - J$ model, including the quasiparticle peak broadening.

4.2.4 *Relation to experiment*

The formation of kinetically frustrated bound exciton states can be experimentally verified by measurements of the dielectric function or any other charge-excitation measurements. One particular example is **electron energy loss spectroscopy (EELS)**, showing for instance clear signatures of the in-plane charge transfer excitons in cuprates.[44] The EELS cross-section is directly related to the **dielectric function**[45] via the dynamical structure factor $S(q,\omega)$,

$$d\sigma \propto \frac{1}{q^4} S(q,\omega) \propto \frac{1}{q^2} \mathrm{Im}\left[\frac{-1}{\epsilon(q,\omega)}\right] \tag{4.72}$$

with the dynamical structure factor defined as

$$\begin{aligned} S(q,\omega) &= \frac{1}{N} \int \frac{dt}{2\pi} e^{-\epsilon|t|} \sum_{\lambda} \langle \psi_0 | \sum_i e^{-iq\cdot r_i} e^{i(\omega - H)t} | \lambda \rangle \\ &\quad \times \langle \lambda | \sum_j e^{iq\cdot r_j} | \psi_0 \rangle \end{aligned} \tag{4.73}$$

[43] Kane et al., 1989

[44] Wang et al., 1996; and Zhang and Ng, 1998

[45] Schnatterly, 1979

where the sum λ runs over all intermediate states, and $|\psi_0\rangle$ is the initial state of the system. We use the dipole expansion such that

$$e^{iqr_i} = 1 + i\vec{q}\cdot\vec{r}_i + \dots \tag{4.74}$$

where the electron position operator can be expanded in terms of the possible electron wave functions in the tight binding approximation,

$$\sum_i \vec{r}_i = \sum_{ij\sigma} c^\dagger_{i\sigma} c_{j\sigma} \langle\phi_i|\vec{r}|\phi_j\rangle \tag{4.75}$$

where $|\phi_i\rangle$ are the Wannier wave functions of the electron on site i. The z component of $\langle\phi_i|\vec{r}|\phi_j\rangle$ is proportional to the interlayer hopping energy $t_\perp$, which in turn is equal to the the creation operator of an exciton,

$$\begin{aligned} r^z &\propto t_\perp \sum_{i\sigma} c^\dagger_{in\sigma} c_{ip\sigma} + h.c. && (4.76)\\ &\propto t_\perp \sum_i \left(E^\dagger_i + E_i\right) && (4.77) \end{aligned}$$

We recognize the Fourier transform of the $k = 0$ excitonic state, so that we find

$$\begin{aligned} S(q^z,\omega) &\propto (q^z t_\perp)^2 \int \frac{dt}{2\pi} e^{-\epsilon|t|} \sum_\lambda \langle\psi_0|E_{k=0}\, e^{i(\omega-H)t}|\lambda\rangle \\ &\quad \times\langle\lambda|\, E^\dagger_{k=0}|\psi_0\rangle. && (4.78) \end{aligned}$$

We have introduced the term $e^{-\epsilon|t|}$ to ensure convergence of the integral so that we can integrate over t. We find that the dynamic structure factor is directly related to the exciton spectral function

$$\begin{aligned} S(q^z,\omega) &\propto (q^z t_\perp)^2 \langle\psi_0|E_{k=0} \left(\frac{i}{\omega - H + i\epsilon} - \right. \\ &\quad \left. \frac{i}{\omega - H - i\epsilon}\right) E^\dagger_{k=0}|\psi_0\rangle \\ &\propto (q^z t_\perp)^2 A(k=0,\omega) && (4.79) \end{aligned}$$

or in other words

$$\mathrm{Im}\left[\epsilon^{-1}(q^z,\omega)\right] \sim (t_\perp)^2 A(k=0,\omega). \tag{4.80}$$

Consequently, one expects the bound exciton states to show up in EELS measurements when probing the z-axis excitations. In addition to the bound exciton states, a broad electron-hole continuum will show up at high energies.

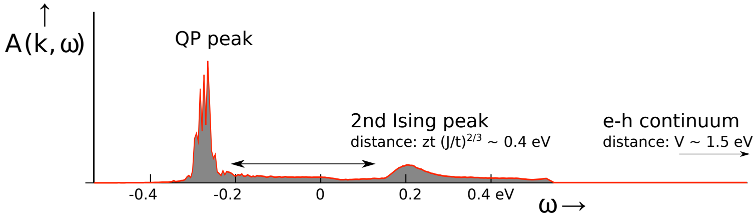

Figure 4.15: Expected zero-momentum exciton spectral function for the c-axis charge-transfer exciton in YBCO bilayers. We used model parameters $J = 0.125$ eV, $t = 0.1$ eV and $\alpha = 0.04$. A pronounced quasiparticle peak is followed at a distance of $zt(J/t)^{2/3}$ by a secondary peak as a sign of Ising confinement. The electron-hole continuum sets in at an energy $V \sim 1.5$ eV above the center of this spectrum. The momentum dependence of this spectrum is shown in figure 4.8.

Another possible way to detect interlayer excitons is to use optical probes. The **optical conductivity** $\sigma(q,\omega)$ of a material is related to the dielectric function[46] by

$$\epsilon^{-1}(q,\omega) = 1 - i\frac{q^2}{\omega}V_c(q)\sigma(q,\omega), \tag{4.81}$$

where $V_c(q)$ is the Fourier transform of the Coulomb potential $\frac{1}{\epsilon_0|r-r'|}$. The real part of the c-axis optical conductivity is therefore proportional to the exciton spectral function. Similar considerations hold when one measures the **Resonant Inelastic X-ray Scattering (RIXS)**[47] spectrum.

When comparing the dielectric function with the computed spectral functions in figures 4.12-4.15, do bear in mind that the latter are shifted over an energy E_0 required to excite an interlayer exciton. This energy is of the order of electron volts. For example, along the ab-plane in cuprates charge-transfer excitons are observed in the range of 1-2 eV.[48] Since the energy required for a charge-transfer excitation is largely dependent on the onsite repulsion, we expect that the c-axis exciton will be visible at comparable energy scales.

How would then the exciton spectrum look like for a realistic material, such as the **bilayer cuprate $\mathbf{YBa_2Cu_3O_{7-\delta}}$ (YBCO)**? Following earlier neutron scattering experiments[49] one can deduce that the effective $J = 125 \pm 5$ meV and $J_\perp = 11 \pm 2$ meV, which corresponds to an effective value of $\alpha = 0.04\alpha_c$ where α_c is the critical value of α.[50] The question remains what a realistic estimate of the exciton binding energy is. The planar excitons are known to be strongly bound[51] with binding energy of the order of 1-2 eV. Since the Coulomb repulsion scales as $V \sim (\epsilon r)^{-1}$, we can relate the binding energy of the interlayer excitons to that of the planar excitons. The distance between the layers is about twice

[46] Bruus and Flensberg, 2004

[47] Ament et al., 2011

[48] Basov and Timusk, 2005

[49] Imada et al., 1998; and Tranquada et al., 1989

[50] Chubukov and Morr, 1995

[51] Zhang and Ng, 1998

the in-plane distance between nearest neighbor copper and oxygen atoms, but simultaneously we expect the dielectric constant ϵ_c along the c-axis to be smaller than ϵ_{ab} due to the anisotropy in the screening. Combining these two effects, we consider it a reasonable assumption that the interlayer exciton binding energy is comparable to the in-plane binding energy. The hopping energy for electrons is approximately $t_e = 0.4$ eV which yields, together with a Coulomb repulsion estimate of $V \sim 1.5$ eV, an effective exciton hopping energy of $t \sim 0.1$ eV. Note that these estimates of V/t justify our use of the strong coupling limit in section 4.1.3.

The spectral function corresponding to these parameters is shown in figure 4.15. Since $t \sim J$ the ladder spectrum is strongly suppressed compared to the aforementioned anti-adiabatic limit. However, the Ising confinement still shows its signature in a small 'second ladder peak' at 0.4 eV energy above the exciton quasiparticle peak. To the best of our knowledge and to our surprise, the c-axis optical conductivity of YBCO has not been measured before in the desired regime with energies above 1 eV.[52] Detection of this second ladder peak in future experiments would suggest that indeed the interlayer excitons in cuprates are frustrated by the spin texture.

[52] Confirmed in private communications with D. van der Marel. In addition, standard review articles on optical absorption in cuprates (such as Basov and Timusk, 2005) indeed only show infrared measurements ($< 1000\,\mathrm{cm}^{-1}$) of the c-axis optical absorption in insulating cuprates.

5

Exciton condensation in the $t - J$ model

THE BOSONIC exciton $t - J$ model derived in the previous section allows for exciton condensation. In this phase, a remarkable cooperation effect arises between the exciton and spin dynamics. In section 5.1 we discuss this specific feature of the strongly correlated exciton condensate. We conclude our study of the exciton $t - J$ model by constructing the full phase diagram in section 5.2.

Completely opposite to the frustration effect presented in section 4.2 is the cooperation between excitons and spins that arises in the context of a **finite densities of excitons**.[1] Much effort has been devoted to create equilibrium finite exciton densities using conventional semiconductors,[2] while exciton condensation has been demonstrated in coupled semiconductor 2DEGs.[3] In strongly correlated p/n heterostructures,[4] however, formation of finite exciton densities is still far from achieved, although recent developments on oxide interfaces indicate exciting potential (see for example Pentcheva et al., 2010). Besides the closely coupled p- and n-doped conducting interface-layers in these $SrTiO_3$-$LaAlO_3$-$SrTiO_3$ heterostructures, further candidates would be closely coupled p- and n-doped cuprates, such as $YBa_2Cu_3O_{7-x}$ or $La_{2-x}Sr_xCuO_4$ with $Nd_{2-x}Ce_xCuO_4$. The feasibility of this has already been experimentally demonstrated, e.g. in Takeuchi et al., 1995, but the exact interface effects need to be investigated in more detail, both experimentally as well as theoretically.

The nontrivial cooperation effect between excitons and spins is only visible in the **exciton condensate phase doped into a Mott**

[1] Ribeiro et al., 2006; and Millis and Schlom, 2010

[2] Moskalenko and Snoke, 2000

[3] Eisenstein and MacDonald, 2004; Butov, 2007; and High et al., 2012

[4] One can wonder whether such physics is already at work in the four-layer material $Ba_2Ca_3Cu_4O_8F_2$ where self-doping effects occur creating simultaneously p and n-doped layers, Chen et al., 2006.

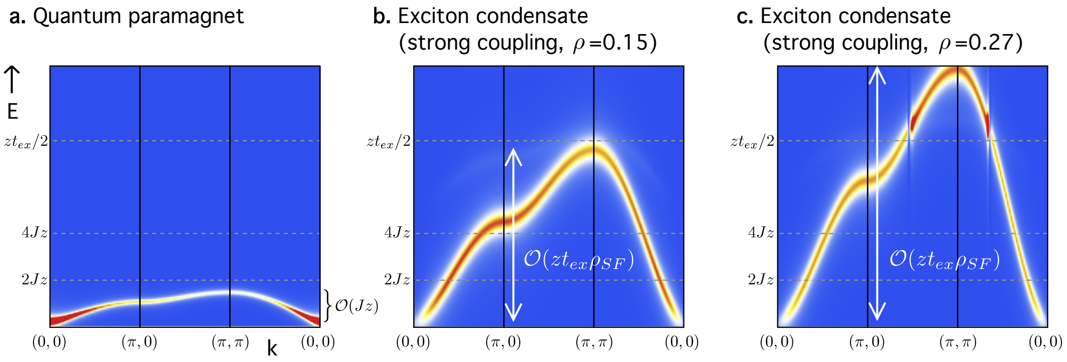

Figure 5.1: The absorptive part of the dynamical magnetic susceptibility $\chi''(\mathbf{q},\omega)$ in a Mott insulating bilayer (a) doped to become an exciton condensate (b,c). **a:** The spectrum of a Mott insulating bilayer with the same gap as the exciton condensates of figure b and c. The bandwidth of the triplon mode is of the order Jz. **b.** In the presence of the exciton condensate, the magnetic excitation spectrum consists of propagating triplets. Instead of the small $\mathcal{O}(Jz)$ bandwidth, the triplet has now an enhanced bandwidth $\mathcal{O}(zt_{ex}\rho_{SF})$, proportional to the superfluid density. This result is computed using a linear spin wave approximation, using model parameters $t_{ex} = 2, J = 0.125, \alpha = 0.04$ and $\rho = 0.15$. **c.** The same result as in b, but now with a higher exciton density $\rho = 0.27$. The triplet mode bandwidth is seen to scale with the exciton superfluid density.

insulating bilayer. The non-condensed electrons form a quantum paramagnet, which has as elementary magnetic excitations the triplet modes (triplons, see the book by Sachdev, 2011). One expects that the bandwidth of the triplons is proportional to the superexchange energy J. However, interlayer exciton condensation now leads to a drastic **increase of the triplon bandwidth**. In this section we show that this enhancement is rooted in the triplons 'borrowing' itineracy from the exciton condensate. The resulting bandwidth turns out to be proportional to the superfluid density, as is shown in figure 5.1. In principle, this enhancement can be detected by measurements of the dynamical magnetic susceptibility. It appears unlikely that such bilayer exciton systems can be manufactured in bulk form which is required for neutron scattering, while there is a real potential to grow these using thin layer techniques. Therefore the detection of the triplon bandwidth enhancement forms a realistic challenge for resonant inelastic X-ray scattering (RIXS)[5] measurements with its claimed sensitivity for interface physics.[6]

5.1 *Enhanced spin itineracy in the exciton condensate*

This section 5.1 is based on Rademaker et al., 2013a.

Let us now introduce the **strongly correlated exciton condensate** is somewhat more detail. As mentioned above, the exciton condensate is the result of the direct interlayer Coulomb attraction, in stark contrast to the retarded phonon mediated electron-electron pairing in superconductors. Consequently, the pairing mechanism

[5] Ament et al., 2011

[6] Dean et al., 2012

is remarkably simple and in the absence of spin-orbit coupling or magnetization the excitons are a singlet pair. The resulting **condensate wavefunction** has the standard BCS-form,

$$|\Psi\rangle = \prod_{\mathbf{k}\sigma} \left(u_{\mathbf{k}} + v_{\mathbf{k}} c^{\dagger}_{\mathbf{k}1\sigma} c_{\mathbf{k}2\sigma} \right) |\Psi_0\rangle \tag{5.1}$$

where $|\Psi_0\rangle$ is the ground state without excitons, $c^{\dagger}_{\mathbf{k}1\sigma}$ creates an electron in the first layer and $c_{\mathbf{k}2\sigma}$ creates a hole in the second layer with opposite spin. The order parameter is independent of spin

$$\Delta_{\mathbf{k}} = u_{\mathbf{k}} v_{\mathbf{k}} = \langle c^{\dagger}_{\mathbf{k}1\sigma} c_{\mathbf{k}2\sigma} \rangle. \tag{5.2}$$

Recall from section 2.1 that the anomalous interlayer tunneling serves as a direct probe of the order parameter.[7]

The enhancement of the triplet mode is an effect that only occurs in the regime of strong electron-electron interactions. The realization of exciton condensates has been suggested to be possible in strongly correlated materials[8] where the cuprates[9] would serve as ideal candidate systems. In Mott insulators electrons localize due to interactions and only their spin remains as a degree of freedom. Such bilayers (figure 4.1) are described by the **bilayer Heisenberg model**[10] introduced in section 4.1, defined by

$$H_J = J \sum_{\langle ij \rangle, \ell} \mathbf{s}_{i\ell} \cdot \mathbf{s}_{j\ell} + J_{\perp} \sum_i \mathbf{s}_{i1} \cdot \mathbf{s}_{i2}. \tag{5.3}$$

The operators $\mathbf{s}_{i\ell}$ denote the spin of a particle on site i in layer ℓ, and via this mechanism of superexchange spin excitations can propagate. The superexchange parameters J are related to the bare electron hopping t by the strong coupling perturbation theory of section 4.1, recall $J = 4t^2/U$ and $J_{\perp} = 4t_{\perp}^2/U$ with U the onsite repulsion. This model represents a paramagnet when $J_{\perp} \gg J$, thus favoring singlet configurations on each interlayer rung. The excitation spectrum consists of propagating triplet modes, with a dispersion $\omega_{\mathbf{k}} = Jz\sqrt{\alpha(\alpha - \gamma_{\mathbf{k}})}$ where $\alpha = J_{\perp}/Jz$ and z is the lattice coordination number. Hence the bandwidth of these triplets in the absence of exciton condensation is set by the superexchange parameter J. We compute the interlayer dynamical magnetic susceptibility[11]

$$\chi_{ij}(\tau) = \langle T_{\tau}(s^{-}_{i1}(\tau) - s^{-}_{i2}(\tau))(s^{+}_{j1} - s^{+}_{j2}) \rangle \tag{5.4}$$

using the well-tested **linear spin wave theory**.[12] The imaginary

[7] Eisenstein and MacDonald, 2004

[8] Ribeiro et al., 2006; and Millis and Schlom, 2010

[9] Imada et al., 1998; and Lee et al., 2006

[10] Manousakis, 1991; and Chubukov and Morr, 1995

[11] Bruus and Flensberg, 2004

[12] This is further elaborated upon in section 5.2.4. See also Manousakis, 1991 and Chubukov and Morr, 1995.

part χ'', which describes the absorption, is in principle measurable by RIXS[13] and a typical spectrum is shown in figure 5.1a.

As for the case of normal carriers in a doped Mott insulator, the nature of the exciton system is drastically different from what is found in uncorrelated semiconductors. The Mott insulator cannot be described by band theory, and instead electron- and hole-doping corresponds with the creation of double occupied sites (doublons) and empty sites (holons), respectively. The doublons and holons attract each other via the Coulomb attraction and can thus form doublon-holon pairs: the strong coupling limit of the exciton. Since in the Mott bilayer all interactions are strong, the relevant case is to assume strong exciton binding such that excitons can be treated as local pairs and the condensation occurs in the BEC sense rather than in the weak coupling BCS sense.[14]

To describe such a doublon-holon pair in a Mott bilayer, we can express the exciton hopping in terms of interlayer rung states: the exciton $|E\rangle$ and the four possible interlayer spin states $|s\ m\rangle$. Recall that the motion of an exciton is governed by[15]

$$H_K = -t_{ex} \sum_{\langle ij \rangle} |E\rangle_j \left(\sum_{sm} |s\ m\rangle_i \langle s\ m|_j \right) \langle E|_i. \tag{5.5}$$

The exciton hopping energy t_{ex} can be related to the electron hopping via perturbation theory, which gives $t_{ex} = t^2/V$ where V equals the binding energy of an exciton.

The system describing coexistence of spins and excitons, given by equations (5.3) and (5.5), is equivalent to a hard-core boson system, reminiscent of attempts to describe cuprate superconductivity using only bosons such as the $SO(5)$ theory of the $t - J$ model.[16] In contrast to these theories, for the excitons in Mott bilayers the mapping onto bosonic physics is fully controlled. The ground state of the 'exciton $t - J$ model' can straightforwardly be found using a $SU(5)$ coherent state. In the next section 5.2 we study this in detail, finding that the dynamical frustration between excitons and spins causes large parts of the phase diagram to be dominated by phase separation. As long as the exciton hopping t is bigger than the exciton-exciton repulsion we find an exciton superfluid as the ground state, where the spins form interlayer singlets. In principle there can be sign problems but these drop out rigorously for this singlet ground state.

The **strongly correlated exciton condensate wavefunction** is

[13] Ament et al., 2011

[14] The BCS theory of electron-hole pairing is discussed in section 3.2.

[15] See section 4.1.

[16] Zhang, 1997

now

$$|\Psi\rangle = \prod_i \left(\sqrt{\rho}\,|E\rangle_i + \sqrt{1-\rho}\,|0\ 0\rangle_i\right) \tag{5.6}$$

where $|0\ 0\rangle$ is the interlayer singlet spin configuration. Indeed, when we set $\Delta_{\mathbf{k}}$ to be independent of momentum the earlier wavefunction (5.1) reduces to the above equation.

Since we are dealing with hard-core bosons forming a mean field ground state, the magnetic excitation spectrum can be computed with linear spin wave theory. We employ the Heisenberg equations of motion[17] which are decoupled exploiting the ground state expectation values.[18] The resulting dynamical magnetic susceptibilities $\chi''(\mathbf{q},\omega)$ are shown in figure 5.1, for two choices of exciton density $\rho = 0.15$ and $\rho = 0.27$.

These figures illustrate the central result of this section: compared to the undoped system (figure 5.1a) we find that the **triplon bandwidth is greatly enhanced** (figures 5.1b and c). The mechanism is actually similar to that in slave-boson theories,[19] where four-operator products $b^\dagger b f^\dagger f$ are decoupled as $\langle b^\dagger\rangle\langle b\rangle f^\dagger f$ yielding kinetic energy for the f-excitations. For Mott bilayers, we can explicitly introduce Fock operators for the exciton $e^\dagger = |E\rangle\langle 0|$ and the triplet $t^\dagger = |1m\rangle\langle 0|$. This implies that the exciton-spin interaction term (4.26) can be written as

$$-t_{ex}\sum_{\langle ij\rangle} e_j^\dagger e_i t_i^\dagger t_j. \tag{5.7}$$

This is a higher order exchange term, which at first sight seems to be irrelevant for the bandwidth of the triplet. However, when the exciton condensate sets in, the operator $e^\dagger$ obtains an expectation value $\langle e^\dagger\rangle = \sqrt{\rho_{\mathrm{SF}}}$, where ρ_{SF} is the condensate density. Consequently this exchange term turns into an effective triplet hopping term

$$-t_{ex}\rho_{\mathrm{SF}}\sum_{\langle ij\rangle} t_i^\dagger t_j. \tag{5.8}$$

The explains why the bandwidth of the triplet excitations is increased by an amount of order $zt_{ex}\rho_{\mathrm{SF}}$.

Surely, we made the argument that this effect leads to a dramatic increase of the bandwidth, for which we have implicitly assumed that t_{ex} is larger than J. Now the exciton hopping energy is related to the electron hopping by $t_{ex} = t^2/V$, while the spin superexchange satisfies $J = 2t^2/U$ where U is the onsite Coulomb

[17] See section 5.2.4.

[18] Zubarev, 1960; and Oles et al., 2000

[19] Lee et al., 2006

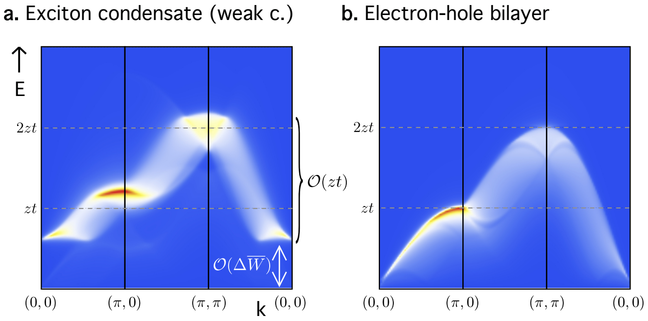
a. Exciton condensate (weak c.)

b. Electron-hole bilayer

Figure 5.2: The absorptive part of the dynamical magnetic susceptibility $\chi''(\mathbf{q},\omega)$ in the weak-coupling limit of both the exciton binding energy and electron-electron interactions. **a:** The magnetic susceptibility is also in the exciton condensate phase dominated by the Lindhard continuum. This is qualitatively different from the triplons found in the strong coupling limit of figure 5.1. Model parameters are $\xi_{1\mathbf{k}} = -zt\gamma_{\mathbf{k}} - \mu = -\xi_{2\mathbf{k}}$, $t_\perp = 0.05zt$, $\mu = -0.8zt$ and $\Delta\overline{W} = t$. **b:** For comparison we computed the $\chi''(\mathbf{q},\omega)$ in an electron-hole bilayer without exciton condensation.

repulsion. Since for obvious reasons $U > V$, we find that indeed the dominant scale controlling the triplon bandwidth is $zt_{ex}\rho_{\text{SF}}$ yielding the predicted bandwidth enhancement.

Since the exciton condensate ground state is independent of the interaction strength, one can **in principle adiabatically continue** the strong coupling results to the weak coupling limit. However, in this limit the magnetic susceptibility as shown in figure 5.2 has a fundamentally different origin. Only with strong interactions the electrons are localized and a true spin degree of freedom arises. This is not the case for weak coupling, where the spin response is still dominated by the Lindhard continuum. The propagation scale of the triplet excitations is now set just by the dispersion of the noninteracting electrons.

To illustrate this point we compute the dynamic magnetic susceptibility for the **weak coupling case** where we depart from a band structure of electrons and holes

$$H_K = \sum_{\mathbf{k}\sigma} \left(\xi_{1\mathbf{k}} c^\dagger_{1\mathbf{k}\sigma} c_{1\mathbf{k}\sigma} + \xi_{2\mathbf{k}} c^\dagger_{2\mathbf{k}\sigma} c_{2\mathbf{k}\sigma} \right) \tag{5.9}$$

plus a weak interlayer tunneling

$$H_\perp = -t_\perp \sum_{\mathbf{k}\sigma} \left(c^\dagger_{1\mathbf{k}\sigma} c_{2\mathbf{k}\sigma} + c^\dagger_{2\mathbf{k}\sigma} c_{1\mathbf{k}\sigma} \right) \tag{5.10}$$

where $\xi_{\ell\mathbf{k}}$ is the band structure of the holes or electrons, depending on the layer. For simplicity, we take $\xi_{1\mathbf{k}} = -zt\gamma_{\mathbf{k}} - \mu = -\xi_{2\mathbf{k}}$ on a square lattice, so that in both layers there is an equal sized Fermi surface with opposite Fermi velocities. The interlayer hopping $t_\perp \ll t$ is assumed to be small given the insulator in between the layers. Both in-plane and the interlayer interactions are given by the Coulomb interaction

$$H_V = \sum_{ij\ell\sigma\sigma'} V_{ij} n_{i\ell\sigma} n_{j\ell\sigma'} + \sum_{ij\sigma\sigma'} W_{ij} n_{i1\sigma} n_{j2\sigma'}, \tag{5.11}$$

where $V_{ij} \propto |r_i - r_j|^{-1}$ and the interlayer Coulomb includes the interlayer distance d, hence $W_{ij} \propto \left((r_i - r_j)^2 + d^2\right)^{-1/2}$. The effects of these interactions are taken into account using the random phase approximation (RPA).[20] In the bilayer case, one needs to extend the usual RPA expression $\chi = \chi_0/(1 - V_q \chi_0)$ to include both intra- and interlayer interactions and bare susceptibilities χ_0.

At some critical temperature the electron-hole bilayer has an instability towards exciton condensation. Based on the standard BCS theory[21] we single out the interactions responsible for the singlet exciton pairing and perform a standard mean field decoupling using our earlier order parameter ansatz (5.2). Let us fix the order parameter at a value of, say, $\Delta\overline{W} = t$. Using the aforementioned RPA expansion we compute the resulting magnetic excitation spectrum shown in figure 5.2a. This spectrum is reminiscent of our strong coupling results of figure 5.1. But instead of the renormalization of the triplet bandwidth, the magnetic excitations closely follow the Bogolyubov quasiparticle spectrum. In fact, the dynamic magnetic susceptibility in the weak coupling limit can be best understood as a gapped variation of the result in absence of a condensate, shown in figure 5.2b. In weak coupling, the gross features of the magnetic excitation spectrum therefore look similar with or without the exciton condensate, whereas the dramatic increase of the overall energy scale of the magnetic excitations is only present in the strong correlations limit.

In conclusion, we have shown explicitly that in a Mott bilayer the **bandwidth of the magnetic excitations is strongly enhanced by the presence of an exciton condensate**. We emphasize that this dynamic enhancement is quite unusual: the interplay between magnetic and charge degrees of freedom most commonly leads to frustration effects such as found in the previous section 4.2. Paradoxically, this effect turns around dealing with excitons in Mott insulators under the condition that they condense. This can promote the propagation of spin.

[20] Bruus and Flensberg, 2004

[21] This is done extensively in section 3.2. See also Bardeen et al., 1957 and De Gennes, 1999.

5.2 *Finite exciton densities: the full phase diagram*

This section is based on Rademaker et al., 2013b.

To conclude our analysis of the bilayer exciton $t - J$ model we will now derive its full **ground state phase diagram**. This can be done since both excitons and spins act as bosons, which is much more tractable than the fermionic doped Mott insulator physics. However, not all 'fermion-like' signs are eliminated: there are still left-over signs of the phase-string type.[22] In section 4.1.4 we show that collinear spin order is a sufficient condition for these signs to cancel out, leaving a truly bosonic dynamics controlling the ground state and long wavelength physics. This is very similar to the 'spin-orbital' physics described by Kugel-Khomskii type models,[23] which can be viewed after all as describing d-d excitons interacting with spins. Also the lattice implementations[24] of the SO(5) model[25] for (cuprate) superconductivity are in this family of bosonic theories.

Such bosonic problems can be handled with standard (semiclassical) **mean field theory**. In most bilayer exciton set-ups, such as the quantum Hall bilayers or the pumped systems, there is no controllable equilibrium exciton density. In these cases one can hardly speak of the exciton density as a conserved quantity, and exciton condensation in the sense of spontaneously broken $U(1)$ symmetry is impossible.[26] However, in Mott insulators the dopant density per layer could be fixed by, for example, chemical doping. The effective exciton chemical potential is then by definition large compared to the recombination rate. Effectively, the excitons are at finite density in equilibrium and hence **true spontaneous $U(1)$ symmetry breaking is possible** in the Mott insulating bilayer at zero temperature.

Besides the exciton superfluid phase one anticipates a **plethora of competing orders**, as is customary in strongly correlated materials. At zero exciton density the bilayer Heisenberg system exhibits already interesting magnetic behavior. Departing from the antiferromagnet for small rung coupling it turns via an $O(3)$-QNLS quantum phase transition into an 'incompressible quantum spin liquid' for larger rung couplings that can be viewed as a continuation of pair singlets ('valence bonds') stacked on the rungs.[27] The natural competitor of the exciton superfluid at finite density is the exciton crystal and one anticipates due to the strong lattice potential this will tend to lock in at commensurate

[22] Weng, 2007

[23] Kugel and Khomskii, 1982

[24] van Duin and Zaanen, 2000

[25] Zhang, 1997

[26] Snoke, 2006

[27] Chubukov and Morr, 1995

densities forming exciton 'Mott insulators'. We will wire this in by taking also the exciton-exciton dipolar interaction into account that surely promotes such orderings. In principle there is the interesting possibility that all these orders may coexist microscopically forming an 'antiferromagnetic supersolid'.[28] We find that at least for the strongly coupled 'small' excitons assumed here this does not happen. The reason is interesting. We already alluded to the dynamical frustration associated with the exciton delocalizing in the antiferromagnetic spin background in section 4.2. At finite densities this turns into a tendency to just **phase separate on a macroscopic scale**, in zero density antiferromagnets, exciton Mott insulators and high density diamagnetic exciton superfluids. For now we notice quickly that the exciton dipole repulsion is actually long-ranged,[29] instead of just the nearest neighbor repulsion discussed in this chapter. This simplification rules out the occurrence of frustrated phase separation as suggested for the electronic order in cuprates.[30] The influence of the long-range nature of the dipolar interaction is discussed in chapter 6.

It is disappointing that apparently in this system only conventional ground states occur. However, this is actually to a degree deceptive. The Hamiltonian describing the physics at the lattice scale describes a physics where the exciton- and spin motions are **entangled**: the way in which these subsystems communicate gets beyond the notion of just being strongly coupled, since the motions of the exciton motions and the spin dynamics cannot be separated. By coarse graining this all the way to the static order parameters (the mean fields) an effective disentanglement eventually results as demonstrated by the product ground states. However, upon going "off-shell" this spin-exciton entanglement becomes directly manifest in the form of unexpected and rather counterintuitive effects on the excitation spectrum. A simple example is the zero exciton density antiferromagnet. From the relatively thorough LSW-SCBA treatment of the one exciton problem[31] we already know that the resulting exciton spectrum can be completely different from that in a simple semiconductor. In this section we compute the linearized excitations around the pure antiferromagnet, recovering the LSW-SCBA result in the adiabatic limit where the exciton hopping is small compared to the exchange energy of the spin system, which leads to a strong enhancement of the exciton mass. In the opposite limit of fast excitons, the energy

[28] Zaanen, 1999

[29] Rademaker et al., 2013d

[30] Zaanen and Gunnarsson, 1989; Emery and Kivelson, 1993; Löw et al., 1994; Tranquada et al., 1995; and Zhang and Henley, 2003

[31] See section 4.2.

scale is recovered but the Ising confinement ladder spectrum revealed by the LSW-SCBA treatment is absent. The reason clear: in the language of this section, the couplings between the exciton- and spin-wave modes become very large and these 'spin wave interactions' need to be resummed in order to arrive at an accurate description of the exciton propagator.

The real novelty in this regard is revealed in the high density **exciton superfluid phase**. As shown in the previous section, by measuring the spin fluctuations one can in principle determine whether the excitons are condensed in a superfluid.

As a reminder let us recall our point of departure: the Hamiltonian describing strongly bound excitons propagating through a bilayer Heisenberg spin $1/2$ system. This model is derived at length in section 4.1 and here we just summarize the outcome. Due to the strong electron-electron interactions the electronic degrees of freedom are reduced to spin operators $\mathbf{s}_{il}$ governed by the bilayer Heisenberg model[32]

$$H_J = J \sum_{\langle ij \rangle, l} \mathbf{s}_{il} \cdot \mathbf{s}_{jl} + J_\perp \sum_i \mathbf{s}_{i1} \cdot \mathbf{s}_{i2}. \tag{5.12}$$

The subscript denotes spin operators on site i in layer $l = 1, 2$. The Heisenberg H_J is antiferromagnetic with $J > 0$ and $J_\perp > 0$. The interlayer exciton can hop around, thereby interchanging places with the spin background. In the strong-coupling limit of exciton binding energies the exciton hopping process is described by the Hamiltonian

$$H_t = -t \sum_{\langle ij \rangle} |E_j\rangle \left(|0\ 0\rangle_i \langle 0\ 0|_j + \sum_m |1\ m\rangle_i \langle 1\ m|_j \right) \langle E_i|. \tag{5.13}$$

where $|E\rangle$ is the exciton state on an interlayer rung, and $|s\ m\rangle$ represent the rung spin states. Whenever an exciton hops, it effectively exchanges the spin configuration on its neighboring site. In order to study the system with a finite density of excitons, we need to enrich the $t - J$ model with two extra terms: a chemical potential and an exciton-exciton interaction.

The **chemical potential** is given by

$$H_\mu = -\mu \sum_i |E_i\rangle \langle E_i| \tag{5.14}$$

which is a rather trivial statement. The exciton-exciton interaction requires some more thought. The bare interaction between two

[32] Manousakis, 1991; and Chubukov and Morr, 1995

interlayer excitons results from their electric dipole moment. Since all interlayer exciton dipole moments are pointing in the same direction the full exciton-exciton interaction is described by a repulsive $1/r^3$ interaction. The interaction strength decays so fast that we consider it reasonable to only include the nearest-neighbor repulsion,

$$H_{V_I} = V_I \sum_{\langle ij \rangle} \left(|E_i\rangle\langle E_i| \right) \left(|E_j\rangle\langle E_j| \right). \tag{5.15}$$

Note that especially in the region where we expect phase separation, the long-range nature of the dipolar interaction will become relevant.[33] For now we set V_I to be the energy scale associated with **nearest neighbor exciton repulsion**. This number can get quite high: given a typical interlayer distance of 8 Å and an intersite distance of 4 Å[34] the bare dipole interaction energy is 14 eV. In reality, we expect this energy to be lower due to quantum corrections and screening effects. However, the exciton-exciton interaction scale remains on the order of electronvolts and thus larger than the estimated Heisenberg J and hopping t.

We must pause here for a while and reflect on the possibility of interlayer hopping of electrons, which leads to the **annihilation of excitons**,

$$H_{t_\perp} = -t_\perp \sum_i |E_i\rangle\langle 0\,0|_i + h.c. \tag{5.16}$$

This term explicitly breaks the $U(1)$ symmetry, which is associated with the conservation of excitons. While this term is almost certainly present in any realistic system, it is a matter of numbers whether it is relevant. In the present case the interlayer tunneling can be incorporated using perturbation theory in a renormalisation of the chemical potential μ. As a consequence we do not need to include the $t_\perp$ term in our model Hamiltonian.

The full model Hamiltonian describing a finite density of excitons in a strongly correlated bilayer is thus

$$H = H_J + H_t + H_\mu + H_{V_I}. \tag{5.17}$$

5.2.1 *Symmetries and an effective XXZ model*

The Hamiltonian (5.17) has five model parameters: J, $J_\perp$, t, V_I and μ. However, most properties of the excitons can be understood by considering the simpler problem of hard-core bosons on a

[33] See chapter 6 for the influence of long-range interactions.

[34] Imada et al., 1998

lattice. In this subsection we will argue that the exciton degrees of freedom can be described by an **effective** XXZ **model**.

Before characterizing different phases of the model we need to assess the **algebraic structure of the exciton** $t-J$ **model**. The set of all operators that act on the local Hilbert space form the **dynamical algebra**, whereas the symmetries of the system are grouped together in the **symmetry algebra**.

To derive the dynamical algebra, it is instructive to start with the bilayer Heisenberg model which has, on each interlayer rung, a $SO(4) \cong SU(2) \times SU(2)$ dynamical algebra. Upon inclusion of the exciton hopping term we need more operators, since now the local Hilbert space on an interlayer rung is five-dimensional (four spin states and the exciton). Consider the spin-to-exciton operator $E^+_{sm} \equiv |E\rangle\langle s\ m|$ and its conjugate $E^-_{sm} = (E^+_{sm})^\dagger$. Their commutator reads

$$[E^+_{sm}, E^-_{sm}] = |E\rangle\langle E| - |s\ m\rangle\langle s\ m| \equiv 2E^z_{sm} \tag{5.18}$$

where we have introduced the operator E^z_{sm} to complete a $SU(2)$ algebraic structure. We could set up such a construction for each of the four spin states $|s\ m\rangle$. Under these definitions the exciton hopping term (5.13) can be rewritten in terms of an XY-**model** for each spin state,

$$\begin{aligned} H_t &= -t \sum_{<ij>,sm} \left(E^+_{sm,i} E^-_{sm,j} + E^-_{sm,i} E^+_{sm,j} \right) && (5.19) \\ &= -2t \sum_{<ij>,sm} \left(E^x_{sm,i} E^x_{sm,j} + E^y_{sm,i} E^y_{sm,j} \right) && (5.20) \end{aligned}$$

where the sum over sm runs over the singlet and the three triplets. Note that the exciton chemical potential (5.14) acts as an externally applied magnetic field to this XY-model, and that the exciton-exciton repulsion (5.15) can be rewritten as an antiferromagnetic Ising term in the E^z_{sm} operators. The dynamical algebra therefore contains four $SU(2)$ algebras in addition to the $SO(4)$ from the bilayer Heisenberg part. The closure of such algebra is necessarily $SU(5)$, which is the largest algebra possible acting on the five-dimensional Hilbert space. Hence we need a full $SU(5)$ dynamical algebra to describe the exciton $t-J$ model at finite density.

From the XY-representation of the hopping term one can already deduce that we have four distinct $U(1)$ symmetries associated with spin-exciton exchange. The bilayer Heisenberg model contains two separate $SU(2)$ symmetries, associated with in-phase and out-phase interlayer magnetic order. Therefore the **full symmetry algebra of the model is** $[SU(2)]^2 \times [U(1)]^4$.

Breaking of the $SU(2)$ symmetry amounts to magnetic ordering, which is most likely antiferromagnetic (and therefore also amounts to a breaking of the lattice symmetry). Each of the $U(1)$ algebras can be broken leading to exciton condensation. Note that next to possible broken continuous symmetries, there also might exist phases with broken translation symmetry. The checkerboard phase is an example of a phase where the lattice symmetry is broken into two sublattices.

Above we showed that the exciton hopping terms are similar to an XY-model. The main reason is that the excitons are, in fact, **hard-core bosons** and thus allow for a mapping onto pseudospin degrees of freedom. Viewed as such, the exciton-exciton interaction (5.15) is similar to an antiferromagnetic Ising term and the exciton chemical potential (5.14) amounts to an external magnetic field in the z-direction. Together they form an XXZ**-model with external field**, which has been investigated in quite some detail before[35] as well as in the context of exciton dynamics in cold atom gases.[36]

In order to understand the basic competition between the checkerboard phase and the superfluid phase of the excitons, it is worthwhile to neglect the magnetic degrees of freedom and study first this effective XXZ-model for the excitons only. In this context the transition between the checkerboard and superfluid phases is known as the **'spin flop'-transition**.[37] Whilst remembering that the exciton degrees of freedom are mapped onto the XXZ pseudospin degrees of freedom, we now quickly review the basics of the XXZ Hamiltonian

$$H = -t \sum_{\langle ij \rangle} \left(E_i^x E_j^x + E_i^y E_j^y \right) - \mu \sum_i E_i^z + V_I \sum_{\langle ij \rangle} E_i^z E_j^z \tag{5.21}$$

where $E^+ = |1\rangle\langle 0| = E^x + iE^y$ creates a hard-core bosonic particle $|1\rangle$ out of the vacuum $|0\rangle$. This model has a built-in competition between $t > 0$, which favors a superfluid state, and $V_I > 0$, which favors a solid state where all particles are on one sublattice and the other sublattice is empty. The external field or chemical potential μ tunes the total particle density. The ground state can now be found using mean field theory. It is known that for pseudospin

[35] Néel, 1936; Fisher and Nelson, 1974; Landau and Binder, 1981; van Otterlo et al., 1995; Kohno and Takahashi, 1997; and Yunoki, 2002

[36] Kantian et al., 2007

[37] Néel, 1936

$S = \frac{1}{2}$ models in $(2+1)$d the quantum fluctuations are not strong enough to defeat classical order, therefore we can rely on mean field theory which is indeed supported by exact diagonalization studies.[38]

To find the ground state we introduce a **variational wavefunction** describing a condensate of excitons,

$$|\Psi\rangle = \prod_i \left(\cos\theta_i e^{i\psi_i}|1\rangle_i + \sin\theta_i|0\rangle_i\right). \tag{5.22}$$

The mean-field approximation amounts to choosing ψ_i constant and θ_i only differing between the two sublattices. We find the following mean-field energy

$$\begin{aligned} E/N &= -\frac{1}{8}tz\sin 2\theta_A \sin 2\theta_B + \frac{1}{8}V_I z\cos 2\theta_A \cos 2\theta_B \\ &\quad -\frac{1}{4}\mu\left(\cos 2\theta_A + \cos 2\theta_B\right). \end{aligned} \tag{5.23}$$

Let's rewrite this in terms of $\overline{\theta} = \theta_A + \theta_B$ and $\Delta\theta = \theta_A - \theta_B$,

$$\begin{aligned} E/N &= \frac{z}{8}\left((V_I - t)\cos^2\Delta\theta + (V_I + t)\cos^2\overline{\theta}\right) \\ &\quad -\frac{1}{2}\mu\cos\Delta\theta\cos\overline{\theta} - \frac{V_I z}{8}. \end{aligned} \tag{5.24}$$

When $|\mu| \geq \frac{1}{2}(V_I z + zt)$ the ground state is fully polarized in the z-direction. This means either zero particle density for negative μ, or a $\rho = 1$ for the positive μ case. Starting from the empty side, increasing μ introduces a smooth distribution of particles. This phase amounts to the superfluid phase of the excitons. The particle density on the two sublattices is equal and the total density is given by

$$\rho = \cos^2\theta = \frac{1}{2}\left(\cos\overline{\theta} + 1\right) = \frac{1}{2}\left(\frac{2\mu}{V_I z + zt} + 1\right). \tag{5.25}$$

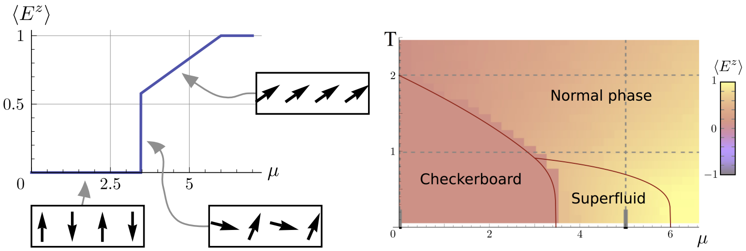

Figure 5.3: **Left:** The ground state phase diagram of the XXZ model (5.21). The graph shows the mean field particle density $\langle E^z \rangle$ as a function of μ, with model parameters $t = 1$ and $V_I = 2t$. One clearly distinguishes the fully polarized phases for large μ, the superfluid phase with a linear $\langle E^z \rangle$ vs μ dependence and the checkerboard phase with $\langle E^z \rangle = 0$. In between the checkerboard and the superfluid phase a non-trivial first order transition exists, with a variety of coexistence ground states with the same ground state energy. The insets show how the (E^x, E^z)-vectors look like in the different phases. **Right:** Finite temperature phase diagram of the XXZ model with the same parameters. The background coloring corresponds to a semi-classical Monte Carlo computation of $\langle E^z \rangle$, the solid lines are analytical mean field results for the phase boundaries. We indeed see the checkerboard phase and the superfluid phase, as well as a high-temperature non-ordered 'normal' phase.

[38] Kohno and Takahashi, 1997

At the critical value of the chemical potential given by

$$(\mu_c)^2 = \left(\frac{1}{2}z\right)^2 (V_I - t)(V_I + t). \tag{5.26}$$

a first order transition occurs towards the checkerboard phase: the spin flop transition. In the resulting phase, which goes under various names such as the antiferromagnetic,[39] solid, checkerboard or Wigner crystalline phase, the sublattice symmetry is broken. The resulting ground state phase diagram is shown in figure 5.3, where a graph of the particle density as a function of μ is given.

At **finite temperatures** in $(2+1)$d there can be algebraic long-range order. At some critical temperature a Kosterlitz-Thouless phase transition[40] will destroy this long-range order. The topology of the phase diagram, however, can be obtained using the finite temperature mean field theory for which we need to minimize the mean field thermodynamic potential[41]

$$\begin{aligned}\Phi/N &= -kT\log\left(2\cosh\left(\frac{\beta m}{2}\right)\right) + \frac{1}{2}m\tanh\left(\frac{\beta m}{2}\right)\\ &\quad +\frac{z}{8}\tanh^2\left(\frac{\beta m}{2}\right)\\ &\quad \times\left[(V_I - t)\cos^2\Delta\theta + (V_I + t)\cos^2\overline{\theta} - V_I\right]\\ &\quad -\frac{\mu}{2}\tanh\left(\frac{\beta m}{2}\right)\cos\Delta\theta\cos\overline{\theta}. \end{aligned} \tag{5.27}$$

Expectation values are now given in the form of

$$\langle S^x_{i\in A}\rangle = \frac{1}{2}\sin 2\theta_A \tanh\left(\frac{\beta m}{2}\right), \tag{5.28}$$

and the parameter m needs to be determined self-consistently. The resulting phase diagram is shown in figure 5.3, right, which is of the form discussed by Fisher and Nelson, 1974.

The **first order quantum critical point** at μ_c turns out to be non-trivial, a point which is usually overlooked in the literature. A trivial first order transition occurs when there are two distinct phases with exactly the same energy. In the case presented here, there is a infinite set of mean field order parameters all yielding different phases yet still having the same energy. A simple analytic calculation shows that the energy of the ground state at the critical point is $E_c = -V_I z/8$. Now rewrite the mean field parameters ρ_A

[39] If we associate the presence of a particle with spin up, and the absence with spin down, then the solid phase is identified with an Ising antiferromagnet. However, one should not confuse this with the *actual* antiferromagnetism present in the spin sector of the full exciton $t - J$ model. To avoid confusion, from now on we will use the term 'antiferromagnetism' only when referring to the spin degrees of freedom in the full exciton $t - J$ model.

[40] Kosterlitz and Thouless, 1973

[41] Yeomans, 1992

and ρ_B into a sum and difference parameter

$$\rho = \frac{1}{2}(\rho_A + \rho_B), \tag{5.29}$$

$$\Delta_\rho = \frac{1}{2}(\rho_A - \rho_B). \tag{5.30}$$

For each value of Δ_ρ with $|\Delta_\rho| \leq (1/2)$ we can find a value of ρ such that the mean field energy is exactly $-V_I z/8$.

This has interesting consequences. If one can control the density instead of the chemical potential around a first order transition, in general phase separation would occur between the two competing phases. From the mean field considerations above it is unclear what would happen in a system described by the XXZ Hamiltonian (5.21). All phases would be equally stable, at least from an energy perspective, and every phase may occur in regions of any size. Such a highly degenerate state may be very sensible to small perturbations. We consider it an interesting open problem to study the dynamics of such a highly degenerate system, and whether this degeneracy may survive the inclusion of quantum corrections.

Note that qualitatively a possible $t_\perp$ term is irrelevant, which can be seen in the XXZ pseudospin language where it takes the form of a tilt of the magnetic field in the x-direction,

$$H_{t_\perp} = -t_\perp \sum_i E_i^x. \tag{5.31}$$

5.2.2 *Ground state phase diagram: variational wavefunction*

In the previous section we have seen that the effective XXZ model predicts the existence of both a exciton **superfluid phase** and a **checkerboard phase**, separated by a first order transition. Further extending these results yields the ground state phase diagram for the full exciton $t-J$ model (5.17).

We will proceed along the same lines as in the previous section. Hence we need a **variational wavefunction**, which we simulate numerically to obtain an unbiased view on the possible ground state phases. Based on the numerical results we apply mean field theory, which is very reliable due to the hard-core bosonic nature of excitons. The analytical mean field also allows us to characterize the three distinct phases: the **antiferromagnet**, the **superfluid** and the **checkerboard**. Finally, combining the numerical results and the analytical mean field results we obtain the ground state phase diagram in figure 5.8.

Recall that the local Hilbert space consists of four spin states $|s\ m\rangle$ and the exciton state $|E\rangle$. We therefore propose a variational wavefunction consisting of a product state of superpositions all five states on each rung. For the spin states we take the $SO(4)$ **coherent state**[42]

$$\begin{aligned}|\Omega_i\rangle &= -\frac{1}{\sqrt{2}}\sin\chi_i\sin\theta_i e^{-i\phi_i}|1\ 1\rangle_i \\ &\quad +\frac{1}{\sqrt{2}}\sin\chi_i\sin\theta_i e^{i\phi_i}|1\ -1\rangle_i \\ &\quad +\sin\chi_i\cos\theta_i|1\ 0\rangle_i-\cos\chi_i|0\ 0\rangle_i \end{aligned} \tag{5.32}$$

which needs to be superposed with the exciton state,

$$|\Psi_i\rangle=\sqrt{\rho_i}e^{i\psi_i}|E_i\rangle+\sqrt{1-\rho_i}|\Omega_i\rangle \tag{5.33}$$

to obtain the total variational wavefunction

$$|\Psi\rangle=\prod_i|\Psi_i\rangle. \tag{5.34}$$

Given this wavefunction, the expectation value of a product of operators on different sites decouples, $\langle A_iB_j\rangle=\langle A_i\rangle\langle B_j\rangle$. The only nonzero expectation values of spin operators are for $\widetilde{\mathbf{S}}_i=\mathbf{s}_{i1}-\mathbf{s}_{i2}$ and it equals

$$\langle\Omega_i|\widetilde{\mathbf{S}}_i|\Omega_i\rangle=\sin 2\chi_i\begin{pmatrix}\sin\theta_i\cos\phi_i\\ \sin\theta_i\sin\phi_i\\ \cos\theta_i\end{pmatrix}=\sin 2\chi_i\ \hat{\mathbf{n}}_i \tag{5.35}$$

where $\hat{\mathbf{n}}_i$ is the unit vector described by the angles θ and ϕ. This variational wavefunction therefore assumes interlayer Néel order of magnitude $\sin 2\chi_i$, which enables us to correctly interpolate between the perfect Néel order at $\chi=\pi/4$ and the singlet phase $\chi=0$ present in the bilayer Heisenberg model. The exciton density at a rung i is trivially given by ρ_i.

Given the variational wavefunction, we can use **simulated annealing** to develop an unbiased view on the possible ground state phases. Therefore we start out with a lattice, on each lattice site the variables θ_i, χ_i, ϕ_i, ψ_i and ρ_i and with periodic boundary

[42] van Duin, 1999

conditions. The energy of a configuration is

$$\begin{aligned} E \;=\; & \frac{1}{2}J \sum_{<ij>} (1-\rho_i)(1-\rho_j)\sin 2\chi_i \sin 2\chi_j \; \hat{n}_i \cdot \hat{n}_j \\ & - J_\perp \sum_i (1-\rho_i)\cos^2\chi_i - \mu \sum_i \rho_i + V_I \sum_{<ij>} \rho_i \rho_j \\ & - \frac{1}{2} t \sum_{<ij>} \sqrt{\rho_i(1-\rho_i)\rho_j(1-\rho_j)}\,\cos(\psi_i - \psi_j) \\ & \times \left(\cos\chi_i \cos\chi_j + \sin\chi_i \sin\chi_j \; \hat{n}_i \cdot \hat{n}_j\right) \qquad (5.36) \end{aligned}$$

We performed standard **Metropolis Monte Carlo updates**[43] of the lattice with fixed total exciton density. The fixed total exciton density is ensured as follows: if during an update the exciton density ρ_i is changed, the exciton density on one of the neighboring sites is corrected such that the total exciton density remains constant.

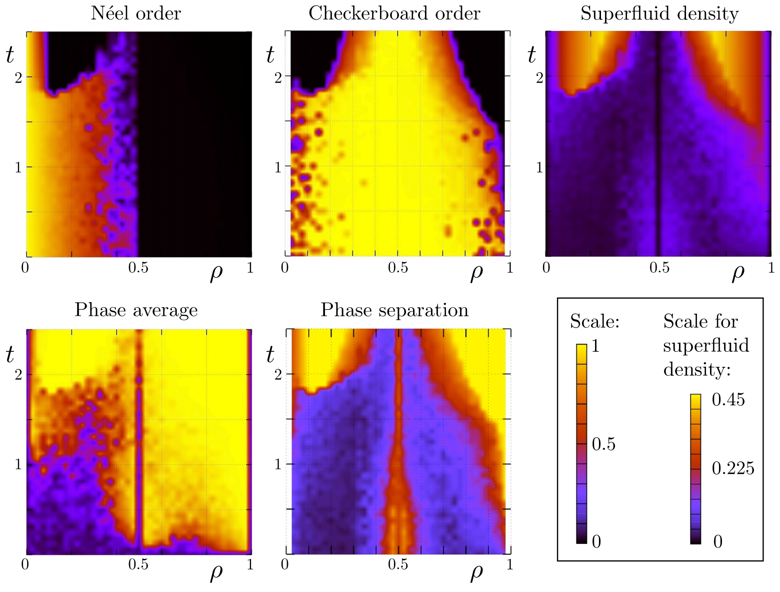

Figure 5.4: Results from the semi-classical Monte Carlo simulations. Here shown are color plots, with on the horizontal axes the exciton density ρ and on the vertical axes the hopping parameter t (in eV). Other parameters are fixed at $J = 125$ meV, $\alpha = 0.04$ and $V_I = 2$ eV. The five measurements shown here are the Néel order parameter (5.37), the checkerboard order parameter (5.38), the superfluid density (5.39), the phase coherence (5.40), and the ratio signaling phase separation according to equation (5.42), 0 means complete phase separation, 1 means no phase separation. Notice that the prominent line at $\rho = 0.5$ signals the checkerboard phase.

The main results of the simulation are shown in figure 5.4, for various values of the hopping parameter t and exciton density ρ. We performed the computations on a 10×10 lattice. Notice that even though true long-range order does not exist in two dimensions, the range of possible ordered phases is longer than the size of our simulated lattice. The other parameters are fixed at

[43] See section 3.3 for a detailed description of Monte Carlo techniques.

$J = 125$ meV, $\alpha = 0.04$ and $V_I = 2$ eV. The Heisenberg couplings $J = 125$ meV and $\alpha = 0.04$ are obtained from measurements of undoped YBCO-samples,[44] which we consider to be qualitatively indicative of all strongly correlated electron bilayers. The dipolar coupling is estimated at 2 eV, following our discussion in the introduction.

For each value of ρ and t we started at relatively high temperatures $T = 0.1$ eV and then slowly reducing the temperature to 10^{-5} eV while performing a full update of the whole lattice 10 million times. We expect that by such a slow annealing we obtain the true ground state of (5.36) without any topological defects or false vacua. Once arrived at the low temperature state, we performed measurements over 200.000 full updates of the system.

We measured six different parameters of interest:

- The **Néel order** parameter defined by

$$\text{Neel} = \left\| \frac{1}{N} \sum_i (-1)^i (1-\rho_i) \sin 2\chi_i \hat{\mathbf{n}}_i \right\| \tag{5.37}$$

  where we first sum over all spin vectors and then take the norm.

- The **checkerboard order**, defined as the difference in exciton density between the sublattices divided by the maximal difference possible. The maximal difference possible equals $\text{Min}(\overline{\rho}, 1 - \overline{\rho})$, so

$$\text{Checkerboard} = \frac{\frac{1}{N}\sum_i (-1)^i \rho_i}{\text{Min}(\overline{\rho}, 1-\overline{\rho})}. \tag{5.38}$$

- The **superfluid density** is given by the expectation value of the exciton operator. Here we don't make a distinction between singlet exciton condensation or triplet exciton condensation. Therefore

$$\text{Superfluid density} = \frac{1}{N} \sum_i \sqrt{\rho_i (1-\rho_i)}. \tag{5.39}$$

- Now the superfluid density is not the only measure of the condensate, we can also probe the **rigidity of the phase** ψ. Therefore we sum up all the phase factors on all sites,

$$\text{Phase average} = \left| \frac{1}{N} \sum_i e^{i\psi_i} \right|. \tag{5.40}$$

[44] Imada et al., 1998; and Tranquada et al., 1989

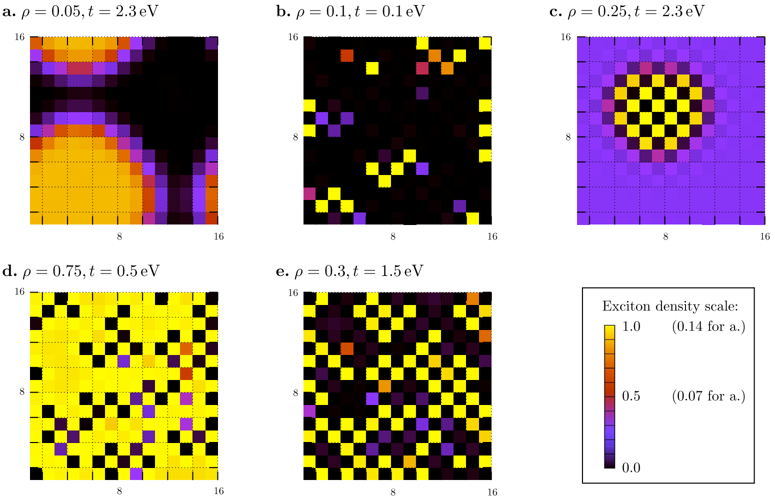

Figure 5.5: Typical configurations for the exciton density per site, obtained in the Monte Carlo simulation on a 16×16 square lattice. The color scale indicates the exciton density. All five figures have model parameters $J = 125$ meV, $\alpha = 0.04$ and $V_I = 2$ eV. **a:** Separation between the antiferromagnetic phase (without excitons, hence shown black) and the exciton condensate with smooth exciton density ($\rho = 0.05$, $t = 2.3$ eV). **b:** Separation between checkerboard-like localized excitons and an antiferromagnetic background ($\rho = 0.1$, $t = 0.1$ eV). **c:** Separation between the checkerboard phase and a low density exciton condensate ($\rho = 0.25$, $t = 2.3$ eV). **d:** Separation between the checkerboard phase and a high density exciton condensate ($\rho = 0.75$, $t = 0.5$ eV). **e:** The region where antiferromagnetic order, checkerboard order and the exciton condensate are all present ($\rho = 0.3$, $t = 1.5$).

If the phase is disordered, this sum tends to zero. On the other hand, complete phase coherence in the condensate phase implies that this quantity equals one.

- Finally, we considered a measure of **phase separation** between the checkerboard phase and the superfluid phase. If the exciton condensate and the checkerboard phase are truly coexisting, then the maximal superfluid density attainable would be

$$\begin{aligned}\text{Max SF density} = & \frac{1}{2}\sqrt{(\bar{\rho}+\Delta_\rho)(1-\bar{\rho}-\Delta_\rho)} \\ & -\frac{1}{2}\sqrt{(\bar{\rho}-\Delta_\rho)(1-\bar{\rho}+\Delta_\rho)} \qquad (5.41)\end{aligned}$$

where $\Delta_\rho = \frac{1}{N}\sum_i (-1)^i \rho_i$. If there is phase separation, however, the actual superfluid density is less than this maximal density. Therefore we also measured the ratio

$$\text{Ratio} = \frac{\text{Superfluid density}}{\text{Max SF density}} \qquad (5.42)$$

to quantify the extent of phase separation. Now if this ratio is less than 1, we have phase separation.

The results for a full scan for the range $0 < \rho < 1$ and $0 < t < 2.5$ eV are shown in figure 5.4. In figures 5.5 and 5.6 we have displayed typical exciton density configurations for various points in the phase diagram. These results combined suggest

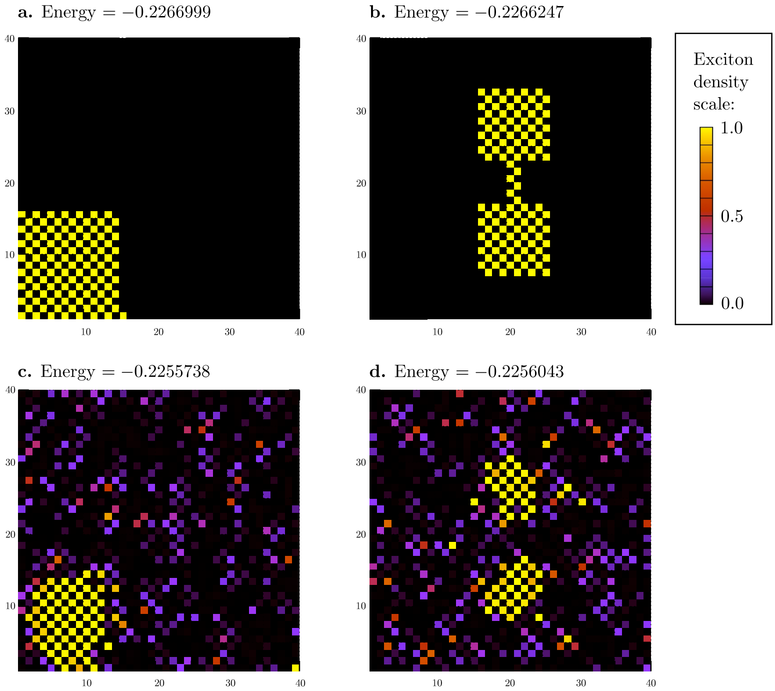

a. Energy = −0.2266999

b. Energy = −0.2266247

c. Energy = −0.2255738

d. Energy = −0.2256043

Figure 5.6: Different exciton configurations with their respective energies on a 40×40 lattice, to show whether there is macroscopic phase separation. The model parameters are $t = 0.5$ eV, $J = 125$ meV, $\alpha = 0.04$, $V_I = 2$ eV and $\rho = 0.06625$. Yellow indicates the presence of excitons, and in the black regions there is antiferromagnetic order. **a:** The lowest energy state is the one with complete macroscopic phase separation. **b:** More complicated phase separation, such as the halter form depicted here, are higher in energy. **c:** Starting at high temperatures with the configuration a, we slowly lowered the temperature. The resulting configuration shown here is a local minimum. **d:** Using the same slow annealing as for c starting from configuration b. The local energy minimum obtained this way is lower in energy than the configuration c. We conclude that even though macroscopic phase separation has the lowest energy, there are many local energy minima without macroscopic phase separation.

that there are **three main phases** present in the system: the antiferromagnet at low exciton densities, the exciton superfluid at high exciton hopping energies and the checkerboard around half-filling. For most parts of the phase diagram, however, the competition between the three phases results in phase separation.

Let us investigate the **phase separation** in somewhat more detail. In section 4.2 we found that the motion of an exciton in an antiferromagnetic background leads to dynamical frustration. In other words: excitons do not want to be together with antiferromagnetism. The introduction of a finite density of excitons will therefore induce phase separation. For large t, we find macroscopic phase separation between the antiferromagnet and the exciton superfluid, see figure 5.5a. At low exciton kinetic energy the excitons will be localized in a checkerboard pattern as can be seen in figure 5.5b.

Close to half-filling the role of the dipole repulsion V_I becomes increasingly relevant. The first order 'spin flop' transition implies that there will be phase separation between the superfluid and the checkerboard order. Figures 5.5c and d show this phase separation. Finally there is a regime where the condensate, the checkerboard order and the Néel order are all present. However, given the dynamical frustration at one hand and the spin-flop transition at the other hand, we again predict phase separation. A typical exciton configuration is shown in figure 5.5e.

Phase separation is thus widespread, based on results obtained by slow annealing starting at high temperatures. However, annealing can lead to the freezing in of defects, which prevents us from reaching the true ground state. In order to investigate whether we have **frustrated or macroscopic phase separation**, we construct custom-made phase separated configurations and compare their energies in figure 5.6. The lowest energy configuration (5.6a) has macroscopic phase separation between the checkerboard and the antiferromagnetic phase. Intermediate states with one blob of excitons (5.6c) are slightly higher in energy than states with two blobs of excitons (5.6d). However, even though macroscopic phase separation has the lowest energy, configurations with more blobs have more entropy. Consequently for any nonzero temperatures complete macroscopic phase separation is not the most favorable option. This is indeed picked up by the numerical simulations: annealing leads to high-entropy states such as figure 5.6d rather than to the lowest energy configuration.

We thus conclude that the dominant phases are the antiferromagnet, the superfluid and the checkerboard. The competition between these three phases leads to phase separation in most parts of the phase diagram. The unbiased Monte Carlo simulations shows the direction in which further analytical research should be directed: we will use mean field theory to characterize the three phases more thoroughly.

5.2.3 *Mean field theory and characterization of the phases*

Given the fact that we are dealing with a hard-core boson problem, we know that **mean field theory is qualitatively correct**. The only open issue is whether one can tune the exciton chemical potential rather than the exciton density in realistic experiments. Since we are prescient about the many first-order phase transitions present, we will perform the analysis with a fixed exciton density (the canonical ensemble). A transformation back to the grand-canonical ensemble can be made given the explicit μ vs. ρ relations.

Now the numerical simulations suggest that the mean field parameters only need to depend on the sublattice,

$$\rho_i = \begin{cases} \rho_A & i \in A \\ \rho_B & i \in B \end{cases} \tag{5.43}$$

and so forth for χ, θ, ψ and ϕ. With this **broken translational symmetry** we anticipate the antiferromagnetic and checkerboard order. Evaluation of the energy $E = \langle\Psi|H|\Psi\rangle$ under the variational wavefunction directly suggests that we can set $\theta = \psi = \phi = 0$ on all sites.[45] We are left with four parameters ρ_A, ρ_B, χ_A and χ_B, and as it turns out it will be more instructive to rewrite these in terms of sum and difference variables,

$$\begin{aligned} \overline{\rho} &= \frac{1}{2}(\rho_A + \rho_B) && (5.44)\\ \Delta_\rho &= \frac{1}{2}(\rho_A - \rho_B) && (5.45)\\ \overline{\chi} &= \chi_A + \chi_B && (5.46)\\ \Delta_\chi &= \chi_A - \chi_B && (5.47) \end{aligned}$$

The mean field energy per site is now given by

$$\begin{aligned} E/N \;=\;& \frac{1}{8}Jz\left((1-\overline{\rho})^2 - \Delta_\rho^2\right)(\cos 2\Delta_\chi - \cos 2\overline{\chi}) \\ & -\frac{1}{2}J_\perp\left[(1-\overline{\rho})(\cos\overline{\chi}\cos\Delta_\chi + 1) + \Delta_\rho \sin\overline{\chi}\sin\Delta_\chi\right] \\ & -\frac{1}{4}zt\sqrt{((1-\overline{\rho})^2 - \Delta_\rho^2)(\overline{\rho}^2 - \Delta_\rho^2)}\cos\Delta_\chi \\ & -\mu\overline{\rho} + \frac{1}{2}zV_I(\overline{\rho}^2 - \Delta_\rho^2). \end{aligned} \tag{5.48}$$

which needs to be minimized for a fixed average exciton density $\overline{\rho}$ with the constraint $|\Delta_\rho| \leq \min(\overline{\rho}, 1-\overline{\rho})$. The resulting mean field phase diagram for typical values of $J, J_\perp$ and V_I, for various $t, \overline{\rho}$, is shown in figure 5.7.

As long as the exciton density is set to zero, the mean field ground state is given by the same ground state as for the bilayer Heisenberg model. That is the **antiferromagnetic phase** parametrized by

$$\rho = 0,\ \overline{\chi} = 0 \text{ and } \cos\Delta_\chi = \frac{J_\perp}{Jz} \equiv \alpha. \tag{5.49}$$

[45] By setting $\theta = \phi = 0$ we restrict the spin vectors to be pointing in the $\pm z$ direction only. Since we anticipate magnetic ordering we have the freedom to choose the direction of the ordering. Similar arguments hold for the choice $\psi = 0$; when breaking the $U(1)$ symmetry associated with exciton condensation we are free to choose the phase direction.

The Néel order is given by

$$\frac{1}{N}\sum_i (-1)^i \langle \widetilde{S}_i^z \rangle = \sqrt{1-\alpha^2} \tag{5.50}$$

and the energy of the antiferromagnetic state is

$$E = -\frac{1}{4} Jz(1+\alpha)^2. \tag{5.51}$$

The introduction of excitons in an antiferromagnetic background leads to dynamical frustration effects which disfavors the coexistence of excitons and antiferromagnetic order.[46] In fact, the numerical simulations already ruled out coexistence of superfluidity and antiferromagnetism.

For large exciton hopping energy t it becomes more favorable to mix delocalized excitons into the ground state. Due to the bosonic nature of the problem this automatically leads to **exciton condensation**. The delocalized excitons completely destroy the antiferromagnetic order and the exciton condensate is described by a superposition of excitons and a singlet background,

$$|\Psi\rangle = \prod_i \left(\sqrt{\rho}|E_i\rangle + \sqrt{1-\rho}|0\ 0\rangle_i \right). \tag{5.52}$$

Here we wish to emphasize the ubiquitous coupling to light of the superfluid. The dipole matrix element allows only zero spin transitions, and since the exciton itself is also $S = 0$ the dipole matrix element is directly related to the superfluid density,

$$\begin{aligned}
\langle \sum_\sigma c^\dagger_{i1\sigma} c_{i2\sigma} \rangle &= \langle E| \left(c^\dagger_{1\uparrow} c_{2\uparrow} + c^\dagger_{1\downarrow} c_{2\downarrow} \right) |0\ 0\rangle \\
&= \frac{1}{\sqrt{2}} \sqrt{\rho(1-\rho)} \langle \uparrow\downarrow_1\ 0_2| \\
&\quad \left(c^\dagger_{1\uparrow} c_{2\uparrow} + c^\dagger_{1\downarrow} c_{2\downarrow} \right) (|\uparrow_1 \downarrow_2\rangle - |\downarrow_1 \uparrow_2\rangle) \\
&= \sqrt{2\rho(1-\rho)}
\end{aligned} \tag{5.53}$$

The dipole matrix element thus acts as the order parameter associated with the superfluid phase. In most bilayer exciton condensates, such as the one in the quantum Hall regime,[47] this order parameter is also nonzero in the normal phase because of interlayer tunneling of electrons. One can therefore not speak strictly about spontaneous breaking of $U(1)$ symmetry in such systems;

[46] See section 4.2.

[47] Eisenstein and MacDonald, 2004

there is already explicit symmetry breaking due to the interlayer tunneling. In strongly correlated electron systems the finite $t_\perp$ can be incorporated as a virtual process since the energy scales associated with the chemical potential are much larger than $t_\perp$. As discussed at the beginning of this section, the Mott insulating bilayers now effectively allow for spontaneous $U(1)$ symmetry breaking, and the above dipole matrix element acts as a true order parameter. Note that the irrelevance of interlayer hopping $t_\perp$ implies that this order parameter is, unfortunately, not reflected in photon emission or interlayer tunneling measurements.

The exciton condensate is in fact a standard **two-dimensional Bose condensate**. The $U(1)$ symmetry present in the XY-type exciton hopping terms is spontaneously broken and we expect a linearly dispersed Goldstone mode in the excitation spectrum, reflecting the rigidity of the condensate.

The energy of the singlet exciton condensate is

$$E = -J_\perp - \frac{(\mu + \frac{1}{4}zt - J_\perp)^2}{zt + 2V_I z} \tag{5.54}$$

and the exciton density is given by

$$\overline{\rho} = 2\frac{\mu + \frac{1}{4}zt - J_\perp}{zt + 2V_I z}. \tag{5.55}$$

Whenever the exciton hopping is small, the introduction of excitons into the system leads to the **'spin flop' transition towards the checkerboard phase**. As shown in the context of the XXZ model, this phase implies that one sublattice is completely filled with excitons and the other sublattice is completely empty. On the empty sublattice, any nonzero $J_\perp$ will guarantee that the singlet spin state has the lowest energy. Hence the average exciton density is here $\overline{\rho} = \Delta_\rho = 1/2$ and the energy of the checkerboard phase is given by

$$E = -\frac{1}{2}J_\perp - \frac{1}{2}\mu. \tag{5.56}$$

It is interesting to note that the checkerboard phase is in fact similar to a Bose Mott insulator: with the new doubled unit cell we have one exciton per unit cell. The nearest neighbor dipole repulsion now acts as the 'on-site' energy preventing extra excitons per unit cell.

The mean field theory also predicts, for a small region with intermediate t and small exciton densities, the **coexistence of antiferromagnetism and the condensate**. This is, however, an artifact of the theory, since the numerical simulations show that here phase separation between the three different phases is favorable.

Finally, when the exciton density is 1 we have a system composed of excitons only. In the parlance of hard-core bosons this amounts to a **exciton Mott insulator**. This rather featureless phase is adiabatically connected to a standard electronic band insulator. Namely, the system is now composed of two layers where each layer has an even number of electrons per unit cell. The energy of the exciton Mott insulator is

$$E = -\mu + \frac{1}{2} V_I z. \tag{5.57}$$

In the mean field theory just described many **phase transitions** were first order, in the sense that the exciton density varies discontinuously along the transition. The critical values of t/J or μ along the second order transitions are

$$\begin{aligned}
(t/J)_{c,\mathrm{AF}\to\mathrm{CO}} &= \frac{2Jz(1+\alpha) - 4\mu}{J_\perp} && (5.58)\\
(t/J)_{c,\mathrm{EC}\to\mathrm{CO}} &= 1 - \frac{2\mu}{Jz} + \sqrt{(1+8\alpha) + \left(\frac{2\mu}{Jz}\right)^2 - 4\left(3\frac{\mu}{Jz} - \frac{2V_I}{J}(1-\alpha)\right)} && (5.59)\\
\mu_{c,\mathrm{EC}\to\mathrm{EI}} &= J_\perp + \frac{1}{4} z t + V_I z && (5.60)
\end{aligned}$$

and the critical values for the first order transitions are

$$\begin{aligned}
\mu_{c,\mathrm{AF}\to\mathrm{CB}} &= \frac{1}{2} Jz(1+\alpha^2) && (5.61)\\
\mu_{c,\mathrm{CB}\to\mathrm{EI}} &= V_I z + J_\perp && (5.62)\\
(t/J)_{c,\mathrm{AF}\to\mathrm{EC}} &= 2(1+\alpha^2) - 4\frac{\mu}{Jz} + 2\sqrt{(1-\alpha^2)\left(4\frac{\mu}{Jz} - (1+\alpha)^2 - 2\frac{V_I}{J}\right)} && (5.63)\\
(t/J)_{c,\mathrm{CB}\to\mathrm{EC}} &= 4\sqrt{\left(\frac{\mu}{Jz} - \alpha\right)\left(\frac{V_I}{J} + \alpha - \frac{\mu}{Jz}\right)} && (5.64)
\end{aligned}$$

$$(t/J)_{c,\mathrm{CO}\to\mathrm{CB}} = \frac{2\alpha^2}{2\frac{\mu}{Jz} - 1} - 2\alpha + \sqrt{\left(1 - \frac{\alpha^2}{2\frac{\mu}{Jz} - 1}\right)\left(2\left(\frac{V_I}{J} + \alpha - \frac{\mu}{Jz}\right) - \frac{\alpha^2}{2\frac{\mu}{Jz} - 1}\right)}. \tag{5.65}$$

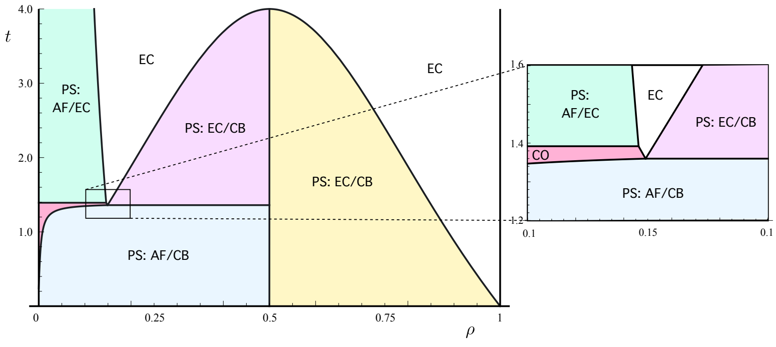

Figure 5.7: The canonical mean-field phase diagram for typical values of $J = 125$ meV, $\alpha = 0.04$ and $V_I = 2$ eV whilst varying t and the exciton density ρ. In the absence of exciton, at $\rho = 0$, we have the pure antiferromagnetic Néel phase (AF). Exactly at half-filling of excitons ($\rho = 1/2$) and small hoping energy $t < 2V_I$ we find the checkerboard phase (CB) where one sublattice is filled with excitons and the other sublattice is filled with singlets. For large values of t we find the singlet exciton condensate (EC), given by the wavefunction $\prod_i \left(\sqrt{\rho}\hat{E}^+_{00,i} + \sqrt{1-\rho}\right)|0\ 0\rangle_i$. The coexistence of antiferromagnetism and superfluidity for small ρ and t is an artifact of the mean field theory. Conform the Monte Carlo results of figure 5.4, for most parts of the phase diagram phase separation (PS) is found. The analytical mean field theory incorrectly predicts coexistence of antiferromagnetism and superfluidity (CO).

Here the subscripts indicate the phases: antiferromagnetic phase (AF), coexistence phase (CO), exciton condensate (EC), exciton Mott insulator (EI), checkerboard phase (CB).

For any nonzero α the **first order transitions** from the antiferromagnetic or coexistence phase towards the checkerboard phase are 'standard' in the sense that at the critical value of μ there are only two mean field states with equal energy. This is also true for the transitions from the antiferromagnet to the exciton condensate except at a single point. At the tricritical point

$$t_c = 2J\sqrt{2V_I/J - 1} \tag{5.66}$$

$$\mu_c = J_\perp - \frac{1}{4}zt + \frac{1}{2}Jz(1-\alpha)\sqrt{2V_I/J + t/J} \tag{5.67}$$

separating the coexistence phase, the antiferromagnetic phase and the exciton condensate, we can set the parameters $\overline{\chi} = 0$, $\Delta_\rho = 0$ and Δ_χ given by the value in the coexistence phase. Now the energy becomes independent of the exciton density $\overline{\rho}$. Similarly, at the critical value of

$$\mu_c = J_\perp + \frac{1}{2}V_I z \pm \frac{1}{4}\sqrt{(2V_I z)^2 - (zt)^2} \tag{5.68}$$

describing the transition between the checkerboard phase to the singlet exciton condensate, we can choose the mean field parameters $\overline{\chi} = 0$, $\Delta_\chi = 0$ and

$$\Delta_\rho = \frac{1}{\sqrt{2}}\sqrt{(1 - 2\rho + 2\rho^2) - \frac{2V_I|1-2\rho|}{\sqrt{4V_I^2 - t^2}}}. \tag{5.69}$$

With these parameters, the energy becomes independent of ρ.

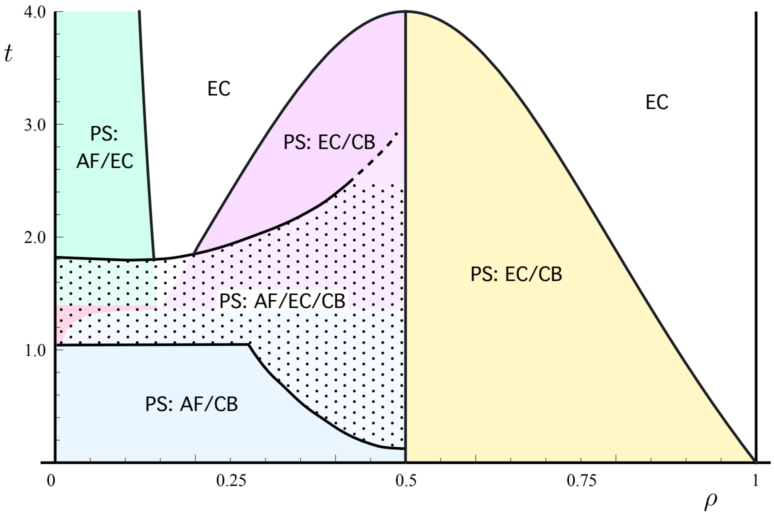

Figure 5.8: The canonical ground state phase diagram of the exciton $t-J$ model, which is a combination of the semi-classical Monte Carlo result and the mean field computations. In the background we have put the mean field phase diagram of figure 5.7, whilst the lines show the phase diagram as obtained from the Monte Carlo simulations. The dotted area represents phase separation between the condensate, antiferromagnetic and checkerboard order. Furthermore: EC means exciton condensate, CB means checkerboard phase, AF means antiferromagnetism and PS stands for phase separation.

This implies that the mean field theory predicts highly degenerate states at the critical values of μ, similar to the one we found in the XXZ model. The phase separation that thus occurs can be between an infinite set of possible ground states that have all a different exciton density. Coincidentally, the numerical simulations indicate that around the two 'degenerate' critical points indeed all the three phases are present. And whilst macroscopic phase separation has probably the lowest energy, the analysis of figure 5.6 suggests that more complicated patterns of phase separation are likely to occur. The degeneracy of the critical points in mean field theory might be responsible for the rich physics in this regions of the phase diagram.

We can **combine the unbiased numerical simulations** of figure 5.4 with the **analytical mean field results** of figure 5.7 to derive the **complete phase diagram of the exciton $t-J$ model** in figure 5.8. There are three main phases: the antiferromagnet at zero exciton density, the checkerboard at $\rho = 1/2$ and the superfluid at high hopping energy t. For most parts of the phase diagram, phase separation between these three phases occurs in any combination possible. The competition between these three phases leads in general to macroscopic phase separation.

Finally, within the limitations of the semi-classical Monte Carlo approach we can make a rough estimate of the **transition temper-**

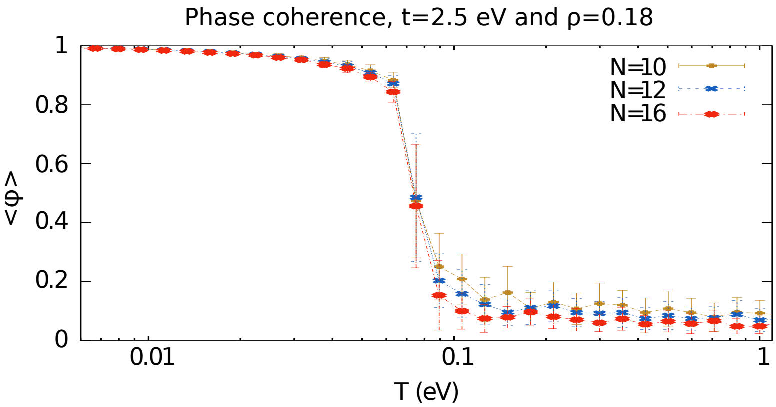

Figure 5.9: Finite temperature graph of the phase coherence in the exciton condensate region of the phase diagram. Here $t = 2.5$ eV and $\rho = 0.18$ and the other parameters are the same as in a. A clear transition is observed at around 0.06 eV, which amounts to a transition temperature of about 700 Kelvin.

ature towards the superfluid state. Given a typical point in the phase diagram where the exciton condensate exists, at $t = 2.5$ eV and $\rho = 0.18$, we find a Kosterlitz-Thouless transition temperature of approximately 700 Kelvin, see figure 5.4c. This number should be taken not too seriously, as the exciton $t - J$ model might not be applicable at such high temperatures given possible exciton dissociation. Additionally, at high temperatures the electron-phonon coupling becomes increasingly important which is something we neglect in our exciton $t - J$ model. Nonetheless, our estimate suggests that exciton superfluidity may extend to quite high finite temperatures.

5.2.4 *The Heisenberg equations of motion method*

In physical experiments one usually probes the **elementary excitations** of a phase. The dispersion of these excitations can be computed using the 'equations of motion'-method based on the work of Zubarev, 1960. The aim of this method is to find the spectrum of excitations, building on the foundations given by the mean field approximation. Let us now introduce this method, and subsequently use it to derive the excitations of the three phases of the exciton $t - J$ model.

Given a full set of local operators $\mathcal{A}_i^\ell$, we can construct the Heisenberg equations of motion

$$i\partial_t \mathcal{A}_i^\ell = [\mathcal{A}_i^\ell, H] \tag{5.70}$$

which is in general impossible to solve. We employ the notation that i indicates the lattice site, and ℓ is the index denoting the type of operator. The right hand side of this equation contains products of operators at different lattice sites. Such **products can be decoupled** within the mean field approximation as [48]

$$\mathcal{A}_i^{\ell}\mathcal{A}_j^{\ell'} \rightarrow \langle \mathcal{A}_i^{\ell} \rangle \mathcal{A}_j^{\ell'} + \mathcal{A}_i^{\ell} \langle \mathcal{A}_j^{\ell'} \rangle \tag{5.71}$$

where i and j are different lattice sites. Upon Fourier transforming lattice position into momentum and time into energy, we thus obtain a set of linear equations for the operators,

$$\omega_q \mathcal{A}^{\ell}(q,\omega) = M^{\ell\ell'}(q)\mathcal{A}^{\ell'}(q,\omega). \tag{5.72}$$

The spectrum of excitations is simply found by solving this eigenvalue equation for the matrix $M(q)$.

In order to find the matrix elements $\langle n|\mathcal{A}^{\ell}(q)|0\rangle$ that enter in susceptibilities we need the following scheme. Assume that the Hamiltonian is of the form

$$H = \sum_{qn} \omega_{qn}\alpha_{qn}^{\dagger}\alpha_{qn} \tag{5.73}$$

where the sum over q runs over momenta, and n indicates the different excited states. Now $\alpha_{qn}^{\dagger}$ is a creation operator, and irrespective of whether we are dealing with fermions or bosons we have the following equations of motion

$$i\partial_t \alpha_{qn}^{\dagger} = -\omega_{qn}\alpha_{qn}^{\dagger}. \tag{5.74}$$

That is: every eigenvector of $M^{\ell\ell'}(q)$ corresponding to a negative eigenvalue can be identified as a creation operator for one of the elementary excitations. However, the eigenvalue equation itself is not enough because it does not yield the proper normalization of $\alpha^{\dagger}$. Since we have the eigenvector solution

$$\alpha_{qn}^{\dagger} = \mathcal{U}^{n\ell}\mathcal{A}^{\ell}(q) \tag{5.75}$$

we can write out the (anti)commutation relation for $\alpha_{qn}^{\dagger}$ in terms of the (anti)commutation relations for the $\mathcal{A}^{\ell}(q)$. Upon requiring that on the mean field level the operators $\alpha_{qn}^{\dagger}$ obey canonical commutation relations, that is for bosons

$$\langle \left[\alpha_{qn}, \alpha_{qn'}^{\dagger}\right] \rangle = \delta_{nn'}, \tag{5.76}$$

[48] Zubarev, 1960; and Oles et al., 2000

we obtain a proper normalization for the new creation operators. We can invert the normalized matrix $\mathcal{U}^{n\ell}$ to express $\mathcal{A}^{\ell}(q)$ in terms of the creation operators $\alpha^{\dagger}_{qn}$. Finally, using $\langle n'|\alpha^{\dagger}_{qn}|0\rangle = \delta_{nn'}$ we can compute the wanted matrix element for $\mathcal{A}^{\ell}(q)$.

As an example of this technique we can compute the matrix element $|\langle n|S^{+}(q)|0\rangle|^2$ for the **antiferromagnetic Heisenberg model** on a square lattice. The mean field ground state is the Néel state, which leads to the following equations of motion,

$$i\partial_t \begin{pmatrix} S^{+}_{qA} \\ S^{+}_{qB} \end{pmatrix} = \frac{1}{2}Jz \begin{pmatrix} 1 & \gamma_q \\ -\gamma_q & -1 \end{pmatrix} \begin{pmatrix} S^{+}_{qA} \\ S^{+}_{qB} \end{pmatrix}. \tag{5.77}$$

where the subscript A and B denote the two different sublattices, and $\gamma_q = \frac{1}{2}(\cos q_x + \cos q_y)$. We quite easily infer that the eigenvalues are

$$\omega_q = \pm\frac{1}{2}Jz\sqrt{1-\gamma_q^2} \tag{5.78}$$

and thus we have one eigenvector corresponding to a creation operator, and one to an annihilation operator. If we define

$$\begin{pmatrix} \alpha^{\dagger} \\ \beta \end{pmatrix} = \mathcal{U} \begin{pmatrix} S^{+}_{qA} \\ S^{+}_{qB} \end{pmatrix} \tag{5.79}$$

then the commutation relations tell us that the eigenvector matrix $\mathcal{U}$ must satisfy

$$1 = \langle[\alpha,\alpha^{\dagger}]\rangle = -2u_{11}^2\langle S^z_A\rangle - 2u_{12}^2\langle S^z_B\rangle = -u_{11}^2 + u_{12}^2. \tag{5.80}$$

The initial S^{+}_q operator, which enters in the spin susceptibility, can be expressed in terms of the eigenvector matrix as

$$\mathcal{S}^{+}_q = \frac{1}{\sqrt{2}}(1\;1)\,\mathcal{U}^{-1} \begin{pmatrix} \alpha^{\dagger} \\ \beta \end{pmatrix}. \tag{5.81}$$

Some straightforward algebra now yields

$$|\langle n|S^{+}(q)|0\rangle|^2 = \frac{1}{2}\sqrt{\frac{1-\gamma_q}{1+\gamma_q}} \tag{5.82}$$

which is the same susceptibility one can obtain by using the Holstein-Primakoff linear spin wave approximation. The approximation scheme we introduced here can therefore be viewed as a *generalization of the linear spin wave approximation*.

Let us now apply this technique to the XXZ **model** of section 5.2.1. The Heisenberg equations of motion are

$$\begin{aligned} i\partial_t E_i^+ &= -t\sum_\delta E_i^z E_{i+\delta}^+ + \mu E_i^+ - V_I \sum_\delta E_i^+ E_{i+\delta}^z, && (5.83)\\ i\partial_t E_i^- &= t\sum_\delta E_i^z E_{i+\delta}^- - \mu E_i^- + V_I \sum_\delta E_i^+ E_{i+\delta}^z, && (5.84)\\ i\partial_t E_i^z &= -\frac{1}{2}t\sum_\delta \left(E_i^+ E_{i+\delta}^- - E_i^- E_{i+\delta}^+\right), && (5.85)\end{aligned}$$

where δ runs over all nearest neighbors. These equations cannot be solved exactly, hence we use an approximation based on the mean field results. Products of operators on different sites are replaced by[49]

$$A_i B_j \to \langle A_i \rangle B_j + A_i \langle B_j \rangle \tag{5.86}$$

where $\langle \ldots \rangle$ denotes the mean field expectation value. By such a decoupling the Heisenberg equations of motion become a coupled set of linear equations which can be solved easily. In the homogeneous phase we thus obtain, after Fourier transforming,

$$\begin{aligned} \omega_k E_k^+ &= -\frac{1}{2}tz\left(\cos 2\theta \gamma_k E_k^+ + \sin 2\theta E_k^z\right) + \mu E_k^+ \\ &\quad -\frac{1}{2}V_I z\left(\cos 2\theta E_k^+ + \sin 2\theta \gamma_k E_k^z\right) && (5.87)\\ \omega_k E_k^- &= \frac{1}{2}tz\left(\cos 2\theta \gamma_k E_k^- + \sin 2\theta E_k^z\right) - \mu E_k^- \\ &\quad +\frac{1}{2}V_I z\left(\cos 2\theta E_k^- + \sin 2\theta \gamma_k E_k^z\right) && (5.88)\\ \omega_k E_k^z &= -\frac{1}{4}tz \sin 2\theta (1-\gamma_k)\left(E_k^+ - E_k^-\right). && (5.89)\end{aligned}$$

We can find an analytical expression for the excitations in the superfluid phase,

$$\begin{aligned} \omega_k &= \frac{1}{2}zt\sqrt{1-\gamma_k}\sqrt{1-\gamma_k(1-2\rho)^2 + \frac{4V_I}{t}\gamma_k(1-\rho)\rho} \\ &= \frac{1}{2}zt\sqrt{\rho(1-\rho)(1+V_I/t)}\;|k| + \ldots && (5.90)\end{aligned}$$

where $\gamma_k = \frac{1}{2}(\cos k_x + \cos k_y)$. For small momenta this excitation has a linear dispersion, conform to the Goldstone theorem requiring a massless excitation as a result of the spontaneously broken $U(1)$ symmetry. Exactly at $\mu = \mu_c$ the dispersion reduces to $\omega_k = zt\sqrt{1-\gamma_k^2}$, hence the gap at $k = (\pi, \pi)$ closes thus signaling a transition towards the checkerboard phase.

---

[49] Zubarev, 1960; and Oles et al., 2000

At the critical point and in the checkerboard phase, we need to take into account the fact that expectation values of operators differ on the two sublattices. The Heisenberg equations of motion now reduce to six (instead of three) linear equations. This is technically more difficult but does not pose a real mathematical challenge.

5.2.5 Collective modes and susceptibilities

Each phase of the excitons in a strongly correlated bilayer has distinct **collective modes**, by which we can experimentally probe the system. In order to obtain the dispersions of the collective modes we employ the technique of the Heisenberg equations of motion, introduced in the previous section 5.2.4. In the case of the exciton $t - J$ model, however, the set of equations is so large that analytical solutions can in general not be obtained. Whenever necessary, we compute the dispersions numerically.

The dispersions itself are not directly experimentally relevant: one measures **dynamical susceptibilities**. Amongst others, we are interested in the absorptive part of the dynamical magnetic susceptibility, defined by

$$\chi''_S(q, \omega) = \sum_n \langle \psi_0 | \widetilde{S}^-(-q) | n \rangle \langle n | \widetilde{S}^+(q) | \psi_0 \rangle \delta(E_n - \omega) \qquad (5.91)$$

Here $|\psi_0\rangle$ is the ground state of the system and $|n\rangle$ are the excited states with energy E_n. This spin susceptibility can be measured with, for example, inelastic neutron scattering.[50] Naturally we can thus define an exciton dynamical susceptibility

$$\chi''_E(q, \omega) = \sum_n \langle \psi_0 | E^-_{00}(-q) | n \rangle \langle n | E^+_{00}(q) | \psi_0 \rangle \delta(E_n - \omega). \qquad (5.92)$$

We use the operator $E_{00}(q)$ because this amounts to the interlayer dipole matrix element, which is detectable using RIXS,[51] EELS[52] or optical absorption (the latter only for $q = 0$).[53]

The **three dominant phases** we encountered in our mean field analysis will have distinct magnetic and optical responses. Starting with the antiferromagnetic phase shown in figures 5.10 to 5.12, we observe that this limit of vanishing exciton density has been studied in a far greater detail in section 4.2. This allows us to compare the results of the equations-of-motion method with a full resummation of spin-exciton interactions using the SCBA. In the

[50] Coleman, 2013

[51] Ament et al., 2011

[52] Schnatterly, 1979

[53] Basov and Timusk, 2005

condensate phase the interplay between excitonic and magnetic degrees of freedom reaches it climax, which was discussed in section 5.1. Here we discuss some remaining details and the checkerboard phase.

Throughout the following discussion, the model parameters are $J = 125$ meV, $\alpha = 0.04$, $V_I = 2$ eV and a varying t and ρ. In order to visualize the susceptibilities we have convoluted χ'' with a Lorentzian of width 0.04 eV. The color scale in the susceptibility plots is on an arbitrary scale.

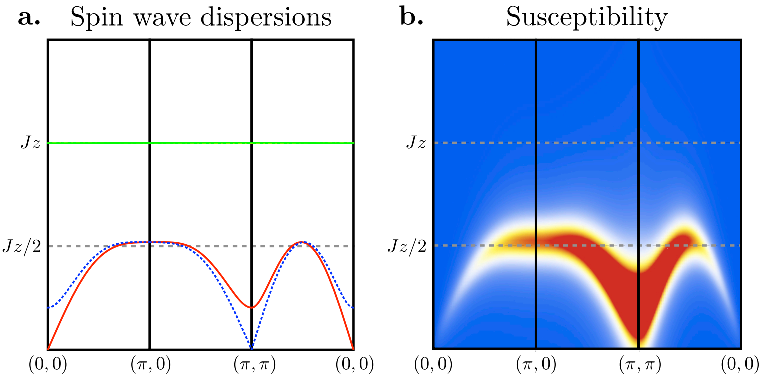

Figure 5.10: The spin wave dispersions (**a.**) and the dynamical magnetic susceptibility (**b.**) in the antiferromagnetic phase. In this phase, the spin wave dispersions are not influenced by exciton dynamics. As is known from previous studies, there are two transversal spin waves and two longitudinal spin waves (Chubukov and Morr, 1995; Rademaker et al., 2012b). The transversal spin waves are gapless around either Γ (solid red line) or the M point (dotted blue line). The longitudinal spin waves, which are associated with interlayer fluctuations (solid green line), are nearly flat and have a gap of order Jz. The dynamic magnetic susceptibility (**b.**) only shows one transversal spin wave. These results and all subsequent figures are obtained using $J = 125$ meV and $\alpha = 0.04$, as is expected for the undoped bilayer cuprate YBCO (Tranquada et al., 1989).

ANTIFERROMAGNETIC PHASE: A SINGLE EXCITON In the limit of zero exciton density we recover the well-known **bilayer Heisenberg** physics. As discussed in section 4.2.1, the spins tend to order antiferromagnetically. The excitations spectrum thus contains a Goldstone spin wave with linear dispersion around Γ and a similar mode centered around (π, π). In addition, the bilayer nature is reflected in the presence of two longitudinal spin waves with a gap of order Jz and a narrow bandwidth of order $J_\perp$. The excitation spectrum and the corresponding magnetic dynamical susceptibility is shown in figure 5.10.

The dynamics of an exciton in an antiferromagnetic background has been studied extensively by means of a linear spin-wave self-consistent Born approximation technique (**LSW-SCBA**) in section 4.2.2. The non-interacting equations of motion method used in this section is certainly less accurate than the full LSW-SCBA computation. However, the mere existence of LSW-SCBA results allows us to compare it with our current non-interacting

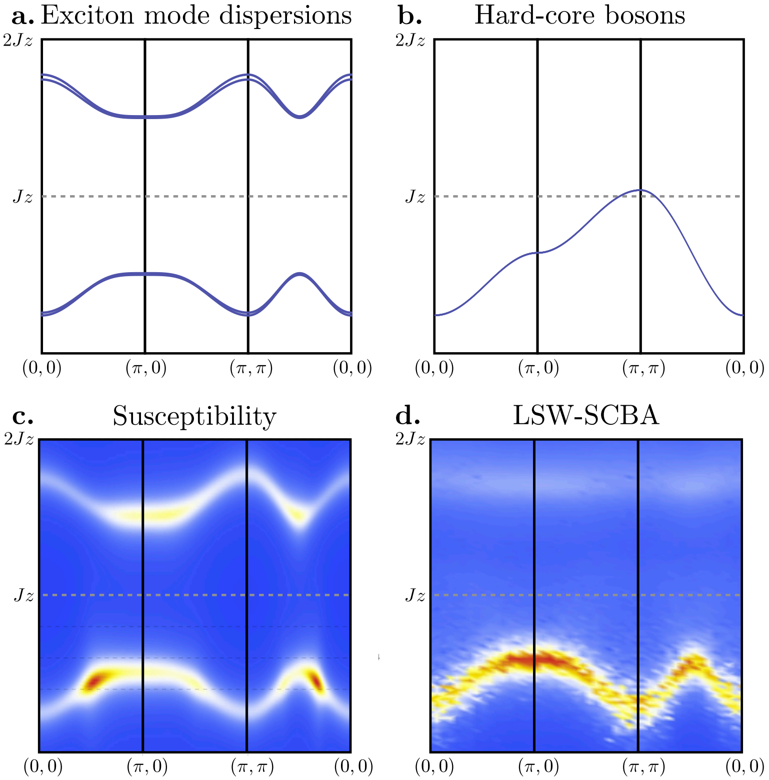

Figure 5.11: The exciton modes in the antiferromagnetic phase in the adiabatic regime $t \ll J$. Here we have chosen $t = 0.1$ eV, $J = 125$ meV and $\alpha = 0.04$. Within the equations of motion picture there are four exciton modes (**a.**), which come in pairs of two with a small interlayer splitting. Due to the antiferromagnetic order the exciton bands are renormalized with respect to a free hard-core boson (**b.**). The susceptibility corresponding to the free exciton motion (**c.**) is verified by the fully interacting LSW-SCBA results (**d.**). This is to be expected: in the adiabatic regime spins react much faster than the exciton motion and the exciton still moves freely dressed by a spin polaron, reducing its bandwidth to order t^2/J.

calculations.

The equations-of-motion method **ignores the interaction** corrections such as dynamical frustration. It treats the excitons as well-defined quasiparticles. As such we can already guess beforehand that the non-interacting results will only be reliable in the adiabatic regime $t \ll J$. Indeed, in the equations-of-motion method we find four exciton modes corresponding to either the singlet E^+_{00} or $m = 0$ triplet exciton E^+_{10} operator, just as in the LSW-SCBA. When $\alpha \to 0$ we can write out an analytical expression for the non-interacting dispersions,

$$\omega_{k,\pm} = \mu \pm \frac{1}{2}\sqrt{(Jz)^2 + \left(\frac{1}{2}zt\gamma_k\right)^2}. \tag{5.93}$$

where each branch is twofold degenerate. This degeneracy is lifted when $\alpha \neq 0$, leading to a splitting of order α which is largest around Γ and M.

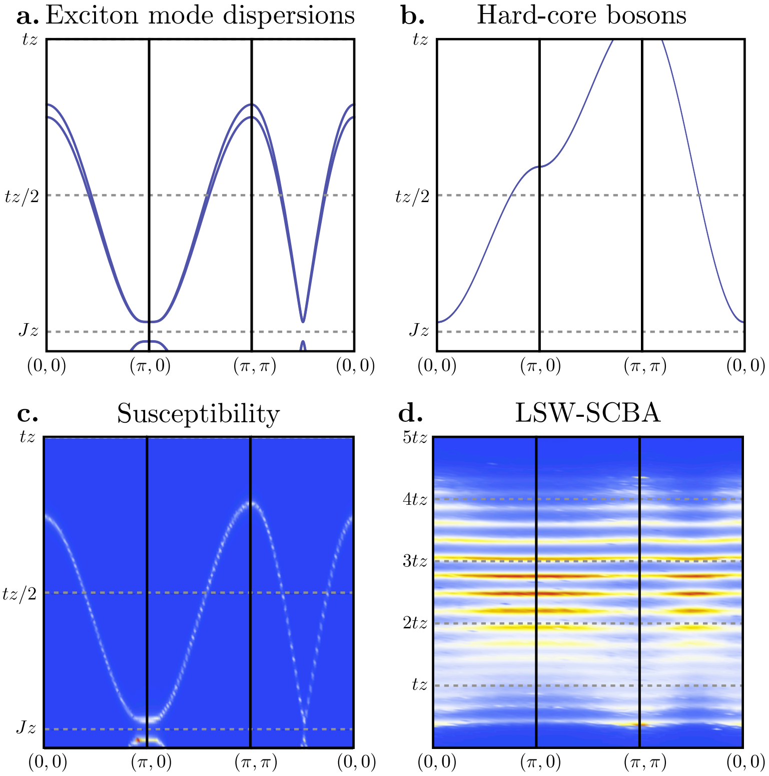

Figure 5.12: The exciton modes in the antiferromagnetic phase in the anti-adiabatic regime $t \gg J$. Here we have chosen $t = 2$ eV, $J = 125$ meV and $\alpha = 0.04$. Just like in figure 5.11 we find four exciton bands (**a.**), renormalized with respect to the free hard-core boson results (**b.**). However, upon inclusion of the interaction the free susceptibility (**c.**) gets extremely renormalized (**d.**). The large exciton kinetic energy together with the relatively spin dynamics create an effective potential for the exciton: the exciton becomes localized and the confinement generates a ladder spectrum. Note that thus in the anti-adiabatic regime the free results (**a.**, **c.**) cannot be trusted.

In the limit of $t \ll J$ the dispersions (5.93) indeed result in an effective exciton bandwidth of order t^2/J, conform the LSW-SCBA as can be seen in figure 5.11. The natural question then arises: how is it possible that in the present non-interacting theory the exciton bandwidth depends on the spin parameter J? For sure, the effective exciton model introduced in section 5.2.1 has no such renormalisation as is shown in figure 5.11. There the exciton bandwidth fully depends on zt.

However, it is important to realize that the exciton operators $E^{+}_{s0,i}$ do not commute with the antiferromagnetic order parameter operator $\widetilde{S}^z_i$. As a result the mean field energy of exciting an exciton is shifted either up or down (depending on the sublattice) yielding a gap between the two exciton branches of $\mathcal{O}(Jz)$. Now for small t, propagation of the exciton requires that one has to 'pay' the energy shift Jz to move through both sublattices. As a result the effective hopping is reduced by a factor t/J. Therefore the

exciton bandwidth renormalisation, seen in the full LSW-SCBA, is already present at the mean field level.

For large t/J, however, we will pay a price for the convenience of the non-interacting equations of motion method. At mean field level one still expects the dispersions to be (5.93), however, upon inclusion of the interaction corrections this picture breaks down completely. The bandwidth of the non-interacting exciton is of order zt, whereas in the interacting theory an incoherent ladder spectrum of the same width arises. Thus for large t/J the non-interacting results cannot be trusted. However, this only applies to the antiferromagnetic phase due to the presence of dynamical frustration. In general one can say that the non-interacting results are qualitatively correct in the absence of gapless modes that need to be excited in order for an exciton to move. This condition is naturally met for the other two phases, and hence we expect that exciton-spin interactions only lead to qualitative changes in the antiferromagnetic phase.

By simple selection rules one can already conclude that the singlet exciton mode couples to light. As a consequence this is the mode that is visible in the **susceptibility**, as seen in figures 5.11d (for $t < J$) and 5.12d (for $t > J$).

Finally, note that at the transition from the antiferromagnetic phase to the checkerboard phase the gap in the exciton spectrum vanishes at (π, π).

SUPERFLUID PHASE The mode spectrum of superfluid phase, shown in figures 5.13 and 5.14, is characterized by a **linearly dispersing Goldstone mode** associated with the broken $U(1)$ symmetry. This superfluid phase mode has vanishing energy at the Γ point, where we find the inescapable linear dispersion relation

$$\omega_k = \frac{1}{4\sqrt{2}} zt \sqrt{(1-\rho)\rho \, (1 + 2V_I/t)} \, |k| + \dots \tag{5.94}$$

The speed of the superfluid phase mode is the same as for the XXZ model in equation (5.90) up to a rescaling of the t and V_I parameters. Indeed, this speed is proportional to the superfluid density $\sqrt{\rho_{\text{SF}}} = \sqrt{\rho(1-\rho)}$. This mode can be seen in the exciton susceptibility, figures 5.13e and f. The Goldstone mode has a gap at (π, π) which decreases monotonically with increasing exciton density. Precisely at the first order transition towards the checkerboard phase this gap closes.

Next to the Goldstone mode there are two triplet excitations, shown in figure 5.14, each one three-fold degenerate. The degeneracy obviously arises from the standard triplet degeneracy $m = -1, 0, +1$. The two branches, however, distinguish between **exciton-dominated** modes and **spin-dominated** modes, let us discuss them separately.

The spin-dominated modes have a gap of order $\Delta_S = Jz \sqrt{\alpha(1+\alpha-\rho)}$, which is similar to the triplet gap in the bilayer Heisenberg model for large α. However, the bandwidth of these excitations scales with t rather than with J, as would be customary in a system without exciton condensation (see figures 5.14a and b). We discussed these modes in great detail in section 5.1, so let us continue onto the other branch of triplets.

The other branch of triplet excitations is dominated by **triplet excitons**, and is therefore barely visible in the spin susceptibility and not visible in the exciton susceptibility (which only shows singlet excitons). That it is indeed dominated by triplet excitons can be inferred from computing the matrix elements of the operator E_{1m}, as is done in figures 5.14g and h. Furthermore, the gap $\Delta_E = (V_I z + tz)\rho - \mu$ is a function of exciton model parameters only. The bandwidth of this mode is of order $\mathcal{O}(zt)$, relatively independent of the exciton density. As a result, for large superfluid densities the exciton-dominated modes cross the spin-dominated triplet modes. One can directly see this in the excitation spectrum for $\rho = 0.27$ as shown in figure 5.14d.

We can compare the triplet spectrum to the mode spectrum of the singlet phase of the bilayer Heisenberg model. When $J_\perp \gg J$ the ground state consists of only rung singlets. The excitation towards a triplet state, shown in figures 5.14a and b, has a gap $Jz\sqrt{\alpha(\alpha-1)}$ and a bandwidth of order Jz, which is considerably smaller than the $\mathcal{O}(zt)$ bandwidth in the condensate. However, because the topology of the triplet mode is the same we expect that the effect of the spin-exciton interactions is the same in the bilayer Heisenberg model as for the superfluid. Since earlier LSW-SCBA showed no changes in the spectrum due to interactions, we infer that the non-interacting results for the superfluid are reliable.

To conclude our review of the excitations of the superfluid phase we want to discuss the influence of the **interlayer tunneling**. In the context of the XXZ model we noticed that interlayer

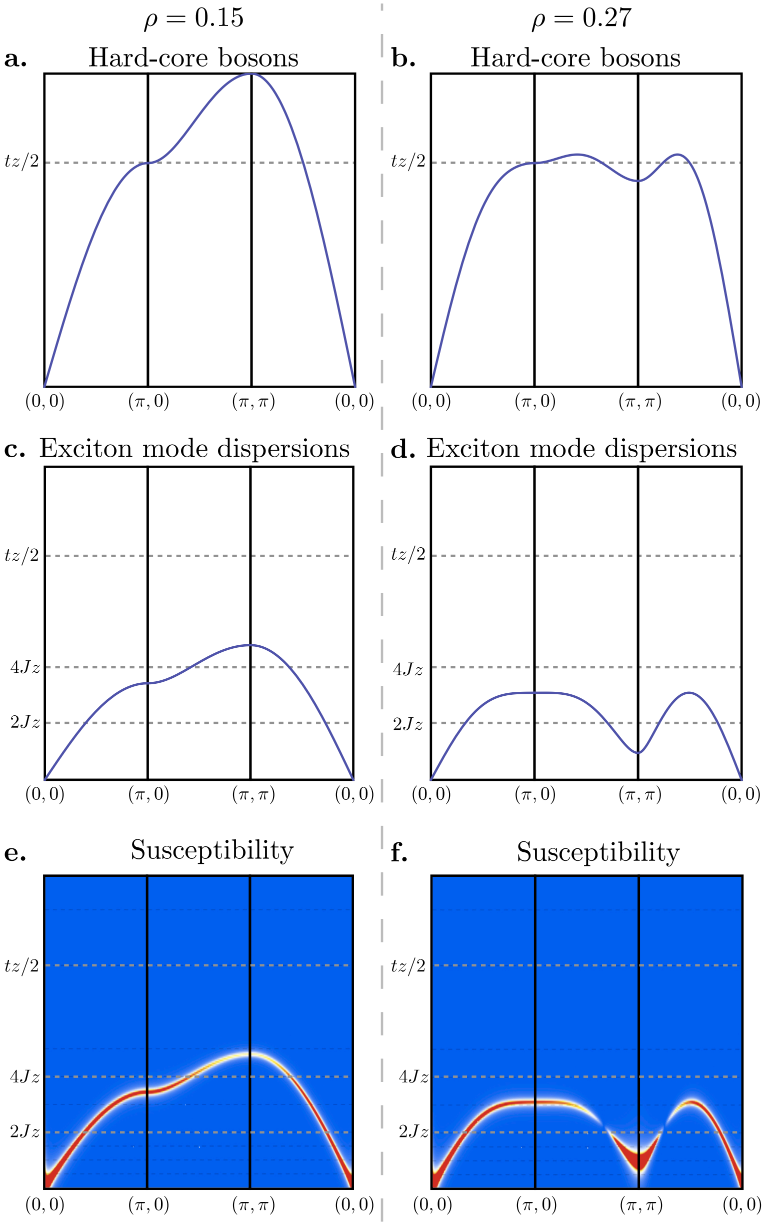

Figure 5.13: Dispersions and susceptibility of the Goldstone mode associated with the exciton condensate. We have set $t = V_I = 2$ eV, $J = 125$ meV and $\alpha = 0.04$, and the exciton density is either $\rho = 0.15$ (left column) or $\rho = 0.27$ (right column). **a, b.** In the simple hard-core boson model the condensate phase clearly show the superfluid phase mode, linear at small momenta. **c,d.** In the full $t - J$ model the Goldstone mode has a similar dispersion as in the XXZ model. The speed of the mode scales with the superfluid density. At higher densities the mode softens around (π, π), and when this gap closes a first order transition to the checkerboard phase sets in. **e,f.** The absorptive part of the exciton susceptibility, which can be measured with for example EELS or RIXS.

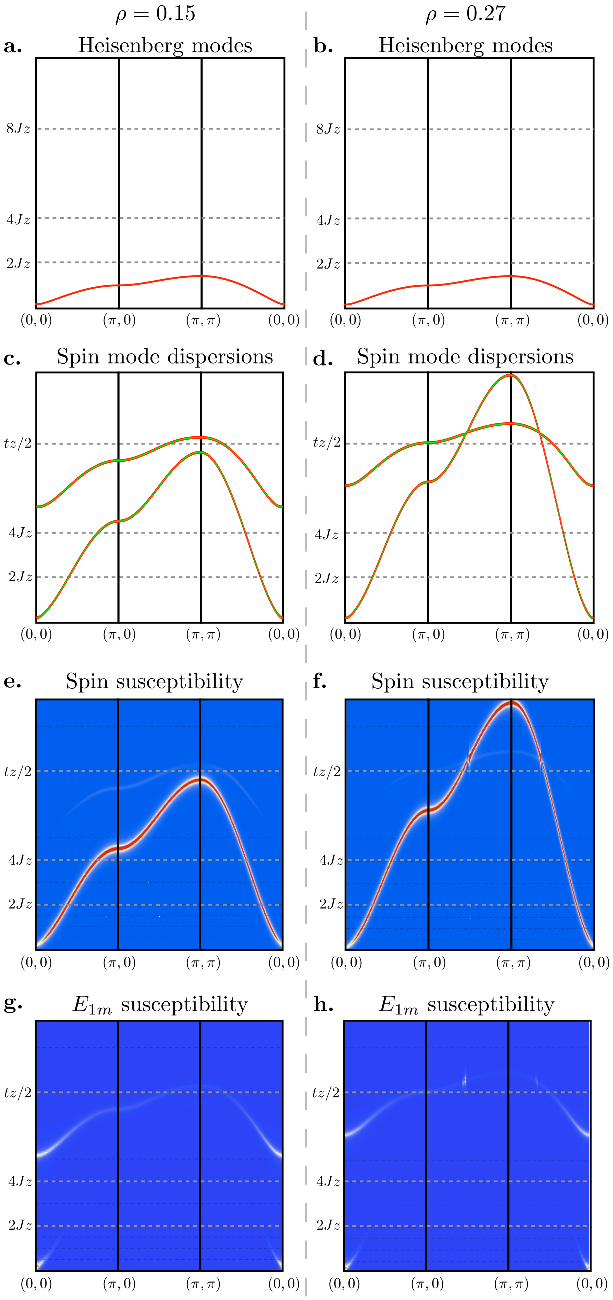

Figure 5.14: Dispersions and magnetic susceptibilities of the exciton condensate. We have set $t = V_I = 2$ eV, $J = 125$ meV and $\alpha = 0.04$, and the exciton density is either $\rho = 0.15$ (left column) or $\rho = 0.27$ (right column). **a,b.** As the exciton condensate is spin singlet, we assume that the excitation spectrum is governed by propagating triplet modes. These modes have a gap of order $J_\perp$ and a bandwidth of order Jz. **c,d.** In contrast to the simple Heisenberg results, the actual triplet modes have enhanced kinetics, see section 5.1. The modes are split in a spin-dominated branch with small gap and large bandwidth proportional to the superfluid density (**e,f.**); and an exciton-dominated branch with a large gap and a small bandwidth (**g,h.**).

tunneling has no qualitative influence on the phase diagram itself. However, the presence of a weak interlayer tunneling may act as phase pinning[54] which opens a gap in the superfluid phase mode spectrum of order $\mathcal{O}(\sqrt{t_\perp(V_I+t)})$. Persistent currents can still exist, but one needs to overcome this gap in order to get the exciton supercurrent flowing.

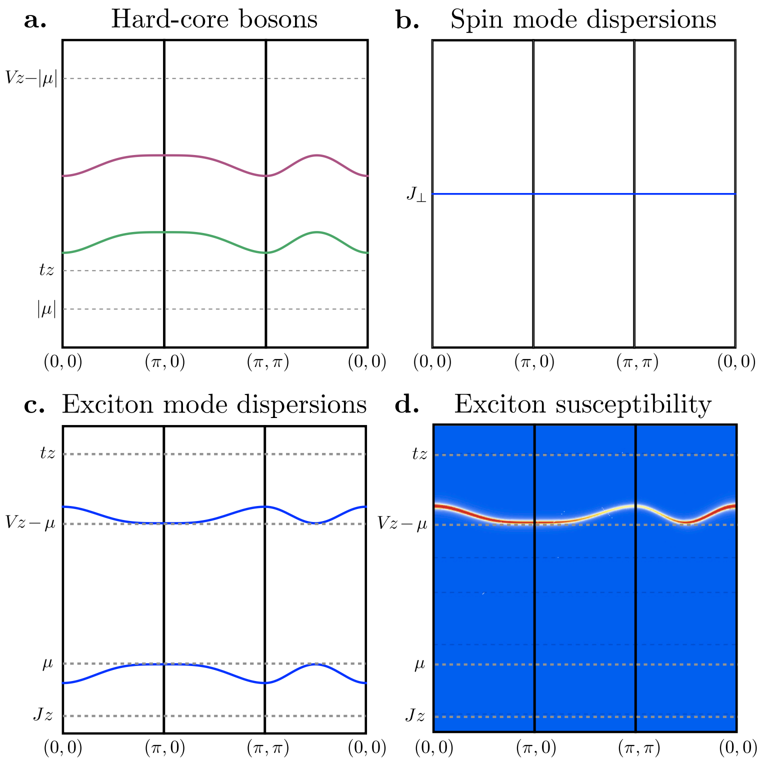

Figure 5.15: The excitation spectrum of the checkerboard phase. **a.** In the simple hard-core boson model there are two exciton modes associated with the 'doublon' and the 'holon' excitation. **b.** The spin modes are decoupled from the exciton modes in the full $t-J$ model. There is only one possible spin excitation: changing the singlet groundstate into a non-propagating triplet. **c.** The exciton modes, on the other hand, can still propagate. The excitation of removing an exciton can propagate through the checkerboard. **d.** The propagating mode that changes an exciton into a singlet is detectable by optical means and thus shows up in the exciton susceptibility.

Checkerboard phase The third homogeneous phase of the exciton $t-J$ model is the checkerboard phase. In this phase the unit cell is effectively doubled with one exciton per unit cell. This state is analogous to a **Bose Mott insulator**. The trivial excitations are then the doublon and the holon: create two bosons per unit cell which costs an energy $V_I z-\mu$ or to remove the boson. The latter will generate a propagating exciton mode, with dispersion

$$\omega_{k,pm} = \frac{1}{2}\left(\pm V_I z + \sqrt{(V_I z)^2 \pm \left(\frac{1}{2} z t \gamma_k\right)^2}\right) \mp \mu \pm J_\perp. \tag{5.95}$$

---

[54] See section 2.2.2 and Rademaker et al., 2011.

There are two such propagating modes: one associated with the **singlet exciton** and one with the triplet exciton. Precisely at the transition towards the superfluid phase, one of these exciton waves becomes gapless. Note that the arguments that lead to the bandwidth renormalisation in the antiferromagnetic phase also apply here, leading to an exciton bandwidth of order t^2/V_I. The dispersions and the corresponding exciton susceptibility can be seen in figure 5.15.

In the spin sector one can excite a **localized spin triplet** on the empty sublattice. The triplet gap is set by the interlayer energy $J_\perp$, and the dispersion is flat because this triplet cannot propagate, as can be seen in figure 5.15b.

6

Influence of long-range interactions

The dipolar interaction between bilayer excitons is long-ranged. Previously in this thesis, we neglected this fact and instead only considered the nearest neighbor repulsion. However, many complicated ordered phases other than just the checkerboard phase may appear if one correctly incorporates the long-range nature of the interactions. As a first step, we investigate which ordered structures will arise for classical particles on a lattice.

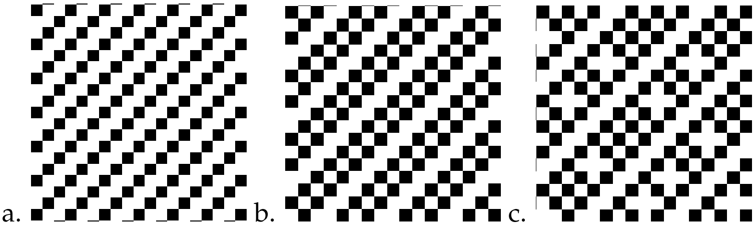

Figure 6.1: Some examples of stripe phases, which arise from long-ranged interactions on a square lattice. **a.** The $\rho = 1/3$ state. **b.** The $\rho = 2/5$ state. **c.** The $\rho = 3/7$ state, but now doped.

6.1 Complex ordering phenomena

This chapter is based on Rademaker et al., 2013d.

The **formation of ordered structures** is one of the main topics in the field of condensed matter physics. Starting from the relative straightforward crystalline order a wide variety of increasingly complex ordering phenomena has been observed and proposed such as stripes[1], charge density waves[2], incommensurate phases[3] and so forth.

These complex ordering patterns usually arise as a result of **competing interactions**. For example, the kinetic energy of holes competes with the tendency towards antiferromagnetic order in cuprates thus forming stripes. In ANNNI models, the next-nearest

[1] Zaanen and Gunnarsson, 1989; Tranquada et al., 1995; Tranquada et al., 1994; Cheong and Hwang, 2000; Salamon and Jaime, 2001; Dagotto, 2005; Boothroyd et al., 2011; and Andrade and Vojta, 2012

[2] Grüner, 1988

[3] Bak, 1982

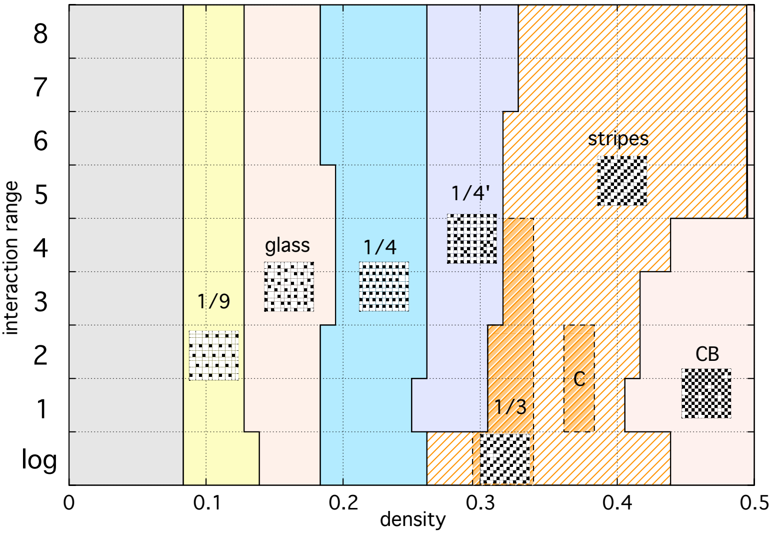

Figure 6.2: The approximate ground state phase diagram of the long-range lattice gas model on a square lattice, based on variational methods as discussed in section 6.2.3. On the vertical axis the type p of the long-range interaction $V(r) = \frac{1}{r^p}$ is given, together with a logarithmic decaying interaction. The horizontal axis represents the particle density. From low to high densities we identify the following phases: The grey area without name depicts the dilute generalized Wigner crystal, followed by the $1/9$ Wigner crystal, the $1/6$ glassy phase described by Lee et al., 2002, the $1/4$ Wigner crystal, the 'checkerboard-in-a-checkerboard' $1/4'$ phase, stripe phases (with a plateau for the $1/3$ stripe phase and 'C' denotes the channelled stripes as described by Lee et al., 2001) and finally the checkerboard phase. Phases below $1/4$ filling are discussed in section 6.2.1, above $1/4$ filling are discussed in section 6.2.2.

neighbor Ising coupling has the opposite sign as the nearest neighbor coupling. The question immediately arises whether higher-order commensurate or incommensurate phases can appear in systems with only one type of interaction.

Of course this is the case. In the continuum the sole presence of long-range interactions will cause particles to form a Wigner crystal. When a fixed number of particles are placed on an underlying lattice the desired Wigner crystalline order may be incommensurate with the lattice, thus leading to frustration.

For the exciton system discussed in this thesis we previously neglected the long-range $1/r^3$ nature of the dipolar interactions. The only charge ordering pattern that arises from the nearest-neighbor repulsion only is the **checkerboard phase**. Because most parts of the phase diagram exhibit phase separation, see figure 5.8, the influence of long-range interactions may topple the delicate energy balance favoring specific exciton-ordered phases. Just like we investigated the competition between the superfluid and checkerboard phase using the simpler XXZ model,[4] here we explore the possible different ordering phases with the classical lattice gas model.

We have thus investigated the **influence of long-range interactions on charge ordering phenomena on a square lattice**. Expanding the results of Lee et al., 2001, 2002 we explored the full

[4] See section 5.2.1.

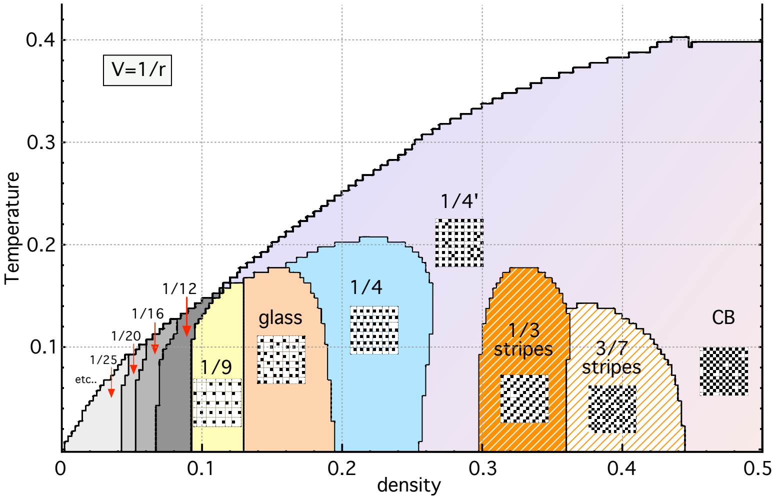

Figure 6.3: Mean field finite temperature phase diagram of the lattice gas model (6.1) on a square lattice with $V \sim 1/r$ interactions, see section 6.2.4. Temperature is in units of the nearest neighbor interaction. The phases are the same as in the zero-temperature phase diagram of Figure 6.2. At low densities we find various Wigner crystalline phases (see section 6.2.1) with densities of the form $1/pq$ with p, q integers. Close to half-filling we find checkerboard order which has a smooth crossover to the 'checkerboard-in-a-checkerboard' $1/4'$ phase. Around $\overline{n} = 1/3$ and $3/7$ there are stripe ordered phases (see section 6.2.2). The transitions towards the $1/4'$ and checkerboard phase are second order, the other transitions are first order.

range of particle densities $0 \leq \rho \leq 1$ and types of long-range interactions $V = 1/r^p$. Our main result is summarized in Figures 6.2 (zero temperature) and 6.3 (finite temperature), where we depict phase diagrams of unusual charge ordered patterns. At low densities the competition between the continuum triangular Wigner lattice and the underlying square lattice indeed leads to a plethora of 'generalised Wigner' crystals. At higher densities, this leas to variations of the checkerboard pattern which is well-known at half-filling. Stripe phases appear as they are rooted in the topological defects of the checkerboard order.

However, we do not claim that the phase diagrams we derived are the exact phase diagrams. As is often the case for frustrated systems, a large set of metastable states persists down to zero temperature. Unbiased numerical computation of the energy for a large ensemble of configurations gives us a strong indication that indeed the phase diagram of Figure 6.2 is correct, however, these indeed be metastable states incorrectly recognized as ground states.

The lay-out of this chapter is as follows. In section 6.1.1 we introduce the lattice gas model, which is the model describing interacting classical particles on a lattice. In the two subsequent sections we discuss qualitatively the ordered structures at low densities (section 6.2.1) and at densities close to half-filling (section

6.2.2). We have performed a Monte Carlo simulation in section 6.2.3 to derive the zero temperature phase diagram of Figure 6.2. In section 6.2.4 we extend these results to finite temperatures using mean field theory, see Figure 6.3.

6.1.1 Long-range lattice gas models

The **lattice gas model** can be defined on any kind of lattice but we focus only on the square lattice. On each of the N lattice sites there can be a particle or not, denoted by $n_i = 1$ or 0 respectively. These particles interact via some general potential V_{ij}. The corresponding Hamiltonian is then

$$H_L = \sum_{i \neq j} V_{ij}(n_i - \rho)(n_j - \rho) - \mu \sum_i n_i. \tag{6.1}$$

We subtract the average particle density ρ to prevent divergent energies. In the grand-canonical ensemble, the chemical potential μ tunes the average particle density $\rho N = \sum_i n_i$. The model (6.1) is in fact **equivalent to the Ising model**[5]. Under the replacement $\sigma_i^z = 2n_i - 1$ and considering only a nonzero nearest neighbor interaction $\frac{1}{4}V_{\langle ij \rangle} = J$ one finds

$$H_I = J \sum_{\langle ij \rangle} \sigma_i^z \sigma_j^z - B \sum_i \sigma_i^z. \tag{6.2}$$

The chemical potential maps onto an external magnetic field $B = \frac{1}{2}\mu - V_{\langle ij \rangle}$, while the particle density maps onto the mean magnetization.

For the ferromagnetic Ising model the ground state is completely magnetically ordered, which amounts to either a full or empty lattice in the lattice gas parlance. In addition, a model with antiferromagnetic coupling will be half-filled with particles if the external magnetic field is small, $|B| < 2J$. Therefore, using the standard grand canonical ensemble will in general not enable us to investigate all possible particle densities: a **canonical ensemble** - fixed particle number - is required.

We argue that most physical realizations of lattice gas models are in fact at a **fixed particle number**, and not at fixed chemical potential. One particular example is the oxygen ordering in YBCO planes, where it is beyond doubt that the number of oxygen ions in the lattice is fixed.[6] The patterns in which the oxygen ions

[5] Lee and Yang, 1952

[6] Fontaine et al., 1990

align themselves are quasi-one-dimensional, in a manner similar to the expected electronic ordering in TTF-TCNQ salts.[7] Whilst studying the latter, Hubbard has developed a general solution for the ground state of a lattice gas model with long-range interactions at any particle density in one dimension. Hubbard's solution only requires the interaction energy as a function of distance to be convex.

The **bilayer exciton system**, as discussed in section 5.2, is also a prime example of a material with fixed particle number. Other two-dimensional realizations of lattice gas models are for example the ordering of ad-atoms on a surface[8], XY systems[9], higher order commensurate magnetic phases[10] or stripe order in high-temperature superconductors.[11] Especially systems with anisotropic short-ranged interactions or competing short- and long-range interactions[12] have acquired considerable attention over the years, therefore we wish to focus here to the case of long-range isotropic interactions.[13]

Most studies of lattice gas models in two dimensions however restrict their attention to **half-filled, empty and full lattices**, due to the aforementioned grand-canonical reasons. There are two notable exceptions: the stripe order discussed in Lee et al., 2001 between 1/3 and 1/2 filling and the glassy dynamics at 1/6 filling.[14] These results were obtained for a 'quasi-logarithmic' repulsive interaction which is a solution of Poisson's equation on a lattice, $\nabla^2 V_{ij} = -2\pi\delta_{ij}$. Given the nontrivial ordering patterns discovered there, as a follow-up we present here a systematic study of the ground state orderings at all densities between 0 and 1/2, for **general repulsive interactions**

$$V_{ij} = \frac{1}{|r_{ij}|^p} > 0. \tag{6.3}$$

6.2 *Generalized Wigner crystals, domain walls and stripes*

In the following two subsections we will first discuss qualitatively such long-range lattice gas models at fixed densities, while in the remaining subsections the picture will be further quantified using numerical simulations and mean field theory.

[7] Hubbard, 1978

[8] Pokrovsky and Uimin, 1978; Bak, 1982; and Feng et al., 2011

[9] Villain, 1977

[10] Fisher and Selke, 1980; Bak, 1982; and Selke, 1988

[11] Löw et al., 1994; Emery and Kivelson, 1993; and Zhang and Henley, 2003

[12] Giuliani et al., 2011; and Giuliani et al., 2013

[13] Lee and Teitel, 1992; Möbius and Rössler, 2009; Tröster, 2010; and Pramudya et al., 2012

[14] Lee et al., 2002

6.2.1 *Dilute densities - Generalized Wigner crystals*

In the previous section we introduced the lattice gas model, that we will now study at fixed densities on the square lattice with long-range repulsive interaction of the form (6.3). In the **limit of very low particle density**, the underlying square lattice becomes irrelevant compared to the average inter-particle distance,

$$\ell_p \gg a \tag{6.4}$$

where a is the lattice constant. In the continuum description of particles repelled by a long-range force, Wigner, 1934 showed that the interaction energy is minimized when the particles form a crystalline structure, which is triangular in two dimensions[15]. In general, one can state that the energy of a **Wigner crystalline state** of the particles is[16]

$$E = JN\rho \sum_{\text{crystal}} \frac{1}{|d|^p} \tag{6.5}$$

where N is the number of lattice sites of the underlying lattice, ρ is the particle density and the summation runs over the particles in the Wigner crystal. The distance between particles in the Wigner crystal ℓ_p scales with the inverse square root of the density. Therefore the energy in the low density limit scales as

$$E \propto JN\rho^{p/2+1}. \tag{6.6}$$

The presence of the underlying lattice is now a source of frustration. Pokrovsky and Uimin, 1978, consider an underlying triangular lattice, leading to frustration only if the density is not of the form $1/p^2$. For example, when $\rho = 1/9$ a perfect triangular Wigner crystal can be formed. On top of a square lattice, however, it is not possible to form a triangular Wigner crystal because $\sqrt{3}$ is irrational. One can nevertheless construct 'almost perfect' triangular crystals. As an example, consider the density $\rho = 1/9$, see figure 6.4. The lowest energy state is there also a triangular crystal of particles, but not equilateral as for a perfect Wigner crystal. In principle such **'almost perfect' Wigner crystals** could exist at densities

$$\rho_{pq} = \frac{1}{pq} \tag{6.7}$$

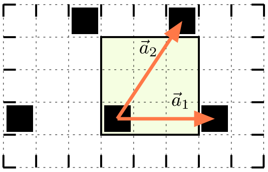

Figure 6.4: At density $\rho = 1/9$ a triangular crystal of particles is formed, which is not equilateral as would be the case for a perfect Wigner crystal. It is thus a prime example of a generalized Wigner crystal. The unit cell and unit vectors of the Wigner crystal are shown.

---

[15] Wigner, 1934 considered quantum particles in second order perturbation theory with $1/r$ interactions, and in that sense Wigner crystallization is not rigorously proven. However, for classical particles the exact energy is equal to the second order perturbation result since that amounts to the expectation value of the interaction energy. For logarithmic interactions we refer to studies of vortex lattices that indicate that triangular lattices are in that case the lowest energy configurations (Kleiner et al., 1964). For $p > 1$ interactions we compared the energy of the triangular lattice with the square lattice, which again favors the triangular lattice.

[16] Pokrovsky and Uimin, 1978

with p, q integers while $p \leq q$, such that the following equilateral triangle relation is approximated by

$$p \sim \frac{1}{2}\sqrt{3}q. \tag{6.8}$$

For example, the densities $\rho = 1/9, 1/12, 1/16$ etcetera would allow such 'almost perfect' triangular crystal. Following the work of Hubbard[17] in one dimensional systems, we will call these particle orderings **'generalized Wigner crystals'**. From this qualitative reasoning we argue that such Wigner crystals *might exist*. Note, however, that one has to resort to a numerical computation to find whether such crystals have indeed the lowest energy at a given density.

[17] Hubbard, 1978

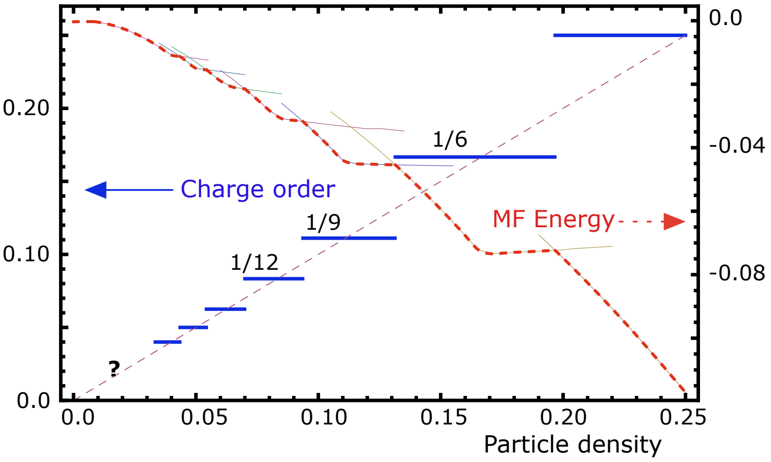

Figure 6.5: A generalized Wigner crystal can be classified according to peaks in the Fourier transformed particle density. For densities close to each specific crystal density (6.7) the associated crystal structure will be maintained. We put forward the hypothesis that this leads to a devil's staircase of generalized Wigner crystals at low densities. The figure shows the crystal structure versus density obtained by mean field theory (see section 6.2.4) at $\beta \rightarrow \infty$, displaying a staircase. The thermodynamic potential (6.16) relative to the disordered state is shown (red dashed line), the thin lines indicate the energy of specific ordered states.

So far we only considered densities of the form $\rho_{pq} = 1/pq$. When the density of a lattice gas is in between such densities, we suspect that it is favorable to maintain a generalized Wigner crystal structure. The deviation from the ρ_{pq} density can be accommodated by a superlattices of crystal defects or interstitial vacancies. If such a superlattice of defects forms, still the original ρ_{pq} order is visible in for example the Fourier transformed particle density, where each crystal type has its own specific Fourier peaks. We expect therefore a 'plateau' at densities in the vicinity of each specific ρ_{pq}, where the associated crystal structure remains intact modulo the interstitial superlattice. As we will describe in more detail later when discussing the numerical results, indeed a 'plateau' is observed for the 1/4, 1/6 and 1/9 states. Using mean field theory, we went as far as the 1/25 crystal phase, as is shown in figure 6.5. We have therefore strong indications the plateau-structure exists all the way to $\rho \to 0$, yielding an infinite staircase of plateaux. This structure is reminiscent of the **devil's staircase**, as exists in the case of the one-dimensional lattice gas in the grand-canonical ensemble[18], where specific charge orderings are stable for a finite window of chemical potential.

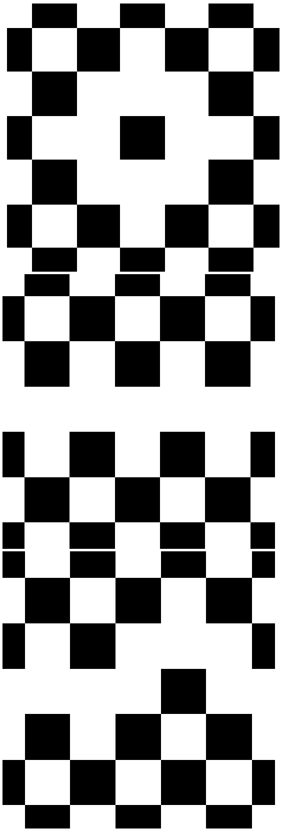

Figure 6.6: Some examples of domain walls between checkerboard phases. **Top.** A particle on the 'wrong' sublattice surrounded by 'holes', which forms the smallest possible domain wall loop. **Middle.** A horizontal domain wall. **Bottom.** Instability of a horizontal domain wall, by moving one particle to the other domain.

Notice that starting at 1/4 filling the generalized Wigner crystal picture certainly fails. If one adds one single particle to the 1/4 crystal, it will be necessarily next to another particle. Since the nearest-neighbor repulsion is the strongest, and nearest-neighbor occupancy can be avoided for any density below half-filling, the 1/4 crystal will be quickly destroyed upon adding particles. For densities above 1/4 it is necessary to start reasoning from the ordering occurring at the half-filled lattice.

6.2.2 *Domain walls and stripes*

Exactly at half-filling the ground state is **checkerboard**-like, or antiferromagnetic in the Ising language. This means that one sublattice is exactly filled and the other sublattice is completely empty. Densities slightly less than half-filling can be obtained by removing particles from the checkerboard pattern, a process we call **hole doping**. The density of holes ρ_h is defined as follows

$$\rho_h = 1 - 2\rho \tag{6.9}$$

where ρ is the total particle density. The same scaling arguments for the dilute particle limit $\rho \ll 1$ can be applied to the dilute hole limit $\rho_h \ll 1$, so close to half-filling the energy scales as

$$E \propto E_{1/2}\left(1 - 2\rho_h\right) + JNc_h\rho_h^{p/2+1} \tag{6.10}$$

where $E_{1/2}$ is the energy of the half-filled checkerboard configuration and c_h is some proportionality constant.

This scaling argument assumes that all particles will remain on the filled sublattice of the checkerboard phase. However, the checkerboard phase is a broken sublattice symmetry phase and therefore **domain walls and topological defects** can exist between regions where the checkerboard phase is realized on different sublattices. Though the ground state at densities slightly less than half-filled

[18] Bak and Bruinsma, 1982

might be unrelated to the checkerboard phase, we discuss in this section possible structures that are related to the checkerboard. Thus the smallest example, which is neglected in the scaling arguments of equation (6.10), is shown in figure 6.6(top). There a single particle on the 'wrong' sublattice is surrounded by holes, which is obviously a stable configuration.

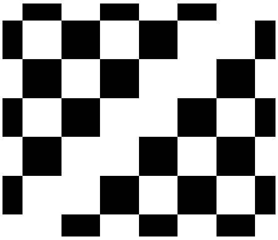

Figure 6.7: Stable, diagonal domain walls can exist for all long-range interactions.

On a large scale domain walls may exist such as the one depicted in figure 6.6b. However, such a **straight domain wall is not stable**. One can imagine a single particle moving to the other side, thus causing the domain wall to meander. The energy difference between the configurations in figure 6.6(middle) and figure 6.6(bottom) is given by the energy of that single moved particle,

$$\begin{aligned} \Delta E &= E_{\text{straight}} - E_{\text{meander}} \\ &\sim \sum_{n \text{ even}}{}' \left(\frac{1}{|n|^p} - \frac{1}{(n^2+1)^{p/2}} \right) > 0 \end{aligned} \tag{6.11}$$

where the prime on the summation means that we should exclude $n = 0$. Since the meandering domain wall has a lower energy than the straight one, the latter is unstable. This argument can be pursued further to the point where one finds that only a **diagonal domain wall**, as shown in figure 6.7, is stable. The resulting domain wall has a surface energy that vanishes in the thermodynamic limit; but is extremely stiff with respect to bending.

Now a single domain wall on a infinite lattice will not affect the average particle density. However, to obtain particle densities away from half-filling one can introduce a **macroscopic number of domain walls**. Such a periodic array of domain walls constitutes a **stripe phase**, similar to the ones discussed in cuprates,[19] nickelates,[20] manganites,[21] or cobaltates[22]. Examples can be seen in figure 6.1 at the beginning of this chapter.

If the ground state of a long-range lattice gas model is perfectly stripy, then the system is effectively reduced to a **one-dimensional system**. The arguments of Hubbard[23] then apply and one can thus find the specific stripe ordering, as is shown in figure 6.1a and b.

But again, for some densities it may pay off not to form perfect stripes but rather to dope a stripe structure as in figure 6.1c. It is then a matter of numerical computation to find out whether the ground state is a Hubbard-type stripe pattern or a **'doped' stripe**

[19] Zaanen and Gunnarsson, 1989; Tranquada et al., 1995; and Dagotto, 2005

[20] Tranquada et al., 1994

[21] Cheong and Hwang, 2000; Salamon and Jaime, 2001; and Dagotto, 2005

[22] Boothroyd et al., 2011; and Andrade and Vojta, 2012

[23] Hubbard, 1978

pattern. Lee et al., 2001 call these doped stripe patterns 'partially filled diagonal channels'. Finally, we must emphasize that the discussion in this section does in no way whatsoever constitute a proof of existence of stripe ordered or hole doped checkerboard phases. The only way to find the state with the lowest energy is a tedious numerical computation.

6.2.3 *Simulations and characterisation of the phases*

Let us now describe the **numerical algorithm** that was used to find the lowest energy configurations. First notice that for each form of order there is symmetry breaking and hence a degeneracy in the ground state. As the simplest example, observe that the checkerboard configuration at half-filling is two-fold degenerate. However, for the purpose of finding the specific type of charge order, we do not need to worry about ground state degeneracy.

In our algorithm we took various different types of **initial configurations**, such as the generalized Wigner crystals of section 6.2.1, stripe structures of section 6.2.2, Wigner crystal structures of defects in the checkerboard, variations of the checkerboard phase, suggestions from literature and a large ensemble of random configurations. We then swapped filled and empty sites randomly. A swap is accepted if it lowers the total energy of the system. The long-range nature of the interaction was taken into account by summing the interaction over all mirror charges as in an Ewald summation.[24] For the quasi-logarithmic interaction we followed the method of Lee et al., 2001.

The major issue is that one cannot know for sure whether this algorithm leads to the global ground state or that one gets stuck in a **local energy minimum**. Indeed, for a frustrated system we expect to find a large number of metastable states. The method of simulated annealing, by which we mean slowly reducing the temperature to zero, was therefore also used to avoid getting stuck in a local energy minimum. Upon comparing the energies of configurations obtained from the various initial configurations, using both zero temperature swapping and simulated annealing, we found a lowest energy state at each density.

Our work was performed on a square lattice with 90×90 and 154×154 sites. These lattice sizes were chosen such that the linear dimension L was divisible by the prime numbers $2, 3, 5$ (for

[24] Essmann et al., 1995

$L = 90$) and 7 and 11 (for $L = 154$). We looked at all densities that were a multiple of the linear dimension, hence $\rho = n/90$ and $\rho = n/154$ for all integers $n = 1 \ldots L/2$.

After obtaining the ground state configuration, a **Fourier transform** of the particle density was taken,

$$n(k) = \frac{1}{N}\sum_i e^{-ikr_i} n_i. \qquad (6.12)$$

The peaks in the Fourier spectrum were used to **identify the specific orderings** at each density, as can be seen in figure 6.8. The ground state energy as a function of density is shown in figure 6.9, rescaled such that the energy at half-filling equals $E = 1$. Indeed the general scaling behavior close to zero and half-filling, as described in the previous two sections, is retrieved. This is most explicit in the limit of $p \to \infty$, the energy becomes constant between $\rho = 0$ and $\rho = 1/4$, and linear between $\rho = 1/4$ and $\rho = 1/2$. Notice an extra kink in the energy around $\rho = 1/3$, which signals the onset of the stripe order.

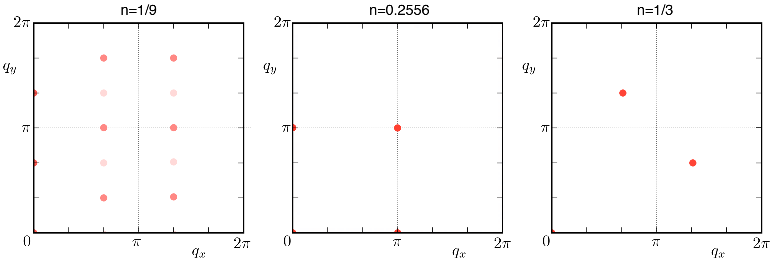

Figure 6.8: Fourier transformed density at fillings 1/9, 0.25556 and 1/3; on a 90×90 lattice with $1/r$ interactions. The different ordering wave vectors are clearly visible. These peaks are used to identify the phases that lead to the phase diagram of figure 6.2.

With the caution that the resulting configurations might be in fact metastable states incredibly close to the actual ground state, we constructed the **zero temperature phase diagram** in figure 6.2. At low densities the finite lattice size used in our numerical simulations form a limitation with regard to the precision of the results. The first unequivocal observed charge ordering state is the $1/9$ **generalized Wigner crystal phase**, which is stable for a considerable range of densities around $\rho = 1/9$. Interestingly, the presence of this phase is remarkably independent of the interaction range p.

This is followed by the $1/6$ phase which is extensively discussed in the work of Lee et al., 2002. There the $1/6$ phase is characterized

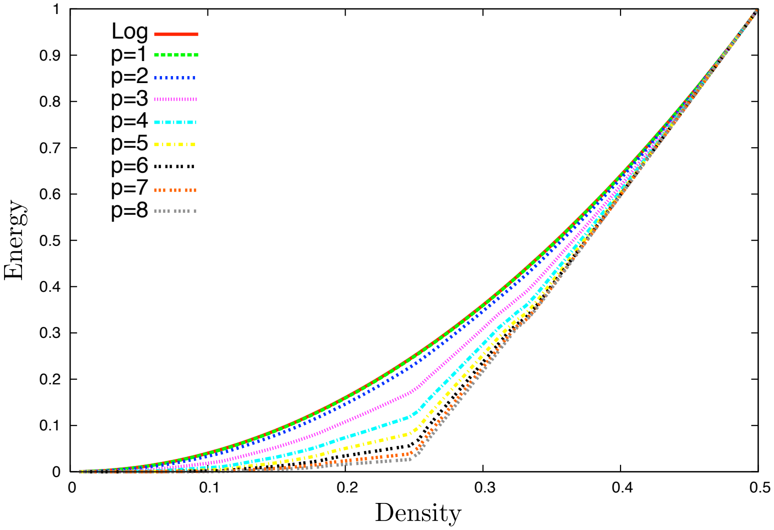

Figure 6.9: Ground state energy of the long-range lattice gas model as a function of density, for various types of interaction. All energies are rescaled such that $E(\rho = 1/2) = 1$. We have a logarithmic interaction and furthermore the p implies an interaction of the form $1/r^p$. Notice the scaling behavior in the limit $p \to \infty$ and notice the kink around $\rho = 1/3$ signalling stripe order.

as a **glassy phase**, with infinite ground state degeneracy due to the infinite ways one can tile unit cells of 2×3 lattice sites. For further details we refer to Lee et al., 2002.

Directly below $\rho = 1/4$ densities the $1/4$ generalized Wigner crystal phase is stable. As described before, introduction of particles to densities higher than $\rho = 1/4$ leads to a superlattice of interstitials which can be called a '**checkerboard-in-a-checkerboard phase**', which seems to be absent in the case of logarithmic interactions.

Here the logarithmic interactions seem to play a special role, in that for a much larger density regime than for algebraic interactions the **stripe phases** seem to be stable. We find, contradictory to the results of Lee et al., 2001, only stripe order of the Hubbard kind and no channelled stripes in the region between $1/4$ and $4/9$, see figure 6.10. Only the $1/3$-stripe order seemed to be present for a larger region of densities. We have found 'partially filled diagonal channels', or equivalently doped stripe orders, only for interaction types $p = 1$ and $p = 2$ in a very narrow density range. Our approach differs from Lee et al., 2001 in two aspects: we have looked at the ground state, while they looked at low temperature results obtained by simulated annealing only, and we considered non-local particle swaps in the configuration while they restricted the system to local swaps only. We have compared the energy of

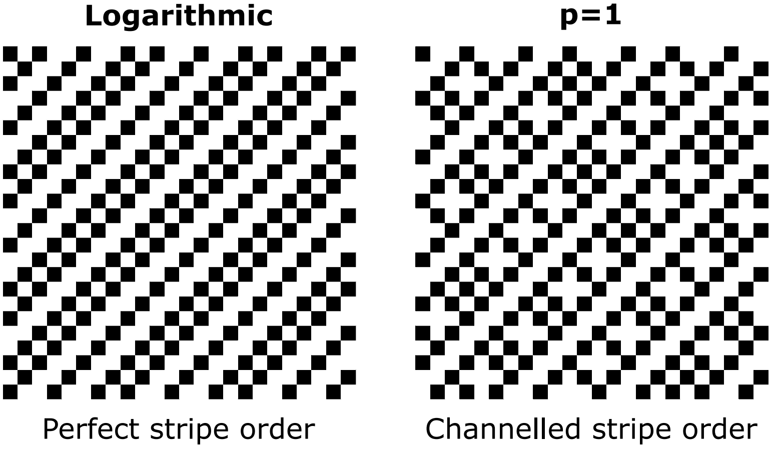

Figure 6.10: Detail of the charge configurations of the lowest energy states at a density of $n = 29/77 \approx 0.377$ and $L = 154$. For logarithmic interactions the perfect stripe order is 9×10^{-5}% lower in energy than the channelled stripe order, in contrast to Lee et al., 2001 who finds channelled stripes here. For $p = 1$ interactions the channelled stripes are 0.0014% lower in energy than the perfect stripes.

the ground states we found with the explicit ground states of Lee et al., 2001, taking into account the specific commensurability with the finite lattice size of their doped stripe orders. Figure 6.10 gives an example of this energy comparison at $n = \frac{29}{77}$. For all densities that we checked, it was found that our ground state energies are lower - be it only by a very small amount.

Notice that for algebraic interactions, the stripe phase shifts to higher densities when p increases. For large p, the stripe phase seems to dominate in the whole region between 1/3 and 1/2 fillings.

We also computed the ground state phase diagram for interactions with a **finite screening length** of the form

$$V(r) = \frac{e^{-r/\lambda}}{r^p} \tag{6.13}$$

turning into a Bessel function $K_0(r/\lambda)$ for the 'screened logarithmic' interaction. We find that the corresponding phase diagram for screened interactions is largely similar to figure 6.2, with only small quantitative differences that do grow with decreasing screening length λ.

6.2.4 *Finite temperature*

The phases described in the previous section **survive at finite temperatures**, because we are dealing with a system with discrete symmetry in two dimensions. We have computed a finite temperature mean field phase diagram using standard mean field theory,[25] for the $1/r$ interaction ($p = 1$).

It is of course highly questionable whether **mean field theory** correctly describes the competition between various phases. For example the rich phase diagram of the ANNNI model is constructed using mean field theory,[26] but corrections beyond mean field are shown to tip the delicate balance between different phases and reduce the critical temperature.[27] At the same time Monte Carlo simulations of the ANNNI miss incommensurate phases that are clearly present in analytical extensions of mean field theory.[28] Results from the ANNNI model thus suggests that mean field theory acts as a qualitatively reliable first approximation towards the understanding of complex ordering patterns.

Let us now briefly summarise the quintessence of our mean field theory. For the model Hamiltonian (6.1) we postulate an **ansatz for the density**,

$$\langle n_i \rangle = \overline{n} + \sum_\alpha m_\alpha \cos(Q_\alpha \cdot r_i) \tag{6.14}$$

where there can be as many ordering wave vectors Q_α as one needs to correctly describe the specific charge order. For example, the 1/9 order has ordering wave vectors $Q_1 = \left(0, \frac{2\pi}{3}\right)$, $Q_2 = \left(\frac{2\pi}{3}, \frac{2\pi}{9}\right)$ and all linear combinations inside the first Brillouin zone. When $m_\alpha \neq 0$ the translational invariance is spontaneously broken. Using the ansatz (6.14) one constructs a **mean field Hamiltonian**

$$H_0 = \sum_i \left[-\mu + \sum_\alpha m_\alpha V_{Q_\alpha} \cos(Q_\alpha \cdot r_i) \right] n_i. \tag{6.15}$$

We then minimise the thermodynamic potential

$$\Phi = \mathcal{F}_0 + \langle H - H_0 \rangle_0 \tag{6.16}$$

with respect to the mean field parameters m_α, where the free energy is $\mathcal{F}_0 = -\frac{1}{\beta} \log \operatorname{Tr} e^{-\beta H_0}$ and $\langle \ldots \rangle_0$ implies a thermal average with respect to the mean field Hamiltonian H_0. Every charge order we found at zero temperature acts as a possible ansatz, and we **numerically minimize** at each temperature and density the thermodynamic potential Φ.

Since mean field theory gives only a qualitative phase diagram, and because the zero-temperature phase diagram of figure 6.2

[25] Yeomans, 1992

[26] Bak, 1982

[27] Desimone and Stratt, 1985

[28] Bak, 1982

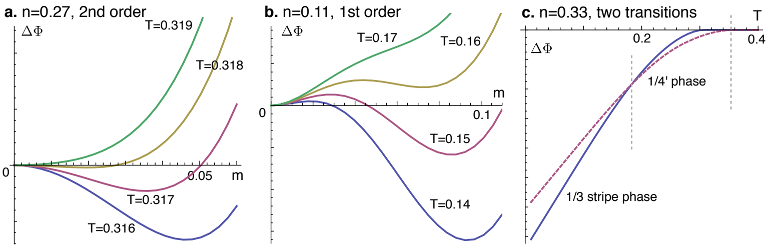

Figure 6.11: Thermodynamic potential relative to the disordered state ΔΦ plotted around various phase transitions. **a.** At $n = 0.27$ there is a second order phase transition into the $1/4'$ state, clearly visible by the Mexican hat potential. The second order phase transition is common for transitions in the Ising universality class. **b.** At $n = 1/9$ there is a first order transition toward the Wigner crystal, as is customary for solidification transitions. **c.** At $n = 1/3$ there are two transitions: a second order transition into the 1/4′ state followed by a first order transition towards the stripe phase. The 1/4′ and the stripe phases are locally stable however for a longer range of temperatures. This implies the possibility of supercooling the 1/4′ phase.

suggests little qualitative difference between various interaction ranges, we restrict ourselves to the **Coulomb interaction** $V = 1/r$. The resulting **phase diagram** is shown in figure 6.3. In addition to the $1/9$ Wigner crystal phase we also considered $1/12$, $1/16$, $1/20$ and $1/25$ crystals. As for the stripe phases, we only studied the $1/3$ and the $3/7$ 'channeled' state. The phase diagram we thus find indeed matches the zero-temperature phase diagram obtained by numerical simulations of the previous section. We emphasize that further studies are needed to understand the possible incommensurate stripe phases in between $1/3$ and $4/7$ filling.

The transition to the checkerboard phase and the similar $1/4'$ phase is of the **second order** type within the Ising universality class.[29] The thermodynamic potential for some temperatures around T_c, with its typical second order transition behaviour, is shown in figure 6.11a. The question arises whether this $1/4'$ 'phase' is an artefact of the mean field theory. As is known at half-filling, a liquid-like state with local checkerboard order exists in the presence of long-range interactions.[30] Such correlated liquid phase can also be present away from half-filling, but will be beyond the scope of standard mean field theory.

The phase transitions to more complicated orders are always of the **first order** kind, an example of which is shown in figure 6.11b at 1/9 filling. This is a natural result because transitions from solid to liquid phases are usually discontinuous.[31] The existence of such first order transition implies that one can supercool the high-temperature (or 1/4′) state.[32] At $\rho = 1/3$ for example, the $1/4'$ phase remains a local minimum of the free energy even though its energy is higher than that of the stripe phase, see figure 6.11c. This suggests that it might be hard to actually trap the

[29] Möbius and Rössler, 2009

[30] Pramudya et al., 2011

[31] Brazovskii, 1975

[32] Das, 2011

system in the lowest energy state.

In combination with our earlier observation that a correlated liquid-like state at intermediate temperatures might exist, we then also expect **glassy physics upon supercooling**.[33] With 'glassy' we mean that there are macroscopically many local minima of the free energy, leading to slow relaxation rates. There is a difference however with the glassy physics found at $\rho = 1/6$ densities.[34] There the glassy nature is a ground state property, where glassy physics around a first order transition vanishes if the temperature is low enough.

The mean field theory shows the possibility of supercooling, the consequences thereof such as possible glass-like behaviour needs to be addressed differently. Finite temperature numerical simulations however have the great disadvantage that they get easily stuck in such a complicated free energy landscape. It remains thus an open challenge to quantitatively describe the finite temperature phase diagram of the long-range Ising model away from half-filling.

6.2.5 *Conclusions and outlook*

In conclusion, we computed the **full ground state and finite temperature phase diagram** of a lattice gas model at fixed density on a square lattice with general long-range interactions. We were motivated by the potentiality of nontrivial charge ordering phenomena given the long-ranged dipolar exciton interaction. Most notable ordering patterns are the generalized Wigner crystals at low densities, supplanted by the stripe order at densities between $1/4$ and $1/2$. All phases are shown in figure 6.2 at zero temperature and in figure 6.3 for finite temperatures.

The results of this chapter extend mainly the work of Lee et al., 2001, in that we have derived complex ordering patterns in the absence of anisotropy or competing interactions. In this case, we suggest that the frustration between the underlying square lattice and the preferable Wigner crystalline state causes the complex ordering. In the vicinity of half-filling this mechanism is supplanted by periodic domain walls in the checkerboard phase. It is these domain walls that cause the formation of stripes.

The finite temperature phase diagram has been obtained using mean field theory, yielding only a qualitative description. Nu-

[33] Schmalian and Wolynes, 2000

[34] Lee et al., 2002

merical and/or analytical extensions of the classical mean field theory will increase the accuracy of the finite temperature phase diagram. Thereby one can address the possibility of supercooling and glassy physics.

A possible next step is to include the kinetic energy of the particles present. This also allows for an extension to quantum particles[35] or $O(n)$ spin variables[36] instead of the classical particles we have considered thusfar. The inclusion of the quantum nature of the particles will also bring us closer towards an understanding of the exciton physics in the correlated bilayer.

[35] Sengupta et al., 2005

[36] Nussinov, 2001

7

Conclusions and outlook

Our study of excitons in strongly correlated bilayers has yielded several experimentally testable predictions.

- Using phenomenological Ginzburg-Landau theory we predict that an exciton condensate must exhibit **flux quantization**.[1]
- The fermionic Hubbard model can describe strongly correlated bilayers. An unreliable mean field theory predicts room-temperature superfluidity.[2] The numerical **Determinant Quantum Monte Carlo** suggests that exciton condensation might occur around 15-20% doping, but the applicability of this method is severely limited by the sign problem.[3]
- We derive a low energy bosonic model[4] called the exciton $t - J$ model. For most parts of the phase diagram there is **phase separation** between the superfluid, the exciton solid and the antiferromagnet.[5]
- In the limit of low exciton density, there is **frustration** between moving excitons and the antiferromagnetic background leading to Ising confinement. This can be seen in optical experiments of for example undoped YBCO bilayers.[6]
- Exciton condensation within the $t - J$ model exists at large exciton kinetic energies. There the magnetic triplet excitations 'borrow' kinetic energy from the exciton which is visible in a **large triplon bandwidth**, proportional to the superfluid density.[7]
- The long-range dipolar interaction might cause the formation of **complex ordered phases**, such as generalized Wigner crystals or stripe phases.[8]

[1] Section 2.2.

[2] Section 3.2.

[3] Section 3.3.

[4] Section 4.1.

[5] Section 5.2.

[6] Section 4.2.

[7] Section 5.1.

[8] Chapter 6.

Despite these several predictions, the theory related to excitons in strongly correlated bilayers is **far ahead of the experimental progress**. This poses a limitation on further theoretical progress, since questions must always be driven by experiments. Nevertheless, there are a few interesting open theoretical questions which are worth mentioning.

Most of our predictions were obtained in the strong coupling limit, where the electron and hole are tightly bound into a boson. It is then natural to ask what happens at intermediate exciton coupling. Most likely the excitons will be spatially **broadened**, reintroducing the complicated fermion sign structure. The inclusion of finite temperatures puts forward the issue of **dissociation** of the excitons into separate holes and electrons. This can be viewed as the extreme limit of spatial broadening. The broadening and formation of excitons is certainly the most interesting open problem regarding the cuprate bilayers, but the fermion sign problem stands in the way of simple answers.

Another possible theoretical direction is to study **exciton-mediated superconductivity**. Superconductivity in the BCS sense[9] requires a bosonic glue to form Cooper pairs, and excitons could play this role.[10] Though this proposal is quite old, there are as of yet no known exciton-mediated superconductors. Condensation of the excitons themselves, especially in the case of imbalanced electron-hole densities, could increase the probability of electron-electron pairing. Whether exciton-mediated superconductivity is truly possible is still an open debate, especially within the cuprate family.

Besides the two major theoretical proposals one can extend the analysis of this thesis to **similar systems**. For example, we can consider different interlayer couplings. In 214 systems such as $La_{2-x}Sr_xCuO_4$ the copper atoms in nearest neighbor layers do not lie directly above each other. Consequently, instead of an interlayer antiferromagnetic coupling one finds a Dzyaloshinskii-Moriya interaction. In addition to different interlayer couplings we could also study different lattice structures, such as the hexagonal lattice.[11] The choice of different lattices and interactions, however, should be guided by actually existing materials that are expected to have these properties.

Let us therefore discuss the **experimental progress** on cuprate bilayers. The main practical difficulty lies in the fabrication of both

[9] See section 3.2.

[10] Allender et al., 1973; and Inkson and Anderson, 1973

[11] Meng et al., 2010

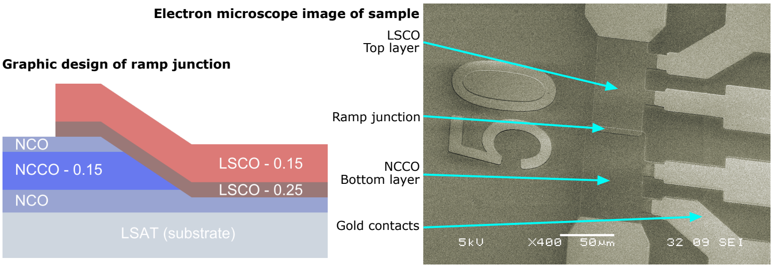

Figure 7.1: In Twente ramp contacts combining p and n-type cuprates were constructed. On the left the design is shown. On the right an electron microscope image of the actual sample is shown. Both layers are visible, and the junction in between them.

p and n-type cuprates in a single sample. Marcel Hoek, Francesco Coneri and Hans Hilgenkamp at the University of Twente are currently making heterostructures of the hole-doped $La_{2-x}Sr_xCuO_4$ (LSCO) and electron-doped $Nd_{2-x}Ce_x$ CuO_4 (NCCO), see figure 3.2 for their crystal structure. This is done by **pulsed laser deposition** (PLD). This technique involves focussing a high power laser on a target in a vacuum chamber, which results in a plasma plume of the target material. The plume deposits on a substrate as a thin film. By tuning the amount of laser pulses, one can construct heterostructures one unit cell layer at a time. The problem is, however, that p- and n-type cuprates need different growth conditions in the PLD process. To obtain superconducting LSCO one needs to anneal the substrate in oxygen, whereas NCCO usually requires annealing in vacuum. The Twente group has managed to successfully create NCCO layers under the growth conditions of LSCO.

Subsequently they have fabricated p/n heterostructures with both LSCO and NCCO in a single sample. The strategy thereby is to first deposit NCCO layers and on top of that an insulator such as $SrTiO_3$. A ramp edge is etched and on top of that a LSCO layer is deposited. This results in a **ramp contact** as shown in figure 7.1.

The p/n contacts are of extreme importance within semiconductor technology. Such p/n junctions consisting of Mott insulators have been little studied.[12] One might for example wonder whether a Josephson current between n and p-type superconductors is possible. Back-of-the-envelope theory predicts that p/n-Josephson junctions might behave qualitatively different from normal Josephson junctions. Transport measurements on these p/n ramp contacts are on the way. At the same time RIXS measurements similar to the one proposed in section 5.1 are started on

[12] Manousakis, 2010

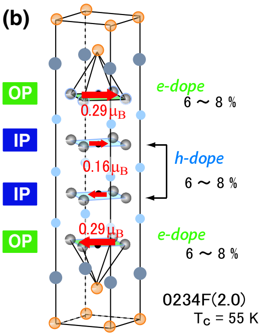

Figure 7.2: In the four-layer cuprate F0234 selfdoping yields electron- and hole-type layers close to each other. From Shimizu et al., 2007.

p/n heterostructures.

Still, the experimental progress in LSCO/NCCO heterostructures is far away from the p/n bilayers studied in this thesis. Probably the closest connection with experiment this thesis has, lies in cuprates that themselves are bi- or multilayered. In section 4.2 we showed that we expect the dynamical frustration to occur also in the undoped **bilayered YBCO**, for which experiments are underway.

Another Mott compound, **$Ba_2Ca_3Cu_4O_8F_2$ or F0234**, shows the unique property of selfdoping.[13] In F0234 the CuO_2 layers come in groups of four. The outer two layers are electron doped and the inner two layers are hole doped (see figure 7.2). One might wonder whether the physics of the exciton $t-J$ model is already at work. Following the phase diagram of figure 5.8, one might expect that F0234 should exhibit microscopic phase separation between antiferromagnetism and exciton superfluidity. Whereas the latter is not observed (nor excluded), NMR studies[14] clearly show the coexistence of superconductivity and antiferromagnetism. A study of the magnetic excitations, following the work of chapter 4, would further elucidate the interlayer properties in F0234.

Finally, we mention the novel area of **interface conductance in oxide insulators**, which entails intriguing prospects to realize closely coupled p- and n-type conductors. An example has been provided by Pentcheva et al., 2010 for the case of 2 unit cells of $LaAlO_3$ and 1 unit cell of $SrTiO_3$ grown epitaxially on a TiO_2-terminated $SrTiO_3$ substrate. This research-area also extends to interfaces with Mott insulator compounds such as $LaVO_3/SrTiO_3$.[15]

Despite the considerable distance between theory and experiment, the exciton $t-J$ model gives room for many interesting theoretical advances. Microscopic phase separation, frustration, strongly correlated physics: these are effects that are usually associated with fermions. Now that we find such complicated phenomena in a purely bosonic setting one can investigate the relevance of fermion signs in quantum matter.

7.1 Propositions on quantum matter

In this thesis we studied properties of a strongly correlated bilayer, a material that is commonly categorized as 'quantum matter'.[16]

[13] Chen et al., 2006

[14] Shimizu et al., 2007

[15] Hotta et al., 2007

[16] See the introductory chapter 1.

Following the wide variety of quantum theories (phenomenologically, fermionic and bosonic) that were presented in this thesis we are now in the position to state some open questions regarding the research field of quantum matter.

At first glance the 'quantum' distinguishes itself from classical phenomena only through the concept of **superposition**. However, not all superpositions necessarily exclude a classical description. Any macroscopic object such as a coffee mug or an airplane is in a superposition of many of its momentum eigenstates - nonetheless they are clearly classical objects.

One must therefore be more precise in separating the classical from the quantum, by which we now imply superpositions that cannot be untwined into classical objects. Those states are called **entangled**, and the simplest example of an entangled state is two electrons in a singlet state,

$$|\Psi\rangle = \frac{1}{\sqrt{2}}\left(|\uparrow_1 \otimes \downarrow_2\rangle - |\downarrow_1 \otimes \uparrow_2\rangle\right). \tag{7.1}$$

This state has no classical analogue, as is shown by the famous Einstein-Podolsky-Rosen experiment.[17]

Observe that the singlet state (7.1) describes two **indistinguishable particles**: we cannot say which of the two particles is in the spin up state, and which is in the spin down state. In fact, there is a close connection between indistinguishability and entanglement. The requirement of indistinguishability implies that the wavefunction of a collection of quantum particles is highly entangled. In the case of fermions the wavefunctions can be written as a **Slater determinant**, thus correctly incorporating the fermion minus signs. For example, three indistinguishable fermions occupying states A, B and C are described by the wavefunction

$$\begin{aligned}|\Psi\rangle &= \frac{1}{\sqrt{6}}\left(|A_1B_2C_3\rangle - |A_1C_2B_3\rangle + |B_1C_2A_3\rangle\right.\\ &\quad \left.-|B_1A_2C_3\rangle + |C_1A_2B_3\rangle - |C_1B_2A_3\rangle\right) \quad (7.2)\\ &= \frac{1}{\sqrt{3!}}\begin{vmatrix}|A_1\rangle & |B_1\rangle & |C_1\rangle\\ |A_2\rangle & |B_2\rangle & |C_2\rangle\\ |A_3\rangle & |B_3\rangle & |C_3\rangle\end{vmatrix}. \quad (7.3)\end{aligned}$$

It would be a grave misnomer, however, to classify this state as a quantum material. By introducing anticommuting creation operators, a procedure known as **second quantization**, this state is simply written as

---

[17] Einstein et al., 1935; and Aspect et al., 1982

$$|\Psi\rangle = c_A^\dagger c_B^\dagger c_C^\dagger |0\rangle. \tag{7.4}$$

What we have just described is the free (classical) Fermi gas, which is not a quantum matter at all. Since basically all macroscopic collections of quantum particles are entangled in the Einstein-Podolsky-Rosen sense, we need yet again a different way to understand the difference between classical and quantum matter.

Therefore we will call the many-particle extension of state (7.4) an **antisymmetrized product state**,[18] since the wavefunction can be fully untwined into separate single-particle wavefunctions. Entanglement is now limited to the antisymmetrization required by the indistinguishability. The distinction thus introduced, between states that can be written as (anti)symmetrized product state and those who cannot, truly captures the difference between classical and quantum states.

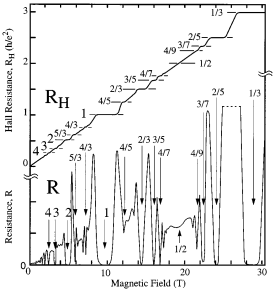

Figure 7.3: A two-dimensional electron gas in a perpendicular magnetic field exhibits plateaus in its Hall resistance. This effect, known as the quantum Hall effect, occurs either at integer or fractional filling fractions. Image from the Nobel Lecture of Stormer, 1999.

A beautiful example of the latter is the Laughlin wavefunction[19] that describes the $\nu = \frac{1}{3}$ **fractional quantum Hall effect** (FQHE),

$$\psi(z_1 \dots z_N) = \prod_{j<k} (z_j - z_k)^3 e^{-\frac{1}{4}\sum_\ell |z_\ell|^2} \tag{7.5}$$

where $z_j = x_j + iy_j$ is the complex coordinate of the jth electron. The single-particle states of an electron in a magnetic field are, in the lowest Landau level, of the form $\psi(z) \sim z^m e^{-\frac{1}{4}|z|^2}$. The construction of an antisymmetrized product state out of these single-particle states yields

$$\psi(z_1 \dots z_N) = \prod_{j<k} (z_j - z_k) e^{-\frac{1}{4}\sum_\ell |z_\ell|^2}, \tag{7.6}$$

the wavefunction of the $\nu = 1$ integer quantum Hall state. The Laughlin state, however, can only be expressed as a **superposition of antisymmetrized product states**. It is therefore considered to be a true quantum liquid.

The concept of superposing different antisymmetrized states can be taken further, starting with the singlet or **valence bond**[20]

$$|\psi\rangle = \frac{1}{\sqrt{2}} \left(c_{i\uparrow}^\dagger c_{j\downarrow}^\dagger - c_{i\downarrow}^\dagger c_{j\uparrow}^\dagger \right) |0\rangle. \tag{7.7}$$

The quantum paramagnetic phase of the bilayer Heisenberg model consists of such singlets on each interlayer rung,[21] and is therefore called a valence bond solid. A macroscopically entangled extension is the **resonating valence bond** (RVB) state, which consists of a superposition of all possible pairings of two particles into a singlet state. When high T_c superconductivity was discovered, Anderson proposed that the cuprates can in fact be described by a long-range RVB state.[22]

---

[18] For many-boson systems this will become a symmetrized product state.

[19] Laughlin, 1983

[20] In first quantization language this state is given by $|\psi\rangle = 4^{-1/2}(|i\uparrow\rangle_1 |j\downarrow\rangle_2 - |j\downarrow\rangle_1 |i\uparrow\rangle_2 - |i\downarrow\rangle_1 |j\uparrow\rangle_2 + |j\uparrow\rangle_1 |i\downarrow\rangle_2)$.

[21] See the phase diagram, figure 4.2, and equations (4.2) and (4.37).

But is it truly a long-range quantum entangled state? The long-range RVB state on a square lattice has a finite overlap with the **Néel state** describing antiferromagnetism,[23]

$$|\Psi\rangle_{\mathrm{AF}} = |\uparrow_1 \downarrow_2 \uparrow_3 \cdots\rangle = \prod_{i\in A} c^\dagger_{i\uparrow} \prod_{j\in B} c^\dagger_{j\downarrow} |0\rangle \tag{7.8}$$

where the lattice is broken into two sublattices A and B. The Néel state, however, is a clearcut example of a product state. So is the ground state of the Heisenberg model (4.10) a quantum state or a classical state?

The antiferromagnetic long-range RVB state of Liang et al., 1988 is the currently best known approximation to the ground state of the Heisenberg model. It satisfies the rule designed by Marshall, 1955, who proved that the ground state of the Heisenberg model can be written as a superposition of spin configuration states $\mathcal{C}$,

$$\begin{aligned} |\Psi\rangle_0 &= w_1 |\uparrow_1 \downarrow_2 \uparrow_3 \cdots\rangle + w_2 |\downarrow_1 \uparrow_2 \uparrow_3 \cdots\rangle + \ldots && (7.9) \\ &\equiv \sum_{\mathcal{C}} w_{\mathcal{C}} |\mathcal{C}\rangle && (7.10) \end{aligned}$$

where the sign of each weight $w_{\mathcal{C}}$ is determined by the number of up spins on the A sublattice,

$$w_{\mathcal{C}} = (-1)^{N_A^\uparrow} |w_{\mathcal{C}}|. \tag{7.11}$$

With the **sign structure** thus imprinted into the set of basis kets, the Heisenberg model on a square lattice at half-filling can be described purely in terms of positive-definite weights. Similarly, in the high-temperature expansion or Suzuki-Trotter decomposition[24] of $e^{-\beta H}$ all statistical weights and/or matrix elements are positive definite.

On a frustrated lattice such as the **triangular lattice**, however, a short-range RVB state may be the lowest in energy.[25] This might indeed constitute a realization of a quantum material. Another obvious candidate is the ground state of the Hubbard model at finite doping.[26]

[22] Anderson, 1973; and Anderson, 1987

[23] Liang et al., 1988

[24] See section 3.3.

[25] Anderson, 1973

[26] See section 3.1.

Summarizing, we defined quantum materials as a superposition of different antisymmetrized product states. However, once the sign structure of this superposition is known one can relate the apparent quantum state to a classical product state, as is shown for the long-range RVB and Néel state. The main question therefore remains whether there exist *macroscopic quantum (long-range entangled) states which cannot be reduced to classical (antisymmetrized product) states*. In terms of the fermion sign problem language we should ask whether there are superposition states with an **irreducible sign structure**.

In the case of the exciton $t-J$ model presented in this thesis, we implicitly employed this reduction. Even though the model has an as of yet unknown sign structure,[27] variational mean field theory[28] yields a product state that has finite overlap with the true ground state. Similarly the recent experimental detection of 'current loop order' in cuprates[29] suggests that in the end a quantum sign-full strongly correlated material might still be represented by a classical product state.

Once the correct product state is found, the question arises what the **quantum corrections** should be. A systematic way to answer this is by means of spin wave theory: equation (4.63) in section 4.2.1 shows how the ground state of the Heisenberg model can be approximated by a superposition $|\psi_0\rangle$ of the Néel state $|G\rangle$ and its quantum corrections. Many authors call these corrections **quantum fluctuations**, but I perceive this as a misleading picture. *There is nothing fluctuating about a superposition.* For example, saying that the singlet state (7.1) is fluctuating between $|\uparrow_1\downarrow_2\rangle$ and $|\downarrow_1\uparrow_2\rangle$ fundamentally misunderstands the quantum nature of that state.[30]

How a macroscopic superposition should be understood is therefore an open question. Experimental realization of superpositions of classically distinct configurations is being pursued by several research groups. A superposition of two opposite circular supercurrents in a SQUID is a prime example thereof.[31] Following the phase diagram of section 5.2 another suggestion is to consider **first order quantum phase transitions**. At such a transition, there are two macroscopically fundamentally different states with the same energy which can therefore be put in a superposition. The possibility of a superposition is competing with the more classical first order effects of phase separation and the idea that the system can actually be fluctuating between the two phases.[32] *First*

[27] See section 4.1.4.

[28] See section 5.2.

[29] Varma, 1997; Shekhter et al., 2013; and Zaanen, 2013

[30] Note that the spin liquid community uses the words 'fluctuation' and 'superposition' interchangeably, see the review by Balents, 2010.

[31] Friedman et al., 2000; and van der Wal et al., 2000

[32] As for example in supercooled water, where numerics suggest 'phase flipping' between the high and low density liquid. Kesselring et al., 2012.

order quantum phase transitions are therefore ideal candidate systems to elucidate the notions of quantum superpositions and fluctuations.

Yet another way to combine two different phases of matter is as a **statistical mixture** of states. This is done within the thermal density matrix formalism. In general, a quantum system at temperature T is believed to be described by the density matrix $\rho = e^{-H/k_B T}$. However, in the case of **spontaneous symmetry breaking** ρ is at best ill-defined in the thermodynamic limit and at worst incorrect: a magnet is never in a mixed state of its different possible magnetization directions. The fact that an infinitesimal symmetry breaking field radically changes the density matrix implies that ρ in zero field is singular. On top of that, the thermal density matrix misses interesting superposition effects such as in the aforementioned SQUID experiments.[33] Therefore, *a good understanding of quantum matter at finite temperature, specifically regarding the role of macroscopic superpositions and entanglement, requires a novel approach beyond the thermal density matrix.*

In this thesis we have considered the existence of fermions as fundamental. A completely different approach to quantum matter discards this notion of fermions as being fundamental entities. Just like phonons[34] are emergent quantized particles, fermions could be **emergent**. Examples are the emergence of fermions in string-net condensates[35] or in complex weighted networks.[36] Close to the Mott state, the fermions might not even act as fermions due to their localization constraint, leading to novel statistical effects.[37] In one-dimensional systems effects such as spin-charge separation of fermions are well understood. Nevertheless, *in higher dimensions the breakdown or emergence of fermionic behavior deserves more research attention.*

Let us conclude that the mysteries of quantum mechanics become increasingly relevant in the understanding of actually existing materials, such as cuprates. This presents the opportunity to study basic quantum phenomena without the need of building billion-dollar accelerators or satellites. Instead, the greatest mysteries of modern condensed matter can be held in one's hand. And hopefully, just like the specific heat anomaly experiments paved the way for the development of quantum statistical theory, the current stream of ill-understood experimental results will lead to new fundamental insights into the laws of nature.

[33] Which can be viewed as a magnet in a superposition of two opposite magnetizations.

[34] Phonons are quantized lattice vibrations.

[35] Wen, 2007

[36] Garlaschelli and Loffredo, 2009

[37] Zaanen and Overbosch, 2011

Bibliography

A. A. Abrikosov, I. E. Dzyaloshinskii, and L. P. Gor'kov. *Quantum Field Theoretical Methods in Statistical Physics*. Dover Publications, New York, 1965.

D. Allender, J. W. Bray, and J. Bardeen. *Model for an Exciton Mechanism of Superconductivity*. Physical Review B **7**, 1020, 1973.

L. J. P. Ament, M. van Veenendaal, T. P. Devereaux, J. P. Hill, and J. V. den Brink. *Resonant inelastic x-ray scattering studies of elementary excitations*. Rev. Mod. Phys. **83**, 705, 2011.

P. W. Anderson. *An Approximate Quantum Theory of the Antiferromagnetic Ground State*. Phys. Rev. **86**, 694, 1952.

P. W. Anderson. *New Approach to the Theory of Superexchange Interactions*. Phys. Rev. **115**, 2, 1959.

P. W. Anderson. *Resonating valence bonds: A new kind of insulator?*. Materials Research Bulletin **8** 2, 153 – 160, 1973.

P. W. Anderson. *Basic notions of condensed matter physics*. Frontiers in physics. Benjamin/Cummings Pub. Co., Advanced Book Program, 1984.

P. W. Anderson. *The resonating valence bond state in* La_2CuO_4 *and superconductivity*. Science 1987.

E. C. Andrade and M. Vojta. *Disorder, cluster spin glass, and hourglass spectra in striped magnetic insulators*. arXiv **cond-mat.str-el**, 2012. arXiv:1204.6323.

A. Aspect, P. Grangier, and G. Roger. *Experimental Realization of Einstein-Podolsky-Rosen-Bohm Gedankenexperiment: A New Violation of Bell's Inequalities*. Phys. Rev. Lett. **49**, 91, 1982.

E. Babaev. *Vortex matter, effective magnetic charges, and generalizations of the dipolar superfluidity concept in layered systems*. Phys. Rev. B **77**, 54512, 2008.

S. Bae, H. Kim, Y. Lee, X. Xu, J.-S. Park, Y. Zheng, J. Balakrishnan, T. Lei, H. R. Kim, Y. I. Song, Y.-J. Kim, K. S. Kim, B. Özyilmaz, J.-H. Ahn, B. H. Hong, and S. Iijima. *Roll-to-roll production of 30-inch graphene films for transparent electrodes*. Nat. Nanotech. **5**, 574, 2010.

P. Bak. *Commensurate phases, incommensurate phases and the devil's staircase*. Rep Prog Phys **45** 6, 587–629, 1982.

P. Bak and R. Bruinsma. *One-Dimensional Ising Model and the Complete Devil's Staircase*. Phys. Rev. Lett. **49**, 249, 1982.

A. V. Balatsky, Y. N. Joglekar, and P. B. Littlewood. *Dipolar Superfluidity in Electron-Hole Bilayer Systems*. Phys. Rev. Lett. **93** 26, 266801, 2004.

L. Balents. *Spin liquids in frustrated magnets*. Nature **464** 7286, 199–208, 2010.

J. Bardeen, L. N. Cooper, and J. R. Schrieffer. *Theory of Superconductivity*. Phys. Rev. **108**, 1175, 1957.

D. Basov and T. Timusk. *Electrodynamics of high-T_c superconductors*. Rev. Mod. Phys. **77** 2, 721–779, 2005.

R. Blankenbecler, D. J. Scalapino, and R. L. Sugar. *Monte Carlo calculations of coupled boson-fermion systems. I*. Phys. Rev. D 1981.

J. M. Blatt, K. Boer, and W. Brandt. *Bose-einstein condensation of excitons*. Phys. Rev. **126** 5, 1691–1692, 1962.

A. T. Boothroyd, P. Babkevich, D. Prabhakaran, and P. G. Freeman. *An hour-glass magnetic spectrum in an insulating, hole-doped antiferromagnet*. Nature **471** 7338, 341–344, 2011.

S. A. Brazovskii. *Phase transition of an isotropic system to a nonuniform state*. Sov. Phys. JETP **41**, 85, 1975.

W. Brinkman and T. M. Rice. *Single-particle excitations in magnetic insulators*. Phys. Rev. B **2** 5, 1324–&, 1970.

H. Bruus and K. Flensberg. *Many-Body Quantum Theory in Condensed Matter Physics: An Introduction*. Oxford Graduate Texts. Oxford University Press, Oxford, 2004.

L. N. Bulaevskii, E. L. Nagaev, and D. I. Khomskii. *A New Type of Auto-localized State of a Conduction Electron in an Antiferromagnetic Semiconductor*. Sov. Phys. JETP **27** 5, 836, 1968.

L. V. Butov. *Exciton condensation in coupled quantum wells*. Solid state communications **127**, 89, 2003.

L. V. Butov. *Cold exciton gases in coupled quantum well structures*. J. Phys.: Condens. Matter **19**, 5202, 2007.

S. Chakravarty, B. Halperin, and D. Nelson. *Two-dimensional quantum Heisenberg antiferromagnet at low temperatures*. Phys. Rev. B **39** 4, 2344–2371, 1989.

K. A. Chao, J. Spalek, and A. M. Oles. *Kinetic exchange interaction in a narrow S-band*. Journal of Physics C: Solid State Physics **10**, L271, 1977.

Y. Chen, A. Iyo, W. Yang, X. Zhou, D. Lu, H. Eisaki, T. P. Devereaux, Z. Hussain, and Z. X. Shen. *Anomalous Fermi-Surface Dependent Pairing in a Self-Doped High-Tc Superconductor*. Phys. Rev. Lett. **97** 23, 236401, 2006.

S. W. Cheong and H. Y. Hwang. *Ferromagnetism vs charge/orbital ordering in mixed-valence manganites*. In Y. Tokura (editor), *Colossal Magnetoresistive Oxides*. Gordon and Breach, New York, 2000.

A. V. Chubukov and D. Morr. *Phase transition, longitudinal spin fluctuations, and scaling in a two-layer antiferromagnet*. Phys. Rev. B **52** 5, 3521–3532, 1995.

D. Clarke and S. Strong. *'Confined coherence' in strongly correlated anisotropic metals*. Adv. Phys. **46** 6, 545–650, 1997.

P. Coleman. *Introduction to Many Body Physics*. Cambridge University Press, 2013.

S. Cooper and K. Gray. *Anisotropy and Interlayer Coupling in the High Tc Cuprates*. Physical Properties of High Temperature Superconductors IV 1994.

E. Dagotto. *Correlated electrons in high-temperature superconductors*. Rev. Mod. Phys. **66** 3, 763–840, 1994.

E. Dagotto. *Complexity in Strongly Correlated Electronic Systems*. Science **309** 5732, 257–262, 2005.

A. Damascelli, Z. Hussain, and Z. X. Shen. *Angle-resolved photoemission studies of the cuprate superconductors*. Rev. Mod. Phys. **75** 2, 473–541, 2003.

S. P. Das. *Statistical physics of liquids at freezing and beyond*. Cambridge University Press, 2011.

P. G. De Gennes. *Superconductivity Of Metals And Alloys*. Advanced Book Classics. Advanced Book Program, Perseus Books, 1999.

M. P. M. Dean, R. S. Springell, C. Monney, K. J. Zhou, J. Pereiro, I. Bozovic, B. D. Piazza, H. M. Rønnow, E. Morenzoni, J. van den Brink, T. Schmitt, and J. P. Hill. *Spin excitations in a single La_2CuO_4 layer*. Nat. Mater. **11** 10, 850–854, 2012.

T. Desimone and R. M. Stratt. *Some developments in the theory of modulated order. I. The role of fluctuations in the axial next-nearest-neighbor Ising model and the relevance of the Thouless-Anderson-Palmer equation*. Phys. Rev. B **32**, 1537, 1985.

R. Dillenschneider and J. H. Han. *Exciton formation in graphene bilayer*. Phys. Rev. B **78** 4, 045401, 2008.

P. A. M. Dirac. *The Principles of Quantum Mechanics*. Oxford University Press, 1958.

C. N. A. van Duin. *On Quantum Magnetism in Cuprate Superconductors*. Leiden University, 1999.

C. N. A. van Duin and J. Zaanen. *On the origin of the quantum-critical transition in the bilayer Heisenberg model*. Phys. Rev. Lett. **78**, 3019, 1997. cond-mat/9701035v1.

C. N. A. van Duin and J. Zaanen. *Interplay of superconductivity and magnetism in strong coupling*. Phys. Rev. B **61**, 3676, 2000.

F. J. Dyson. *General Theory of Spin-Wave Interactions*. Phys. Rev. **102**, 1217, 1956.

A. Einstein, B. Podolsky, and N. Rosen. *Can Quantum-Mechanical Description of Physical Reality Be Considered Complete?*. Phys. Rev. **47**, 777, 1935.

J. Eisenstein and A. H. MacDonald. *Bose-Einstein condensation of excitons in bilayer electron systems*. Nature **432** 7018, 691–694, 2004.

V. J. Emery and S. A. Kivelson. *Frustrated electronic phase separation and high-temperature superconductors*. Physica C **209**, 597, 1993.

U. Essmann, L. Perera, M. L. Berkowitz, T. Darden, H. Lee, and L. G. Pedersen. *A smooth particle mesh Ewald method*. The Journal of Chemical Physics **103**, 8577, 1995.

X. Feng, H. Blöte, and B. Nienhuis. *Lattice gas with nearest- and next-to-nearest-neighbor exclusion*. Phys. Rev. E **83** 6, 061153, 2011.

A. L. Fetter and J. D. Walecka. *Quantum Theory of Many-Particle Systems*. Dover Books on Physics. Dover Publications Incorporated, 2003.

A. Finck, J. Eisenstein, L. Pfeiffer, and K. W. West. *Exciton Transport and Andreev Reflection in a Bilayer Quantum Hall System*. Phys. Rev. Lett. **106** 23, 236807, 2011.

M. Fisher and W. Selke. *Infinitely many commensurate phases in a simple Ising-model*. Phys. Rev. Lett. **44** 23, 1502–1505, 1980.

M. E. Fisher and D. R. Nelson. *Spin Flop, Supersolids, and Bicritical and Tetracritical Points*. Phys. Rev. Lett. **32**, 1350, 1974.

D. D. Fontaine, G. Ceder, and M. Asta. *Low-temperature long-range oxygen order in* $YBa_2Cu_3O_z$. Nature **343** 6258, 544–546, 1990.

J. R. Friedman, V. Patel, W. Chen, S. K. Tolpygo, and J. E. Lukens. *Quantum superposition of distinct macroscopic states*. Nature **406**, 43, 2000.

J. Gao, W. A. M. Aarnink, G. J. Gerritsma, and H. Rogalla. *Controlled preparation of all high-Tc SNS-type edge junctions and DC SQUIDs*. Physica C **171**, 126, 1990.

D. Garlaschelli and M. Loffredo. *Generalized Bose-Fermi Statistics and Structural Correlations in Weighted Networks*. Phys. Rev. Lett. **102** 3, 038701, 2009.

M. P. Gelfand. *Zero-temperature spin-wave spectrum of the critical two-layer S=1/2 antiferromagnet*. Phys. Rev. B **53**, 11309, 1996.

A. Giuliani, J. L. Lebowitz, and E. H. Lieb. *Checkerboards, stripes, and corner energies in spin models with competing interactions*. Phys. Rev. B **84** 6, 064205, 2011.

A. Giuliani, E. H. Lieb, and R. Seiringer. *Formation of stripes and slabs near the ferromagnetic transition*. arXiv **math-ph**, 2013. arXiv:1304.6344.

A. S. Goldhaber. *Comment on "Topological quantum effects for neutral particles"*. Phys. Rev. Lett. **62**, 482, 1989.

G. Grüner. *The dynamics of charge-density waves*. Rev. Mod. Phys. **60** 4, 1129–1182, 1988.

K. Hida. *Low Temperature Properties of the Double Layer Quantum Heisenberg Antiferromagnet —Modified Spin Wave Method—*. J. Phys. Soc. Japan **59**, 2230, 1990.

K. Hida. *Quantum Disordered State without Frustration in the Double Layer Heisenberg Antiferromagnet —Dimer Expansion and Projector Monte Carlo Study—*. J. Phys. Soc. Japan **61**, 1013, 1992.

A. A. High, J. R. Leonard, M. Remeika, L. V. Butov, M. Hanson, and A. C. Gossard. *Condensation of Excitons in a Trap*. Nano Lett. **12** 5, 2605–2609, 2012.

H. Hilgenkamp, Ariando, H.-J. H. Smilde, D. H. A. Blank, G. Rijnders, H. Rogalla, J. R. Kirtley, and C. C. Tsuei. *Ordering and manipulation of the magnetic moments in large-scale superconducting pi-loop arrays*. Nature **422**, 50, 2003.

Y. Hotta, T. Susaki, and H. Hwang. *Polar Discontinuity Doping of the LaVO3/SrTiO3 Interface*. Phys. Rev. Lett. **99** 23, 236805, 2007.

X. Huang, W. Dietsche, M. Hauser, and K. V. Klitzing. *Coupling of Josephson Currents in Quantum Hall Bilayers*. Phys. Rev. Lett. **109** 15, 156802, 2012.

J. Hubbard. *Electron Correlations in Narrow Energy Bands*. Proc. Roy. Soc. Lon. A **276**, 238, 1963.

J. Hubbard. *Generalized Wigner lattices in one dimension and some applications to tetracyanoquinodimethane (TCNQ) salts*. Phys. Rev. B **17**, 494, 1978.

D. A. Huse. *Ground-state staggered magnetization of two-dimensional quantum Heisenberg antiferromagnets*. Physical Review B (Condensed Matter) **37**, 2380, 1988.

M. Imada, A. Fujimori, and Y. Tokura. *Metal-insulator transitions*. Rev. Mod. Phys. **70** 4, 1039–1263, 1998.

J. C. Inkson and P. W. Anderson. *Comment on "Model for an Exciton Mechanism of Superconductivity"*. Physical Review B **8**, 4429, 1973.

C. L. Kane, P. A. Lee, and N. Read. *Motion of a single hole in a quantum antiferromagnet*. Phys. Rev. B **39** 10, 6880–6897, 1989.

T. Kaneko, S. Ejima, H. Fehske, and Y. Ohta. *Exact-diagonalization study of exciton condensation in electron bilayers*. arXiv **cond-mat.str-el**, 2013. arXiv:1305.7298.

A. Kantian, A. J. Daley, P. Törmä, and P. Zoller. *Atomic lattice excitons: from condensates to crystals*. New J. Phys. **9**, 407, 2007.

T. Kato. *On the Convergence of the Perturbation Method. I.*. Prog. Theor. Phys. **4** 4, 514–523, 1949.

L. V. Keldysh and Y. V. Kopaev. *Possible instability of semimetallic state toward coulomb interaction*. Soviet Phys. - Solid State **6** 9, 2219, 1965.

T. A. Kesselring, G. Franzese, S. V. Buldyrev, H. J. Herrmann, and H. E. Stanley. *Nanoscale Dynamics of Phase Flipping in Water near its Hypothesized Liquid-Liquid Critical Point*. Sci. Rep. **2**, 1–6, 2012.

M. Y. Kharitonov and K. B. Efetov. *Electron screening and excitonic condensation in double-layer graphene systems*. Phys. Rev. B **78** 24, 241401, 2008.

D. Klein and W. Seitz. *Perturbation expansion of the linear Hubbard model*. Phys. Rev. B **8** 5, 2236, 1973.

W. H. Kleiner, L. M. Roth, and S. H. Autler. *Bulk Solution of Ginzburg-Landau Equations for Type II Superconductors: Upper Critical Field Region*. Phys. Rev. **133**, 1226, 1964.

M. Kohno and M. Takahashi. *Magnetization process of the spin-1/2 XXZ models on square and cubic lattices*. Phys. Rev. B **56**, 3212, 1997.

J. M. Kosterlitz and D. J. Thouless. *Ordering, metastability and phase transitions in two-dimensional systems*. Journal of Physics C: Solid State Physics **6**, 1181, 1973.

V. N. Kotov, O. Sushkov, Z. Weihong, and J. Oitmaa. *Novel Approach to Description of Spin-Liquid Phases in Low-Dimensional Quantum Antiferromagnets*. Phys. Rev. Lett. **80**, 5790, 1998.

R. Kubo. *The Spin-Wave Theory of Antiferromagnetics*. Phys. Rev. **87**, 568, 1952.

K. I. Kugel and D. I. Khomskii. *The Jahn-Teller effect and magnetism: transition metal compounds*. Soviet Phys. Uspekhi **25**, 231, 1982.

D. P. Landau and K. Binder. *Phase diagrams and critical behavior of a two-dimensional anisotropic Heisenberg antiferromagnet*. Phys. Rev. B **24**, 1391, 1981.

R. B. Laughlin. *Anomalous quantum Hall effect - An incompressible quantum fluid with fractionally charged excitations*. Phys. Rev. Lett. **50**, 1395, 1983.

J.-R. Lee and S. Teitel. *Phase transitions in classical two-dimensional lattice Coulomb gases*. Phys. Rev. B **46**, 3247, 1992.

P. A. Lee, N. Nagaosa, and X.-G. Wen. *Doping a Mott insulator: Physics of high-temperature superconductivity*. Rev. Mod. Phys. **78** 1, 17–85, 2006.

S. Lee, J.-R. Lee, and B. Kim. *Patterns of Striped Order in the Classical Lattice Coulomb Gas*. Phys. Rev. Lett. **88** 2, 025701, 2001.

S. J. Lee, B. Kim, and J. Lee. *Infinite ground state degeneracy and glassy dynamics in the frustrated XY model and lattice Coulomb gas with f=1/6*. Physica A **315**, 314, 2002.

T. D. Lee and C. N. Yang. *Statistical Theory of Equations of State and Phase Transitions. II. Lattice Gas and Ising Model.* Phys. Rev. **87**, 410, 1952.

A. J. Leggett. *Quantum Liquids: Bose Condensation and Cooper Pairing in Condensed-matter Systems.* Oxford graduate texts in mathematics. Oxford University Press, Oxford, 2006.

B. W. A. Leurs, Z. Nazario, D. I. Santiago, and J. Zaanen. *Non-Abelian hydrodynamics and the flow of spin in spin orbit coupled substances.* Annals of Physics **323**, 907–945, 2008.

X. Li, W. Cai, J. An, S. Kim, J. Nah, D. Yang, R. Piner, A. Velamakanni, I. Jung, E. Tutuc, S. K. Banerjee, L. Colombo, and R. S. Ruoff. *Large-Area Synthesis of High-Quality and Uniform Graphene Films on Copper Foils.* Science **324** 5932, 1312–1314, 2009.

S. Liang, B. Doucot, and P. W. Anderson. *Some New Variational Resonating-Valence-Bond-Type Wave Functions for the Spin-1/2 Antiferromagnetic Heisenberg Model on a Square Lattice.* Phys. Rev. Lett. **61** 3, 365–368, 1988.

E. M. Lifshitz and L. P. Pitaevskii. *Statistical physics. Part 2, Theory of the condensed state.* Butterworth-Heinemann, Oxford, 1980.

U. Löw, V. J. Emery, K. Fabricius, and S. A. Kivelson. *Study of an Ising model with competing long- and short-range interactions.* Phys. Rev. Lett. **72**, 1918, 1994.

Y. E. Lozovik and A. Sokolik. *Electron-hole pair condensation in a graphene bilayer.* JETP Letters **87** 1, 55–59, 2008.

Y. E. Lozovik and V. Yudson. *A new mechanism for superconductivity: pairing between spatially separated electrons and holes.* Soviet Phys. JETP **44** 2, 389–397, 1976.

G. D. Mahan. *Many Particle Physics.* Physics of Solids and Liquids. Springer, 2000.

E. Manousakis. *The spin-1/2 Heisenberg antiferromagnet on a square lattice and its application to the cuprous oxides.* Rev. Mod. Phys. **63** 1, 1–62, 1991.

E. Manousakis. *Photovoltaic effect for narrow-gap Mott insulators.* Phys. Rev. B **82** 12, 125109, 2010.

W. Marshall. *Antiferromagnetism*. Proc. Roy. Soc. Lon. A **232** 1188, 48–68, 1955.

G. Martinez and P. Horsch. *Spin polarons in the t-J model*. Phys. Rev. B **44**, 317, 1991.

T. Matsuda and K. Hida. *Ground State Properties of the Double Layer Quantum Heisenberg Antiferromagnet —Spin Wave Approximation—*. J. Phys. Soc. Japan **59**, 2223, 1990.

Y. Matsushita, M. P. Gelfand, and C. Ishii. *Bond-operator mean field theory for the bilayer Heisenberg model*. J. Phys. Soc. Japan **68** 1, 247–252, 1999.

Z. Y. Meng, T. C. Lang, S. Wessel, F. F. Assaad, and A. Muramatsu. *Quantum spin liquid emerging in two-dimensional correlated Dirac fermions*. Nature **464** 7290, 847–851, 2010.

A. J. Millis and H. Monien. *Spin Gaps and Spin Dynamics in* $La_{2-x}Sr_xCuO_4$ *and* $YBa_2Cu_3O_{7-\delta}$. Phys. Rev. Lett. **70** 18, 2810–2813, 1993.

A. J. Millis and D. G. Schlom. *Electron-hole liquids in transition-metal oxide heterostructures*. Phys. Rev. B **82** 7, 073101, 2010.

H. Min, R. Bistritzer, J.-J. Su, and A. H. MacDonald. *Room-temperature superfluidity in graphene bilayers*. Phys. Rev. B **78** 12, 121401, 2008.

T. Miyazaki, I. Nakamura, and D. Yoshioka. *Bilayer Heisenberg model studied by the Schwinger-boson Gutzwiller-projection method*. Phys. Rev. B **53**, 74246, 1996.

A. Möbius and U. Rössler. *Critical behavior of the Coulomb-glass model in the zero-disorder limit: Ising universality in a system with long-range interactions*. Phys. Rev. B **79** 17, 174206, 2009.

K. Moon, H. Mori, K. Yang, S. Girvin, A. H. MacDonald, L. Zheng, D. Yoshioka, and S.-C. Zhang. *Spontaneous interlayer coherence in double-layer quantum Hall systems: Charged vortices and Kosterlitz-Thouless phase transitions*. Phys. Rev. B **51** 8, 5138–5170, 1995.

S. A. Moskalenko and D. Snoke. *Bose-Einstein condensation of excitons and biexcitons*. Cambridge University Press 2000.

N. F. Mott. *The Basis of the Electron Theory of Metals, with Special Reference to the Transition Metals*. Proceedings of the Physical Society **62**, 416, 1949.

S. Murakami, N. Nagaosa, and S.-C. Zhang. *Dissipationless Quantum Spin Current at Room Temperature*. Science **301**, 1348, 2003.

L. Néel. *Propriétés magnétiques de l'état magnétique et énergie d'interaction entre atomes magnétiques*. Ann. Phys. (Paris) **5**, 232, 1936.

E. A. Nowadnick, S. Johnston, B. Moritz, R. T. Scalettar, and T. P. Devereaux. *Competition Between Antiferromagnetic and Charge-Density-Wave Order in the Half-Filled Hubbard-Holstein Model*. Phys. Rev. Lett. **109** 24, 246404, 2012.

P. Nozieres and D. Pines. *Theory of Quantum Liquids*. Advanced Books Classics. Westview Press, 1999.

Z. Nussinov. *Commensurate and Incommensurate O(n) Spin Systems: Novel Even-Odd Effects, A Generalized Mermin-Wagner-Coleman Theorem, and Ground States*. arXiv **cond-mat.stat-mech**, 2001. cond-mat/0105253v12.

A. M. Oles, L. F. Feiner, and J. Zaanen. *Quantum melting of magnetic long-range order near orbital degeneracy: Classical phases and Gaussian fluctuations*. Phys. Rev. B **61**, 6257, 2000.

A. van Otterlo, K.-H. Wagenblast, R. Baltin, C. Bruder, R. Fazio, and G. Schön. *Quantum phase transitions of interacting bosons and the supersolid phase*. Phys. Rev. B **52**, 90486, 1995.

R. Pentcheva, M. Huijben, K. Otte, W. E. Pickett, J. E. Kleibeuker, J. Huijben, H. Boschker, D. Kockmann, W. Siemons, G. Koster, H. J. W. Zandvliet, G. Rijnders, D. H. A. Blank, H. Hilgenkamp, and A. Brinkman. *Parallel Electron-Hole Bilayer Conductivity from Electronic Interface Reconstruction*. Phys. Rev. Lett. **104**, 166804, 2010.

V. L. Pokrovsky and G. V. Uimin. *On the properties of monolayers of adsorbed atoms*. Journal of Physics C: Solid State Physics **11**, 3535, 1978.

Y. Pramudya, H. Terletska, S. Pankov, E. Manousakis, and V. Dobrosavljevic. *Nearly frozen Coulomb liquids*. Phys. Rev. B **84** 12, 125120, 2011.

Y. Pramudya, H. Terletska, S. Pankov, E. Manousakis, and V. Dobrosavljevic. *Geometrically-frustrated pseudogap phase of Coulomb liquids*. Physica B **407** 11, 1711–1714, 2012.

L. Rademaker, J. van den Brink, H. Hilgenkamp, and J. Zaanen. *Enhancement of spin propagation due to interlayer exciton condensation*. Phys. Rev. B **88**, 121101(R), 2013a.

L. Rademaker, J. van den Brink, J. Zaanen, and H. Hilgenkamp. *Exciton condensation in strongly correlated electron bilayers* 2013d. arXiv:1310.0685.

L. Rademaker, S. Johnston, J. Zaanen, and J. van den Brink. *Determinant quantum Monte Carlo study of exciton condensation in the bilayer Hubbard model* 2013b. arXiv:1310.0623.

L. Rademaker, Y. Pramudya, J. Zaanen, and V. Dobrosavljević. *Influence of long-range interactions on charge ordering phenomena on a square lattice*. Phys. Rev. E **88**, 032121, 2013c.

L. Rademaker, K. Wu, H. Hilgenkamp, and J. Zaanen. *The dynamical frustration of interlayer excitons delocalizing in bilayer quantum antiferromagnets*. Europhys. Lett. **97**, 27004, 2012a.

L. Rademaker, K. Wu, and J. Zaanen. *Dynamics of a single exciton in strongly correlated bilayers*. New J. Phys. **14**, 3040, 2012b.

L. Rademaker, J. Zaanen, and H. Hilgenkamp. *Prediction of quantization of magnetic flux in double-layer exciton superfluids*. Phys. Rev. B **83** 1, 012504, 2011.

T. C. Ribeiro, A. Seidel, J. H. Han, and D.-H. Lee. *The electronic states of two oppositely doped Mott insulators bilayers*. Europhys. Lett. **76**, 891, 2006.

S. Sachdev. *Quantum Phase Transitions, Second Edition*. Cambridge University Press, 2011.

M. B. Salamon and M. Jaime. *The physics of manganites: Structure and transport*. Rev. Mod. Phys. **73**, 583, 2001.

A. W. Sandvik, A. V. Chubukov, and S. Sachdev. *Quantum critical behavior in a two-layer antiferromagnet*. Phys. Rev. B **51**, 16483, 1995.

A. W. Sandvik and D. J. Scalapino. *Order-disorder transition in a two-layer quantum antiferromagnet*. Phys. Rev. Lett. **72** 17, 2777, 1994.

J. Schmalian and P. G. Wolynes. *Stripe Glasses: Self-Generated Randomness in a Uniformly Frustrated System*. Phys. Rev. Lett. **85**, 836, 2000.

S. Schmitt-Rink, C. M. Varma, and A. E. Ruckenstein. *Spectral Function of Holes in a Quantum Antiferromagnet*. Phys. Rev. Lett. **60** 26, 2793–2796, 1988.

S. E. Schnatterly. *Inelastic Electron Scattering Spectroscopy*. Solid State Phys. **24**, 274, 1979.

W. Selke. *The ANNNI model - Theoretical analysis and experimental application*. Phys Rep **170** 4, 213–264, 1988.

P. Sengupta, L. P. Pryadko, F. Alet, M. Troyer, and G. Schmid. *Supersolids versus Phase Separation in Two-Dimensional Lattice Bosons*. Phys. Rev. Lett. **94** 20, 207202, 2005.

B. Seradjeh, J. E. Moore, and M. Franz. *Exciton Condensation and Charge Fractionalization in a Topological Insulator Film*. Phys. Rev. Lett. **103**, 66402, 2009.

B. Seradjeh, H. Weber, and M. Franz. *Vortices, Zero Modes, and Fractionalization in the Bilayer-Graphene Exciton Condensate*. Phys. Rev. Lett. **101** 24, 246404, 2008.

A. Shekhter, B. J. Ramshaw, R. Liang, W. N. Hardy, D. A. Bonn, F. F. Balakirev, R. D. Mcdonald, J. B. Betts, S. C. Riggs, and A. Migliori. *Bounding the pseudogap with a line of phase transitions in* $YBa_2Cu_3O_{6+\delta}$. Nature **498** 7452, 75–77, 2013.

D. N. Sheng, Y. C. Chen, and Z.-Y. Weng. *Phase String Effect in a Doped Antiferromagnet*. Phys. Rev. Lett. **77**, 5102, 1996.

S. I. Shevchenko. *Theory of superconductivity of systems with pairing of spatially separated electrons and holes*. Soviet J. Low Temp. Phys. **2** 4, 251–257, 1976.

S. Shimizu, H. Mukuda, Y. Kitaoka, A. Iyo, Y. Tanaka, Y. Kodama, K. Tokiwa, and T. Watanabe. *Uniform Mixing of Antiferromagnetism and High-Temperature Superconductivity in Electron-Doped Layers of Four-Layered* $Ba_2Ca_3Cu_4O_8F_2$*: A New Phenomenon in an Electron Underdoped Regime*. Phys. Rev. Lett. **98** 25, 257002, 2007.

D. Snoke. *Condensed-matter physics - Coherent questions*. Nature **443** 7110, 403–404, 2006.

T. Sommer, M. Vojta, and K. Becker. *Magnetic properties and spin waves of bilayer magnets in a uniform field*. Eur. Phys. J B **23** 3, 329–339, 2001.

I. Spielman, J. Eisenstein, L. Pfeiffer, and K. W. West. *Resonantly enhanced tunneling in a double layer quantum Hall ferromagnet*. Phys. Rev. Lett. **84** 25, 5808–5811, 2000.

H. L. Stormer. *Nobel Lecture: The fractional quantum Hall effect*. Reviews of Modern Physics **71**, 875, 1999.

J.-J. Su and A. H. MacDonald. *How to make a bilayer exciton condensate flow*. Nat. Phys. **4** 10, 799–802, 2008.

M. Takahashi. *Half-filled Hubbard model at low temperature*. J. Phys.: Condens. Matter **10**, 1289, 1977.

I. Takeuchi, S. N. Mao, X. X. Xi, K. Petersen, C. J. Lobb, and T. Venkatesan. *Observation of Josephson effect in* $YBa_2Cu_3O_{7-x}/Nd_{1.85}Ce_{0.15}CuO_{4-y}$ *bilayer junctions*. Applied Physics Letters **67**, 2872, 1995.

J. M. Tranquada, D. J. Buttrey, V. Sachan, and J. E. Lorenzo. *Simultaneous ordering of holes and spins in* $La_2NiO_{4.125}$. Phys. Rev. Lett. **73**, 1003, 1994.

J. M. Tranquada, G. Shirane, B. Keimer, S. Shamoto, and M. Sato. *Neutron scattering study of magnetic excitations in* $YBa_2Cu_3O_{6+x}$. Phys. Rev. B **40**, 4503, 1989.

J. M. Tranquada, B. J. Sternlieb, J. D. Axe, Y. Nakamura, and S. Uchida. *Evidence for stripe correlations of spins and holes in copper oxide superconductors*. Nature **375**, 561, 1995.

N. Trivedi and M. Randeria. *Deviations from Fermi-Liquid Behavior above Tc in 2D Short Coherence Length Superconductors*. Phys. Rev. Lett. **75**, 312, 1995.

N. Trivedi, R. T. Scalettar, and M. Randeria. *Superconductor-insulator transition in a disordered electronic system*. Phys. Rev. B **54** 6, 3756–3759, 1996.

A. Tröster. *Short-range character of the antiferromagnetic Ising model with $1/r^p$ interaction*. Phys. Rev. B **81** 1, 012406, 2010.

M. Troyer and U. Wiese. *Computational complexity and fundamental limitations to fermionic quantum monte carlo simulations*. Phys. Rev. Lett. **94** 17, 170201, 2005.

C. M. Varma. *Non-Fermi-liquid states and pairing instability of a general model of copper oxide metals*. Physical Review B (Condensed Matter) **55**, 83284, 1997.

J. Villain. *Two-level systems in a spin-glass model. I. General formalism and two-dimensional model*. Journal of Physics C: Solid State Physics **10**, 4793, 1977.

M. Vojta and K. Becker. *Doped bilayer antiferromagnets: Hole dynamics on both sides of a magnetic ordering transition*. Phys. Rev. B **60** 22, 15201–15213, 1999.

C. H. van der Wal, A. C. J. T. Haar, F. K. Wilhelm, R. N. Schouten, C. J. P. M. Harmans, T. P. Orlando, S. Lloyd, and J. E. Mooij. *Quantum Superposition of Macroscopic Persistent-Current States*. Science **290** 5492, 773–777, 2000.

Y. Y. Wang, F. C. Zhang, V. P. Dravid, K. K. Ng, M. V. Klein, S. E. Schnatterly, and L. L. Miller. *Momentum-Dependent Charge Transfer Excitations in $Sr_2CuO_2Cl_2$ Angle-Resolved Electron Energy Loss Spectroscopy*. Phys. Rev. Lett. **77**, 1809, 1996.

Z. Weihong. *Various series expansions for the bilayer S= Heisenberg antiferromagnet*. Phys. Rev. B **55**, 74343, 1997.

X.-G. Wen. *Quantum Field Theory of Many-Body Systems: From the Origin of Sound to an Origin of Light and Electrons*. Oxford Graduate Texts. Oxford University Press, Oxford, 2007.

Z.-Y. Weng. *Phase String Theory for Doped Antiferromagnets*. Int. J. Mod. Phy. B **21** 6, 773, 2007.

S. R. White, D. J. Scalapino, R. L. Sugar, N. Bickers, and R. T. Scalettar. *Attractive and repulsive pairing interaction vertices for the two-dimensional Hubbard model*. Phys. Rev. B **39** 1, 839–842, 1989a.

S. R. White, D. J. Scalapino, R. L. Sugar, E. Y. Loh, J. E. Gubernatis, and R. T. Scalettar. *Numerical study of the two-dimensional Hubbard model*. Phys. Rev. B **40**, 506, 1989b.

E. Wigner. *On the Interaction of Electrons in Metals*. Phys. Rev. **46**, 1002, 1934.

K. Wu, Z.-Y. Weng, and J. Zaanen. *Sign structure of the tJ model*. Phys. Rev. B **77** 15, 155102, 2008.

J. M. Yeomans. *Statistical Mechanics of Phase Transitions*. Oxford University Press, 1992.

D. Yu, Q. Gu, H. Wang, and J. Shen. *Bond-operator approach to the bilayer Heisenberg antiferromagnet*. Phys. Rev. B **59** 1, 111–114, 1999.

S. Yunoki. *Numerical study of the spin-flop transition in anisotropic spin-1/2 antiferromagnets*. Phys. Rev. B **65**, 92402, 2002.

J. Zaanen. *The Classical Condensates, from Crystals to Fermi-liquids*. Lorentz Institute for Theoretical Physics, 1996.

J. Zaanen. *Quantum phase transitions in cuprates: stripes and antiferromagnetic supersolids*. Physica C **317**, 217, 1999.

J. Zaanen. *The sound of a hidden order*. Nature **498**, 41, 2013.

J. Zaanen and O. Gunnarsson. *Charged magnetic domain lines and the magnetism of high-Tc oxides*. Phys. Rev. B **40** 10, 7391–7394, 1989.

J. Zaanen and B. J. Overbosch. *Mottness collapse and statistical quantum criticality*. Phil. Trans. R. Soc. A **369**, 1599, 2011.

C.-H. Zhang and Y. N. Joglekar. *Excitonic condensation of massless fermions in graphene bilayers*. Phys. Rev. B **77** 23, 233405, 2008.

F. C. Zhang and K. K. Ng. *Theory of excitons in the insulating Cu-O2 plane*. Phys. Rev. B **58**, 13520, 1998.

N. Zhang and C. Henley. *Stripes and holes in a two-dimensional model of spinless fermions or hardcore bosons*. Phys. Rev. B **68** 1, 014506, 2003.

S.-C. Zhang. *A unified theory based on SO(5) symmetry of superconductivity and antiferromagnetism*. Science **275** 5303, 1089–1096, 1997.

D. N. Zubarev. *Double-Time Green Functions in Statistical Physics*. Soviet Phys. Uspekhi **3**, 320, 1960.

Samenvatting

Dit proefschrift gaat over **kwantummaterie**, oftewel de collectieve gedragingen van een veelheid aan kwantumdeeltjes. In een stukje metaal of legering zitten circa 10^{26} atomen die zich meestal gezamenlijk ordenen in een kristalstructuur. Natuurkundigen kijken dan ook niet naar de eigenschappen van een enkel atoom, maar naar het totale systeem: het geheel is meer dan de som der delen. Zaken als elektrische geleidbaarheid of de magnetisatie zijn vaak het gevolg van het gezamenlijk gedrag van elektronen, die relatief vrij door het kristalrooster van atomen kunnen bewegen.

Elektronen zijn kwantumdeeltjes. Nu hebben kwantumdeeltjes de bijzondere eigenschap dat ze **ononderscheidbaar** zijn, wat het beste uitgelegd kan worden met een voorbeeld. Neem twee 'kwantumdeeltjes' die kop of munt kunnen zijn met 50% kans. De kans dat deze twee kwantumdeeltjes allebei kop zijn is 33%, bij twee gewone munten is die kans 25%. De kwantumdeeltjes met deze eigenschap noemen we **bosonen**, lichtdeeltjes (fotonen) vallen in deze categorie. Uit het voorbeeld blijkt dat een verzameling bosonen relatief vaak allemaal 'hetzelfde' willen doen.

Daarentegen is er in de kwantumstatistische fysica ook een ander type kwantumdeeltje, dat zich juist extreem individualistisch gedraagt. Deze noemen we **fermionen**. Het Pauli **uitsluitingsprincipe** verbiedt dat meer dan twee fermionen in dezelfde toestand zitten. Voorbeelden van fermionen zijn elektronen, protonen en neutronen. De elektronen die in een kristalstructuur bewegen hebben dankzij het uitsluitingsprincipe elk een andere snelheid. De gemiddelde bewegingsenergie van elektronen in een metaal is daardoor veel hoger dan je zonder kwantumtheorie zou verwachten.

Het uitsluitingsprincipe lijkt op het eerste gezicht te suggereren dat fermionen onderscheidbaar zijn: elke fermion zit immers in

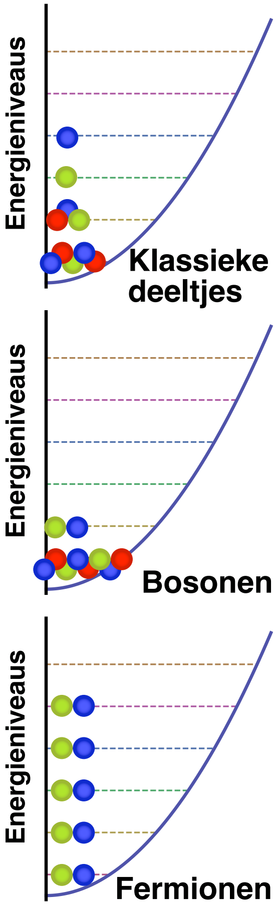

Figuur 1: Het verschil tussen klassieke deeltjes, de conformistische bosonen en de individualistische fermionen. De kleuren geven de spin van de deeltjes weer, zie voetnoot 42.

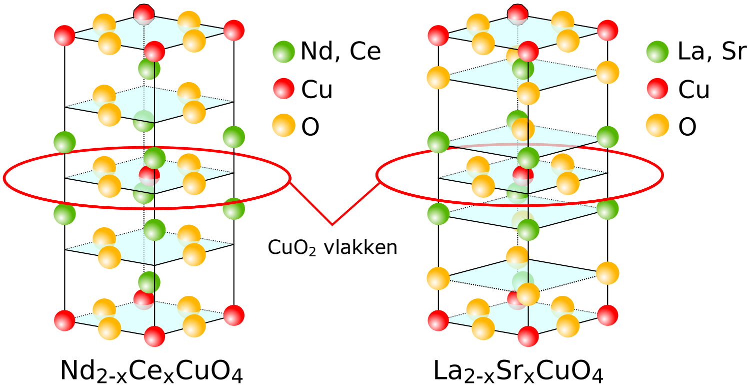

Figuur 2: De kristalstructuur van neodymiumceriumkoperoxide en lanthaanstrontiumkoperoxide, twee voorbeelden van cupraten. Ter indicatie is in beide materialen een koperoxidevlak omcirkelt. De natuurkundige eigenschappen komen voort uit de elektronen in deze koperoxidevlakken.

een andere toestand. Toch zijn fermionen ononderscheidbaar, omdat je namelijk niet kunt zeggen welke fermion in welke toestand zit. Neem bijvoorbeeld twee elektronen op plaats A en B. Dan kunnen we niet zeggen of elektron 1 op plaats A en elektron 2 op plaats B is ($|A_1B_2\rangle$), of andersom ($|B_1A_2\rangle$). Net zoals Schrödingers kat levend én dood tegelijk is, zijn deze twee elektronen op plaats A én B tegelijk. Dit wordt weergegeven met

$$|A_1B_2\rangle - |B_1A_2\rangle,$$

het schoolvoorbeeld van **verstrengeling**.

Fermionen hebben dus de bijzondere eigenschap dat ze met elkaar zijn verstrengeld, ook over langere afstanden. Daarbij bestaat het probleem dat men vaak niet weet waar mintekens geplaatst moeten worden om de toestand van veel verstrengelde fermionen te beschrijven. Dat wordt het '**fermion mintekenprobleem**' genoemd en vormt één van de grootste mysteries van de moderne theoretische natuurkunde. In simpele metalen zoals koper of aluminium speelt de verstrengeling geen rol omdat de elektronen beschreven kunnen worden in een **producttoestand**. Dat wil zeggen dat de verstrengeling ontward kan worden, en de toestand van het geheel beschreven kan worden als het product van de toestand van kleinere, niet verstrengelde delen.

Nu zijn er materialen die niet beschreven worden door zo'n producttoestand, en waarvoor dan ook geen goede theoretische beschrijving bestaat. De **cupraten**, een legering van koperroest met zeldzame aardmetalen zoals in afbeeldingen 2 en 3, zijn een

Figuur 3: Cupraten zijn bekend geworden door hun supergeleidende eigenschappen. Hier is een stuk yttrium-barium-koperoxide (YBCO) te zien, dat door middel van een magneet zwevend gehouden kan worden.

belangrijk voorbeeld. Vrijwel alle fysische eigenschappen komen voort uit de sterk wisselwerkende elektronen in de koperoxidevlakken. Deze groep materialen heeft de hoogste temperatuur waarbij supergeleiding mogelijk is, afhankelijk van de precieze verhouding tussen de zeldzame aardmetalen.

Als een cupraat ongedoteerd is, dat wil zeggen dat $x = 0$ in de chemische formule in figuur 2, is er per koperatoom één elektron vrij beschikbaar. Door de sterke afstotende kracht tussen elektronen ontstaat een file: bij elk koperatoom zit één elektron 'vast'. Deze toestand wordt de **Mott-isolator** genoemd.

Ten opzichte van de Mott-isolator kan je elektronen toevoegen of verwijderen. Daarmee worden 'dubbelbezette' of 'lege' koperatomen gecreëerd.[38] Je kan het materiaal nu beschrijven in termen van de dubbelbezette en lege plaatsen, in plaats van de oorspronkelijke elektronen. Dezelfde elektrische kracht die ervoor zorgt dat elektronen elkaar afstoten, zorgt er nu voor dat dubbelbezette en lege plaatsen elkaar aantrekken. De gebonden toestand van een dubbelbezette en een lege plaats wordt een **exciton** genoemd, zie figuur 4.

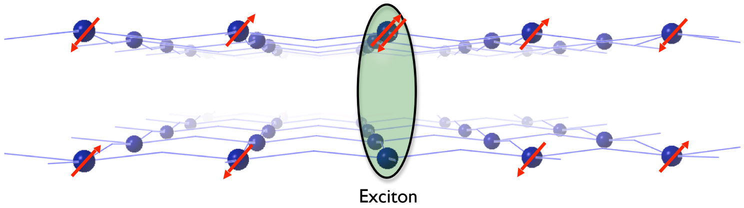

Figuur 4: Het zijaanzicht van een dubbellaagssysteem. De rode pijltjes stellen de spin van de elektronen voor. De dubbelbezette en lege plaats trekken elkaar aan en vormen samen een **exciton**.

De dubbelbezette en lege plaatsen gedragen zich afzonderlijk elk als een fermion. Doordat ze samengebonden worden door de elektrische kracht, gebeurt er iets bijzonders: **samen vormen ze een boson**. Dat betekent enerzijds dat het systeem eenvoudiger theoretisch te beschrijven is, omdat bosonen niet de ingewikkelde langedrachtsverstrengeling kennen die fermionen kenmerken. Anderzijds leidt dat tot de mogelijkheid dat alle excitonen spontaan hetzelfde gaan doen. Dit proces wordt **excitoncondensatie** genoemd. Bij lage temperaturen gedragen alle bosonen zich als één, met als gevolg dat er bosonenstromen kunnen lopen zonder weerstand. Een condensaat wordt daarom ook wel een **supervloeistof** genoemd.

---

[38] Een dubbelbezette plaats wordt een **doublon** genoemd, een lege plaats een **holon**. Het toevoegen van doublonen wordt n-dotering genoemd, het toevoegen van holonen heet p-dotering.

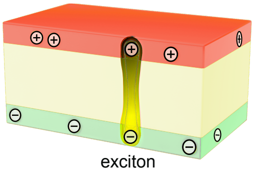

Figuur 5: Een sandwich van verschillende materialen, waarin een dubbellaagsexciton kan ontstaan dat niet annihileert.

Het belangrijkste obstakel voor het vormen van excitoncondensaten is dat excitonen kunnen annihileren. Daarbij verplaatst het 'extra' elektron van de dubbelbezette plaats naar de lege plaats, met als gevolg dat het exciton verdwenen is. Om dit te voorkomen kun je het materiaal met de dubbelbezette plaatsen fysiek scheiden van het materiaal met de lege plaatsen. Dit kan gedaan worden door een **dubbellaagssysteem** te maken, een soort sandwich van het dubbelbezette en lege materiaal zoals in figuur 5.

In de groep van Hans Hilgenkamp aan de Universiteit Twente wordt geprobeerd om zulke sandwiches te maken van cupraten. Mijn theoretische onderzoeksvragen zijn daarbij: *is het mogelijk om excitoncondensaten te maken in de cupraten? Zo ja, wat voor eigenschappen heeft zo'n excitoncondensaat?*

Fenomenologie van excitoncondensaten

In hoofdstuk 2 beschrijf ik wat dubbellaags-excitoncondensaten zijn, en in het bijzonder de gallium-arsenide sandwiches waarin het al gelukt is om condensatie te bereiken. Dankzij universele eigenschappen van de natuurwetten is het mogelijk om onafhankelijk van de details van een systeem al vrij veel effecten te voorspellen. Om die voorspellingen te kunnen doen leid ik de vrije energie van een excitoncondensaat af, deze manier van werken wordt **fenomenologie** genoemd.

Als je een excitoncondensaat hebt, kun je afleiden dat een **excitonstroom** zonder weerstand moet kunnen bestaan. In het geval van een circulaire stroom spelen kwantummechanische effecten op. Immers: alle excitonen gedragen zich als één, en de stroom

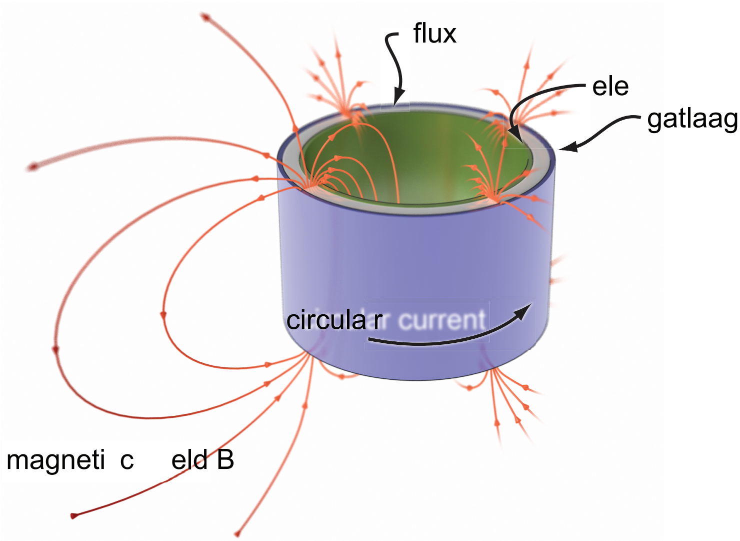

Figuur 6: Het magnetisch veld tussen de twee lagen van het dubbellaagsexcitoncondensaat is gekwantiseerd.

van alle excitonen wordt bepaald door de fase van een complexe golffunctie. Een complexe fase is periodiek,[39] en dientengevolge kan een circulaire stroom alleen maar in bepaalde hoeveelheden voorkomen. Daaruit volgt weer dat het magnetisch veld tussen de p en n-laag **gekwantiseerd**[40] moet zijn.

Fermionische modellen

Vervolgens introduceer ik in hoofdstuk 3 de specifieke theorie die van toepassing is op de cupraten. Binnen het **Hubbard-model** kunnen de elektronen vrijelijk van het ene koperatoom naar het andere springen. Daarnaast kost het energie om twee elektronen op één plaats samen te brengen. Hoe simpel dit model ook klinkt, natuurkundigen zijn er nog steeds niet in geslaagd dit model volledig te begrijpen.

Een manier om dit model op te lossen is met **gemiddelde-veldentheorie**. Daarmee probeer je een producttoestand te formuleren, waarbij de verstrengeling van de fermionen ontward wordt. Dit is echter een onbetrouwbare benadering, omdat je daarbij impliciet aangenomen hebt dat de elektron-elektron interacties zwak zijn terwijl die in de cupraten juist sterk zijn.

Een andere manier is om te proberen met supercomputers kleine systemen exact op te lossen. De methode die we hiervoor gebruiken heet **Determinant Quantum Monte Carlo**, waarbij we de eigenschappen van een groot aantal willekeurig geconstrueerde toestanden uitrekenen.[41] Een grote beperking is echter dat het fermion mintekenprobleem tot grote onzekerheden in de resultaten leidt. We kunnen daarom niet met zekerheid zeggen of er excitoncondensatie optreedt in het dubbellaags Hubbard-model.

---

[39] Net zoals de wijzers op een klok: 13 uur is hetzelfde als 1 uur, bijvoorbeeld.

[40] Het kan alleen bepaalde waarden aannemen. Bijvoorbeeld: als je telt ga je van 1 naar 2, daar kan niets tussen in zitten zolang je jezelf beperkt tot gehele getallen.

Effectieve bosonische modellen

Het grootste nadeel van de fermionische modellen is dan ook het fermion mintekenprobleem. Daarentegen, als de interacties sterk zijn kun je de cupraatsandwich beschrijven met **alleen bosonen**. Naast de excitonen heb je daarbij ook de spin[42] van het elektron. In hoofdstuk 4 leiden we het **exciton-spin** $t - J$ **model** af gebaseerd op het Hubbard-model.

In de Mott-isolator op de vierkante roosterstructuur van de koperatomen ordenen de elektronspins zich als een antiferromagneet. Dat betekent dat op de helft van de koperatomen de spin omhoog wijst, en op de andere helft omlaag, zodanig dat een omhoog-spin altijd omgeven is door spins die omlaag wijzen. Een exciton kan zich in zo'n achtergrond niet goed bewegen. Zolang de antiferromagnetische orde bestaat, is een exciton **gefrustreerd** en de gevolgen daarvan moet je kunnen zien in het lichtabsorptiespectrum van cupraten.

In hoofdstuk 5 bespreken we dan uiteindelijk het excitoncondensaat in een cupraatsandwich. Excitoncondensatie blijkt mogelijk te zijn zolang de bewegingsenergie van de excitonen groot genoeg is. In plaats van frustratie te veroorzaken helpen de spins en excitonen elkaar nu. In het condensaat **lenen de spins bewegingsenergie** van de excitonen, met als gevolg dat je de condensaatdichtheid kan meten via de bewegingsenergie van de spins.

Als de bewegingsenergie van de excitonen niet groot genoeg is om een condensaat te vormen, ontstaat er **fasescheiding** tussen de antiferromagneet, het condensaat en een exciton vaste stof.

In een **exciton vaste stof** zitten de excitonen vast op een specifieke plaats en kunnen niet bewegen, net zoals atomen vastzitten in een blok metaal. Zo'n vaste toestand ontstaat als de afstotende krachten tussen de excitonen groter zijn dan de bewegingsenergie.

[41] De naam is inderdaad afkomstig van het Monte Carlo casino. Men kan namelijk het resultaat van veel willekeurig gespeelde spellen precies voorspellen, zolang het inderdaad heel veel spellen zijn.

[42] Spin is de interne rotatie van een elektron. Dat is een kwantummechanisch fenomeen dat wordt weergegeven door middel van een pijltje met een willekeurige richting.

De simpelste manier om de krachten te beschrijven is om alleen de afstoting tussen twee naastgelegen excitonen te beschouwen. In hoofdstuk 5 laten we zien dat dit leidt tot een **schaakbord**-patroon van excitonen. Maar in werkelijkheid is de afstoting tussen excitonen voelbaar over langere afstanden. Deze lange-afstandsinteractie zorgt ervoor dat een hele verzameling verschillende exciton vaste stoffen kunnen ontstaan. Dit beschrijven we in hoofdstuk 6, waar we voor het gemak de bewegingsenergie van de excitonen verwaarlozen.

Conclusie en vooruitblik

Het is theoretisch dus mogelijk om een excitoncondensaat te maken in cupraatsandwiches. Ik heb daarbij enkele experimentele voorstellen gedaan om dit condensaat te kunnen onderzoeken. Het probleem is echter dat de **theorie ver voor de experimenten uit loopt**. De grootste uitdaging voor dit vakgebied is dan ook de experimentele realisatie van de cupraatsandwiches.

De verschillende fenomenologische, fermionische en bosonische modellen die in dit proefschrift gebruikt zijn dienen als inspiratie om nog eens na te denken over langeafstandsverstrengeling. In hoofdstuk 7 bespreek ik dan ook enkele ideeën over kwantummaterie die leiden tot stellingen behorend bij dit proefschrift.

Curriculum Vitae

I WAS BORN on 26 November 1986 in Vleuten, the Netherlands. Upon completion of my secondary education in 2002 at the Dalton-Vatel in Voorburg, I started studying mathematics and astronomy at Leiden University. I obtained my BSc degree in both fields in 2006, with a thesis under the supervision of Vincent Icke and Vivi Rottschäfer on shock waves in planetary nebulae.

Subsequently, I started to do theoretical physics, for which I obtained a cum laude Masters degree in September 2008. The corresponding thesis under supervision of Koenraad Schalm was entitled "Phase Transitions in Matrix Models". Soon thereafter I decided to switch to theoretical condensed matter physics, and in January 2009 I started to work part-time on my PhD research with Jan Zaanen, Jeroen van den Brink and Hans Hilgenkamp. I was based at the Lorentz Institute, Leiden University, though I had the privilege of visiting Twente University; Stanford University, CA; IFW-Dresden, Germany and the National High Magnetic Field Laboratory in Tallahassee, FL. My teaching duties consisted of assisting the courses Theory of Condensed Matter (2009), Quantum Field Theory (2010-2013) and Effective Field Theory (2011-2013). As a member of the PhD Council of the Dutch Research School for Theoretical Physics I was one of the organisers of the annual PhD-Day (2011-2013) and the Trends in Theory 2013 conference. Additionally I was member of the Instituutsraad of the Leiden Institute of Physics (LION).

Next to my scientific work I have been active in politics. Since 2006 I have been an elected member of the city council of Leiden, as a representative for the Socialist Party.

Publications

- Louk Rademaker, Jan Zaanen and Hans Hilgenkamp, *Prediction of quantization of magnetic flux in double-layer exciton superfluids*, Phys. Rev. B **83**, 012504 (2011); arXiv:1009.1793. See section 2.2.
- Louk Rademaker, Kai Wu, Hans Hilgenkamp and Jan Zaanen, *The dynamical frustration of interlayer excitons delocalizing in bilayer quantum antiferromagnets*. Europhys. Lett. **97**, 27004 (2012); arXiv:1106.5347. See section 4.2.
- Louk Rademaker, Kai Wu and Jan Zaanen, *Dynamics of a single exciton in strongly correlated bilayers*, New J. Phys. **14**, 3040 (2012); arXiv:1202.3616. See section 4.2.
- Louk Rademaker, Jeroen van den Brink, Hans Hilgenkamp and Jan Zaanen, *Enhancement of spin propagation due to interlayer exciton condensation*, Phys. Rev. B **88**, 121101(R) (2013); arXiv:1304.3643. See section 5.1.
- Louk Rademaker, Yohanes Pramudya, Jan Zaanen and Vladimir Dobrosavljević, *Influence of long-range interactions on charge ordering phenomena on a square lattice*, Phys. Rev. E **88**, 032121 (2013); arXiv:1306.4765. See chapter 6.
- Louk Rademaker, Jeroen van den Brink, Jan Zaanen and Hans Hilgenkamp, *Exciton condensation in strongly correlated electron bilayers*, arXiv:1310.0685. See section 5.2.
- Louk Rademaker, Steve Johnston, Jan Zaanen and Jeroen van den Brink, *Determinant quantum Monte Carlo study of exciton condensation in the bilayer Hubbard model*, arXiv:1310.0623. See section 3.3.

Acknowledgements

I feel privileged that I have been able to work at the Lorentz Institute, a place buzzing with interesting people and seminars. I wish to thank all members of the Stripe Club, with special mention to Kai Wu with whom I collaborated most closely. Furthermore, Pierre van Baal, Henk Blöte and Sergei Mukhin have helped me a great deal in my development as a theoretical physicist. The Lorentz Institute itself would be lost without the support of Marianne, Fran and Trudy. As for myself, I could not have finished my thesis without the friendship of my two roommates, first Sjoerd Hardeman and later Robert-Jan Slager.

My friends in Twente, in particular Marcel Hoek and Francesco Coneri, always reminded me of the primacy of experiments over theory. I thank Jeroen Huijben for the beautiful pictures he made. Additionally I had the opportunity to make several foreign visits: to the group of Tom Devereaux at Stanford University where I thank especially Brian Moritz and Steve Johnston for teaching me Monte Carlo techniques, to the IFW-Dresden and finally, to the National High Magnetic Field Lab in Tallahassee, Florida, where I wish to thank Yohanes Pramudya, Vladimir Dobrosavljević and in particular Samiyeh Mahmoudian.

The acknowledgements section is just too short too name everybody, instead, let me hereby thank all other people that I have had inspiring physics discussions with.

From a scientific point of view this might be contested, but life is more than physics. I want to thank all my friends, though they did not contribute directly to the content of this thesis, they did contribute in keeping me sane and happy. The same holds true for my family, especially my brother Merijn, my father Jan and mother Ruth.